

Adaptive micro electret vibrational energy harvester

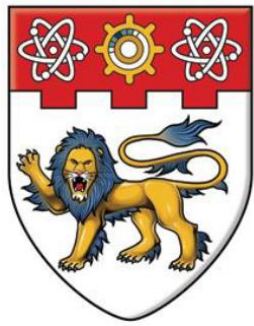
Tao, Kai

2016

Tao, K. (2016). Adaptive micro electret vibrational energy harvester. Doctoral thesis, Nanyang Technological University, Singapore.

<https://hdl.handle.net/10356/68571>

<https://doi.org/10.32657/10356/68571>



NANYANG
TECHNOLOGICAL
UNIVERSITY

**ADAPTIVE MICRO ELECTRET VIBRATIONAL
ENERGY HARVESTER**

TAO KAI

SCHOOL OF MECHANICAL & AEROSPACE ENGINEERING

2016

ADAPTIVE MICRO ELECTRET VIBRATIONAL ENERGY HARVESTER

TAO KAI

School of Mechanical & Aerospace Engineering

A thesis submitted to Nanyang Technological University in partial
fulfilment of the requirements for the degree of
Doctor of Philosophy

2016

ABSTRACT

Recent advances in embedded autonomous wireless sensors and low-power electronic devices have led to the rapid emergence of micro-scale energy harvesting technologies. Such harvesters may pave the primary step forward to actualizing of self-autonomous devices and performing of intelligent monitoring activities. Most resonant-based energy harvesters are currently only efficient in a narrow bandwidth near the sole resonance and could only perform optimally when their oscillation is precisely aligned with the single designed excitation direction. Such characteristics would limit their applications in the real-world environment where a wide spectrum with frequency-variant or direction-random vibrations usually exists.

This thesis investigates adaptive methods to extend frequency spectrum bandwidth and multi-directional response of the harvester from both sophisticated electromechanical coupling of electrostatic energy harvesting systems and advanced mechanical configuration perspectives. Electret-based electrostatic vibration energy harvesters (e-VEHs) are explored in this work as they are advantageous in terms of silicon CMOS compatible processes, low operating frequencies as well as great flexibilities via the capability to design the mechanical and electrical features separately.

To make the energy harvester adaptive to multiple excitation directions, two-dimensional (2D) dynamic response of a symmetrical spring-mass resonant system was investigated by combining its two primary orthogonal oscillation modes. The energy harvesting efficiency of the proposed 2D resonators were theoretically calculated to be superior to conventional 1D counterpart. A rotational symmetrical circular resonator composing of a movable disk-shaped seismic mass and suspended by three sets of spiral springs had been successfully designed, fabricated and characterized. A general numerical model based on the experiment results was created

to describe the dynamic motion of the seismic mass, which would form a basis in developing a real 2D energy harvester. Prototype with sandwich structure was studied that had two separate capacitive circuits 180° out-of-phase with each other to be integrated into a single seismic mass system. This configuration had its merits in that both the vertical pull-in electrostatic force as well as the horizontal damping force could be reduced. With the present prototype, an overall output power of $0.12 \mu\text{W}$ was obtained for the two capacitive parts at an acceleration of $0.2g$ at 125 Hz .

To cater to the broadband spectrum exhibited by ambient vibrations, two approaches were intensively investigated that sought to expand frequency spectrum of energy harvesters, namely ‘nonlinear technique’ and ‘multi-frequency energy harvesting’. Nonlinear technique was considered to be an effective way to enlarge the frequency spectrum by utilizing spring softening and hardening effects. Although numerous methods had been proposed to induce nonlinearities of energy harvesting system previously, electrostatic nonlinearity introduced by electret surface potential, as an inherent feature of e-EVHs, was seldom studied up to date. It was practically more advantageous and readily compatible with Micro-Electro-Mechanical-System (MEMS) energy harvesting devices. To study the spring softening nonlinear phenomenon of electret-based energy harvesting system, an analytical nonlinear model of e-VEH was derived, where the electromechanical coupling effect arising from mechanical and electrical domains was incorporated. As a proof of concept, an out-of-plane energy harvester device with dual-charged electret plates has also been designed and fabricated. At a high excitation level of $0.48 g$, the experimental results showed that the 3-dB bandwidth was enlarged by 2.85 times from 1.3 Hz (bandwidth of linear response) to 3.7 Hz . An optimal output power of $0.95 \mu\text{W}$ was also achieved with a low resonance of 95 Hz .

Compared with other broadband approaches involving extra mechanical components and tuning efforts, multi-frequency technique exploiting multiple vibration modes of

single two-degree-of-freedom (2DOF) system provides a simple and reliable solution to increase the energy harvesting effectiveness. By precisely tuning the accessory mass, the first two resonances of primary mass can be tuned close to each other while maintaining comparable magnitudes. This enables both modes to contribute towards the overall energy harvesting. A lumped parametric model of 2DOF vibrational system was built and examined for its energy harvesting capabilities. Electret-based MEMS devices are particularly suited to such multi-frequency technique, where various parameters, such as beam width and seismic mass, can be precisely controlled through lithography process. Thereby, a 2DOF e-VEH was designed and implemented as proof of concept. The experimental results were in good agreement with the numerical models and Finite Element Analysis (FEA). With further increased excitation accelerations, the 2DOF e-VEH system demonstrated a spring hardening nonlinear effect, where the first peak was capable of being driven towards convergence with the second one to achieve a broadband energy harvesting system. Such novel nonlinear two-degree-of-freedom (2DOF) energy harvesting system combines advantages of both multi-modal energy harvesting and the nonlinear technique, which offers new insight of increasing bandwidth with hybrid broadband mechanisms.

ACKNOWLEDGEMENTS

I would like to express my deep sense of gratitude to my supervisor Prof. Lye Sun Woh for his consistent support, encouragement and guidance during my entire Ph.D period. I would never forget his sacrifice for spending hours and hours with me on discussion of research topic, scope, methodology as well as the corrections and revisions of my papers and thesis. He has given me the freedom of selecting research topics and dealing the problems in my own way, while constantly challenges my ideas and makes me learn how to defend and develop my ideas in a logical way and grow intellectually. The critical thinking skill learnt during the Ph.D study is beneficial and invaluable for my future life. I cannot think of a better research experience than my past four years under the supervisor of Prof. Lye.

I would like to thank Prof. Miao Jianmin for his consistent concern and assistance. I'm really fortunate to join his vibrant MEMS group and work in Micromachines Lab which was built by himself several years ago. He has profound knowledge in MEMS device design and fabrication and his technical advice always inspires me to come up with fresh ideas. I'm also very thankful to Prof. Hu for guiding me to tap into the exciting world of material science and giving me precious suggestions.

I would also like to express my great gratitude towards my senior, Dr. Liu Shuwei, for devoting her resources to full support this study and providing precious advices when I encounter difficulties. Her contribution cannot be understated and is truly appreciated. Special thanks should also be given to my senior Dr. Tang Lihua from University of Auckland. He helps to clarify some electromechanical coupling and modelling issues. The collaborative work with him is always fruitful and enjoyable. Thanks should also be given to Dr. Xia Xin for his unconditional help in both fabrication process and corrections of writings.

I would like to thank my labmates in Micromachines Lab, especially Maciej Baranski, Lu Jingyu, Shen Zhiyuan, Nay Lin, Ajay Kottapalli, Hendrik Hans, Mohsen, Pan Shanshan, Xue Fei, Wang Nan, Hu Liangsheng, Elgar, Sanathanan, Hooi Chee Quen for their rewarding discussions and constant support. I would like to thank FYP students Lee Weixiang, Teo Jingsheng, Lim Song Kiat Jacob for their assistance. I would like to thank all the Micromachines Lab and Mechanics of Micromachines Lab technicians Mr. Hoong Sinpoh, Mr. Pek Soo Siong, Mr. Ho Kar Kiat, Mr. Nordin Bin Abdul Kassim, Mrs. Halimatun and Mr. Cheo. They have been very supportive in my experiment.

Last but not the least, I would like to express my deepest appreciation to my wife Yang, Lixia and my family in China for their constant encouragement and unwavering love in each day of my life. They make my life so colorful and exciting. Finally, all the contributions from the many not named above are not forgotten, but greatly appreciated.

CONTENTS

	Page
ABSTRACT	I
ACKNOWLEDGEMENTS	IV
CONTENTS	VI
LIST OF FIGURES	IX
LIST OF TABLES	XVI
LIST OF ABBREVIATIONS	XVII
 1. INTRODUCTION	
1.1 Background	1
1.2 State-of-art challenges	4
1.3 Objectives	10
1.4 Organization of thesis and research roadmap	12
 2. LITERATURE REVIEW	
2.1 Vibration-to-electricity transduction mechanisms	15
2.1.1 Piezoelectric power generator	16
2.1. 2 Electromagnetic power generator	23
2.1. 3 Electrostatic power generator	27
2.2 Multi-directional vibration energy harvesting	47
2.3 Frequency broadening energy harvesting strategies	52
2.3.1Broadband energy harvesting using nonlinear mechanisms	52
2.3.2 Multi-frequency energy harvesting	57
2.4 Comparative review of energy harvesting schemes	61
 3. SANDWICH-STRUCTURED 2D ELECTRET MICRO POWER GENERATOR	 63
3.1 Introduction	63
3.2 Device design and modeling	66

3.2.1 Device configuration	66
3.2.2 Mechanical analysis	67
3.2.3 Electrostatic Force analysis	69
3.3 Fabrication Process	73
3.4 Power generation experiment	78
3.5 Summery of findings	84
4. 2D ELECTRET MICRO POWER GENERATOR WITH SPIRAL SPRINGS	85
4.1 Introduction	85
4.2 Device design and modelling	88
4.2.1 Device configuration	88
4.2.2 Mechanical spring analysis	89
4.2.3 Dynamic modal analysis	94
4.3 Comparative study of the effectiveness for 1D and 2D systems	95
4.4 Fabrication	98
4.4.1 Micro-patterning of electret thin films	98
4.4.2 Fabrication of spring-mass architecture and assembly	101
4.5 Power generation experiment	103
4.5 Summery of findings	108
5. OUT-OF-PLANE NONLINEAR MEMS ELECTRET POWER GENERATOR	110
5.1 Introduction	110
5.2 Device design and fabrication	112
5.2.1 Device configuration	112
5.2.2 Microfabrication	113
5.3 Modeling	116
5.3.1 Mechanical modeling	116
5.3.2 Electro-mechanical dynamic modeling	118
5.4 Results and discussion	122
5.4.1 Weak excitation mode	123

5.4.2 Moderate excitation mode	124
5.4.3 Strong excitation mode	126
5.4.4 Output power evaluation	127
5.5 Summery of findings	130
6. A NONLINEAR 2DOF MEMS ELECTRET VIBRATIONAL POWER GENERATOR	132
6.1 Introduction	132
6.2 Numerical modeling of 2DOF system	134
6.3 Device design and fabrication	139
6.3.1 Device configuration	139
6.3.2 Microfabrication	141
6.4 Mechanical dynamic analysis	144
6.4.1 Modal analysis	144
6.4.2 Harmonic analysis	146
6.5 Device characterization	148
6.5.1 Linear 2DOF frequency responses	149
6.5.2 Resonant frequency and amplitude responses	151
6.5.3 Nonlinear 2DOF responses with increased excitations	154
6.5.4 Frequency responses at high excitation levels	158
6.6 Summery of findings	159
7. CONCLUSIONS AND FUTURE WORK	161
7.1 Conclusions on current work	161
7.2 Original contributions	163
7.3 Recommendations for future work	164
REFERENCES	167
AUTHOR'S PUBLICATIONS	181

LIST OF FIGURES

CHAPTER 1

- Figure 1.1 Typical block diagram of the wireless integrated sensor nodes (a); An assembled sensor network node of Tyndall 25(b)
- Figure 1.2 Superimposed frequency spectrums of 67 trains in the Arlberg-Tunnel
- Figure 1.3 Acceleration PSD versus frequency for compressor base ((a) and (b)) and fan belt cage ((c) and (d))
- Figure 1.4 PSD (power spectral density) of a car tire vibrations at a car speed of 50 km/h with an example of a sole resonant energy harvesters (500 Hz) with a narrow bandwidth of 2.7 Hz
- Figure 1.5 Schematic of the thesis structure layout of proposed MEMS e-VEH device

CHAPTER 2

- Figure 2.1 Two types of piezoelectric energy harvesters (a) d_{31} mode and (b) d_{33} mode
- Figure 2.2 SEM photograph of two types of piezoelectric MEMS generators (a) d_{31} mode and (b) d_{33} mode
- Figure 2.3 Integrating three devices for parasitic power harvesting in shoes: (a) a PVDF insole stave; (b) a Thunder PZT unimorph; (c) a shoe mounted rotary magnetic generator; (d) exploded view of integration of piezos.
- Figure 2.4 (a) AlN-based MEMS piezoelectric energy harvester packaged in between glass substrates; (b) the harvester prototype mounted on a supportive board
- Figure 2.5 An AA sized vibration based micro generator: the micro power transducer's inner structure (left); the power management circuit and the micro power transducer, and an assembled AA-sized MPG containing the power manage circuit and two MPTs
- Figure 2.6 MEMS-based electrostatic transducer by Menninger et al.
- Figure 2.7 Three different electrostatic conversion modes: (a) In-plane overlap varying; (b) In-plane gap closing; (c) Out-of-plane gap varying
- Figure 2.8 Exploded view (left) and prototype (right) of power generator
- Figure 2.9 Schematic of the transducer layout (left) and micro power generator chips packaged in CLCC packages (right)

- Figure 2.10 Two operation modes of e-VEHs: (a) In-plane overlapping type; (b) Out-of-plane gap closing
- Figure 2.11 A simplified model of in-plane e-VEH excluding the mechanical configurations
- Figure 2.12 DRIE patterned $\text{SiO}_2/\text{Si}_3\text{N}_4$ electret: (a) cross section view, (b) $\text{SiO}_2/\text{Si}_3\text{N}_4$ layer coated with HMDS, (c) (d) corner and overall image
- Figure 2.13 Schematic of electrets generator: (a) cross section view; (b) 3-D view of 4-pole rotor and stator
- Figure 2.14 The corona discharging needle-grid setup
- Figure 2.15 Fabrication process of micro-patterning of (a) Polymer-based CYTOP electret [84]; (b) SiO_2 -based $\text{SiO}_2/\text{Si}_3\text{N}_4$ electret
- Figure 2.16 (a) Demonstration of wafer-level simultaneous polarization of multiple electrets and (b) fabrication process of situ wafer-level polarization of electret films
- Figure 2.17 Typical corona charging apparatus and novel charging setup using buried guard electrode
- Figure 2.18 Conceptual diagram of the soft X-ray charging based on local photoionization
- Figure 2.19 3D schematic and real image of electrostatic power generator
- Figure 2.20 Cross-section structure view (left) and wheel with sensors (right) of patterned-electret-based energy harvester for tire pressure monitoring systems
- Figure 2.21 Schematic structure and packaged prototype of in-plane micro electret vibration generator proposed by Suzuki et al.
- Figure 2.22 Proposed principle and schematic of an electret power generator based on fringe field effect
- Figure 2.23 (a) schematic view of out-of-plane e-VEH with FPCB electrode, (b) side view and (c) cross section of the springs
- Figure 2.24 SEM images of a rotary comb capacitive generator and located enlarged components
- Figure 2.25 SEM images of the fabricated 2-DOF MEMS ultrasonic energy harvesting device and packaged prototype
- Figure 2.26 Schematic view of the 2D resonator and enlarged SEM image of the fabricated circular springs
- Figure 2.27 (a) Schematic of the proposed piezoelectric nonlinear energy harvester using mass and permanent magnet interactions; (b) Nonlinear energy

harvesting outperforming linear resonance

- Figure 2.28 Mechanical stretching induced spring hardening nonlinearity with clamped-beam configurations
- Figure 2.29 (a) Schematic of a modified wideband nonlinear energy harvester induced by mechanical stopper effect; (b) Comparison of numerical and experimental frequency–response curves of the RMS load voltage
- Figure 2.30 (a) Optical micrograph of MEMS electrostatic energy harvester with bistable curved springs; (b) RMS output voltage versus frequency for both up- and down-sweeps at different acceleration amplitudes.
- Figure 2.31 Proposed broadband MEMS electromagnetic power generator by Sari et al.
- Figure 2.32 Proposed multi-frequency MEMS piezoelectric power generator by Ferrari et al.
- Figure 2.33 Proposed multi-frequency electromagnetic energy harvester by yang et al.
- Figure 2.34 Proposed multi-frequency vibration energy harvester based on a double-mass piezoelectric cantilever beam by Ou et al.

CHAPTER 3

- Figure 3.1 Schematic illustrations of force reduction mechanisms in both in-plane and out-of-plane directions for sandwich-structured electret power generator: (a) initial state for two-plate structure; (b) small oscillations within two-plate structure; (c) initial state for three-plate structure; (d) small oscillations of the middle plate within three-plate structure
- Figure 3.2 3-D schematic view of the energy harvester
- Figure 3.3 Modal simulation of Spring-mass system: (a) mode I; (b) mode II; (c) mode III
- Figure 3.4 Cross-section view of the sandwich-structured e-VEH
- Figure 3.5 Contours of the potential gradient and vectors of electric field distribution: (a) two-plate structure; (b) sandwiched structure
- Figure 3.6 Vertical electrostatic forces as a function of comparative displacement for the two-plate structure and sandwich structure
- Figure 3.7 Capacitance variations of TCC and BCC as a function of comparative displacement within the sandwich-structured e-VEH
- Figure 3.8 Calculated horizontal electrostatic damping forces for the TCC, BCC and the net force operated on the seismic mass

- Figure 3.9 Fabrication flow and assembly process of the sandwich-structured electret generator
- Figure 3.10 (a) Image of the fabricated spring-mass structure; (b) (c) enlarged views of the alignment holes and elastic beam flexures; (d) SEM image of electrode cells on the seismic mass
- Figure 3.11 SEM image of micro charge distribution (negative charged) and surface potential decay as a function of time
- Figure 3.12 Assembled sandwich-structured electret power generator compared with a ten cents coin
- Figure 3.13 Photograph of the measurement setup
- Figure 3.14 Output voltages as a function of frequencies from 110 to 140 Hz with different excitation angles at 0.2 g
- Figure 3.15 Output voltages as a function of frequencies from 110 to 140 Hz with different excitation angles at 0.2 g
- Figure 3.16 Voltage outputs as a function of time at an acceleration of 0.2 g and a resistance of 10 M Ω for two capacitive ports
- Figure 3.17 Voltages and power outputs against different resistances at the frequency of 125 Hz at 0.2 g
- Figure 3.18 Peak-peak voltage responses at various accelerations ranging from 0.03 to 0.3 g at the frequency of 125 Hz

CHAPTER 4

- Figure 4.1 Simplified equivalent circuit model of the proposed e-VEH
- Figure 4.2 Schematic of the proposed 2D e-VEH device
- Figure 3.3 Three types of spring configurations in xy plane: (a) two-beam spiral springs; (b) three-beam spiral springs; (c) circular-ring springs
- Figure 4.4 Schematic of the proposed resonant architectures with associated parameters: (a) overview of the spring-mass resonant structures; (b) Top view of the configuration; (c) calculated spring stiffness in horizontal 360 °plane
- Figure 4.5 First three vibration modes of the spring-mass resonant system
- Figure 4.6 Comparison of normalized energy harvesting effectiveness for 1D and 2D resonators as a function of excitation angle under viscous damped conditions
- Figure 4.7 Process flow of the localized corona charging of LDPE electret thin

films

- Figure 4.8 SEM images of the charged LDPE electret thin films and associated with the surface potential decay result within three days
- Figure 4.9 SEM images of the fabricated parallel-spiral-spring architectures with associated measurements
- Figure 4.10 Photograph of the fabricated e-VEH device and the top plate with the spiral spring-mass architecture
- Figure 4.11 Experimental setup
- Figure 4.12 Frequency responses of the proposed device when the excitation directions vary from 15° to 105°
- Figure 4.13 Measured output voltages of the proposed device at modes II and III at various excitation directions
- Figure 4.14 Seismic mass oscillation amplitudes for modes II and III at various excitation directions at the acceleration of 0.05 g
- Figure 4.15 Performance comparison of the proposed device with the state-of-the-art electrostatic harvesters

CHAPTER 5

- Figure 5.1 Schematic of the conventional out-of-plane e-VEH and the proposed e-VEH with double-charged electrets and a mechanical elastic stopper
- Figure 5.2 Schematic drawing of the proposed e-VEH device
- Figure 5.3 Optical images of the assembled MEMS e-VEH device and released spring-mass resonant structure
- Figure 5.4 Surface potential decay of corona charged LDPE thin film with a thickness of $15\text{ }\mu\text{m}$
- Figure 5.5 (a) Simulated stress distribution of the e-VEH resonant system when displacement of the seismic mass is fixed at $500\text{ }\mu\text{m}$; (b) resonant frequency and mode shape of the modal analysis
- Figure 5.6 Calculated principle stress and resonant frequencies versus different spiral beam widths
- Figure 5.7 Calculated principle stress and resonant frequencies versus different wafer thicknesses
- Figure 5.8 Lumped equivalent circuit model of the e-VEH device
- Figure 5.9 Simulated results of seismic mass displacement against frequency-up and -down sweeps at accelerations of 0.6, 1.2, 2.4 and 5 m/s^2 with a load

resistance of 1 G Ω

- Figure 5.10 Dynamic response of seismic mass at various load resistance from 50 M Ω to 1 G Ω at an excitation acceleration of 0.3 g
- Figure 5.11 Diagram of experiment setup
- Figure 5.12 Measured peak voltage of frequency-up and -down sweeps at the excitations of 0.12 g and 0.18 g with a load resistance of 4 M Ω
- Figure 5.13 Measured peak voltage of frequency-up and -down sweeps at the excitations of 0.24 g and 0.36 g with a load resistance of 4 M Ω
- Figure 5.14 Output power and voltage against various resistances at resonance with an excitation acceleration of 0.36 g
- Figure 5.15 Measured peak voltage of frequency-up and -down sweeps at the excitations of 0.42 g and 0.48 g with a load resistance of 4 M Ω
- Figure 5.16 Output voltages and resonant frequencies as a function of various excitation accelerations in the range of 0.12~0.6 g for frequency-up and -down sweeps
- Figure 5.17 Optimal output power and normalized power density as a function of various excitation accelerations in the range of 0.12~0.6 g
- Figure 5.18 Normalized power density comparisons with the state-of-the-art electrostatic vibration energy harvesters

CHAPTER 6

- Figure 6.1 Two configurations of harvesters: (a) proposed 2DOF energy harvesting model; (b) conventional 1DOF vibrational energy harvesting model
- Figure 6.2 Dimensionless output power at various mass ratios (μ) and frequency tuning ratios (Ω) for different normalized excitation frequencies: (a) $\alpha=1.1$; (b) $\alpha=1$; (c) $\alpha=0.9$; (d) $\alpha=0.8$
- Figure 6.3 Dimensionless power output of proposed 2DOF system compared with conventional 1DOF system at various frequency tuning ratios (α) and excitation frequencies (Ω) for different mass ratios: (a) $\mu=0.04$; (b) $\mu=0.16$
- Figure 6.4 3D schematic of 2DOF e-VEH device
- Figure 6.5 Fabrication process of the proposed 2DOF spring-mass system by double-side DRIE process
- Figure 6.6 (a) Optical image of the fabricated spring-mass structure; (b) SEM images of the secondary mass with inner spiral springs; (c) (d) trimetric views of the primary mass and beam structures

- Figure 6.7 Optical images of the assembled MEMS e-VEH device compared with a ten cents coin
- Figure 6.8 Top view of the proposed 2DOF spring-mass resonant system
- Figure 6.9 Modal simulation of Spring-mass structure: (a) mode I; (b) mode II
- Figure 6.10 Harmonic response of the primary mass for the proposed 2DOF e-VEH device within a frequency spectrum of 500 to 800 Hz
- Figure 6.11 Harmonic response of the primary mass with an enhanced stiffness of the outer circular beam within a frequency spectrum of 550 to 850 Hz
- Figure 6.12 Vibration response of the 2DOF energy harvester prototype with a frequency sweeping from 400 to 900 Hz: (a) Raw time-domain data records by DAQ system; (b) frequency domain signal by fast Fourier transform
- Figure 6.13 Measured output voltage in frequency sweeps at the excitations of 1.9, 3.2, 4.4 m/s^2 with a resistance of 4 $\text{M}\Omega$
- Figure 6.14 Measured voltage amplitude derivation trend at the various excitation levels: (a) Overall range from 0.64 to 12.8 m/s^2 ; (b) enlarged first portion from 0.64 to 5.6 m/s^2 ; (c) enlarge second portion from 5.6 to 12.8 m/s^2
- Figure 6.15 Measured two resonant frequencies at various excitation levels in the range of: (a) 0.64 to 6.4 m/s^2 ; (b) 6.4 to 13.8 m/s^2 ; (c) 0.64 to 13.8 m/s^2
- Figure 6.16 Output voltage and power against different resistances at the resonance with an acceleration excitation of 2.8 m/s^2
- Figure 6.17 Measured raw voltage time-domain response by DAQ system at the excitation acceleration of 6.4 m/s^2
- Figure 6.18 Measured raw voltage time-domain response by DAQ system at the excitation acceleration of 10 m/s^2
- Figure 6.19 Measured raw voltage time-domain response by DAQ system at the excitation acceleration of 12.8 m/s^2
- Figure 6.20 Measured output voltage in frequency sweeps at the excitations of 2.8, 6.4, 10 and 12.8 m/s^2
- Figure 6.21 Measured voltage time-domain and frequency-domain responses by DAQ system against frequency-up and -down sweeps at the excitation acceleration of 6.4 m/s^2 with a load resistance of 1 $\text{M}\Omega$
- Figure 6.22 Measured voltage time-domain and frequency-domain responses by DAQ system at the excitation acceleration of 19.2 m/s^2 with a load resistance of 1 $\text{M}\Omega$

LIST OF TABLES

Table 1.1	Comparison of energy harvesting methods in the environment
Table 1.2	Survey of ambient vibrations
Table 2.1	Key properties of some representative piezoelectric material used in energy harvesting systems
Table 2.2	Summary of vibration-based MEMS piezoelectric energy harvesters
Table 2.3	Comparison of the state-of-art micro electromagnetic energy harvesters 25
Table 2.4	Summary of the state-of-the-art electrets for e-VEHs
Table 2.5	Summary of the-state-of-the-art micro-patterning techniques for e-VEHs
Table 2.6	Comparison of the state-of-the-art electrostatic energy harvesters
Table 2.7	Comparison of 2D vibrational energy harvesters to the state of the art
Table 2.8	Summary of merits, weakness and applicability of several nonlinear implementation techniques
Table 3.1	Designed parameters and specifications of the proposed MEMS electret power generator
Table 3.2	Comparison of 2D electrostatic VEHs to the state of the art
Table 4.1	Comparisons of stiffness for different types of springs
Table 4.2	Designed specifications and parameters of the 2D e-VEH device
Table 5.1	Parameters of the proposed e-VEH device
Table 6.1	Designed parameters and specifications of the electromagnetic energy harvesting chip

LIST OF ABBREVIATIONS

WSN	Wireless sensor network
CMOS	Complementary Metal-Oxide Semiconductor
IC	Integrated circuit
MEMS	Micro-Electro-Mechanical Systems
PZT	Lead zirconate titanate
PVDF	Polyvinylidene fluoride
DOF	Degree-of-Freedom
PSD	Power spectral density
VEH	Vibrational Energy Harvester
e-VEH	Electret-based Vibrational Energy Harvester
LDPE	Low-density polyethylene
NPD	Normalized power density
MFC	Macro Fiber Composite
SmCo	Samarium–cobalt magnet
NdFeB	Neodymium magnet
VDRG	Velocity-damped resonant generators
DRIE	Deep Reactive Ion Etching
RIE	Reactive Ion Etching
CVD	Chemical Vapour Deposition
PECVD	Plasma-enhanced Chemical Vapour Deposition
TPMS	Tire Pressure Monitoring Systems
FEM	Finite Element Analysis
TCC	Top Capacitive Circuit
BCC	Bottom Capacitive Circuit
HAR	High-Aspect-Ratio
LCP	Liquid Crystal Polymer
PDMS	Polydimethylsiloxane
DAQ	Data Acquisition System

Chapter 1 Introduction

1.1 Background

The continual evolution of integrated circuit (IC) manufacturing techniques and wireless communication technologies has led to microelectronic devices becoming smaller, wireless, portable and consuming less power. It is envisaged that a large amount of wireless sensor nodes (WSNs) would be developed for various applications ranging from national defences, health and environment monitoring, smart sensing and telecommunications to medical implants. To cater for the ever increasing demand of such small devices, CMOS technology and CMOS related MEMS (Micro-Electro-Mechanical Systems) technologies have been widely employed to create miniaturized devices and complex circuit modules through batch-fabrication processes. MEMS devices take advantages of integrated circuit fabrication techniques and thus are inherently compatible with microelectronics devices. They are ideally suited for miniaturization, low power consumption, low cost, and ease of integration with electronics.

A typical WSN mainly composed of four basic components[1]: a sensing component (microelectronic sensors), a data processing unit (ADC module), a data transmitting part (RF transmitter) and the power supply (battery). A block diagram of a wireless integrated sensor node, as shown in Figure 1.1(a), is capable of sending data to a remote location. Figure 1.1 (b) depicts an assembly of miniature sensor network node complete with wireless transmission capability as well as intelligent data mining and storage [2]. The multifunctional micromachined sensor unit based on MEMS technology has been integrated with the highly modular and programmable Tyndall 25 mote with an overall volume of about 30 cm³. These WSNs are expected to be inconspicuous and small acting as self-contained sensor nodes that can be deployed in abundance for monitoring, data collection and transmission about the physical

environment or conditions [3]. Thus, such kinds of sensor nodes are implemented in a “deploy and forget” scenario. Currently, their proliferation in use is however constrained by the amount of power it can generate.

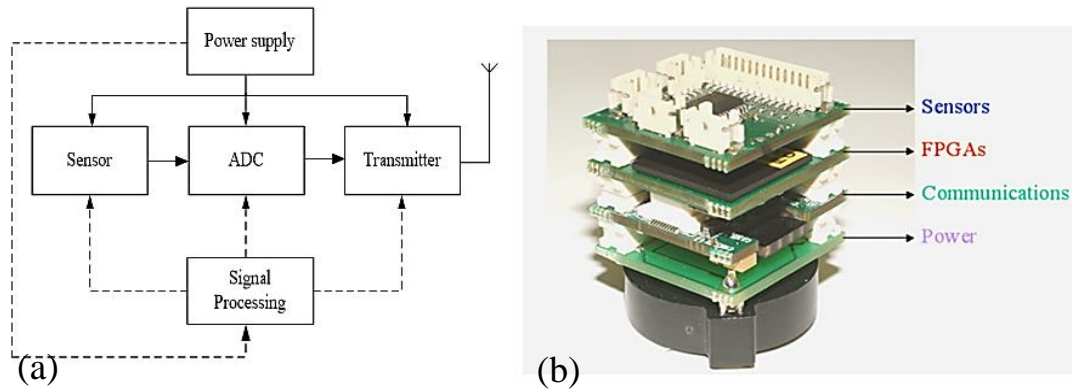


Figure 1.1 Typical block diagram of the wireless integrated sensor nodes(a) [3]; An assembled sensor network node of Tyndall 25(b) [2]

By now, batteries are employed to provide the power source for WSNs which are intended to operate over long period with ease of maintenance. However, as the distributed sensor network grows and electronic devices become smaller in size, providing sustainable power represents a great challenge. This challenge is further compounded if WSNs are deployed in hazardous and non-accessible areas, where replacement of batteries would not be viable. Secondary power source in addition to or replacement of batteries would therefore need to be established. Clearly, harvesting ambient energy to supplement or replace batteries to provide adequate power to operate low-power wireless electronic devices would be an invaluable alternative to have.

There are several existing energy source candidates in the environment for harvesting, including light, mechanical motion, temperature gradient, acoustic and radiofrequency (RF) energy. Table 1.1 provides summary of these sources’ power densities. Energy harvesting from direct outdoor sunlight is clearly the most effective one. Unfortunately, it is not the case for indoor lighting which operates at a level

comparable with thermal and air flow energy. Thermoelectric energy harvesting is constrained by minor temperature gradient over a short length, where energy can be only generated through temporal temperature difference using pyroelectric materials. RF and acoustic energy is several orders of magnitude less than other forms of energy sources. Among these, mechanical vibration energy is attractive because of its versatility and ubiquitous characteristics. Ambient motions can be derived from structures, human body, vehicles, machinery, or air/water flows. Due to their pervasive existence, it is more suitable for small-scale embedded and deployable applications, which fits the goal of sustainable development in reducing the use of battery and performing intelligent monitoring.

Table 1.1 Comparison of energy harvesting methods in the environment

Energy types	Forms	Energy level	Conversion mechanisms	Reference
Solar energy	sunlight	Outdoors: 150 mW/cm ³ Indoors: 10 μ W/cm ³	photovoltaic	[4, 5]
Thermal energy	Temperature gradient	5-100 mW/cm ³	Seebeck effect Thermoelectric	[4-6]
Acoustic noise	Wave	0.003 μ W/cm ³ at 75dB 0.96 μ W/cm ³ at 100dB	Piezoelectric	[7]
Radiation	RF signal	< 1 μ W/cm ²	Electromagnetic	[5, 8]
Fluid flow	Wind ventilation, wave, flowing water	Air: 200-800 μ W/cm ³ Water: 500 mW/cm ³	Electromagnetic piezoelectric	[4]
Kinetic Vibrations	structure and machine vibrations human motion	4-800 μ W/cm ³	Electromagnetic Piezoelectric Electrostatic	[3, 9-11]

Vibration energy can be harvested via different materials and mechanisms. Typical vibration-based energy harvesters normally make use of electromagnetic, piezoelectric, or electrostatic transduction mechanism. Piezoelectric harvesters make

use of certain piezoelectric materials, such as PZT and PVDF, which have the ability to generate an electrical potential when subjected to mechanical strain. Electromagnetic harvesters are developed on the Faraday's law of induction principle in which electrical power is generated via a change of the magnetic flux in the coil. Electrostatic harvesters are based on the capacitance change of the variable capacitors under constant voltage/charge bias, either by an external voltage source or pre-charged electret material. The recent advances as well as merits and drawbacks of various kinetic energy conversion mechanisms will be reviewed in the following chapter.

1.2 State-of-art challenges

Regardless of the various vibrational energy harvesting approaches adopted, resonant-based energy harvesters are usually only efficient in a narrow bandwidth near the sole resonance and could only perform optimally when their oscillation is precisely aligned with single designed excitation direction. Such characteristics would limit their applications in the vast majority of real world environment that usually have a wide spectrum with frequency-variant or direction-random vibrations. These necessitated the following two fundamental issues of vibrational energy harvesting technologies to be explored and addressed:

Narrow Bandwidth Issue

For typical resonant-based energy harvesters, one fundamental issue is that they are only efficient in a narrow bandwidth near the sole resonance when the resonant frequency of the harvesters match the frequency of excitation sources. However, most ambient vibrations such as car-tire vibrations[12], train and car vibrations[13], hard disk vibrations[14], railway vibrations[15, 16] have wide frequency spectra or the main frequency peak can vary over time, which limit the applicability of the

traditional linear vibration-based harvesters with fixed resonance and narrow bandwidth. Figure 1.2 shows an example of superimposed frequency spectrums of 67 trains in the Arlberg-Tunnel [15]. It can be seen that the dominant frequencies exhibit multiple resonances and vary in a broadband range around each resonance, instead of a single resonant peak. If the harvesters are designed for a particular frequency within a narrow bandwidth, once there is a shift from the resonant frequency, the output power of the harvesters drop drastically. As depicted in Figure 1.2, it is assumed that the harvester can only operate at the sole resonance of 600 Hz with narrow bandwidth of tens of Hz. It can be seen that a large amount of vibration energy located at other frequencies would be totally lost, resulting in severe deterioration of overall energy harvesting effectiveness.

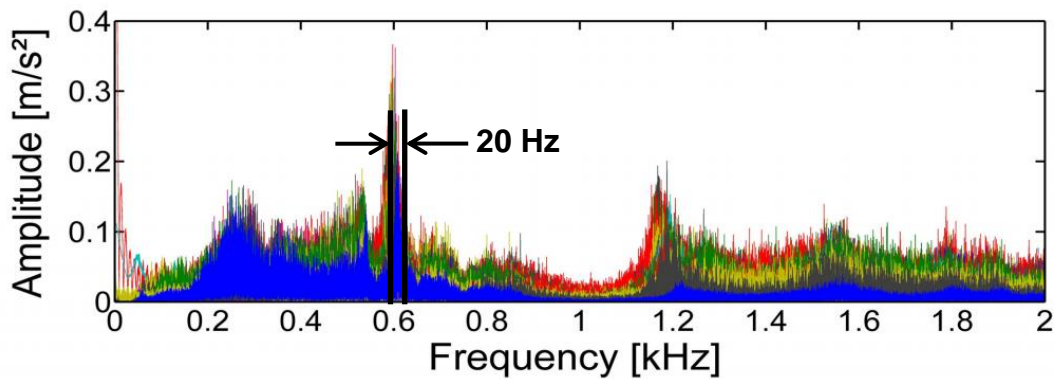


Figure 1.2 Superimposed frequency spectrums of 67 trains in the Arlberg-Tunnel [15]

Such broadband and multi-frequency phenomena are also prevalent in other circumstances such as HVAC (Heating, Ventilation and Air Conditioning) system [17]. Figure 1.3 shows the acceleration power spectral density (PSD) versus frequency for compressor base and fan belt cage. It can be seen that the four vertical fan belt cage exhibit a broadband spectrum in the range of 0~250 Hz, while the dominant frequency peaks for the fan are at 20, 22 and 45 Hz. The compressor base also exhibits three frequency peaks at 30, 60 and 354 Hz.

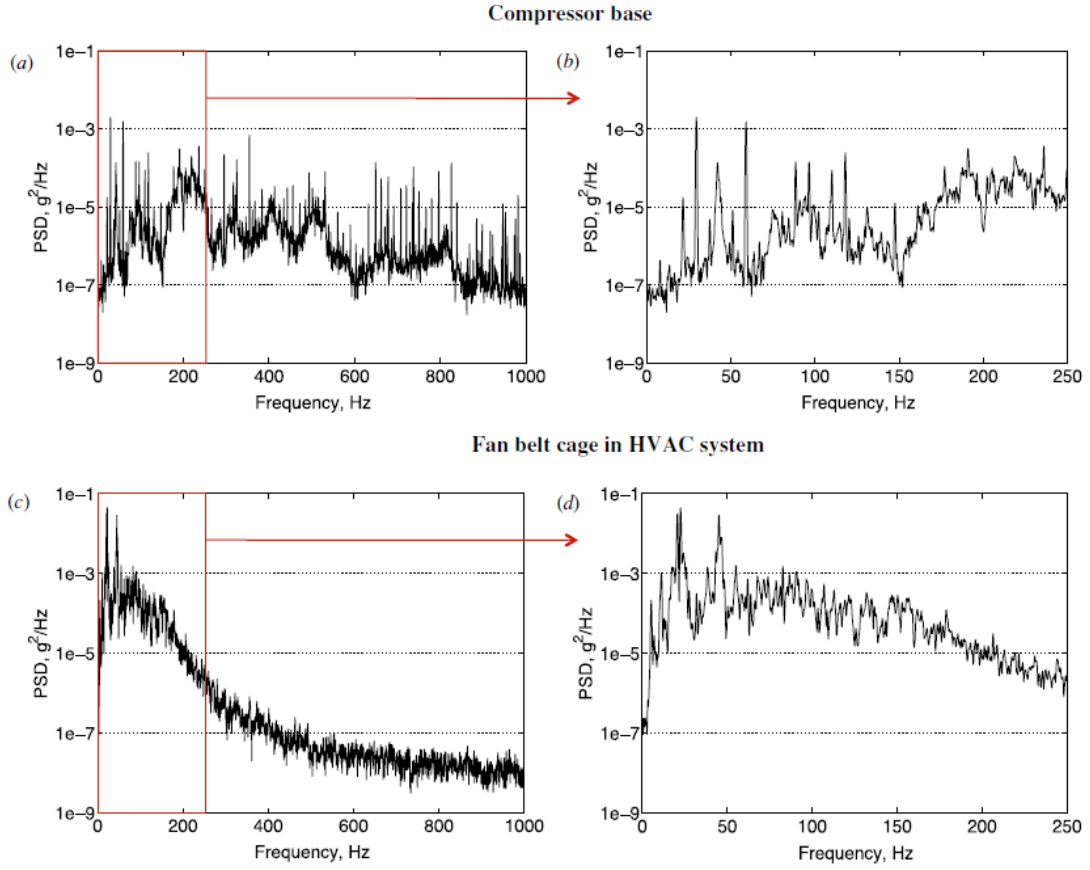


Figure 1.3 Acceleration PSD versus frequency for compressor base ((a) and (b)) and fan belt cage ((c) and (d))[17]

Figure 1.4 depicts PSD of a tire vibration profile at a car speed of 50 km/h having a sole resonant energy harvester at 500 Hz with a narrow bandwidth of 2.7 Hz [18]. It can be clearly seen that such harvesters with fixed resonance and narrow bandwidth could not operate optimally in such conditions. They can only harvest vibrational energy around their resonance within a narrow frequency spectrum. Once the vibration frequencies vary according to the change in car speeds, the performance would drop dramatically, leading to ineffective energy harvesting under off-resonance circumstances.

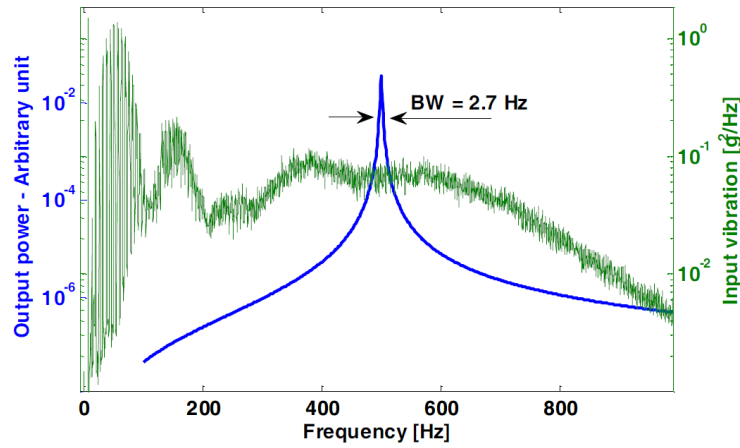


Figure 1.4 PSD (power spectral density) of a car tire vibrations at a car speed of 50 km/h with an example of a sole resonant energy harvesters (500 Hz) with a narrow bandwidth of 2.7 Hz[18]

To better handle the broadband spectrum exhibited by such ambient vibrations, two frequency broadening strategies are proposed, namely nonlinear technique and multi-frequency energy harvesting. Nonlinear technique has been found to be promising to broaden frequency bandwidth by utilizing spring softening and hardening effects [19, 20]. In specific, softening effect could enhance the output power by tuning the resonant peak toward a lower frequency, while hardening effect broadens the bandwidth by bending the resonant peak toward a higher frequency. Although numerous methods have been proposed to induce nonlinearities of energy harvesting system previously, electrostatic nonlinearity introduced by electret surface potential, as an inherent feature of e-EVHs, is seldom explored. Recent attempts of exploiting multiple resonant frequencies of a multi-DOF system have demonstrated their advantages in creating multiple peaks in a certain spectrum. However, most devices encounter the challenges that their high-order modes are usually separated far away from the fundamental mode [21, 22]. Hence, energy harvesting derived from these high-order modes tend to be insignificant. If multi-DOF energy harvesting systems can be designed where close and effective resonant peaks can be established, then the overall energy harvesting effectiveness can be enhanced.

Restricted Single-direction Issue

Currently, most resonant energy harvesters are designed for only single direction excitation in which a set of springs is only flexible along the desired axis while the out-of-axis directions are kept stiff. On planar movement, unlike a cantilever based piezoelectric energy harvesters which only work in an out-of-plane direction, electrostatic energy harvesting structures with multiple folded springs mostly operate in a specific in-plane direction. They only perform optimally when their oscillation is precisely aligned with the single designated excitation vibration. A slight misalignment between the predefined oscillation direction and external excitation source may severely affect or lower its performance. It poses a challenge when the dominant vibration directions in the ambient environment are usually unpredictable or even multidirectional. Take a Statasys 3D printer as an example; it exhibits three different resonant frequencies of 28.0, 28.3 and 44.7Hz along different axes. Another example is the washing machine which exhibits a resonant frequency of 85.0Hz in both 1- and 3-axes according to Reilly's survey[14]. Table 1.2 presents a comprehensive survey of ambient vibrations conducted by Reilly *et al.* [14]. A W500 Lenovo laptop exhibits two resonant frequency peaks along 1- and 3-axes at frequencies of 85.2 and 119 Hz. If the harvester can only harvest energy along a fixed dominant direction, the kinetic energy would be almost completely lost when it is acting orthogonally or perpendicularly to the dominant vibration directions.

Table 1.2 Survey of ambient vibrations[14]

	Frequency (Hz)	Acceleration (g)	Resultant of axes	Characterization
Statasys 3D printer	28.0	0.044	1	s
	28.3	0.060	2	s
	44.7	0.017	3	s
W500 Lenovo laptop	119.0	0.199	3	s
	85.2	0.205	3	s
	119.0	0.141	1	s
	85.2	0.158	1	s
Milwaukee Cordless Drill	0.2	1.080	2	i
	15.2	0.363	2	s
External HD	119.3	0.014	3	s
	119.3	0.012	1	s
Washing Machine	85.0	0.314	3	s
	85.0	0.287	1	s
Monarch Lathe Splatter Guard	15.5	0.069	2	s
	24.5	0.052	2	s
Delta Drill Press	41.3	0.407	1	s/bb
	184.8	0.172	2	s/bb
HVAC Roof	184.5	0.252	2	bb
	184.5	0.236	1	bb
HVAC Vent	21.8	0.469	1	bb
	29.0	0.344	1	bb
	127.3	0.214	1	bb
Driving 2002 Toyota Camry	0.2	0.210	2	i
	42.8	0.022	1	bb
	24.0	0.073	1	bb
Scraper Bike	0.2	0.091	2	i
	15.0	0.062	1	s/bb
Running	1.5	2.045	2	s/lf
	5.1	0.762	1	s/lf
Walking	1.0	0.430	3	s/bb/lf
	3.7	0.305	1	s/bb/lf
Refrigerator	58.7	0.018	3	s
Electric Tea Pot	241.0	0.019	2	bb
Poster Printer	92.5	0.200	3	s
Server/computer	35.3	0.016	1	s

To make the energy harvester adaptive to multiple excitation directions from ambient environment, one strategy to overcome such restrictions of one dimensional (1D) energy harvesting is to make use of axial or rotational symmetrical structures capable of resonating in two orthogonal directions. By combining two orthogonal vibration modes, kinetic energy from two-dimensional (2D) directions can be scavenged. Previously studies have reported 2D harvesters based on piezoelectric, electromagnetic and electrostatic mechanisms [23-27]. The electrostatic harvesters are advantageous and demonstrate more flexibility to decouple the mechanical structure and the energy conversion component. However, it is found a great challenge to design low-resonant-frequency structures within a small confined space while maintain multi-directional energy harvesting capabilities, which need to be further improved and investigated.

1.3 Objectives

The objective of this work is to investigate and develop effective methods that are adaptable to real-world environment in harvesting energy from a wide spectrum with frequency-variant or random-direction vibrations based on electret micro power generators. To achieve this goal, efforts should be devoted to addressing the two primary challenges in vibration-based e-VEHs: the restricted single-direction issue and the narrow bandwidth issue. These have necessitated the following several major objectives of e-VEHs to be explored:

- ❖ To develop approaches for a 2D e-VEH device that can enhance output power and simultaneously minimize the unwanted vertical pull-in and horizontal damping electrostatic force. To analyse both the vertical pull-in electrostatic force as well as the horizontal damping force by combining finite element method and numerical calculations. To experimentally examine the 2D energy harvesting capabilities of the fabricated e-VEH device under multi-directional excitation conditions.

- ❖ To investigate spring-mass architectures for 2D e-VEHs that could harvest energy from arbitrary in-plane directions by using their two primary orthogonal vibration modes. To study the energy harvesting effectiveness of the 2D resonators when compared to their conventional 1D counterpart. To derive a general numerical model based on experimental results that can be used to describe the dynamic motion of the seismic mass, which would form the basis in developing a real 2D energy harvester. To experimentally demonstrate the 2D energy harvesting capabilities of the proposed e-VEH based on rotational symmetrical resonators for arbitrary in-plane low-frequency vibrational energy harvesting.

- ❖ To exploit spring softening nonlinearity induced by strong electromechanical coupling arising from high surface potential provided by charged electret for the first time. To derive an analytical model for the electret-based vibration energy harvesting system, where the electromechanical coupling effect arising from mechanical and electrical domains would be incorporated. To design, fabricate and characterize of a novel out-of-plane e-VEH device with dual-charged electret plates as a proof of concept. To characterize and analyse of the performance of the proposed harvester prototype under different excitation levels to evaluate the usefulness of the spring softening nonlinearity induced by the strong electrostatic force as well as spring hardening nonlinearity induced by end-stop effect.

- ❖ To explore multi-frequency energy harvesting system based on two-degree-of-freedom (2DOF) electret-based MEMS energy converters, which have not been reported before. To derive a lumped parametric model of 2DOF system for energy harvesting applications. To investigate the energy harvesting effectiveness of the proposed 2DOF system by adjusting various parameters, such as frequency tuning ratio (Ω), mass ratio (μ) and normalized excitation frequency (α), where two close resonances with comparable magnitudes would be achieved.

To design, fabricate and simulate a novel 2DOF MEMS e-VEH device based on silicon. To investigate the dynamic mechanical response of the proposed 2DOF resonator through modal and harmonic analysis through ANYSY. To characterize the performance of the fabricated prototype under different excitation accelerations with swept frequencies. To compare the experimental results with the previous numerical and finite element modelling.

1.4 Organization of thesis and research roadmap

The thesis is organized into seven main chapters. Following introduction chapter, Chapter 2 reviews the state-of-the-art vibration energy harvesting techniques with a focus placed on micro electrostatic/electret energy conversion mechanisms. Various efficiency enhancement approaches and frequency bandwidth broadening methods are summarised, critiques are assessed and solutions are proposed to overcome the limitations. Schematic of thesis structure layout is shown in Figure 1.5.

Chapter 3 investigates an axial symmetrical square resonator with sandwich architecture for 2D low-level ambient kinetic energy harvesting. The symmetrical resonator consists of a double-sided electrode-patterned seismic mass suspended by four-folded parallel beam flexures. Sandwich structure is adopted in the proposed device that has two separate capacitive circuits 180° out-of-phase with each other to be integrated into a single seismic mass system. This configuration has its merits in that both the vertical pull-in electrostatic force as well as the horizontal damping force can be reduced.

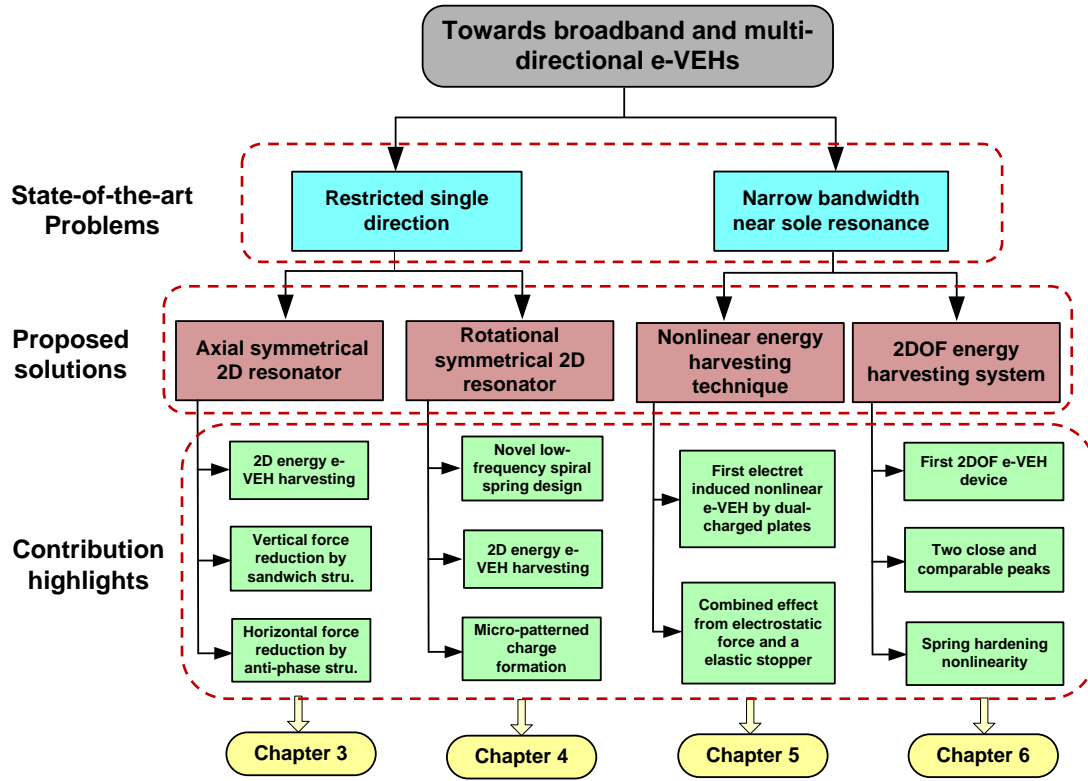


Figure 1.5 Schematic of the thesis structure layout of proposed MEMS e-VEH device

Chapter 4 looks into in-plane mechanical and electrical responses of a low-frequency 2D electret-based vibration energy harvester. The device is based on a rotational symmetrical resonator which consists of a movable disk-shaped seismic mass suspended by three sets of spiral springs. Corona localized charging is utilized to create micro-sized charge distribution on the electret thin film for the prototype fabrication. The energy harvesting effectiveness of 2D resonant system is evaluated compared to the conventional 1D system.

Chapter 5 presents a new design methodology of achieving broadband MEMS energy harvesting device by using the inherent feature of electret-based energy harvesters that high electromechanical coupling arising from high surface potential provided by charged electret as well as a mechanical stopper. A new spring-softening nonlinear model is created in Matlab by the coupling of electrical and mechanical domains to predict the nonlinear phenomenon in the energy conversion system. An out-of-plane

energy harvester device with dual-charged electret plates is designed and implemented as a proof of concept.

Chapter 6 develops a novel nonlinear 2DOF MEMS electret-based energy harvester to obtain broadband energy harvesting. A lumped parametric model of 2DOF system is built and examined in respect of energy harvesting capabilities. It is proved more advantageous than the conventional 1DOF system. The spring-hardening nonlinearity introduced by the end-stop effects is also studied.

Chapter 7 provides a conclusion of the accomplished work in this thesis and highlights the major contributions of this research and suggests for future work.

Chapter 2 Literature review

This chapter begins with a comprehensive review of the-state-of-the-art vibrational energy harvesting techniques with special emphasis placed on micro electret-based electrostatic energy conversion mechanisms. It then goes on to look into various approaches to address the current challenges of vibration-based energy harvesters, namely restricted single-direction issue and narrow bandwidth issue. Finally, recent advances in multi-directional techniques as well as frequency broadening schemes are summarized and compared in detail with regards to their respective merits and drawbacks in various circumstances.

2.1 Vibration-to-electricity transduction mechanisms

Kinetic energy is one of the most readily low level ubiquitous energy sources available in ambient environment. The energy sources can be derived from human movement, structural and machinery vibrations. Mechanical energy can be transformed to electricity by exploiting the mechanical strain or relative movement in the transducer. In mechanical strain, the energy from structure deformation can be extracted by employing active materials, such as piezoelectric or magnetostrictive. As for the relative movement, inertial generators with spring-mass inertial structure can be deployed to extract the vibration energy. This involves a spring-mass frame system which transmits the vibrations to a suspended inertial mass producing a relative displacement between them. At resonance, the excitation amplitude of external vibration sources can be significantly amplified by relative displacement of the spring-mass frame systems [28]. For this inertial spring-mass structure, there are three commonly used transduction mechanisms, i.e. electromagnetic, electrostatic and piezoelectric. Details of the principles and recent advances of these three transducers will be presented in this section later.

2.1.1 Piezoelectric power generator

Piezoelectric effect was first discovered by Jacques Curie and Pierre Curie in 1880 [29]. They found that certain materials have the ability to generate an electrical potential when subjected to mechanical strain. Conversely, when these materials are subjected to an electrical field, deformations would also take place. Piezoelectric power generators are based on the piezoelectric effect, where the external vibration causes the deflection of the piezoelectric structure to undergo compression and tension in the material, and thus gives rise to electricity. The performance of piezoelectric power generator is largely dependent on piezoelectric characteristics of the materials. There are commonly several kinds of piezoelectric materials utilized for piezoelectric power generator in various forms such as hard piezoceramic (PZT-4) and soft piezoceramic (PZT-5H), barium titanate (BaTiO_3), thin film (zinc oxide (ZnO) or Alumina nitride (AlN)), thick film based on piezoceramic powder and polymeric materials (polyvinylidenefluoride (PVDF)). Key properties of these representative piezoelectric materials used in energy harvesting systems are given in Table 2.1 [30]. It can be seen that the piezoelectric coefficients d_{33} , d_{31} and d_{15} of the ferroelectric material, such as PZT and BaTiO_3 , have an order of magnitude larger than those of the nonferroelectric materials, such as AlN and ZnO . The relative permittivity ε_{33}^S and ε_{33}^T of ferroelectric materials under constant stress and strain also demonstrates two orders larger than those of nonferroelectric materials.

Table 2.1 Key properties of some representative piezoelectric material used in energy harvesting systems[30]

Materials	AlN	ZnO	BaTiO ₃	PZT-4 'Hard PZT'	PZT-5H 'Soft PZT'	PMN-PT	PVDF
Const. strain	10	8.84	910	635	1470	680	5-13
Rel. perm. (ϵ^s_{33})							
Const. strain	11.9	11.0	1200	1300	3400	8200	7.6
Rel. perm. (ϵ^T_{33})							
d_{33} pC/N ⁻¹	5	12.4	149	289	593	2820	-33
d_{31} pC/N ⁻¹	-2	-5	-58	-123	-274	-1330	21
d_{15} pC/N ⁻¹	3.6	-8.3	242	495	741	146	-27
Mechanical quality (Q _m)	2800	1770	400	500	65	43-2050	3-10
Electromechanical coupling (k_{33})	—	0.48	0.49	0.7	0.75	0.94	0.19

The constitutive equations for piezoelectric material, which describe the behaviour between strain and charge, are given by

$$\delta = \frac{\sigma}{Y} + d_{ij}E \quad (2.1)$$

$$D = \epsilon E + d_{ij}\sigma \quad (2.2)$$

Where δ is the strain, σ is the stress, Y is the Young's modulus, d is the piezoelectric strain coefficient, D is the charge density, E is the electrical field, ϵ is the material dielectric constant and d_{ij} is the piezoelectric strain coefficient. Because piezoelectric material typically exhibit anisotropic characteristics, the piezoelectric strain coefficient has two subscripts. The first one indicates the direction of the field and the second one denotes the direction of strain. For example, for d_{33} mode, the applied stress and electric field are in the same direction along the polarization axis; for d_{31} mode, the stress is the same direction as before, but the electric field is perpendicular to the stress. They are two most common modes used in piezoelectric energy harvesting. The working principles are shown in Figure 2.1 [10].

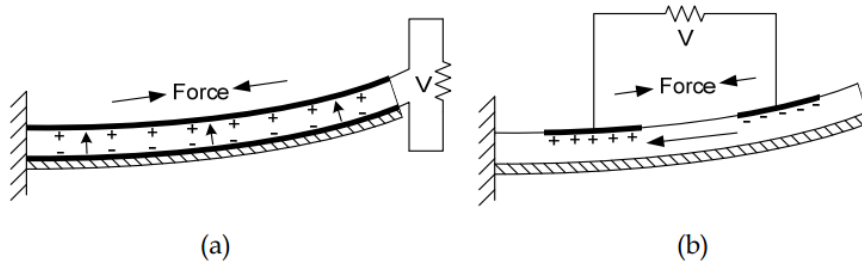


Figure 2.1 Two types of piezoelectric harvesters (a) d_{31} mode and (b) d_{33} mode [10]

Both piezoelectric coefficient and coupling constant of d_{33} mode are higher than that of d_{31} in piezoelectric materials. Although the piezoelectric coefficient of d_{31} mode is lower than that of d_{33} mode, it is more flexible, which results in more deformation when subjected to a certain input force [3]. Therefore, d_{31} mode power generator is commonly used in vibration energy harvesting. When utilized in static force energy harvesting applications, the d_{33} mode power generators are more efficient [3, 31]. Rather than commonly used parallel electrodes, inter-digital electrodes have also been designed to realize a d_{33} mode piezoelectric coupling. Lee *et al.* [32] have designed and fabricated two piezoelectric energy harvesters with d_{31} mode and d_{33} mode electrodes as shown in Figure 2.2. Such kinds of inter-digital electrodes design are also widely employed for in-plane electret-based vibrational energy harvesters, which would be discussed in the following sections.

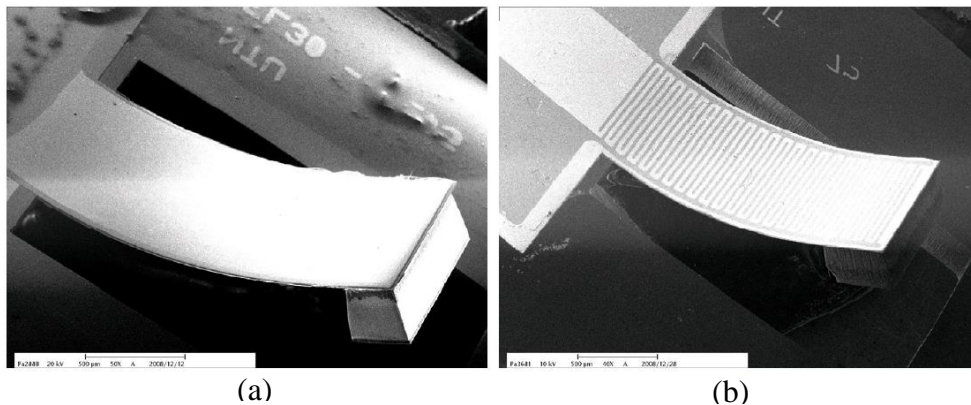


Figure 2.2 SEM photograph of two types of piezoelectric MEMS generators (a) d_{31} mode and (b) d_{33} mode [32]

The method of utilizing piezoelectric materials for energy harvesting has been investigated by a large number of groups and a wide range of devices and applications have been reported. General reviews of piezoelectric energy harvesting have been published [11, 33-36]. A lot of methods have been exploited in order to enhance the power output such as modifying the piezoelectric materials, altering the poling and stress direction, changing the electrode pattern and increasing the bandwidth or tuning the resonant frequency of the devices. One of the early applications using this power conversion mechanism was performed by Paradiso *et al.* [37] in 1998, as shown in Figure 2.3. They successfully implemented these power generators into shoes while maintaining the design and comfort of the shoe. They integrated three different devices into a shoe: a unimorph strip made from piezoceramic composite material, a stave made from laminated PVDF foil and a shoe mounted rotary magnetic generator. In the self-powered application, a digital RFID signal can be periodically broadcasts while the bearer walks.

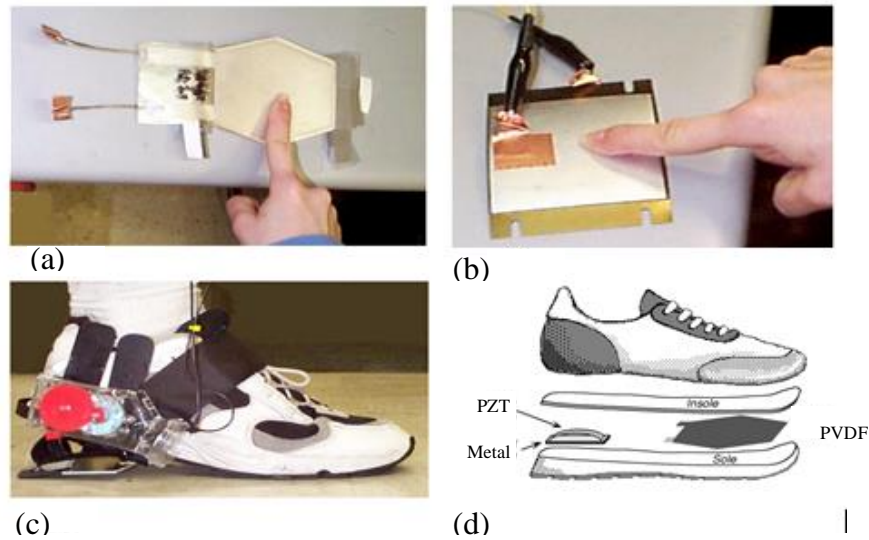


Figure 2.3 Integrating three devices for parasitic power harvesting in shoes: (a) a PVDF insole stave; (b) a Thunder PZT unimorph; (c) a shoe mounted rotary magnetic generator; (d) exploded view of integration of piezos.[37]

AlN is another commonly utilized piezoelectric material for energy harvesting due to its CMOS compatibility and relatively easy deposition process. Elfrink *et al.* [38]

from IMEC/Holst Centre have successfully demonstrated a piezoelectric energy harvester using an uniform AlN micro cantilever. The cantilever beams with length of 1.01~2.01 mm and width of 3~7 μm are encapsulated by two glass wafers, as shown in Figure 2.4(a). The energy harvester prototype mounted on a supportive board is depicted in Figure 2.4(b). The resonant frequencies of the AlN-based MEMS piezoelectric energy harvester can be tuned from 200~1200 Hz by adjusting the dimensions of the beam and mass parameters. The generator can achieve a maximum power of 60 μW at the resonant frequency of 572 Hz with an excitation acceleration of 2g.

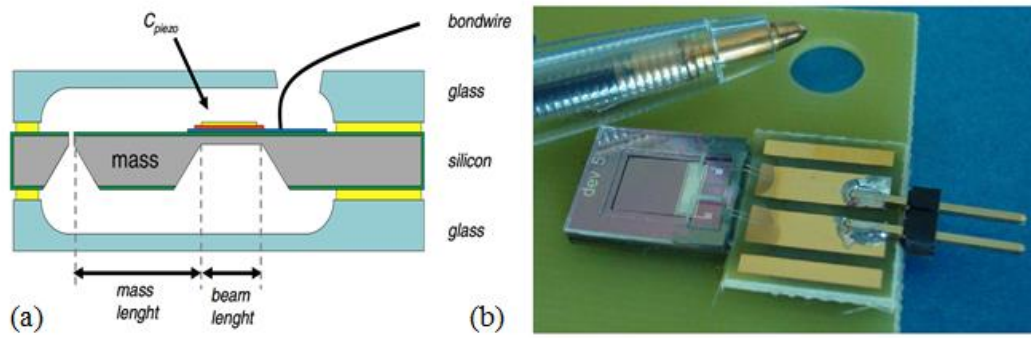


Figure 2.4 (a) AlN-based MEMS piezoelectric energy harvester packaged in between glass substrates; (b) the harvester prototype mounted on a supportive board [38]

The performance of piezoelectric MEMS energy harvester can be evaluated by using common metrics such as resonant frequency, input acceleration, device volume, output power and normalized power density (NPD). NPD is defined as $\text{power}/\text{volume}/\text{acceleration}^2$ which is first proposed by Beeby *et al.* [39] and then widely adopted in the energy harvesting communities to evaluate the performance of vibration-based energy harvesters. The stated output power is first normalized to input excitation acceleration levels and then divided by the volume of the whole device. The state-of-the-art performance of vibration-based MEMS piezoelectric energy harvesters are evaluated by output power and NPD as summarized in Table 2.2.

Most piezoelectric energy harvesters are designed with a cantilever configuration where the piezoelectric beam serves as both mechanical vibration components and energy conversion elements. The output power relies on bending and stretching of the piezoelectric beam where fatigue of piezoelectric materials may easily set in after long-term operation. Moreover, such linear cantilever-based structures usually operate in a predefined out-of-plane direction with a narrow bandwidth near its sole resonance. This limits their applicability in ambient environment where the frequency spectrum is wide with various excitation directions. The commonly used brittle and stiff piezoelectric materials, such as PZT and Macro-Fiber Composites (MFC), would also encounter severe miniaturization and integration challenges.

Table 2.2 Summary of vibration-based MEMS piezoelectric energy harvesters

Reference	Piezoelectric material	Frequency (Hz)	Volume (mm ³)	Acceleration (m•s ⁻²)	Power (μW)	NPD (μW•cm ⁻³ •g ⁻²)
Mehdi <i>et al.</i> 2015[40]	AlN	380.8	18.9	40	1.37	12.23
Shen <i>et al.</i> 2015[41]	PZT d_{33}	1560	5600c	80	8.6	0.024
Tang <i>et al.</i> 2014[42]	PMN-PT	514.1	0.401	15	7.18	7636
Tang <i>et al.</i> 2014[43]	PZT	514	1.2b	10	11.56	9600
Liu <i>et al.</i> 2012 [44]	PZT d_{31}	27.4	8.7b	0.6	1.1×10^{-3}	35.1
Xu <i>et al.</i> 2012[45]	PZT bimorph	330	60	10	7.35	122.5
Liu <i>et al.</i> 2012[46]	PZT d_{31}	25	8.7b	8	0.87	156
Yen <i>et al.</i> 2011 [47]	AlN	853	1.6	10	0.17	106.25
Park <i>et al.</i> 2010[48]	PZT d_{33}	528	1	3.9	1.1	7300
Shen <i>et al.</i> 2009[49]	PZT d_{31}	183.8	0.769	7.5	3.2×10^{-1}	739
Lee <i>et al.</i> 2009[32]	PZT d_{33}	214	2.8	20	1.29	464
Lee <i>et al.</i> 2009[32]	PZT d_{31}	256	2.6	20	2.10	807
Elfrink <i>et al.</i> 2009[38]	AlN	17	572	20	60	882

^aEffective volume is the sum of the beam volume and the seismic volume

^bThe device volume could be estimated by the device area and plate thickness provided by the authors.

^c The device volume could be estimated by the device area and plate thickness provided by the authors.

2.1.2 Electromagnetic power generator

The electromagnetic transducer works on the principle of Faraday's law of electromagnetic induction, which states that the change in magnetic flux generates a voltage in the coil. The voltage is proportional to the time rate of change of the magnetic flux linkage, as given below

$$V = -\frac{d\Phi}{dt} = NBl_c \frac{dy}{dt} \quad (2.3)$$

Where Φ the flux linkage in the coil, N is the number of turns in the coil, B is the magnetic field strength, l_c is the effective length of the turn, y is the relative distance between the coil and magnet. The electromagnetic induction can be realized by either moving magnet with fixed coil or moving coil with fixed magnet. Owing to the flexibilities of its design, a wide range of possible electromechanical coupling can be implemented.

One of the earliest descriptions of an inertial micro generator utilizing electromagnetic mechanism is presented by Williams *et al.* [50] in 1996. They formulated and analysed an equation for power generation for linear inertial generators, which serves as a guide for inertial resonator design. The energy harvesting system consists of a moving mass (m) suspended by a spring (k) and damped by an energy transducer (η_e) and parasitic damping element (η_m). For a sinusoidal excitation vibration ($y = Y\sin(\omega t)$), Williams and Yates have shown that the output power can be derived in equation (2.4) as

$$P_{W\&Y} = \frac{m_1 \zeta_t A^2 \omega^3 \left(\frac{\omega}{\omega_n}\right)^3}{\left(1 - \left(\frac{\omega}{\omega_n}\right)^2\right)^2 + \left[2\zeta_t \left(\frac{\omega}{\omega_n}\right)\right]^2} \quad (2.4)$$

where ζ_t is the total damping ratio, ω_n is the resonant frequency, A and ω are the amplitude and frequency of the excitation, respectively. When the excitation

frequency equals the natural frequency ($\omega/\omega_n = 1$), the average power can be simplified as

$$p_{av} = \frac{\zeta_e}{4(\zeta_p + \zeta_e)^2} m Y_0^2 \omega_n^3 \quad (2.5)$$

If further assumed $\zeta_e = \zeta_p = \zeta/2$, the maximum power output of the energy harvesting system can be obtained and expressed as

$$p_{av} = \frac{m Y_0^2 \omega_n^3}{16 \zeta_p} \quad (2.6)$$

In this case, the maximum power output can achieve the theoretical conversion efficiency, which is 50% of the total power from the frame vibration. The average power output can be obtained when the natural frequency of the spring-mass system is equal to the excitation vibration and when the electrical damping rate is equal to the mechanical parasitic damping rate. From Equation 2.6, it can be seen that the average power output is found to be proportional to the masses, the square of the excitation amplitude and three times of the natural frequency.

In 1997, Shearwood *et al.* [51] presented a preliminary micro power generator based on a 2.4mg bulk-micromachined SmCo permanent magnet. It can produce a peak power of $0.3 \mu W$ at a vibration frequency of 4.4 kHz. This was followed by other reported works. One interesting research was conducted by Yuen *et al.* [52], where a micro power generators using MEMS laser micromachining technology was developed. The micro generator comprises NdFeB magnets is supported by laser micro machined Cu spring structures as shown in Figure 2.5. With two micro power transducer connected in series, the electromagnetic micro power generator could gain a maximum power output of $120 \mu W$ at the frequency of 80 Hz with input acceleration below 0.5 g. This battery sized generator was able to operate a wireless RF thermometer at a continuous vibration for 32 seconds.

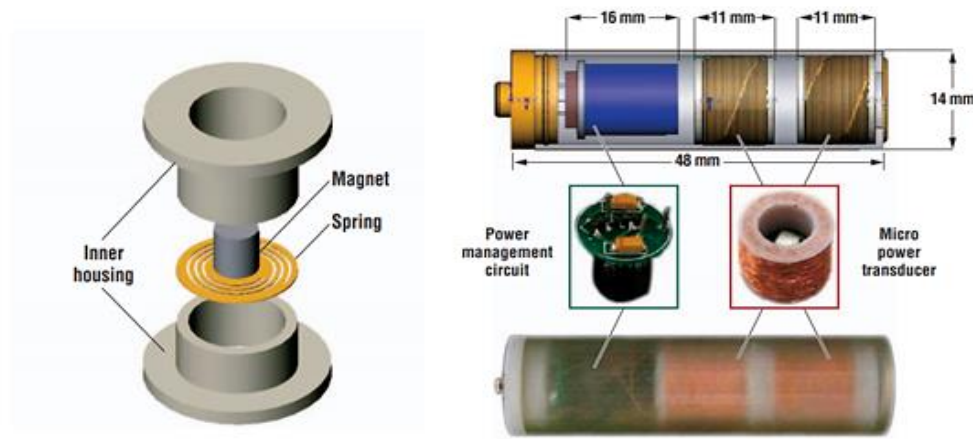


Figure 2.5 An AA sized vibration based micro generator: the micro power transducer's inner structure (left); the power management circuit and the micro power transducer, and an assembled AA-sized MPG containing the power manage circuit and two MPTs [52]

The recent advances of micro vibration-based electromagnetic energy harvesters are summarized in Table 2.3 including various parameters such as resonant frequencies, device volumes, excitation accelerations, output powers and NPD. In general, electromagnetic energy harvesters can produce relatively high output current level for macro devices. No input voltage sources and no mechanical constraints are needed for electromagnetic devices compared with electrostatic conversion. However, the power output of electromagnetic energy harvesting strongly relies on their size. The performance of electromagnetic generators deteriorates significantly in micro scale [53]. The conversion efficiency of electromagnetic mechanism reduces ten times faster than that of electrostatic one. This was highlighted by Scott *et al.* [54] who have conducted a review of electromagnetic vibration-based energy harvester with respect to the scaling laws based on experimentally demonstrated characteristics. Another concern is the integration problems. Although various techniques have been developed to integrate the coils and permanent material into micro devices, the system is still complex and bulky and it is difficult to integrate electromagnetic generators with MEMS fabrication process.

Table 2.3 Comparison of the state-of-art micro electromagnetic energy harvesters

Reference	MEMS device features	Frequency (Hz)	Volume (mm ³)	Acceleration (m•s ⁻²)	Power (μW)	NPD (μW•cm ⁻³ •g ⁻²)
Lei <i>et al.</i> 2014[55]	Assembled	124.2	1824	5	205	456
Moss <i>et al.</i> 2014[56]	Rotational	5.4	9700 ^b	5	33000	13.6
Liu <i>et al.</i> 2013[57]	In-plane nonlinear	146.5	320 ^b	30	1.8×10 ⁻³	6.2×10 ⁻⁴
Liu <i>et al.</i> 2013[58]	Multi-frequency	840	350	10	5.5×10 ⁻³	1.6×10 ⁻²
Wang <i>et al.</i> 2012[59]	Sandwich structured	281	315	8	21.7	107
Liu <i>et al.</i> 2012 [26]	Multi-directional	1470	36	10	1.8×10 ⁻³	0.242
Dai <i>et al.</i> 2012[60]	Nonlinear spring	190	108	8	4.9×10 ⁻³	7.1×10 ⁻²
Tao <i>et al.</i> 2012[61]	Fully integrated	365	20	10	1.6×10 ⁻⁵	8.0×10 ⁻⁴
Cepnik <i>et al.</i> 2011[62]	Multiple magnetic circuit	142	900	1	12	1333
Zhang <i>et al.</i> 2011[63]	Fully integrated	350	78	4.8	2×10 ⁻⁶	1.1×10 ⁻¹⁰
Jiang <i>et al.</i> 2011[64]	Fully assembled	115	100	11.7	1.2×10 ⁻¹	8.8×10 ⁻²
Sari <i>et al.</i> 2010[65]	Up-frequency	113	148	220 ^a	6.6×10 ⁻⁶	9.2×10 ⁻⁵
Wang <i>et al.</i> 2009[66]	Fully integrated	530	14	10	2.3×10 ⁻⁵	1.6×10 ⁻³

^aEstimated using the formula $\alpha = Y\omega^2$, where α and Y are the acceleration and excitation amplitude, respectively

^bCalculated with the power density provided by the author, then calculated the volume by the power provided

2.1.3 Electrostatic power generator

2.1.3.1 Electret-free electrostatic power generators

Electrostatic power generators are based on capacitance change of variable capacitors. Electrical power is generated from capacitance change between the two parallel plates, which are electrically isolated from each other by vacuum, air, oil or insulator. The magnitude of the storage of the charge (Q) is determined by voltage (V) difference of the two charging plates and the variable capacitance (C) between the two plates. The fundamental equation of the capacitance is $C = Q/V$. For a parallel capacitor, the capacitance is given by

$$C = \varepsilon \frac{A}{d} \quad (2.7)$$

Where C is capacitance in farads, ε is the permittivity of the material between the plates, A is the area of the plates and d is the distance of the two plates. If the ε_0 is the permittivity of the free space, the voltage difference within the plates can be given by

$$V = \frac{Qd}{\varepsilon_0 A} \quad (2.8)$$

The energy stored in a capacitor can be expressed as

$$E = \frac{1}{2} QV = \frac{1}{2} CV^2 = \frac{1}{2} \frac{Q^2}{C} \quad (2.9)$$

If the charge of the plates is held constant, the electrostatic force between the variable plates is given by

$$E = \frac{1}{2} \frac{Q^2 d}{\varepsilon A} \quad (2.10)$$

If the voltage is kept at constant, the electrostatic force between the variable plates is

given by

$$E = \frac{1}{2} \frac{\epsilon A V^2}{d} \quad (2.11)$$

Harvesting vibration energy from MEMS electrostatic transducer was first reported by a group of researchers at MIT. They first present the structure of electrostatic harvester and discuss the properties for modes operating at constant charge and constant voltage. As shown in Figure 2.6, Meninger *et al.* [67, 68] designed and fabricated an electrostatic vibration energy harvester based on MEMS technology. Both generator and associated circuitry were discussed. Based on the predicted value of capacitance and simulation, it was estimated that the converter can produce $8.6 \mu\text{W}$ power in in-plane overlap varying mode, where $3 \mu\text{W}$ would be consumed in the associated circuitry.

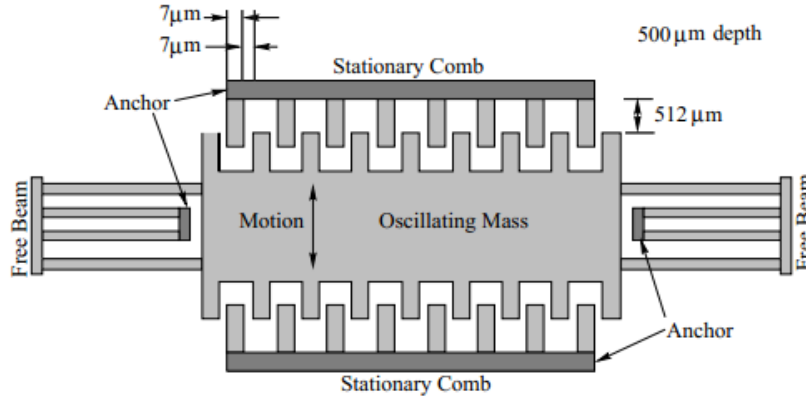


Figure 2.6 MEMS-based electrostatic transducer by Menninger *et al.* [67]

Based on previous work, Roundy *et al.* [69] from Berkeley group summarized and analyzed the electrostatic converters and grouped them into three conversion types such as in-plane overlap varying, in-plane gap closing and out-of-plane gap varying, as shown in Figure 2.7. The three approaches are evaluated through the theoretical modelling, and in-plane gap closing type has the preferred topology according to simulation and practical considerations. Although variable gap type devices are less sensitive to the parasitic capacitance, these devices exhibit higher loss due to air

damping and large surface area which might result in electrostatic stability problems. This will be intensively discussed in Chapter 5. The devices were fabricated by DRIE process that etches MEMS structures in the top layer of SOI wafer. Roundy *et al.* predicted the optimal power output for a $0.25\ \mu\text{m}$ minimum gap of in-plane overlap varying type is $116\ \mu\text{W}/\text{cm}^3$.

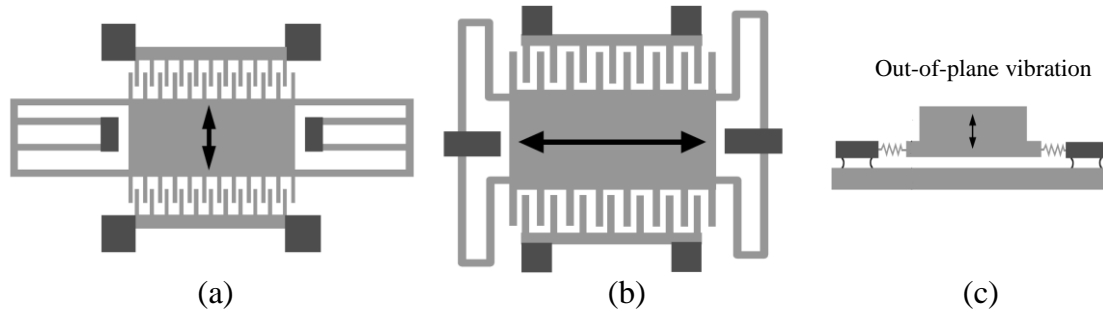


Figure 2.7 Three different electrostatic conversion modes: (a) In-plane overlap varying; (b) In-plane gap closing; (c) Out-of-plane gap varying[69]

Another influential group from Imperial College of London has made significant progress in the electrostatic energy harvesting. Mitcheson *et al.* [3, 28, 70-72] investigated several forms of vibration-driven MEMS micro generators, such as velocity-damped resonant generators (VDRGs), Coulomb-damped resonant generators (CDRGs) and Coulomb-force parametric generators (CFPGs)[28]. They showed CFPG had better performance than the other two resonant generators for applications where source frequency was likely to vary. It also suggested that when the source motion amplitude was much larger than internal displacement of the device, a non-resonant generator was more efficient than resonant one. For these reasons, a non-resonant device catering to a wide range of input frequencies has been designed and fabricated as shown in Figure 2.8. The inertial mass was suspended by a low stiffness spring. The bottom plate contained a counter electrode and charging studs. Initially the moving mass was at its lowest position contacted with charging studs. The capacitance was at its maximum state. When sufficient acceleration is applied,

the plate will be moved up and separate from the bottom plate. The charge on the plate is held constant and the capacitance decreases, which results in voltage increases. Finally the centre mass would discharge and electricity could be generate. Test results based on the device shown in Figure 2.8 could produce 120 nJ power per cycle and more power output could be achieved by fine tuning the operating parameters such as reducing the damping, increasing the initial capacitance and modifying the mass vibration direction.

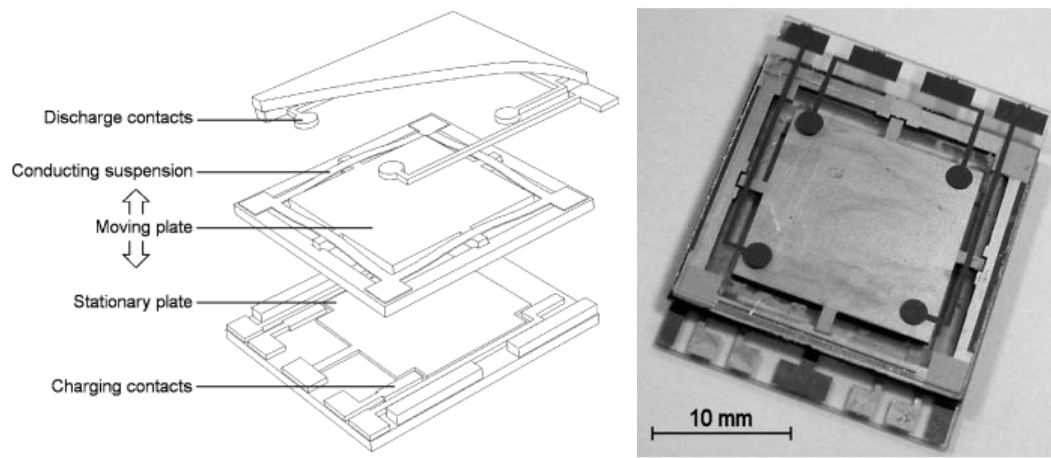


Figure 2.8 Exploded view(left) and prototype(right) of power generator [70]

Comb drive is one of the most common designs of electrostatic transducers which are adopted by a vast majority of researchers. This usually achieved by using SOI wafer to develop inertial transducers [73-75]. Researchers from HSG-IMIT and IMTEK from Germany[73] have developed chip size electrostatic generators which can produce a total net energy of 13.38 mJ in a period of 2h. An elastic stopper was adopted to limit the displacement of the mass. The prototype after completely packaged has an area of 5mm by 6mm. A schematic of the transducer layout and micro power generator chips packaged in CLCC packages are shown in Figure 2.9.

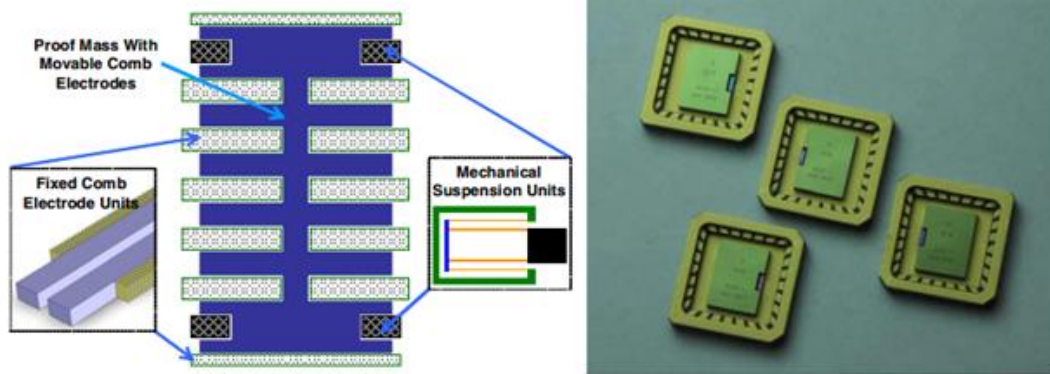


Figure 2.9 Schematic of the transducer layout (left) and micro power generator chips packaged in CLCC packages(right) [73]

However, one of the main problems of the electrostatic energy harvesting devices is that an external voltage source is required to provide the initial charge to the capacitors. Although the extra charge pump can be designed by the external circuits, the device volume would be increased substantially as well as the complexity of the energy harvesting system. To address this problem, a new type of electret-based vibration energy harvesters (e-VEHs) has been developed.

2.1.3.2 Electret-based electrostatic power generator

a) Operating principles of the electret based energy harvester

In electret-based energy harvesting systems, electrical power is generated from capacitance change between the two parallel plates, which is similar to the previous electrostatic energy harvesters. The particularity of electret-based energy harvester utilizes an electret as its negative/positive permanent surface voltage source. Electrets are dielectrics with quasi-permanent electric charge or dipole polarization, which can form a permanent electric field for several years around the structure.

Wax was initially used as electrets by Eguchi *et al* [76]. They poled carnauba wax under a high static electric field above its melting temperature and they further found the charges can be trapped for a very long period. Electrets have been mostly used in

microphones [77] and air dust filtering systems [78]. In recent years, researchers seek to integrate electret to the electrostatic configuration for vibration energy harvesting.

Based on the same principle of the electrostatic energy conversion modes shown in Figure 2.7, the electret-based vibration energy generator (e-VEH) operates in three different configurations as shown in Figure 2.10 such as out-of-plane gap closing, in-plane overlapping and in-plane dielectric varying [79]. The in-plane type works on the variation of the overlapping area of two parallel plates (shown in Figure 2.10(a)), while out-of-plane type mainly operates on the change of the dielectric gap between the electrodes (shown in Figure 2.10(b)). Interdigital electrodes and patterned electret layers are usually employed to enhance the rate of change of the overlapping area.

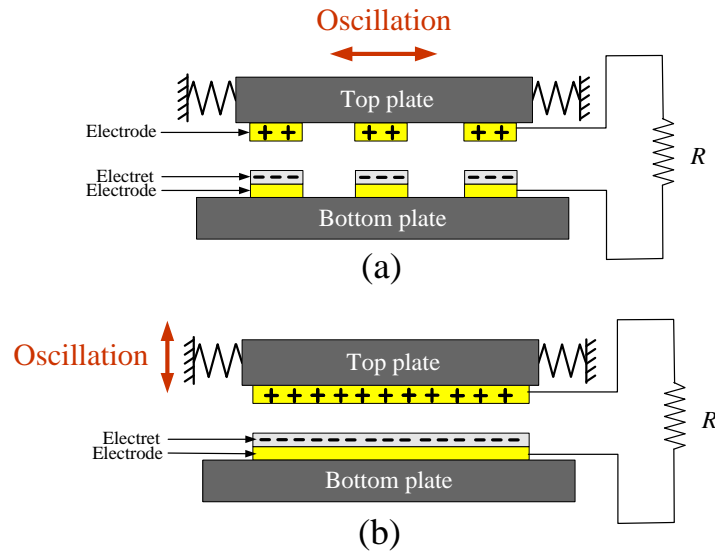


Figure 2.10 Two operation modes of e-VEHs: (a) In-plane overlapping type; (b) Out-of-plane gap closing

A simplified model of in-plane overlapping e-VEH excluding the mechanical spring-mass configuration is shown in Figure 2.11. It consists of mainly a counter electrode, a base electrode, an electret layer and an external resistance. Charges trapped in the electret can induce opposite charges in the base electrode and counter electrode creating an electric field. When there is an oscillation, the change of the

overlapping area between the two electrodes will lead to variations in the amount of charges induced by electret. An alternating current in the external resistive load is then formed.

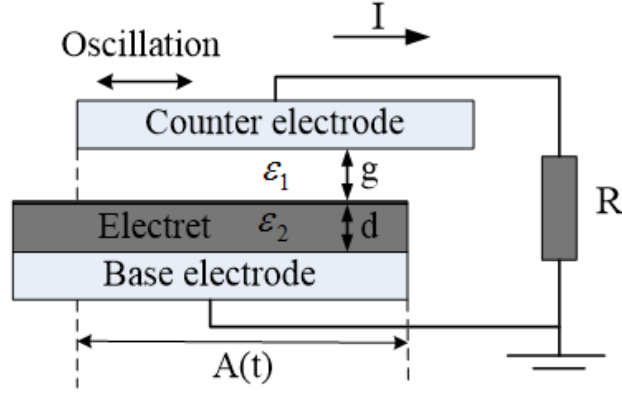


Figure 2.11 A simplified model of in-plane e-VEH excluding the mechanical configurations

By neglecting the parasitic capacitance change, the power output for the electrets based electrostatic power generators can be modeled using the following equation [80] with the resistive load is made to match with the impedance

$$P_{max} = \frac{\sigma^2}{\frac{4\varepsilon_0\varepsilon_2}{d}(\frac{\varepsilon_2 g}{\varepsilon_1 d} + 1)} \cdot \frac{dA(t)}{dt} \quad (2.12)$$

where P_{max} is the maximum power output, σ is the surface charge density of the electrets, ε_0 is the vacuum permittivity, ε_1 is the dielectric constant of the air, ε_2 is the dielectric constant of the electret, d is the electret thickness, g is the gap between the surface of the electret and the top electrode, $A(t)$ is the variable overlapping area between the parallel electrode plate. Based on the equation, it can be observed that the power output is greatly influenced by electret surface charge density and the gap distance between the two parallel plates. This is for increasing the surface charge density and reducing the gap distance can result in a larger power output.

b) Electret materials for micro electret vibration generator

As the surface charge density of electret could significantly impact the output power of the electrostatic energy harvesters, studies into electret forming and charging are of cardinal significance. Generally, electret materials are divided into two categories: SiO₂-based inorganic (SiO₂, Si₃N₄) electrets and Polymer-based organic (Teflon, Parylene, PVDF, LDPE, CYTOP) electrets.

The SiO₂-based inorganic electrets have merits in providing extremely high surface charge density (up to 12mC/m² [81]) and are compatible with MEMS fabrication process. However, the inorganic electrets are quite susceptible to charge decay for long-term operation. In order to solve this problem, SiO₂/Si₃N₄ multilayer structures are often utilized. Efforts have also been made by several groups in the world, such as IMEC[81-83], CEA France[84, 85] and University of Tokyo[86]. Leonov *et al.* [82] from IMEC found that the field emission and atmospheric ions are the key contributing factors causing charge decay. They achieve good performance for patterning of a SiO₂/Si₃N₄ electret feature size of 20 μ m while leaving SiO₂ unpatterned. The discharging rate is almost the same as the pattern with linewidth of 7mm. Boisseau *et al.* [84] from CEA proposed a method of developing a continuous SiO₂/Si₃N₄ patterned electret by using DRIE technology to decrease the charge decay and increase the capacitance variation, as shown in Figure 2.12. Excellent stability with high surface charge density (up to 5mC/m²) has been achieved.

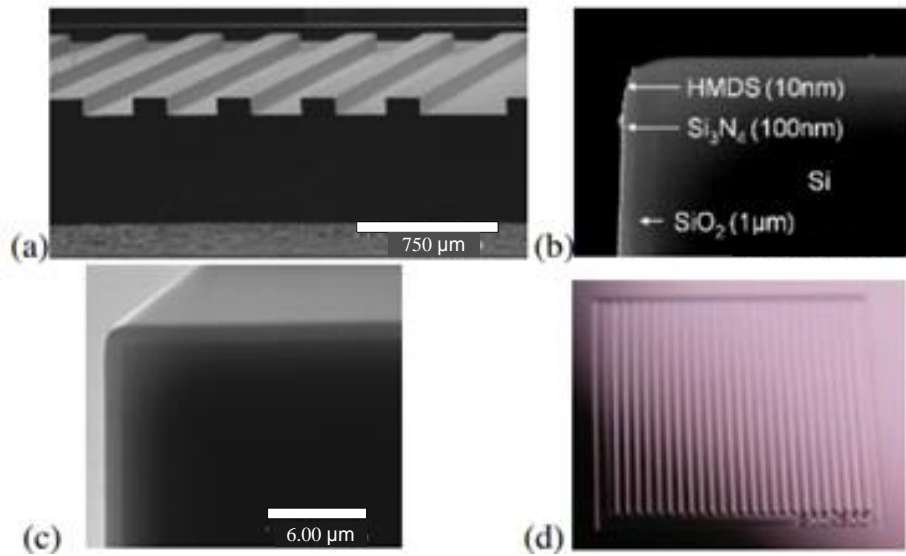


Figure 2.12 DRIE patterned $\text{SiO}_2/\text{Si}_3\text{N}_4$ electret: (a) cross section view, (b) $\text{SiO}_2/\text{Si}_3\text{N}_4$ layer coated with HMDS, (c)(d) corner and overall image.

In recent years, a large number of studies have been done to develop polymer based organic electret due to its relatively high surface charge density (up to 3.7mC/m^2 [87]) and long-term stability. One of the earlier works was done by Boland *et al.* [80, 88] from Caltech. They applied an electret coupled to an electrostatic energy harvesting. Teflon AF thin films are patterned into four poles, as depicted in Figure 2.13, which shows a perfluorinated cyclic structure as electrets for a rotational electret power generator. The device was reported to be able to generate a power of $25\text{ }\mu\text{W}$ at a rotational speed of 4170 rpm. Several years later, Lo *et al.* [87, 89] found that parylene HT thin film could be prepared Chemical Vapour Deposition (CVD) at room temperature and further patterned by oxygen plasma etching. This kind of Parylene HT could provide high surface charge density of up to 3.69mC/m^2 with a film thickness of $7.3\text{ }\mu\text{m}$.

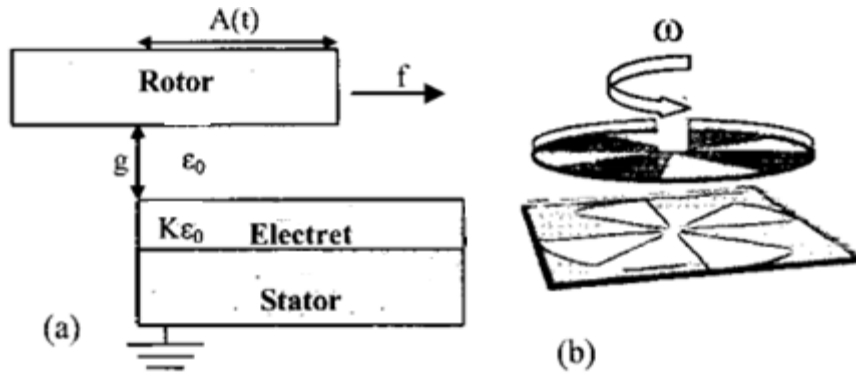


Figure 2.13 Schematic of electrets generator: (a) cross section view; (b) 3-D view of 4-pole rotor and stator [80]

In 2005, Tsutsumin *et al.* [90, 91] from University of Tokyo reported that the amorphous perfluorinated polymer CYTOP (Asahi Glass Co. Ltd) could provide a high surface charge density and applied it into electrostatic energy harvesters. Comparing with Teflon AF, CYTOP was reported with several significant advantages such as notably high thermal and chemical stability, and high surface charge density. The thickness of electret thin film can achieve up to $20\text{ }\mu\text{m}$ and the spin coating process is compatible with MEMS fabrication process. Since then, CYTOP has been considered as one of the mainstream materials for e-VEH, which has been utilized by several research groups [79]. By doping silane-coupling reagent into the polymer, Sakane *et al.* [92] obtained a CYTOP film of $15\text{ }\mu\text{m}$ thickness with a surface charge density of up to 1.5 mC/m^2 , which is three times larger than Teflon AF. A power output of 0.7 mW at a frequency of 20 Hz can be obtained by attaching a $20\times 20\text{ mm}^2$ CYTOP electret film to an oscillator.

Table 2.4 lists the deposition methods, dielectric strength and dielectric constant of several mainstream electret materials used in the e-VEHs. As can be seen from the table, LDPE has the highest dielectric strength with comparable dielectric constant. Compared with CYTOP and Teflon AF which may produce toxic substances during the curing process, LDPE is more cost effective, environmentally friendly and suited

for electret-based energy harvesting applications. LDPE thin film bought from Goodfellow Cambridge Limited is used as electret material in the current project.

Table 2.4 Summary of the state-of-the-art electrets for e-VEHs

Electret	Deposition method	Dielectric strength (MV/m)	Dielectric constant	References in e-VEHs
SiO ₂ -based	Thermal oxidation PECVD/LPCVD	500[93]	4[93]	[84, 85] [86]
CYTOP	Spin-coating	110[92]	2.1[92]	[92] [90, 91]
Parylene HT	CVD	270[93]	2.2[87]	[87, 89]
Teflon AF	Spin-coating	20[80]	1.9[80]	[80, 88]
LDPE	Bulk bonded	741[94]	2.5[95]	[96-98]
PTFE	Bulk bonded	18[87]	2.1[87]	[99, 100]

c) Micro-patterning and charging of electrets for e-VEHs

Currently, there are four major methods used for electret charging, such as corona charging, thermal poling, contact charging and electron beam irradiation. Among these, corona charging is commonly used both in industry and research laboratories. This method involves ionizing the surrounding gas and making charge accumulation near the surface of the electret. Owing to the strong electrostatic field between the grid and substrate, charges are transferred from ions to the electret surface. Most of the coronas charging systems make use of the needle-grid setup, as shown in Figure 2.14. There are two main advantages of this method. Firstly, the surface potential of the electret can be easily controlled by adjusting the magnitude of the grid voltage. Secondly, the surface charge density can be uniformly distributed by the three electrode charging system. It ought to be mentioned that surface charges on the electret are susceptible to be neutralized by the air. To improve the stability, the material is subjected to thermal annealing which enables the charges to penetrate deeper into the material rather than remaining on the surface.

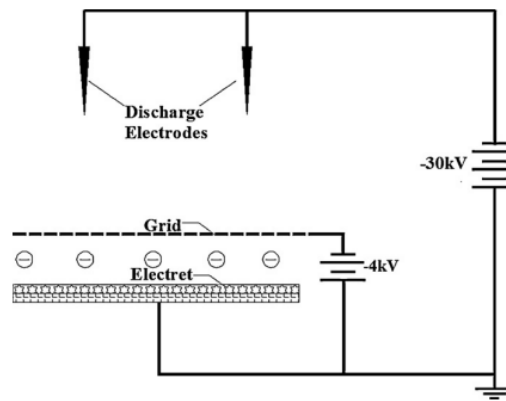


Figure 2.14 Corona discharging needle-grid setup[101]

In-plane overlapping type e-VEHs are the one of the most commonly used electret energy harvesting techniques. For in-plane overlapping micro energy harvesters, high and stable surface potential on micro-sized electrets is preferred owing to the small rate of change in the overlapping area. In order to enhance the power output, the electret films would first need to be micro-patterned and etched before being charged. One typical way to micro-pattern of polymer-based CYTOP electret is presented by Sakane *et al.* [92], as shown in Figure 2.15 (a). Surface potential have hundreds of volts has been achieved by this method. Nevertheless, complicated fabrication processes are required, including base-electrode sputtering, CYTOP spin coating, metal shadow formation, final CYTOP etching and mask removal. Figure 2.15 (b) illustrates the main processes of micro-patterning of SiO_2 -based $\text{SiO}_2/\text{Si}_3\text{N}_4$ electret presented by Boisseau *et al.* [93]. Both of these methods however inevitably involve the chemical treatment of electret materials, where damage of the material properties may readily set in. Furthermore, for micro structures patterned using photolithography, low charge efficiency and rapid charge decay can readily set in. The smaller their dimensions, the faster the charge decays [102]. A common observation is that discharge takes place at the edge of the patterned electrets or electret sample. This puts severe limitations on the performance of the miniaturized electret patterns. The fabrication process may also encounter difficulties in mass production and high cost.

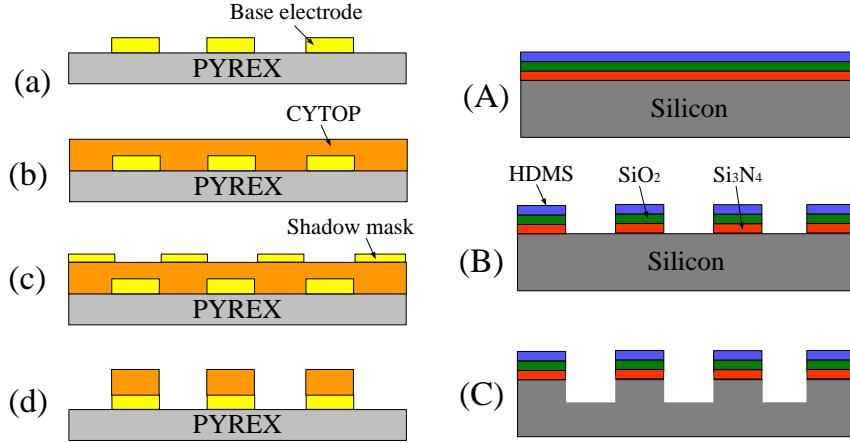


Figure 2.15 Fabrication process of micro-patterning of (a) Polymer-based CYTOP electret [92]; (b) SiO_2 -based $\text{SiO}_2/\text{Si}_3\text{N}_4$ electret [93]

Genda *et al.* [103, 104] developed a new charging method for micro-patterned electrets using contact electrification. Mercury was selected as the contact material because it was suitable to provide uniform contact having different patterns. The electrons are transferred from mercury to electrets due to different Fermi level between two contact materials. By this method, they found the surface potential of the $0.5\mu\text{m}$ thick SiO_2 electrets with proper modification could range from -50 to -80V. However, it seems the surface potential is still not enough for e-VEH applications.

Nowadays, most devices that employ electret polymer films are fabricated in two individual processes; electret formation and charging followed by macro scale assembly of the polymer into the micro device. This two-step process encounters a number of fabrication challenges such as electret decay and misalignment with counter electrode during the assembly and cannot be mass-produced. To overcome these challenges, Kranz *et al.* [105] proposed a method of *in-situ* polarization of electrets embedded within the MEMS devices. Similar to most of corona charging systems, they introduce self-aligned charging grid integration into the devices. Figure 2.16(a) shows simultaneous polarization of multiple electrets on the wafer-level fabrication process.

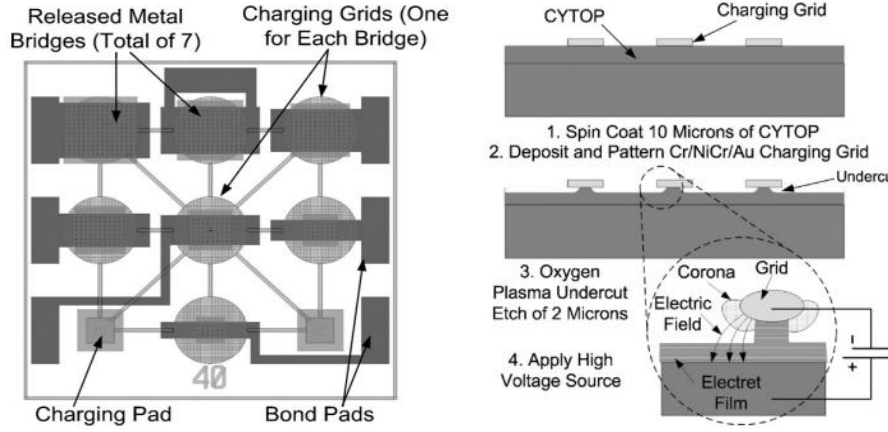


Figure 2.16 (a) Demonstration of wafer-level simultaneous polarization of multiple electrets and (b) fabrication process of situ wafer-level polarization of electret films[105]

Fujita *et al.* [106] employed another approach based on buried grid-electrodes with bias voltage to obtain a charged electret. This approach reduces the complicated patterning and etching processes of the electret. A peak-to-peak surface potential of 200V could also be obtained. Figure 2.17 demonstrates the comparison between the typical corona charging apparatus and novel charging setup using buried guard electrode.

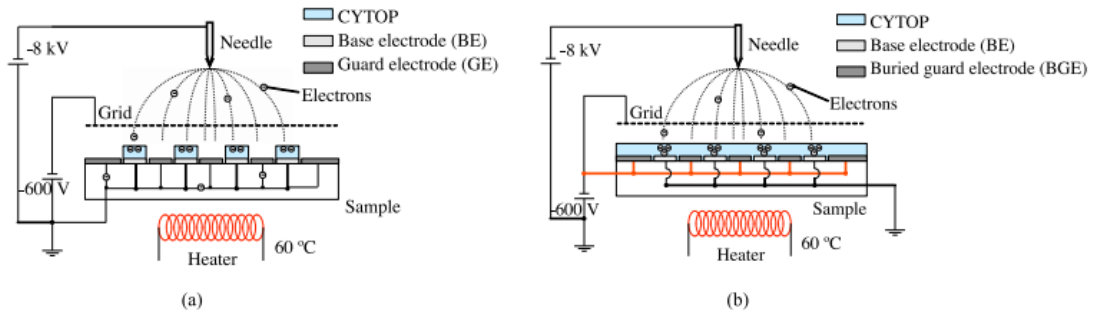


Figure 2.17 Typical corona charging apparatus and novel charging setup using buried guard electrode[106]

Honzumi *et al.* [107] developed another innovative charging method using soft X-ray irradiation. The soft X-rays could ionize gas molecules around the electret, which would then be attracted into the electret by an external electric field. They applied this method to charge vertical electret for in-plane single wafer transducer. A

depth of 80 μm vertical electrets with a 52V surface potential could be formed. Yue *et al.* [108] used soft X-ray to realize uniform artificial dipoles of parylene vertical structures. The conceptual diagram of the soft X-ray charging based on local photoionization was shown in Figure 2.18. According to their findings, charge and voltage sensitivities of 9600 pC/N and 960 V/N at resonant frequency could be achieved using this approach. Table 2.5 summarizes several state-of-the-art micro-patterning techniques for e-VEHs with their respective merits and materials used as well as surface potential achieved.

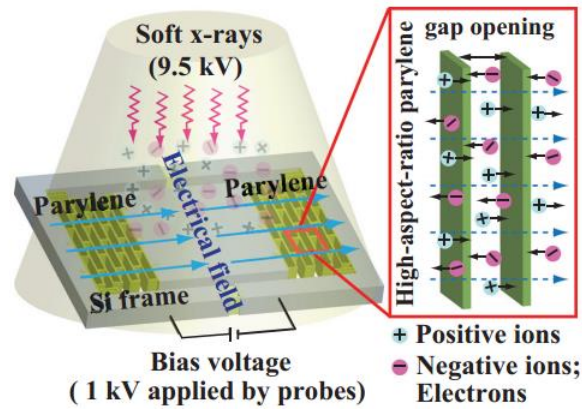


Figure 2.18 Conceptual diagram of the soft X-ray charging based on local photoionization[107]

Table 2.5 Summary of the-state-of-the-art micro-patterning techniques for e-VEHs

Methods	Materials	Surface potentials	Merits	References in e-VEHs
Chemical etching & charging	CYTOP	600 V	High surface potential	[92]
Chemical etching & charging	SiO ₂ -based	800V	High surface potential	[86]
Contact electrification	Mercury/SiO ₂	60-80V	Uniform charged	[103, 104]
In-situ polarization	CYTOP	200V	In-situ wafer-level	[105]
Grid-electrodes shadowed charging	CYTOP	200V	Post-assembled charging	[106]
X-ray irradiation	Parylene C	52V	Vertical charging	[107]

d) e-VEHs using patterned electrets for in-plane oscillations

In-plane type e-VEH that operates on the variation of the overlapping area is the most commonly used vibration mode in electret-based energy harvesting techniques. Interdigital electrodes and patterned electret layers are usually employed to enhance the rate of change of the overlapping area. The electret vibration energy harvester usually makes use of silicon as the structure materials. Special silicon micromachining technique like DRIE is commonly used to provide soft springs in micro scale that could have a low resonant frequency and large oscillation amplitude. High-Aspect-Ratio (HAR) Si springs are normally fabricated on SOI wafers. Figure 2.19 presents a silicon-spring-based batch-processed electrostatic energy harvester proposed by Basset *et al.* [109]. The structure of the energy conversion part is only 11mm×6mm. It can obtain a power output of 61 nW on a 60 MΩ resistive load with an acceleration of 0.25 g at 250 Hz.

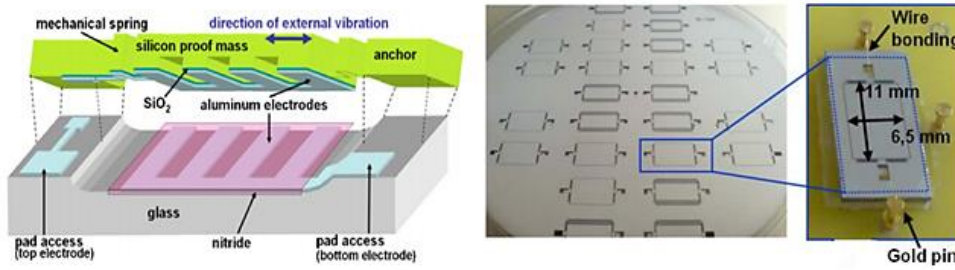


Figure 2.19 3D schematic and real image of electrostatic power generator[109]

Eskild *et al.* [12] successfully utilized a silicon-based micro electret power generator as the power source in the application of tire pressure monitoring systems (TPMS) in cars. This can be a realistic alternative approach to replace batteries. The cross-section structure are demonstrated in Figure 2.20, where the generator is shown on the left and wheel with TPMS on the inner of the tire is presented on the right side. The generator structure should have a low stiffness in x-direction and high stiffness in the z direction. Design considerations of the micro electret generator were discussed and a specific design was proposed. According to their numerical simulation, sufficient power ($4.5 \mu\text{m}$) for the TPMS systems can be generated with a silicon proof mass of $400\mu\text{m} \times 3.8\text{mm} \times 4.34\text{mm}$ when the driving speed reached 50 km/h.

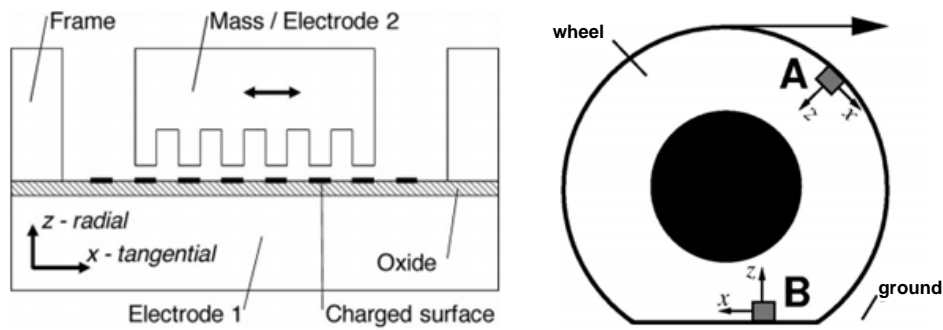


Figure 2.20 Cross-section structure view(left) and wheel with sensors(right) of patterned-electret-based energy harvester for tire pressure monitoring systems[12]

Suzuki *et al.* [110] from university of Tokyo proposed an electret based parallel-plate model and a series of literature [92, 110-116] were reported about the improvement of the structure. The overall schematic structure and packaged prototype of in-plane

micro electret vibration generator are shown in Figure 2.21. In 2008, Suzuki *et al.* [110] integrated high-aspect-ratio Parylene springs into the electret vibration generator. They developed a low-resonant frequency MEMS generator with resonant frequency as low as 37Hz and large in-plane amplitude of 0.8 mm. In 2011, Suzuki *et al.* [116] improved their micro electret power generator devices and used it to power an autonomous wireless sensor. Total power output of 2 μW has been achieved with 1g acceleration at a broadband frequency of 16-38Hz.

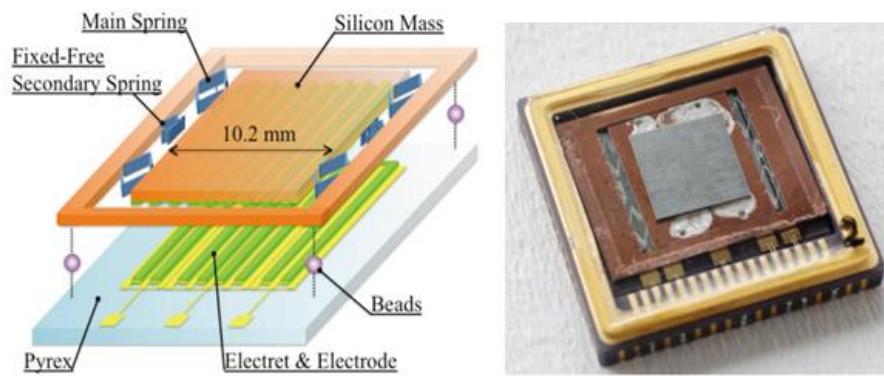


Figure 2.21 Schematic structure and packaged prototype of in-plane micro electret vibration generator proposed by Suzuki *et al.* [116]

Takahashi *et al.* [117] proposed a novel electret energy harvesting method based on fringing field effect. They embedded the electret and electrode in the trench on quartz substrate. The capacitance variation between the base and counter electrode is caused by lateral movement of the seismic mass. Compared with the conventional method, this approach has the following merits: (a) implanted charges are not easy to discharge; (b) pull-in effect may hardly occur; (c) gap between mass and substrate can be as narrow as possible; (d) large capacitance variation can be obtained. Figure 2.22 shows the proposed principle and schematic of an electret power generator based on fringe field effect. They achieved an experimental output of 0.75 μW at the frequency of 80 Hz with amplitude of 80 μm .

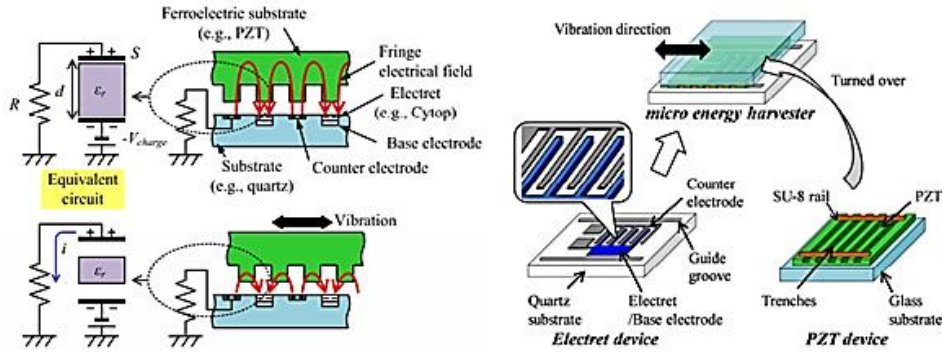


Figure 2.22 Proposed principle and schematic of an electret power generator based on fringe field effect[117]

e) e-VEHs using non-patterned electrets for out-of-plane oscillations

Electret-based vibration energy harvesters with an out-of-plane gap closing scheme has also been investigated. A conventional in-plane e-VEH usually has an in-plane movable proof mass patterned with parallel-interdigital electrodes and the corresponding stripe-shaped electrets. The electrical current is generated when the overlapping area varies in response to an external horizontal vibration source. In order to enhance the performance, the values of electret pattern width are usually designed in ten to hundred micrometer level to be compatible with the tiny displacement of the proof mass[118]. This, however, gives rise to problems in terms of low charging efficiency and rapid charge decay [82, 102]. Furthermore, the optimal working condition for such harvester is when two electrodes have precisely aligned to each other. Even small scale of misalignment may affect or lower its output performance. In order to overcome these problems, Chiu *et al.* [119] proposed an out-of-plane e-VEH with a non-patterned negative-charged plate that operates on the variation of the air gap, where neither precise alignment or micro-patterning of the electret film is necessary. The top view and side view of the out-of-plane e-VEH are shown in Figure 2.23. Boisseau *et al.* [85] also introduced an out-of-plane e-VEH with cantilever beam-mass system with a positive charged electret plate as permanent voltage source. However, the fabrication of these devices is based on manual cutting process that is

neither practical for mass-production nor compatible to integration with other electronic devices.

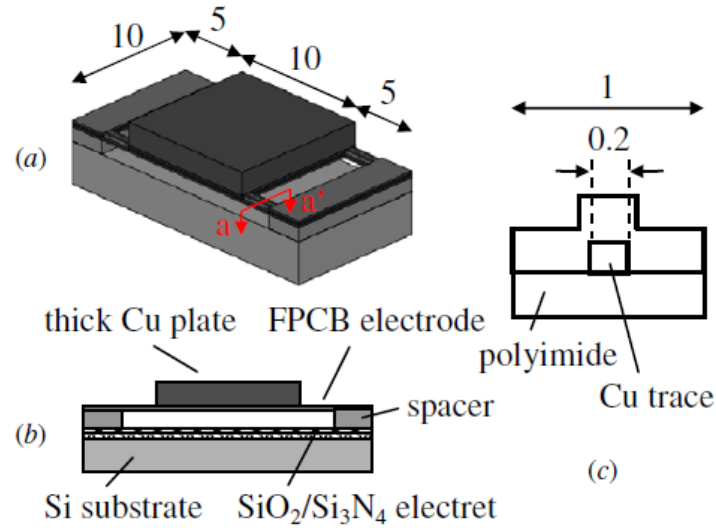


Figure 2.23 (a) schematic view of out-of-plane e-VEH with FPCB electrode, (b) side view and (c) cross section of the springs [119]

f) Summary of recent electrostatic energy harvesters

Table 2.6 summarizes the performance data of the most recent electrostatic energy harvesters. Various evaluation metrics are incorporated, such as operating directions, resonant frequencies, bias voltages, device volumes, excitation accelerations, output power and NPD. Electret-based power generators are highly suited for small-scale energy harvesting since they are self-sustaining and can generate a high power output while eliminating the need for a stand-by power source. In order to improve the performance, lots of work has been done as aforementioned on high-performance electret material development, novel charging methods, gap and parasitic capacitance control and novel low-resonant-frequency spring designs.

However, most devices reported are only for unidirectional vibration with a narrow bandwidth. Typically, for an in-plane type e-VEH, multi-folded springs with high aspect ratio (HAR) are employed to make the system only flexible along the desired

axis while other directions are kept stiff. It is inefficient when the excitation directions do not precisely act along the predefined directions. For out-of-plane type e-VEHs that usually make use of cantilever beam, the response only exhibits a narrow bandwidth. The electrostatic force, as an inherent nonlinear force in the electrostatic energy harvesting system, has not been fully utilized. Considering the circumstances that the frequencies and oscillation directions of the ambient vibrations are sometimes unpredictable and random, certain broadband and multiple directional energy harvesting techniques are highly demanded.

2.2 Multi-directional vibration energy harvesting

As aforementioned in the previous section, currently most resonant energy harvesters are designed for only single direction excitation in which a set of springs is only flexible along the desired axis while the out-of-axis directions are kept stiff. Typically, a cantilever-based energy harvester can only operate in an out-of-plane direction; while an energy harvesting structure with multiple folded springs mostly operate in a specific in-plane direction. This poses a challenge when the dominant vibration directions in the ambient environment are usually unpredictable or even multidirectional.

To scavenge energy in such vibration scenarios, various designs for multidirectional energy harvesting have been reported. In order to harvest energy from planar vibrations, Yang *et al.* [24] developed a capacitive generator with in-plane rotary combs. Figure 2.24 shows the SEM image of a rotary comb capacitive generator and located enlarged components that are fabricated in SOI wafers by deep silicon etching technology. The dimensions of the prototype are 7.5mm×7.5mm×0.7mm. By introducing a ladder shown in the figure, a low resonant frequency of 110 Hz is achieved. The maximum electrical power output is 0.39 μ W at 0.25 g.

Table 2.6 Comparison of the state-of-the-art electrostatic energy harvesters

Reference	Operation direction	Frequency (Hz)	Bias voltage (V)	Volume (mm ³)	Acceleration (m•s ⁻²)	Power (μW)	NPD (μW•cm ⁻³ •g ⁻²)
Yi <i>et al.</i> 2015[120]	In-plane	1900	6	0.014	78.4	2.9×10 ⁻¹	336
Wang <i>et al.</i> 2014[121]	Out-of-plane	96	-400	286	10	1.5×10 ⁻¹	0.52
Basset <i>et al.</i> 2014[122]	In-plane	140-160	30	—	20	2.0	—
Tao <i>et al.</i> 2014[123]	In-plane	78.5	-560	120	0.5	1.2×10 ⁻³	4.0
Nguyen <i>et al.</i> 2013[124]	In-plane	373-1088	150	100 ^a	10	3.4	0.34
Andrea <i>et al.</i> 2013[125]	In-plane	179	-140	150	0.3	3.3×10 ⁻²	240.7
Chiu <i>et al.</i> 2013[119]	Out-of-plane	110	-400	484	20	2.1×10 ¹	10.7
Kim <i>et al.</i> 2013[126]	In-plane	191	4.5	48.6	1.2	3.5×10 ⁻²	50.0
Liu <i>et al.</i> 2012[97]	In-plane	44.2	50	324	0.25	2.5×10 ⁻⁵	0.12
Sheu <i>et al.</i> 2011[74]	In-plane	105	30	4.5	4.3	9.2×10 ⁻²	110.9
Boisseau <i>et al.</i> 2011[85]	Out-of-plane	50	1400	3640	1	5.0×10 ¹	1373
Matsumoto 2011[127]	In-plane	26-40	-800	305 ^b	14	3.0	5.0
Yang <i>et al.</i> 2010[24]	In-plane	110	20	39.4	25	3.5×10 ⁻¹	1.42
Miki <i>et al.</i> 2010[114]	In-plane	63	-180	305 ^b	20	1.0	0.82
Basset <i>et al.</i> 2009[109]	In-plane	250	6	61.5	2.5	6.1×10 ⁻²	15.9
Hoffmann <i>et al.</i> 2009[73]	In-plane	1300-1500	50	200	130	3.5	0.10

^aThe authors have provided the device area of 1cm×1cm and the device volume is estimated by considering the thickness of SOI wafer.

^bThe device volume could be estimated as 305 mm³ by the device area and plate thickness provided by the authors.

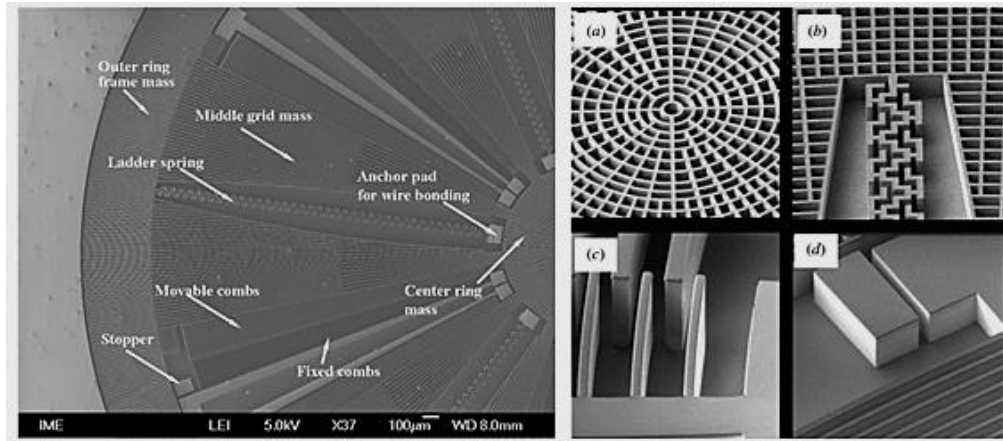


Figure 2.24 SEM images of a rotary comb capacitive generator and located enlarged components [24]

Zhu *et al.* [25] also brought up a 2D MEMS ultrasonic energy harvester based on 2DOF motion flexures. Figure 2.25 shows a packaged ultrasonic energy harvesting prototype of an MEMS device. The comb drive structure is suspended by two orthogonal frames (X and Y) which are anchored to the four corners. With the 2-DOF structure, two close resonant frequencies of 3.872 and 3.852 kHz are achieved in the X and Y directions, respectively. The device was able to achieve 21.4 nW and 22.7 nW in the X and Y directions respectively when it was driven by an ultrasonic transducer in the resonate directions.

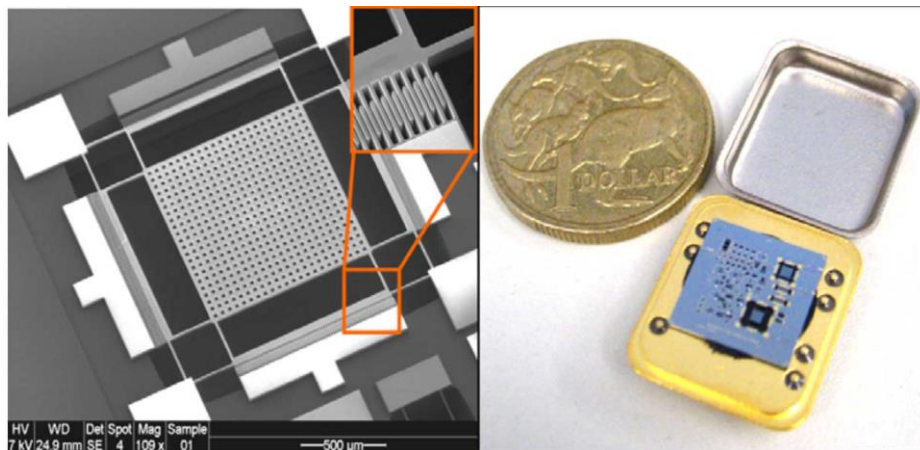


Figure 2.25 SEM images of the fabricated 2DOF MEMS ultrasonic energy harvesting device and packaged prototype

Bartsch *et al.* [23, 128] introduced a two-dimensional resonator with circular spring-mass configuration which has the potential to extract energy from arbitrary planar ambient vibrations. Schematic view of the 2D resonator and enlarged SEM image of the fabricated circular springs are shown in Figure 2.26. The center circular seismic mass enables two close resonant frequencies of 370.5 Hz and 373.7 Hz in two orthogonal directions with a maximum power of 100 pW obtained. Based on the similar design, Liu *et al.* [26] developed a 3D electromagnetic MEMS energy harvester with concentric circular springs with several sets of planar aluminum coils. By this rotational symmetrical design, the device is able to vibrate in an out-of-plane direction and oscillate at two in-plane directions. The first mode is at 1285 Hz with the second and third modes at 1470 Hz and 1550 Hz, respectively. With an excitation acceleration of 1g, an optimum output power of 8.7 nW in the in-plane direction could be achieved.

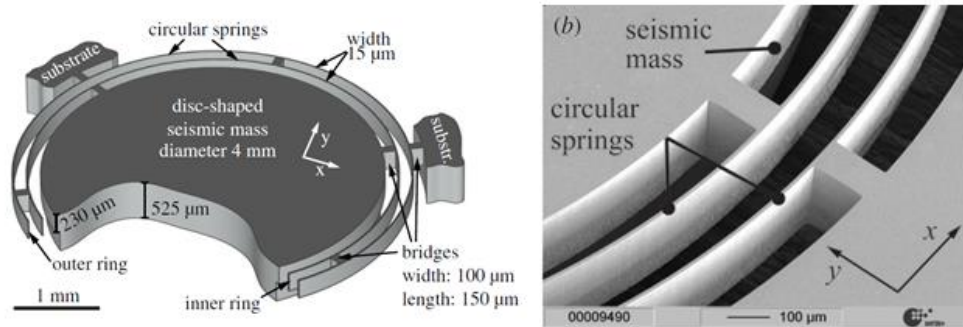


Figure 2.26 Schematic view of the 2D resonator and enlarged SEM image of the fabricated circular springs

Table 2.7 presents a summary of the state-of-the-art 2D vibrational energy harvesters. It can be seen that most of the reported 2D vibrational energy harvesters are based on electrostatic mechanisms. Compared with cantilever-based piezoelectric counterparts, electrostatic harvesters offer more flexibility to decouple the mechanical structure and the energy conversion component. Therefore, they are more advantageous to implement various energy harvesting schemes with abundant spring-mass configurations, such as rotary comb drive structure in [24] and square beam drive

structure in [25]. However, these harvesters require an external charge pump to initiate the energy conversion process. Bartsch *et al.* [23] utilized an electret layer as a charge pump to realize a 2D energy harvesting by having concentric circular spring-mass architectures. The use of electret could eliminate the charge pump and make the electrostatic energy harvesting more independent and self-sustaining. However, the resonant frequencies are hundreds or thousands of Hz with an output power only in 100 pW level, which is far from real ambient energy harvesting applications. More investigative works are needed to achieve multi-directional energy harvesting schemes with largely reduced resonances and effectively enhanced output power.

Table 2.7 Comparison of 2D vibrational energy harvesters to the state of the art

Reference	Working mechanisms	Frequency (Hz)	Acceleration ($\text{m}\cdot\text{s}^{-2}$)	Volume (mm^3)	Power (μW)	NPD ($\mu\text{W}\cdot\text{cm}^{-3}\cdot\text{g}^{-2}$)
Wu <i>et al.</i> 2014[27]	Piezoelectric	36.8/37.2	2	$5.1\times 10^{5*}$	2.9×10^3	142
Yang <i>et al.</i> 2013[129]	Magnetoelect ric	22.5	6	—	6.0×10^2	—
Kim <i>et al.</i> 2013[126]	Electrostatic	191/194	1.2	48.6	3.5×10^{-2}	50.0
Liu <i>et al.</i> 2012[26]	Electro-magnetic	1470/1550	10	36	8.7×10^{-3}	0.242
Zhu <i>et al.</i> 2010[25]	Electrostatic	38725/ 38520	—		2.1×10^{-2}	—
Yang <i>et al.</i> 2010[24]	Electrostatic	110	25	39.4	3.5×10^{-1}	1.42
Bartsch <i>et al.</i> 2009[23]	Electret	370.5/373.7	—	—	1.0×10^{-4}	—

*The device volume is estimated from the frame length and thickness ($\varnothing 90\text{ mm}\times 20\text{ mm}$) provided by the author.

2.3 Frequency broadening energy harvesting strategies

Regardless of the approach adopted (piezoelectric, electrostatic, and electromagnetic), most resonant energy harvesters are designed based on linear resonators which suffer from a narrow bandwidth around its resonance. A slight shift of the excitation frequency from its resonance would give rise to severe deterioration of the overall performance, whereas ambient vibrations are usually distributed over a wide spectrum. To address this shortcoming, this section reviews the recent reported strategies on nonlinear techniques and multi-frequency methods to increase the operating bandwidth of energy harvesters.

2.3.1 Broadband energy harvesting using nonlinear mechanisms

Non-linearities of suspensions have been proposed to be one of the most effective techniques to enlarge the bandwidth, where a significant broadband spectrum can be obtained by utilizing spring softening and hardening effects. Theoretically, the spring softening nonlinearity enhances the output power toward a lower frequency, while a spring hardening nonlinearity broadens the bandwidth by bending the resonant peak toward a higher frequency[130, 131]. This section reviews various designing methods to introduce nonlinearities for broadband energy harvesting.

Nonlinearity induced by magnetic force

An earlier research work by Stanton *et al.* [132] proposed a piezoelectric beam-based energy harvester with a magnetic end mass, as shown in Figure 2.27(a). By tuning the nonlinear magnetic interactions between magnetic end mass and stationary oppositely poled magnet, both the spring hardening and softening response of the piezoelectric beam were implemented. In the experimental validation, it was found that both the output power and bandwidth were largely increased by a linearly frequency sweep-down process, as shown in Figure 2.27(b). However, the presence of the two

magnets in single energy harvesting system may cause undesired force in the whole system, where stiction may easily take place. The enhanced magnetic field may also affect the nearby electronics or magnetic components.

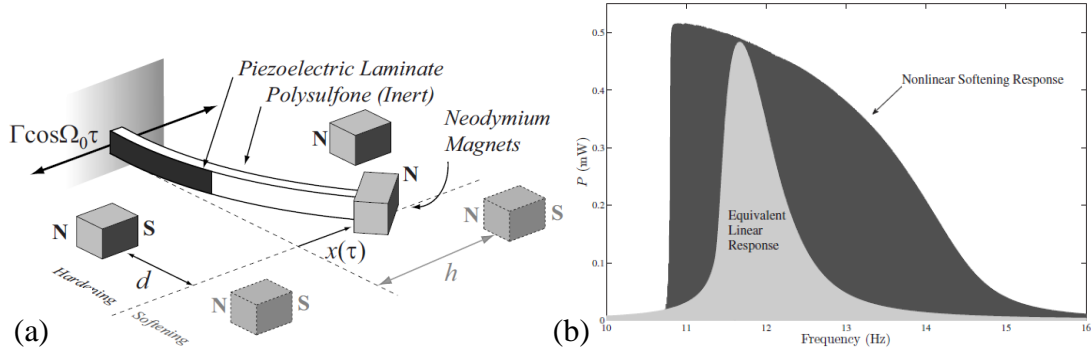


Figure 2.27 (a) Schematic of the proposed piezoelectric nonlinear energy harvester using mass and permanent magnet interactions; (b) Nonlinear energy harvesting outperforming linear resonance [132]

Nonlinearity introduced by mechanical stretching

In this design, the spring hardening nonlinearity of the Duffing effect can be simply achieved by a clamp-clamp beam structure or elastic membrane that experiences mechanical stretching when subjects to large deflections. Hajati *et al.* [133] presented an ultra-wideband piezoelectric energy harvester by exploiting the nonlinear stiffness of a clamped-clamped beam PZT structure of MEMS resonator, as shown in Figure 2.28. The stretching strain provides a passive nonlinear feedback and gives rise to more than one order of magnitude improvement in both power density and bandwidth. Huang *et al.* [134] also achieved wide-bandwidth piezoelectric energy harvester with parylene-C beam structures. Since this method does not require external auxiliary components, it can be easily implemented within MEMS devices. However, this type of approach usually requires strong excitations from external vibration sources to induce change of material properties, which may cause damage or fatigue of vibration systems. Furthermore, in order to induce enough strain in silicon structures, the resonant frequencies of such systems are usually hundreds or thousands of Hz, which

may encounter problems in the ambient environment vibrations.

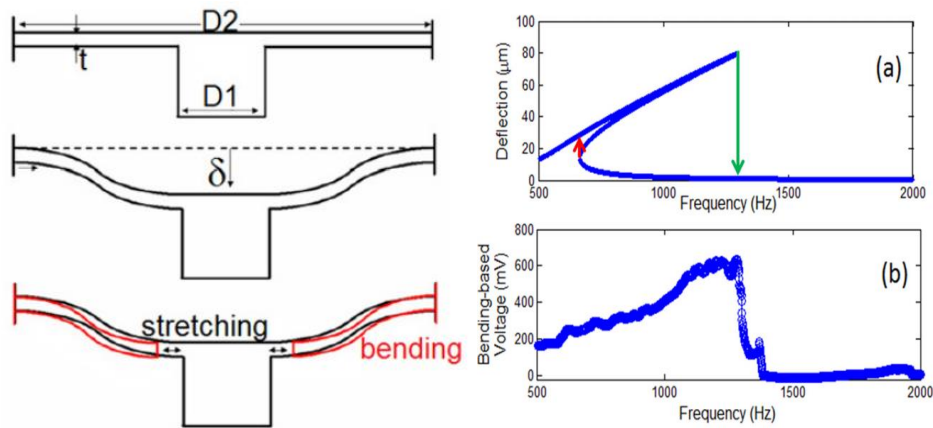


Figure 2.28 Mechanical stretching induced spring hardening nonlinearity with clamped-beam configurations[133]

Nonlinearity induced by mechanical stopper

Another spring hardening nonlinear effect can be simply implemented with increasing the spring stiffness by mechanical stopper effect. Soliman *et al.* [135] investigated an electromagnetic energy harvester with a stopper to adjust the beam stiffness. Figure 2.29(a) depicts the proposed piecewise nonlinear energy harvesting model with mechanical stopper which limits the relative movement of the mass at one side. The spring stiffness increases after collision. Numerical and experimental results have shown the approach could increase the bandwidth of the harvester during a frequency-up sweep, while the spectrum remains the same during a frequency-down sweep. Figure 2.29(b) shows comparison of numerical and experimental frequency–response curves of the root-mean-square (RMS) load voltage. It demonstrated that an increase of 240% bandwidth could be obtained when a frequency-up sweep was applied. With the similar principle, Liu *et al.* [136] investigated the stopper effect on both top and bottom sides of a piezoelectric MEMS device. By adjusting the relative distance of the mechanical stopper and the piezoelectric beam, the power and frequency can be adjusted accordingly. However, the collision would result in energy

and peak loss and it only takes effect during the frequency-up process is applied.

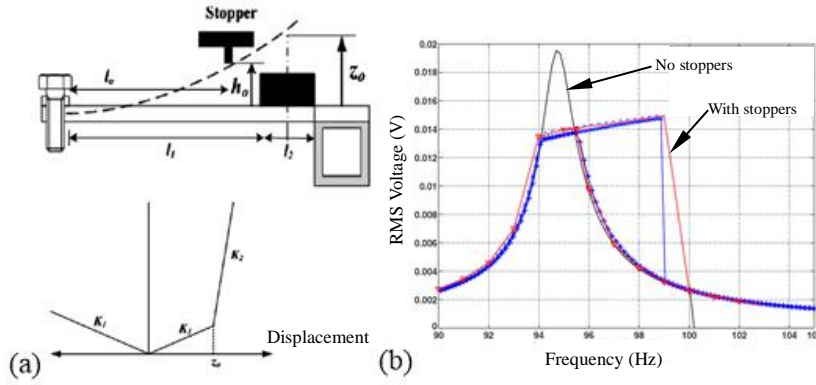


Figure 2.29 (a) Schematic of a modified wideband nonlinear energy harvester induced by mechanical stopper effect; (b) Comparison of numerical and experimental frequency–response curves of the RMS load voltage[135]

Nonlinearity introduced by spring configuration

This work involves increasing the frequency bandwidth by just relying on the nonlinear characteristics of curved beam configuration, which is readily and quite compatible with MEMS fabrication technologies. Nguyen *et al.* [124] presented a microelectromechanical energy harvester with curved beam structure that demonstrates an extremely wide bandwidth. Optical micrograph of MEMS electrostatic energy harvester with bistable curved springs is shown in Figure 2.30(a). Asymmetrical bistable behaviour of the spring is obtained purely according to the geometrical design. Very strong spring softening effect is achieved as shown in Figure 2.30(b), which shows output voltage versus frequency for both up- and down-sweeps at different acceleration amplitudes. For a white noise excitation at the level of $4 \times 10^{-3}/\text{Hz}$, it was reported that the 3-dB bandwidth of the device reached up to 715 Hz, which was more than 250 times wider than in linear-spring regime. White noise is a random signal with a constant power spectral density. However, for such straight beam structures, the resonant frequencies reported usually are extremely high, which are hundreds or thousands of Hz due to small volume of the whole structure.

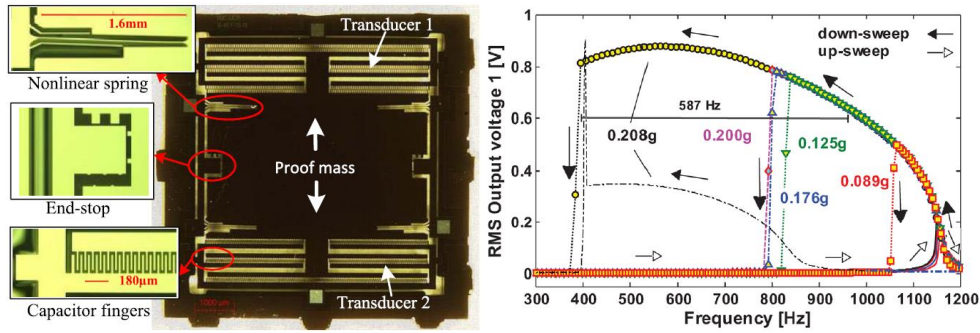


Figure 2.30 (a) Optical micrograph of MEMS electrostatic energy harvester with bistable curved springs; (b) RMS output voltage versus frequency for both up- and down-sweeps at different acceleration amplitudes[124]

Table 2.8 lists a concise qualitative summary of merits, weakness and applicability of these four nonlinear implementation techniques for vibrational energy harvesting. Magnetic force method has the advantages for large external force and frequency tuning range, but its complexity and adverse effect to adjacent magnetic electronics make it hard for applications in micro-scale MEMS device. Mechanical stretching is more applicable for soft and flexible materials which easily introduce passive nonlinear feedback within the materials itself. However, large external excitations and high operating frequencies are required to induce nonlinear effect. With the help of spring-hardening nonlinear effect by end stoppers, the frequency bandwidths can be largely enhanced during a frequency sweep-up process. Nevertheless, the magnitude of the vibration amplitude is compromised. It must be said that bandwidth stays unchanged during a frequency sweep-down process, which does not contribute to the energy conversion efficiency. The method of using curved beam to induce nonlinearity seems more advantageous and promising due to its MEMS compatible process and ultra-wideband response, but it also encounters problems at high operating frequencies. Besides these reported methods, electrostatic nonlinearity introduced by electret surface potential, as an inherent feature of e-EVHs, has seldom been investigated. The nonlinearity of the energy harvesting system does not rely on any external conditions. It is practically more advantageous and readily compatible with MEMS fabrication processes and thus detailed studies are highly desired.

Table 2.8 Summary of merits, weakness and applicability of several nonlinear implementation techniques

Implementation methods	Merits, weakness and applicability	References
Magnetic force	<ul style="list-style-type: none"> ➤ Strong frequency tuning range ➤ Not applicable to micro device ➤ Needs precise control 	[137] [132]
Mechanical stretching	<ul style="list-style-type: none"> ➤ Easy implementation ➤ small frequency tuning range ➤ Usually large excitation & high frequency required ➤ Mostly use clamped-beam structures 	[138] [133] [134]
Mechanical stopper	<ul style="list-style-type: none"> ➤ Easy implementation with MEMS ➤ Only effective for frequency up-sweep ➤ Suitable for low-frequency source ➤ Energy peak loss at resonant frequency 	[136] [139, 140] [57]
Spring configuration	<ul style="list-style-type: none"> ➤ Easy implementation with MEMS ➤ Large frequency tuning range ➤ Usually implemented with electrostatic mechanisms 	[124, 141, 142]

2.3.2 Multi-frequency energy harvesting

Implementing multi-frequency by cantilever array configuration

To get broadband vibrational energy harvesting, one of the most straightforward methods is to integrate an array of harvester units with various spring or mass dimensions [143-146]. These individual harvester units with different resonant frequencies are carefully analysed to cover a designated range of frequencies over a wideband operation. Sari *et al.* [146] proposed a wideband MEMS electromagnetic vibrational micro power generator by incorporating a series of cantilevers with micro-patterned coils, as shown in Figure 2.31. The power is generated by the relative motion between a static magnet and the oscillating cantilever arrays of various lengths. The overall frequency spectrum is the sum of the natural frequency of each individual cantilever. It was reported that a continuous output power of 0.4 μW was achieved

covering a wide external vibration spectrum of 4.2~5 kHz. Based on similar principle, Ferrari *et al.* [144] presented a multi-frequency MEMS piezoelectric converter which composed of multiple bimorph cantilevers with different natural frequencies, as shown in Figure 2.32. Liu *et al.* [145] proposed a wideband MEMS piezoelectric power generator based on thick-film PZT cantilevers. A measured performance of 3.98 μW was achieved. With the cantilever array configurations, broadband energy harvesting can be achieved without sacrificing the systemic Q factors.

Such designs are however inefficient in terms of power density, since only one unit is active and effective for energy generating at each time while others just stay off-resonance status. Micro-fabrication of such a complex and large volume systems also encounters great challenges.

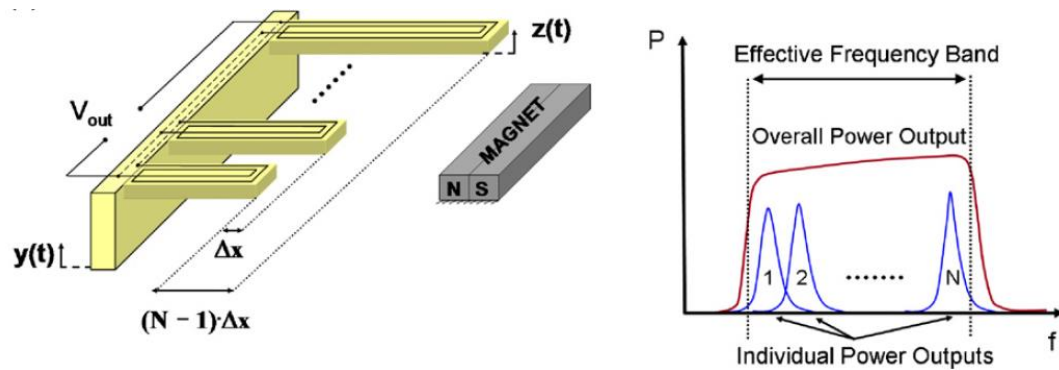


Figure 2.31 Proposed broadband MEMS electromagnetic power generator by Sari *et al.* [146]

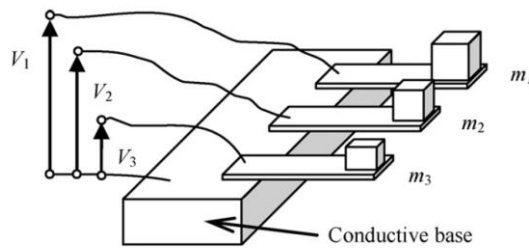


Figure 2.32 Proposed multi-frequency MEMS piezoelectric power generator by Ferrari *et al.* [144]

Exploiting multiple vibration modes of a single spring-mass system

Rather than combining an array of harvester units, another interesting method for multiple frequency energy harvesting is to exploit multiple vibration modes from a multi-degree-of-freedom system. Roundy *et al.* [147] initially proposed an idea of integrating multiple mass into a single beam system to obtain broader bandwidth. Based on this idea, Yang *et al.* [148] developed a multi-frequency electromagnetic energy harvester. It consists mainly of three permanent magnets located at different locations of an acrylic beam and three sets of two-layer copper coils. It was reported that the device could harvest at its first three vibration modes at frequencies of 369 Hz, 938 Hz and 1184 Hz. The device configuration as well as the mode shapes and resonant frequencies of the first three vibration modes are depicted in Figure 2.33. Tadesse *et al.* [149] also achieved multi-modal energy harvesting by a hybrid system with both electromagnetic and piezoelectric mechanisms at resonances of 20 Hz and 100 Hz, respectively. Ou *et al.* [150] proposed a multi-modal two-mass cantilever beam with resonances at about 50 Hz and 360 Hz as well. The proposed multi-modal energy harvester based on double-mass on piezoelectric beam is shown in Figure 2.34.

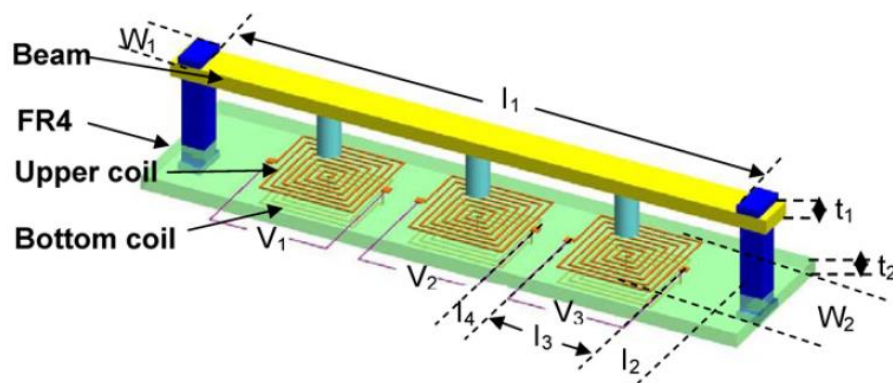


Figure 2.33 Proposed multi-frequency electromagnetic energy harvester by Yang *et al.* [148]

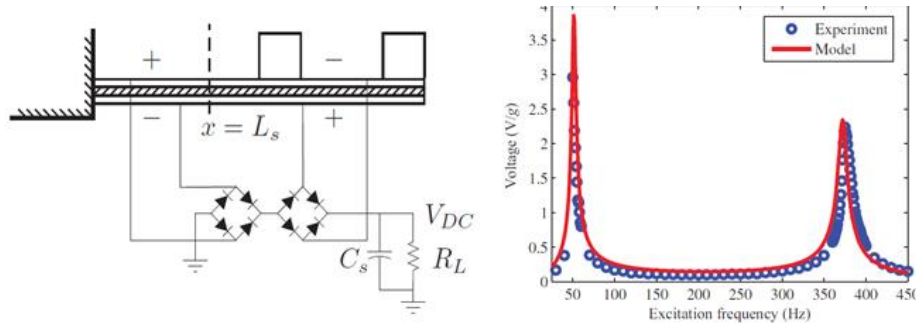


Figure 2.34 Proposed multi-frequency vibration energy harvester based on a double-mass piezoelectric cantilever beam by Ou et al. [150]

However, in most of multimodal structures, their high-order modes are separated far away from the fundamental vibration mode and with a significantly smaller magnitude as in aforementioned literature. The contribution to energy harvesting from higher vibration modes besides the primary mode is usually negligible. Obviously, it is desirable to develop not only a system with multiple vibration modes but also have each peak to be close to each other with effective magnitudes to contribute to overall energy harvesting. Since dynamic behaviors of such multi-frequency structure are dominated by the parameters of spring-mass system, this necessitates the precise control of the dimensions of the beam and seismic mass.

Electret-based MEMS devices are promising since they are particularly suited for batch fabrication using Si CMOS compatible processes where various parameters of spring-mass system, such as the thickness, width and diameters of beam and seismic mass, can be easily and precisely adjusted through lithography process, which makes a multi-frequency e-VEH achievable. By carefully tuning the parameters of the beam and mass, the first several resonances of primary mass can be tuned close to each other while maintaining comparable magnitudes. From the literature review, it is also noted that MEMS devices of multiple-degree-of-freedom system have not been reported up to date. Therefore, it is desirable to explore and develop MEMS electret-based energy converters to achieve multi-frequency energy harvesting while maintaining at effective peaks.

2.4 Comparative review of energy harvesting schemes

This chapter reviews the state-of-the-art vibrational energy harvesting technologies. A comprehensive discussion of micro electret-based electrostatic energy conversion mechanisms relating to its operating principles, electret materials, charging methods as well as both in-plane and out-of-plane harvesters is summarized. Recent advances on adaptive energy harvesting methods, incorporating multi-directional techniques and broadband energy harvesting, are reviewed to address the current challenges of vibration-based energy harvesters, namely restricted single-direction issue and narrow bandwidth issue. Their respective merits, weakness and applicability of each method are compared, summarized and discussed.

From the state-of-the-art multi-directional energy harvesters, electrostatic harvesters are advantageous and demonstrate more flexibility to decouple the mechanical structure and the energy conversion component. The use of electret could eliminate the charge pump and make the energy harvesting more independent and self-sustaining. However, it is also found that to design low-resonant-frequency structures within a small confined space while maintaining multi-directional energy harvesting capabilities would be a great challenge. The output powers reported are still rather low in pW level. Therefore, there is scope to further investigate into achieving a low-frequency multi-directional e-VEH with moderate output powers.

Although numerous methods have been proposed to induce nonlinearities of energy harvesting system, electrostatic nonlinearity introduced by electret surface potential, as an inherent feature of e-EVHs, is seldom examined. The nonlinearity of energy harvesting system does not rely on any external conditions, which are more advantageous and readily available than other counterparts. A more detailed study into such type of mechanisms is highly desirable.

Creating close peaks with effective magnitudes by investigating multiple vibration modes of a multi-degree-of-freedom system is meaningful and beneficial to overall energy harvesting. Electret-based MEMS devices are promising due to their compatible fabrication process with Si CMOS technology, where the parameters of spring-mass system can be easily and precisely tuned through lithography process. From the literature review, MEMS devices for such multiple degree-of-freedom systems have not been reported to date. As such, novel methods in developing an electret-based multi-frequency MEMS energy harvesting device could be made.

Chapter 3 Sandwich-structured 2D electret micro power generator

This chapter investigates a sandwich-structured micro electret power generator for multi-directional vibrational energy harvesting. Sandwich structure integrated with two separate capacitive circuits was adopted as it seeks to enhance the output power and minimize the unwanted vertical pull-in and horizontal damping electrostatic force. Both vertical and horizontal electrostatic forces were analysed by combining finite element method and numerical calculations. The multi-directional energy harvesting capabilities were then studied according to frequency-response characterization results.

3.1 Introduction

According to the literature review of previous chapter, one of the main challenges of multi-directional electrostatic energy harvesting is the low output power. As an inherent feature for electrostatic energy harvester involves the capacitance change of the variable capacitors, the power to be generated is largely dependent on the bias potential and capacitance variation. To derive sufficient output power, high surface voltage of the electrets of up to 1000V with a gap of less than 100 μm are normally required for electret-based generators [79].

This would however give rise to strong electrostatic force between the electret and the counter electrode where the instability of the spring-mass system and stiction problems can readily set in. In order to maintain the air gap, high-aspect-ratio (HAR) springs by deep reactive-ion etching (DRIE) are commonly employed. This is owing to its stiffness ratio between the out-of-plane and in-plane directions being a square of the aspect ratio of the spring height and width. It is to be noted that the stiffness derived is greatly affected by under-cutting resulting from the DRIE process and the

torsional deformation of the beams. Besides employing HAR springs, various additional techniques have also been proposed to control the air gap and avoid stiction. Boland *et al.* [80] employed mercury droplet as a rotor instead of tethers. Lo *et al.* [151] proposed a sliding rotor on top of the stator. Naruse *et al.* [86] and Modafe *et al.* [152] adopted stainless-steel micro ball bearings with micro grooves etched into a silicon substrate. Their works rely mostly on stoppers or mechanical contact, where damage owing to wear and fatigue can readily set in, especially for long operational cycles.

In this work, sandwich structure is adopted as a non-contact passive gap control method that helps to reduce the vertical pull-in electrostatic force as well as the horizontal damping force thereby enhancing the performance of the whole device. Figure 3.1 depicts schematic illustrations of force reduction mechanisms in both in-plane and out-of-plane directions for the proposed sandwich-structured e-VEH device compared with the traditional two-plate structures. Figure 3.1 (a) and (b) depict the initial condition and small movement of the top plate of the two-plate structure, respectively. It can be seen that there exists a strong vertical electrostatic pull-in force at the initial condition as shown in Figure 3.1 (a). When there is a small movement of the top plate, a horizontal electrostatic drag force is generated as well as a vertical pull-in force.

Figure 3.1 (c) and (d) depict the initial condition and small movement of the middle plate within the three-plate structure, respectively. It can be seen that the electrodes on the top and bottom surfaces of the middle plate are designed having 180° out-of-phase arrangement. Similar corresponding counter electret and electrode strips are also patterned on both top and bottom plates as illustrated in Figure 3.1 (c). At the initial state, the electrodes on both plates of the top capacitive circuit (TCC) have a 100% overlapping area, while the overlapping ratio is 0% for the bottom capacitive circuit (BCC). When there is a horizontal oscillation of the middle plate, the overlapping

ratio changes from 100% to 0% for the TCC, with the BCC varying from 0% to 100%. This would bring about the opposite direction of the electrostatic damping force on the two sides of the seismic mass thereby eliminating the horizontal electrostatic damping effects, as shown in Figure 3.1(d). The vertical pull-in electrostatic force is also decreased due to coexistence of vertical attractive forces within both top and bottom capacitive circuits. These aspects will be further deliberated in the ensuing sections with numerical models.

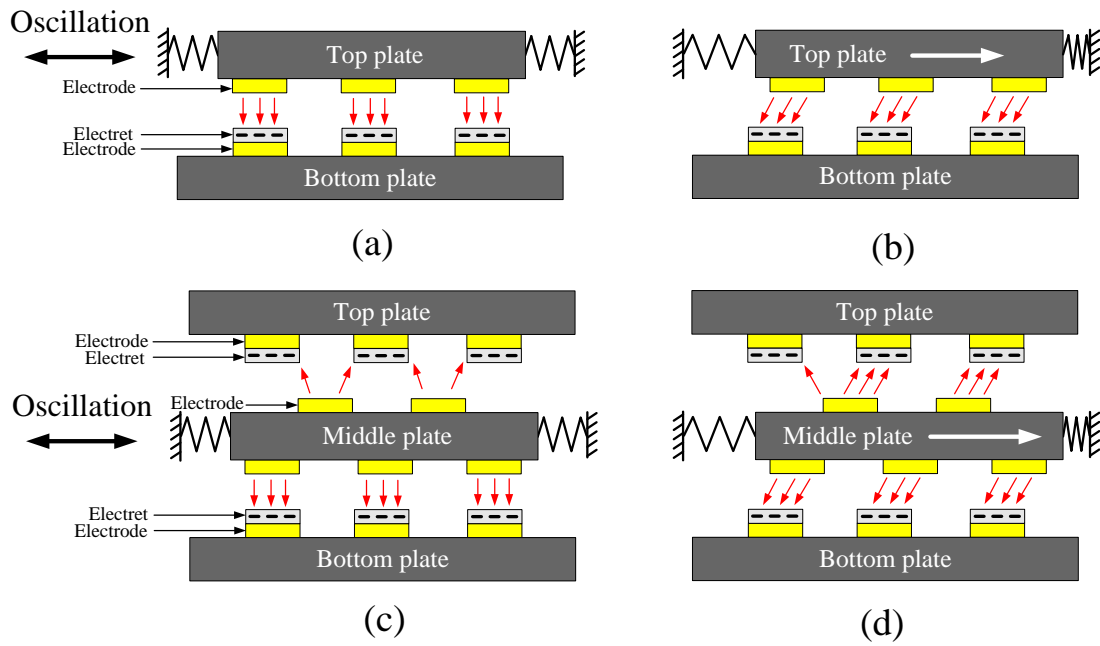


Figure 3.1 Schematic illustrations of force reduction mechanisms in both in-plane and out-of-plane directions for sandwich-structured electret power generator: (a) initial state for two-plate structure; (b) small oscillations within two-plate structure; (c) initial state for three-plate structure; (d) small oscillations of the middle plate within three-plate structure

3.2 Device design and modeling

3.2.1 Device configuration

Figure 3.2 shows the schematic of the sandwich-structured e-VEH that seeks to derive kinetic energy from arbitrary in-plane directions. It consists mainly of three parallel silicon plates. The middle plate composes of a movable spring-mass architecture with double-sided patterned electrodes. The square seismic mass with a height of $300\ \mu\text{m}$ and a width of $1\ \text{cm}$ is suspended around by a set of elastic beam flexures. The flexures consist of four parallel beams with a width of $50\ \mu\text{m}$ and height of $300\ \mu\text{m}$ that are connected with each other at a spacing of $250\ \mu\text{m}$. The design of the spring-mass system has symmetrical structures to create approximate resonant frequencies in two orthogonal in-plane directions. The electrodes having a width of $300\ \mu\text{m}$ on the both sides of the seismic mass are designed with a 180 degree out-of-phase arrangement. The electrets on the bottom/top silicon plates can be charged as a negative/positive permanent surface voltage source. When an external oscillation causes a relative displacement between the middle seismic plate and the top/bottom electret plate, the capacitance variation would generate an alternating current flow in the external circuit.

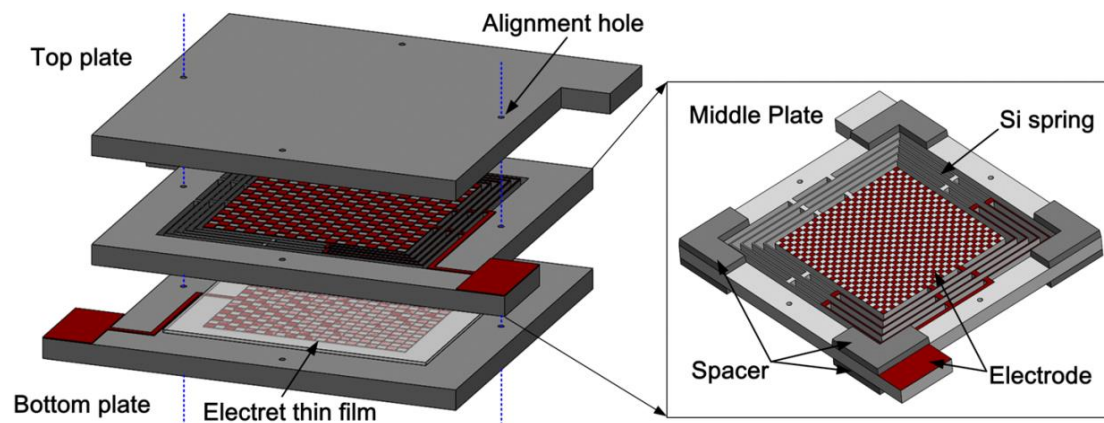


Figure 3.2 3-D schematic view of the energy harvester

3.2.2 Mechanical analysis

A finite element analysis based on ANSYS is employed to construct the model and analyze the vibration behavior of the spring-mass system. In the simulation, the ends of the square spring flexures are anchored and the displacement are set to be zero. Each component makes use of an eight-node brick element. More than 13000 elements are used to mesh the mechanical model. Since the proposed device is fabricated on the standard (100) silicon wafer and the X- and Y- axes of the device are aligned with the $\langle 110 \rangle$ silicon crystal direction, the material properties of the silicon have the elastic coefficients of $C_{11}=C_{22}=194.5$ GPa, $C_{12}=C_{21}=35.7$ GPa, $C_{13}=C_{31}=C_{23}=C_{32}=64.1$ GPa, $C_{33}=165.7$ GPa, $C_{44}=C_{55}=79.6$ GPa, $C_{66}=50.9$ GPa. Details of the designed parameters and specifications of the proposed device are found in Table 3.1. The mode shapes of the first three vibration modes are shown in Figure 3.3(a)–(c) with resonant frequencies of 129.9 Hz, 130.0 Hz and 269.4 Hz, respectively.

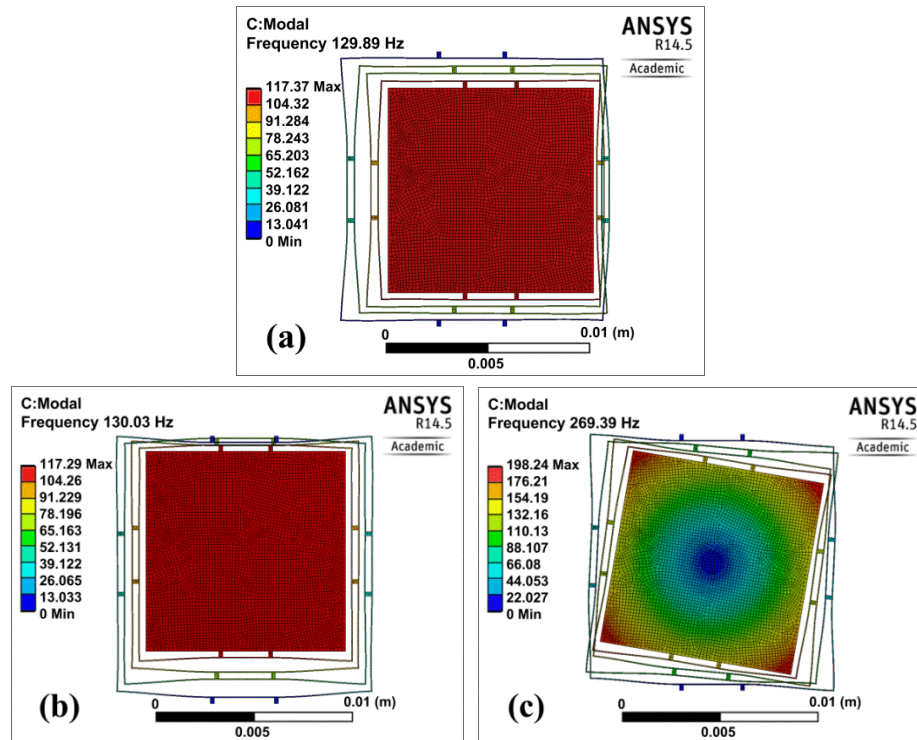


Figure 3.3 Modal simulation of Spring-mass system: (a) mode I; (b) mode II; (c) mode III

From the simulation, it is found that the spring-mass architecture is capable of oscillating in the two orthogonal (X-and Y-) directions at mode I and II, while it is likely to rotate in the plane at mode III. The harvester is thereby able to scavenge kinetic energy from arbitrary directions in the 2D plane by combining its first two oscillation modes. Since the resonant frequency of rotational mode is about twice of that of two orthogonal oscillation modes, it would hardly be excited when the excitation frequencies are below 200 Hz as used in this study.

Table 3.1 Designed parameters and specifications of the proposed MEMS electret power generator

Component	Geometric parameter	Values
Seismic mass	Width d	10 mm
	Height h	300 μm
	Weight m	69.9 mg
Spring flexures	Width w	50 μm
	Height h	300 μm
	Spacing l_s	250 μm
Conjunctions	length l_c	360 μm
	Width w_c	300 μm
Electrode	Ti/Au thickness h_e	50/300nm
	Electrode pattern width	300 μm
Electret	Thickness d	50 μm
	Air gap	120 μm
	Surface potential V_s	-320 V
Device size	Volume V	18×20×1.5 mm ³

3.2.3 Electrostatic Force analysis

In this study, sandwich structure is adopted in the proposed e-VEH device having two separate generator circuits integrated into single device. The cross-section schematic

of the sandwich-structured e-VEH with its associated load circuit is shown in Figure 3.4. In this sandwich structure, a decrease in both the vertical pull-in electrostatic force as well as the horizontal damping force is experienced. These aspects are further studied and estimated by applying the electrostatic module (*es module*) of Comsol Multiphysics simulation since the fringing effect would be taken into account.

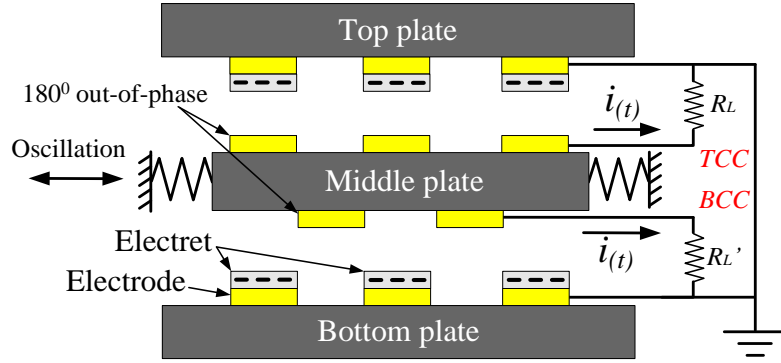


Figure 3.4 Cross-section view of the sandwich-structured e-VEH

Figure 3.5 presents a section of the geometrical layout and electric field distribution of the analytical model for a two-plate and sandwich structure consisting of 30 periodically located strips of electrodes with 10mm in depth. The air gaps between the two electrodes are 120 μm and one of the electrodes is negative biased with a voltage of -320V. From vectors of the electric field distribution in Figure 3.3, it can be seen that strong fringing effect exists around the edge of the electrodes from the FEM analysis model.

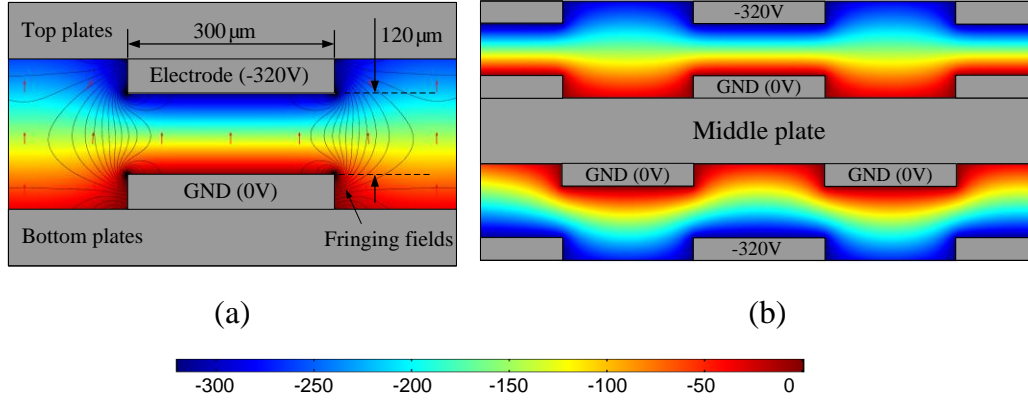


Figure 3.5 Contours of the potential gradient and vectors of electric field distribution: (a) two-plate structure; (b) sandwiched structure

As electret generator operates on in-plane oscillation motions, the vertical electrostatic stability can be directly obtained from the COMSOL electrostatic simulations. Figure 3.6 presents the vertical electrostatic force as a function of the comparative displacement for the two-plate and sandwich structures. The 0 μm displacement on the horizontal axis depicts the position that the top and bottom electrodes are completely overlapped with respect to its center, while 300 μm displacement denotes the two electrodes are in the anti-phase arrangement position. The vertical electrostatic force for two-plate structure varies from 1.73 mN to 1.31 mN but with a sandwich structure, the force reduces to between 0.47 mN and -0.45 mN. This represents approximately 72.8% reduction of the peak vertical electrostatic force for the two-plate structure. This behavior is due to the existence of the vertical attractive force on each side of the seismic mass that counteracts each other. It largely enhances the vertical stability by employing such non-contact passive gap control method.

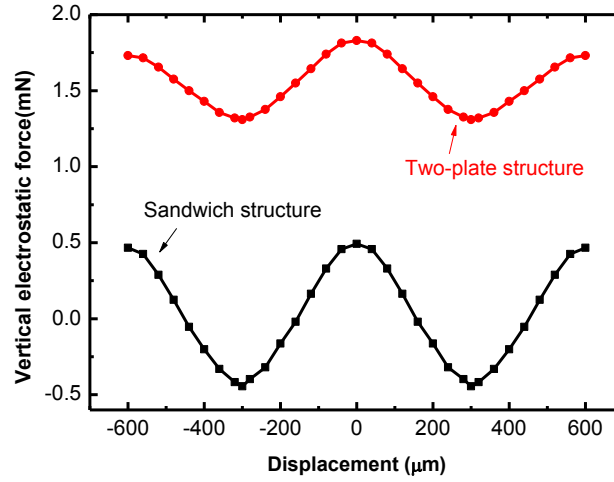


Figure 3.6 Vertical electrostatic forces as a function of comparative displacement for the two-plate structure and sandwich structure

For the horizontal electrostatic damping force $F_e(x)$, it can be deduced by differentiating the total potential energy stored in the capacitor $C(x)$ [73] with respect to the position of the movable counter electrode which can be expressed as:

$$F_e(x) = \frac{1}{2} V_s^2 \frac{\partial C(x)}{\partial x} \quad (3.1)$$

Figure 3.7 illustrates the capacitance variation of the TCC and BCC as a function of comparative displacement within the sandwich-structured e-VEH. It is found that the capacitance variation significantly differs from traditional theoretical model ($C = \epsilon A/d$) which does not take into consideration the strong nonlinear fringing effect around the micro-sized electrode strips. Hence, an analytical expression needs to be derived via curve fitting techniques using the simulated capacitance results at discrete positions. It has been observed that the capacitance variation can be evaluated by a cosine function with two extreme values C_{max} and C_{min} having an electrode strip width w_e , which is similar to the analytical expression proposed by Boisseau *et al* [153]. The expression is as follows

$$C(x) = \frac{C_{max} + C_{min}}{2} - \left(\frac{C_{max} - C_{min}}{2} \right) \times \cos\left(\frac{\pi x}{w_e}\right) \quad (3.2)$$

According to the Figure 3.7, it is also found that the two extreme values are not constant hence another polynomial interpolation is added to better model the dynamic nature of this set of discrete points. The results of the fitted curves as well as the point by point discrete simulation results are shown in Figure 3.7. It can be seen that the capacitance values obtained from the numerical model are in good agreement with the simulation results. Figure 3.8 demonstrates the calculated electrostatic force as a function of displacement for the TCC and BCC compared with a net force on the seismic mass. It can be seen that the horizontal electrostatic damping forces from the TCC and BCC also encounter a 180° phase difference due to the electrode arrangement. It is also observed that the net force acting on the seismic mass does not totally cancel out each other or decrease to zero by the superimposition of the electrostatic forces from the TCC and BCC. The maximum residual magnitude of horizontal damping force was reduced by approximately 46.2% from 0.13 mN to 0.07 mN. Similar phenomenon is also observed based on simulation results by Suzuki *et al.* [115] in that more than 90% decrease of the horizontal electrostatic damping force can be achieved utilizing a dual-phase electrode arrangement within in a single plate.

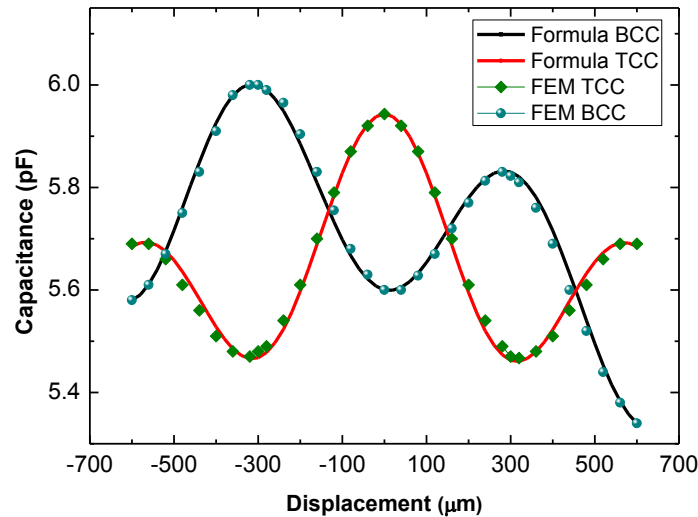


Figure 3.7 Capacitance variations of TCC and BCC as a function of comparative displacement within the sandwich-structured e-VEH

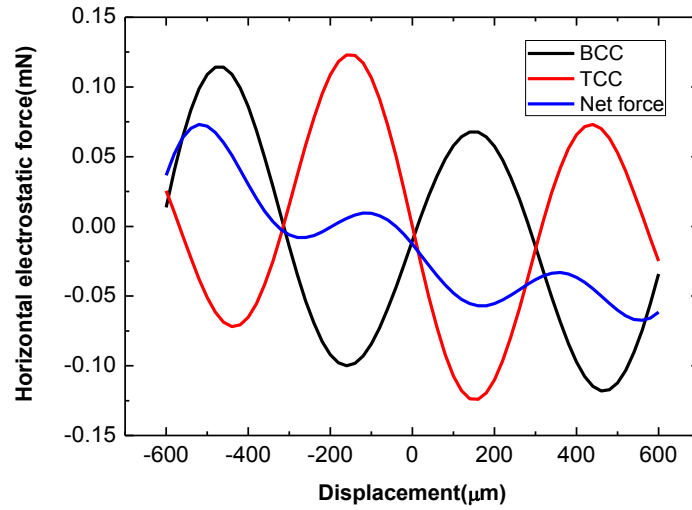


Figure 3.8 Calculated horizontal electrostatic damping forces for the TCC, BCC and the net force operated on the seismic mass

3.3 Fabrication Process

The fabrication flow and assembly process of the sandwich-structured e-VEH were illustrated in the Figure 3.9. The process involved preparation of the top/bottom substrate and middle spring-mass plate, the formation of the shadow mask, the process of localized corona charging and final assembly. Both top and bottom substrates were fabricated on a 300 μm thick (100) Si wafer with a 1 μm oxide layer which was deposited by plasma-enhanced chemical vapor deposition serving also as an insulation layer (a). Gold electrodes were patterned on oxide insulation layer by sputtering Ti (50 nm)/Au (300 nm) and followed by a lift-off process (b). The electret thin film was then mounted on the surface of the substrate using SU-8 or epoxy as a bonding layer (c).

After the top/bottom substrate plate was prepared, a localized corona charging method was used for the production of micro-sized electret array [123, 154], which was devoid of any micro-patterning and etching process of the electret films. A commercial-grade Low-density polyethylene (LDPE, GOODFELLOW, USA) thin film was used as electrets in this prototype fabrication. Wafer-through DRIE process

was used to get an array of micro-scale openings onto a 150 μm thickness silicon wafer which would serve as a shadow mask (A-B). The shadow mask was then deposited with 300nm gold as conductive grid on the top and 500nm silicon oxide as insulation layer on the bottom (C). Finally, the electret thin film was selectively charged by being placed between the shadow mask on the top and the silicon substrate with gold electrode on the bottom during charging process, as depicted in step (d), which showed the corona localized charging system configuration.

The middle spring-mass plate was fabricated on a 4 inch 300 μm thick standard (100) Si wafer as well (I). The gold electrodes were patterned on both sides of the seismic mass through lift-off processes (II) similar to the step (b). This step was followed by sputtering 600 nm Al film as a heat-sink layer on bottom of the structure to facilitate heat dissipation as well as prevent excessive damage in critical dimensions during deep etches. RIE and DRIE were utilized to define the in-plane geometry of the spring-mass architecture (IV). After that, the whole spring-mass structure was released by removing Al layer along with the remaining photoresist (V). When all the components were prepared, a three-parallel sandwich-structured device was constructed by assembling the top/bottom plates with charged electret and the middle spring-mass plate, as shown in step (e).

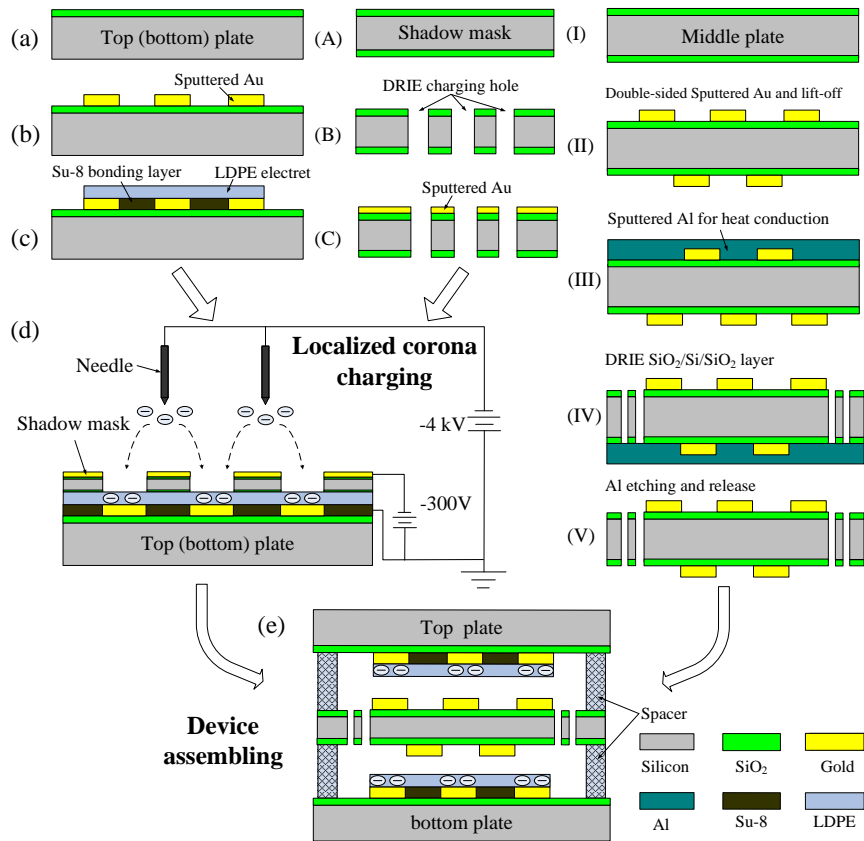


Figure 3.9 Fabrication flow and assembly process of the sandwich-structured electret generator

Figure 3.10 presented the images of released spring-mass structure. For electret/electrostatic generators based on the variation of overlapping areas, small misalignment or rotation would largely influence the rate of change of the overlapping area between electrets and electrodes [155], especially in the current study for the three-layer sandwich structure. In order to facilitate the precise alignment in assembly, four alignment holes with diameter of $400 \mu\text{m}$ were fabricated, as shown in Figure 3.10(b), which was further aided by sticking alignment pins pass through the holes. An enlarged scanning electron microscope (SEM) image of the elastic beam flexures was shown in Figure 3.10(c). It was observed that the beam width decreases from about $51 \mu\text{m}$ at the top to about $45 \mu\text{m}$ at the bottom, which meant the cross-section of the beam has a 1.1° tapered angle and the high aspect ratio was about 6 for this

particular device. The SEM image of electrode patterns with a width of $300\ \mu\text{m}$ on the seismic mass was illustrated in Figure 3.10(d).

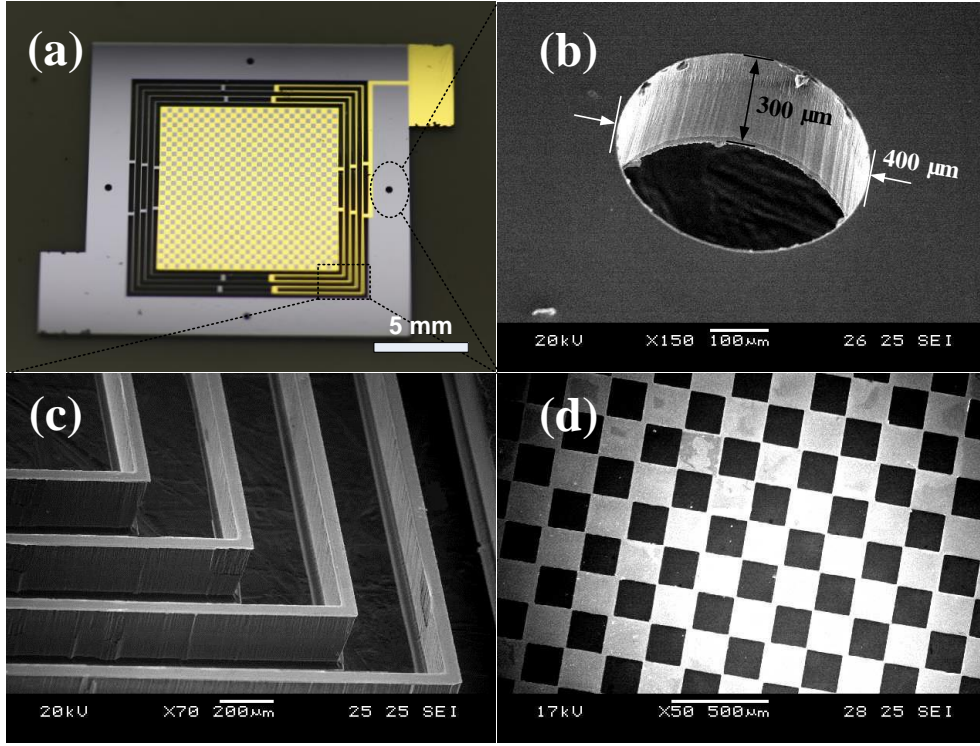


Figure 3.10 (a) Image of the fabricated spring-mass structure; (b) (c) enlarged views of the alignment holes and elastic beam flexures; (d) SEM image of electrode cells on the seismic mass

SEM was also used for mapping the micro-sized charge distribution on the LDPE thin films after charging. The samples were devoid of any sputtering or preparation before SEM imaging process. As shown in Figure 3.11, the bright and dark areas corresponded to the negatively charged and uncharged areas, respectively. It could be seen that good uniformity and high resolution of charge distribution were achieved through this method. After two days, the charged sample was still able to maintain a surface voltage of above -500V . From the previous study [29], the shapes of the charge patterns maintained almost unchanged after 20 days storage even though the potential drops. In order to avoid pull-in effect and facilitate the construction of the sandwiched structure, a surface potential of -320V was selected as a compromise in

the experiment. An assembled sandwich-structured electret power generator compared with a ten cents coin was shown in Figure 3.12.

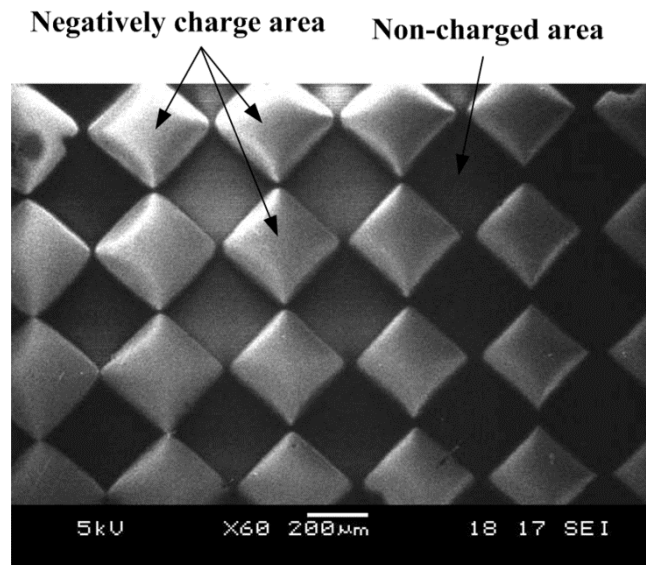


Figure 3.11 SEM image of micro charge distribution (negative charged) and surface potential decay as a function of time

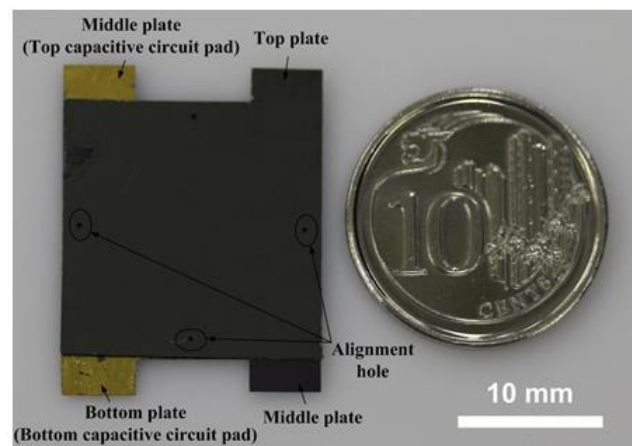


Figure 3.12 Assembled sandwich-structured electret power generator compared with a ten cents coin

3.4 Power generation experiment

The fabricated sandwich-structured e-VEH prototype was characterized using the measurement setup as demonstrated in Figure 3.13. It consisted of a shaker, an

accelerometer, a voltage amplifier, a function generator and a data acquisition system which is connected to a computer. A small rotational stage was fixed onto the L-shaped holder where 2D vibration excitation in the in-plane direction could be performed. An acceleration sensor was fixed onto the base of the holder to monitor the excitation acceleration. A data acquisition system (DAQ NI USB-6289 M series) was utilized to detect the electrical output of the prototype which could be controlled and monitored by a laptop.

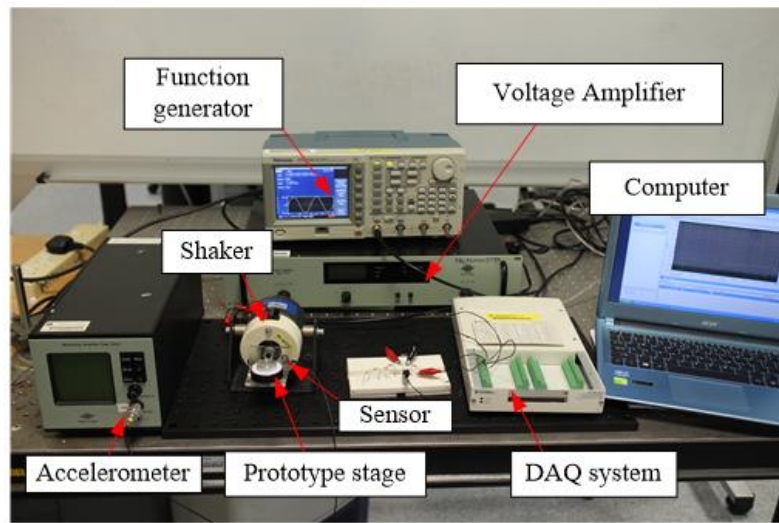


Figure 3.13 Photograph of the measurement setup

Figure 3.14 showed the frequency responses of the generator obtained at different excitation angles for the bottom capacitive circuits (BCC). Due to the symmetrical properties of the generator, only one quarter (0° - 90°) of the whole 2D plane was studied in the experiment. Excitation frequencies from 110 to 140 Hz at a fixed acceleration of 0.2 g were applied to the prototype at various excitation directions at 30° increment intervals with a load resistance of 20 M Ω . The design parameters for the prototype were shown in Table 3.1 similar to the ones used in the previous simulation. It could be seen that vibration mode I took place at the frequency of 121 Hz reaching its maximum at an excitation angle of 0° (X-direction), while mode II occurred at the frequency of 125 Hz with its maximum at an excitation angle of

90 °(Y-direction). When the external excitations were in the diagonal directions (30 ° and 60 °), two resonance peaks with a frequency splitting of 4Hz and smaller magnitudes were generated lying between the two extremes (0 ° and 90 °). It indicated that the dynamic behavior of the device was dominated by Mode I when the excitation frequency was around 121 Hz, while it was determined by Mode II when the excitation frequency was near 125 Hz. If superimposing these two small magnitudes at a specific diagonal excitation direction (e.g. 30 °), the overall effectiveness was still comparable to the two extremes when the excitations were aligned, as depicted in Figure 3.15. The system quality factor could be calculated by $Q = f_r/\Delta f = 89.1$, where f_r was the resonant frequency and Δf was the half power bandwidth. According to the previous simulation, mode I and mode II were expected to take place at X-direction with the frequency of 129.9 Hz and at Y-direction with the frequency of 130.0 Hz, respectively. The experimental results were in good agreement with the simulations except for a frequency variation of less than 7%. The discrepancy may be due to the beam width reduction of the long-term DRIE process and over exposure of lithography. The increase of mass due to electrode patterning also causes frequency reduction and the assembly of three-layer structure is not free of errors.

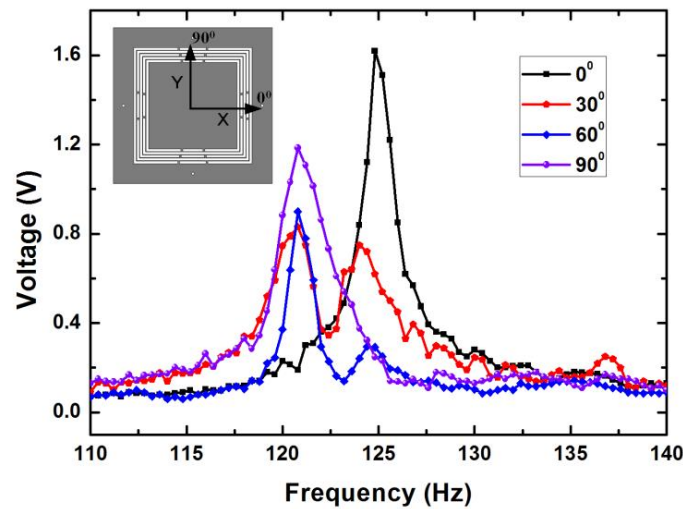


Figure 3.14 Output voltages as a function of frequencies from 110 to 140 Hz with different excitation angles at 0.2g

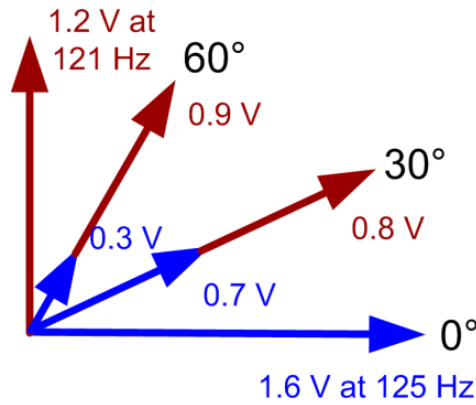


Figure 3.15 Output voltages as a function of frequencies from 110 to 140 Hz with different excitation angles at 0.2g

To further study the comparative performance of the two capacitive circuits, dynamic readings from both the BCC and TCC at the resonance of 125 Hz and excitation angle of 0° (X-direction) were recorded by DAQ system simultaneously. Figure 3.16 demonstrated the output voltage as a function of time at acceleration of 0.2 g and resistance of 10 M Ω for two capacitive ports. According to the wave forms, the output voltages in the BCC and TCC were found to be 180° out of phase with each other. It indicated that the in-plane electrostatic damping forces on both sides of the seismic mass were in the opposite directions and affirmed the inherent damping effect could be reduced by the sandwich-structured e-VEH configuration. Moreover, electrical energy in the sandwich-structured e-VEH could be extracted from both separate capacitive ports which would further enhance the output power. The blue line shown in Figure 3.16 denoted the estimated overall output voltage after superimposition of the outputs from two separate capacitive ports.

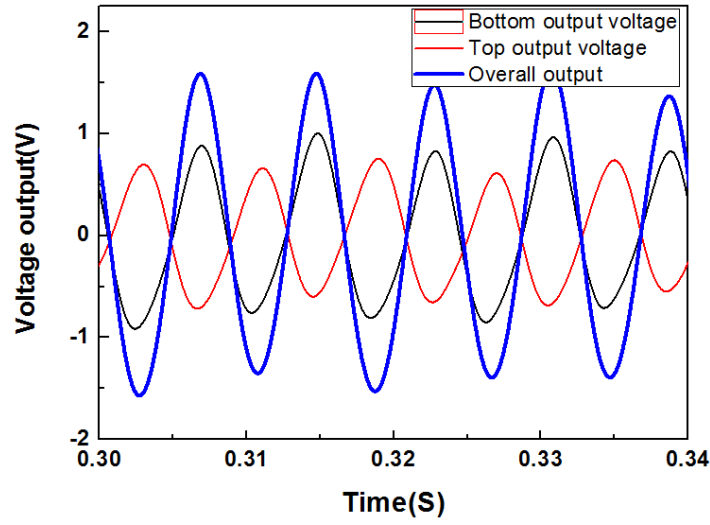


Figure 3.16 Voltage outputs as a function of time at an acceleration of 0.2g and a resistance of 10 MΩ for two capacitive ports

Figure 3.17 presented the output voltage and power for both the TCC and BCC against different resistances at resonance of 125 Hz and 0.2 g. It could be seen that maximum output power of 72 nW and 49 nW were obtained at an optimum load resistance of 20 MΩ for the TCC and BCC, which translated to a maximum output power of 0.12 μW. It was less than the reported work by Masaki *et al.* [36] from OMRON Co.. This was mainly due to the strong parasitic capacitance existed in the whole capacitive energy harvesting system. The parasitic capacitance mainly arose from the MEMS structure interconnection and the external signal cables associated with testing board. The parasitic capacitance was estimated as 5.9 pF. Since the capacitance variation in the whole capacitive vibration system is within 1 pF, the parasitic capacitance accounted for a large portion of the total capacitance. The energy harvesting effectiveness E_H [4] of a power generator with a spring-mass resonant system could be defined as $E_H = P_{out}/P_{VDRG}$, where P_{out} and P_{VDRG} were the output power generated and the maximum retrievable power of a velocity-damped resonant generator (VDRG), respectively. The energy transfer effectiveness of the current fabricated device was 0.48%. This worked out to a normalized power density (NPD), defined as power/volume/acceleration² in [39], of up to 5.56 μW•cm⁻³•g⁻² for

this particular device. Table 3.2 presented the results of the output power and normalized power density (NPD) for the proposed 2D sandwich-structured e-VEH compared with the state of the art. It could be seen that the proposed device compared quite favourably with most of its counterparts. Figure 3.18 showed the voltage responses at various accelerations ranging from 0.03 to 0.3 g for the TCC at the resistance of 20M Ω . It could be seen that the voltage output is almost proportional to the excitation accelerations. When the acceleration increased to above 0.25 g, the output voltage cannot increase anymore. It can be envisaged that the movement of the mass has been constrained by the frame. Therefore, the mass has reached its maximum amplitude within the frame. It indicated that the performance could be further enhanced by increasing the length of movement available for mass displacement for low-level ambient vibration energy harvesting.

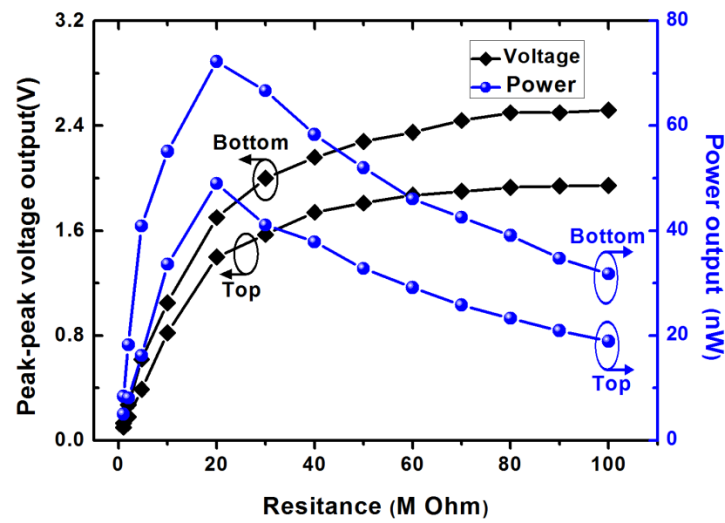


Figure 3.17 Voltages and power outputs against different resistances at the frequency of 125Hz at 0.2g

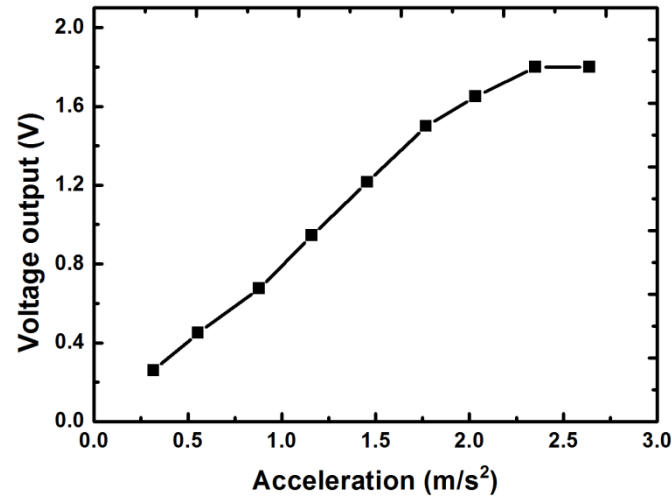


Figure 3.18 Peak-peak voltage responses at various accelerations ranging from 0.03 to 0.3 g at the frequency of 125 Hz

Table 3.2 Comparison of 2D electrostatic VEHs to the state of the art

Reference	Working mechanisms	Frequency (Hz)	Acceleration ($\text{m}\cdot\text{s}^{-2}$)	Volume (mm^3)	Power (μW)	NPD ($\mu\text{W}\cdot\text{cm}^{-3}\cdot\text{g}^{-2}$)
Kim <i>et al.</i> 2013[126]	Electrostatic	191/194	1.2	48.6	3.5×10^{-2}	50.0
Zhu <i>et al.</i> 2010[25]	Electrostatic	38725/ 38520	—	—	2.1×10^{-2}	—
Yang <i>et al.</i> 2010[24]	Electrostatic	110	25	39.4	3.5×10^{-1}	1.42
Bartsch <i>et al.</i> 2009[23]	Electret	370.5/373.7	—	—	1.0×10^{-4}	—
Tao <i>et al.</i> 2014[123]	Electret	75/78.5	0.5	120	1.2×10^{-3}	4.0
This work	Electret	121/125	2	540	1.2×10^{-1}	5.56

*The device volume is estimated from the frame length and thickness ($\varnothing 90\text{ mm}\times 20\text{ mm}$) provided by the author.

3.5 Summery of findings

In this chapter a sandwich-structured 2D MEMS e-VEH has been developed and implemented that seek to scavenge kinetic energy from 2D in-plane vibrations based on two orthogonal vibration modes. Sandwich structure integrating with two separate capacitive circuits is adopted as a non-contact passive gap control method that seeks to independently generate power and minimize the unwanted vertical pull-in and horizontal damping electrostatic force, which could provide a novel effective method for enhancing the output performance as well as electrostatic stability of 2D electrostatic vibration energy harvesting device.

A model for the electrostatic force within sandwiched structure has been developed based on finite element analysis and numerical calculations. Comsol Multiphysics simulations are utilized to calculate the vertical static force and capacitance variations where fringe effect could be taken into account. Matlab is employed to calculate the horizontal force through an analytical expression using curve fitting and Polynomial interpolations. Owing to presence of the vertical attractive forces within both top and bottom capacitive circuits, it is found that the vertical pull-in electrostatic force can be reduced by approximately 72.8% compared with the two-plate structure. By incorporating two separate capacitive circuits 180 °out-of-phase with each other to be integrated into a single seismic mass system, the maximum residual magnitude of horizontal damping force is found to be reduced by approximately 46.2%.

For a comparative low acceleration of 0.2 g and a resonance of 125 Hz, power output of 49 nW and 72 nW are achieved for the TCC and BCC, respectively. This corresponds to an overall output power of 0.12 μW and NPD of 5.56 $\mu\text{W}\cdot\text{cm}^{-3}\cdot\text{g}^{-2}$ for this prototype. The testing results have shown a good potential in realizing a practical 2D vibration-driven energy harvester device for ambient kinetic energy harvesting.

Chapter 4 2D electret micro power generator with spiral springs

This chapter looks into a novel 2D e-VEH based on a rotational symmetrical resonator for low-level ambient vibrational energy harvesting. The design aspects of the low-resonant spiral springs as well as 2D energy harvesting effectiveness were presented. Various fabrication processes involving localized corona charging and high-aspect-ratio (HAR) spring formation were illustrated. At the end of this chapter, the 2D energy harvesting capabilities of the proposed device were experimentally evaluated with a small rotational stage performing 2D excitations in different horizontal directions.

4.1 Introduction

In Chapter 3, a sandwich-structured MEMS e-VEH device is presented for enhanced output performance as well as reduced electrostatic forces in both horizontal and vertical directions. Multi-directional energy harvesting is achieved by exploiting two orthogonal vibration modes of a square axial symmetrical resonator. Consequent interest has arisen to develop energy harvesting device that could not only operate in arbitrary in-plane directions but also be adaptive to out-of-plane direction excitations.

Besides low power output, another challenge of multi-directional energy harvesting is to achieve low-resonant-frequency structures within a small confined space. Curved beam configurations are expected to achieve lower resonances within confined space since they are more efficient in transferring loads than straight beam configurations[156, 157]. As such, investigations are into planar spiral springs for achieving a 2D e-VEH device to be more adaptive to low-frequency and low-acceleration kinetic energy that widely existed in the ambient environment.

Figure 4.1 illustrates an equivalent circuit model of a proposed e-VEH that is capable

of operating both in-plane and out-of-plane schemes. Both the mechanical and electrical domains are included in the model. The top movable electrode plate suspended by a spring structure could oscillate in both in-plane and out-of-plane directions. The electrets with a thickness of d as shown in Figure 4.1 are initially implanted with a total charge of Q_t . Opposite charges are induced in the movable electrode and bottom electrode with a magnitude of Q_1 and Q_2 , respectively. When a relative displacement of the two electrodes takes place, the capacitance variation will lead to a current flow through the external circuit. Here, the external circuit is simplified as a pure resistive load R_L .

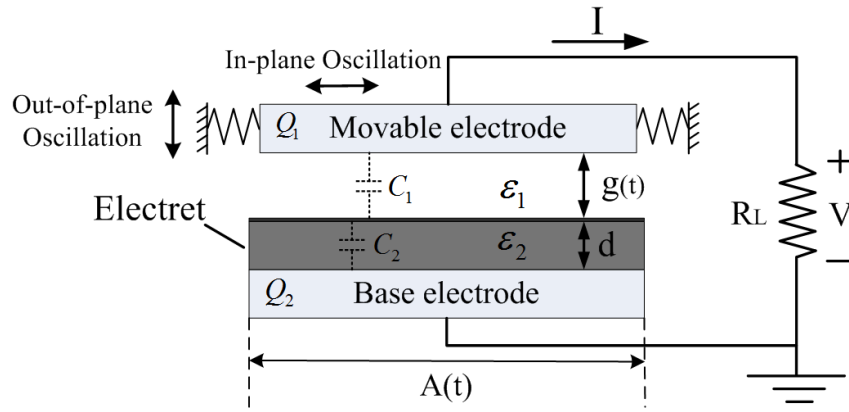


Figure 4.1 Simplified equivalent circuit model of the proposed e-VEH

For the electrical part as depicted in Figure 4.1, the total capacitance $C(t)$ consists mainly of a variable capacitance $C_1(t)$ and the electret capacitance C_2 . $A(t)$ represents the overlapping area between two electrodes. d and $g(t)$ denote the thickness of the electret thin film and the air gap, respectively. The total capacitance $C(t)$ of the harvester can be calculated as

$$C(t) = \frac{\epsilon_0 A(t)}{d/\epsilon_2 + g(t)/\epsilon_1} \quad (4.1)$$

where ϵ_0 is the vacuum permittivity, ϵ_1 is the dielectric constant of the air, ϵ_2 is the dielectric constant of the electret. If the device works on an out-of-plane vibration

mode, $A(t)$ remains constant while the capacitance change is dominated by the variation of the air gap $g(t)$. If the device works on an in-plane vibration mode, $g(t)$ keeps constant while the capacitance change is mainly caused by the variation of overlapping area $A(t)$. For in-plane vibration mode, the oscillation of the movable seismic mass is usually confined to the overall small volume of the whole device, thus interdigital electrodes as well as the corresponding stripe-shape patterned electrets are commonly employed to amplify the capacitance change. In this section, the two-dimensional (2D) oscillation in the in-plane mode will be discussed. The dynamic behavior of the e-VEH can be modeled as

$$m\ddot{x} + b\dot{x} + kx = -m\ddot{y} + F_e \quad (4.2)$$

where k is the spring stiffness, b is the parasitic damping, m is the seismic mass and y is the external vibration excitations ($y = Y\sin(\omega t)$). F_e denotes the electrostatic force, which can be evaluated by differentiating the total potential energy of the capacitive system.

By neglecting the parasitic capacitance change, the power output for the electret-based electrostatic power generators can be modelled using the following equation [80] with the resistive load made to match with the impedance

$$P_{max} = \frac{\sigma^2}{\frac{4\varepsilon_0\varepsilon_2}{d}(\frac{\varepsilon_2 g}{\varepsilon_1 d} + 1)} \cdot \frac{dA(t)}{dt} \quad (4.3)$$

where P_{max} is the maximum power output, σ is the surface charge density of the electrets. This equation is derived based on rotational electret pattern arrangement for in-plane overlapping mode. From the equation, it can be seen that the power output is proportional to the overlapping area ($A(t)$) and the square of charge density (σ^2). This highlights that high charge density with large vibration amplitude are quite critical for electret-based power generator to obtain a large power output.

4.2 Device design and modelling

4.2.2 Device configuration

Figure 4.2 depicts the schematic of the proposed e-VEH device that seeks to achieve 2D energy harvesting with its two in-plane vibration modes. The device is composed of two-parallel-plate structure. The top plate consists of a movable spring-mass structure with electrode patterns. The center movable mass with a circular shape has a diameter of 6 mm and a height of 300 μm . The set of spiral springs is composed of three separate vertically paralleled beams with a spacing of 260 μm . Each spiral beam has a width of 40 μm and height of 300 μm and is anchored to the fixed top plate. Liquid crystal polymer (LCP) is used as spacers to separate the top and bottom plates. LCP is flexible with good insulation properties and small thickness of tens of micros, which is usually used in our experiment for gap control. Low-density polyethylene (LDPE) thin film is used as electrets that is first bonded on the bottom plates and then charged. To avoid the stiction problems for e-VEH, micro-sized ceramic spheres with sizes ranging from 80 μm to 100 μm are dispersed on the surface of electret film. As depicted in the previous section, when the movable seismic mass is excited by an external vibration, the relative displacement between the top and bottom electrode would give rise to an alternating current in the external circuit.

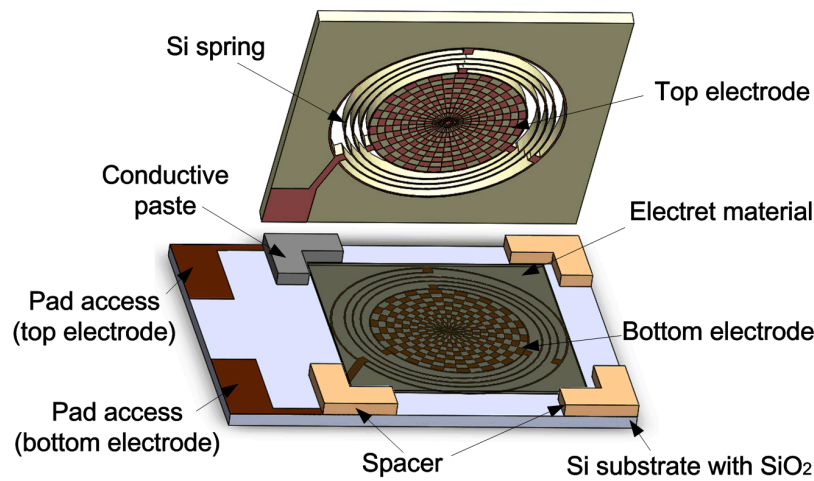


Figure 4.2 Schematic of the proposed 2D e-VEH device

4.2.3 Mechanical spring analysis

As previously highlighted, a key challenge is to design low-resonant-frequency structures within a small confined space while maintaining multi-directional energy harvesting capabilities. This necessitates the spring to be compliant in the whole 2D plane directions in order to respond to the low-level vibrations widely existed in the ambient environment. In addition, a compact design with a single mass system is preferred for 2D energy harvesting so as to minimize the overall weight and volumetric size since the seismic mass usually contributes significantly towards the overall volume of the energy harvester. It is expected to yield higher power density over the combination of several separate orthogonal one-dimensional (1D) resonators, which will be discussed in section 4.3. Besides, as discussed in section 4.1, the oscillation amplitude should be as large as possible within a confined place, since the overall output power is proportional to the change in the overlapping area.

It is well established that curved beams are quite efficient since they are capable of transferring loads through the combined action of bending and stretching. Planar spiral and circular springs are commonly used in the macro world since they reduce the occupied area for the same spring constant. However, they are not commonly used in the MEMS device. In this study, three types of spring configurations for 2D vibration energy harvesting are proposed as shown in Figure 4.3, including the two-beam spiral springs, three-beam spiral springs and circular-ring springs. Due to the complexity of the beam design and the presence of shear deformation, bending and torsion of the curved beam, it is quite difficult to obtain a mathematical model of the proposed design. Finite element analysis was utilized to calculate and simulate the spring constants under different operating conditions. For larger deformation, nonlinear effect of the curved beam should be taken into account in ANSYS. The movable circular seismic mass is 6 mm in diameter. All the beams have a height of 300 μm and a width of 40 μm . The spacing between parallel beams is 260 μm for the

three-beam configuration and circular-ring one. For the two-beam spiral configuration, the beam spacing is $410 \mu\text{m}$. The comparisons of stiffness for different types of springs are shown in Table 4.1. The stiffness ratios of k_y/k_x and k_z/k_x do not show significant differences among all the three types of springs, however, the spring constant of the spiral spring designs are significantly lower than that of the circular one. The stiffness of two-beam and three-beam spiral springs only constitutes 0.8% and 2.0% of that of the circular one, respectively. This is why the current design achieves a much lower resonance than the 2D resonator previously proposed of similar dimensions [128]. The stiffness and travelling length of the two spiral springs are similar; however, the rotation and wobbling vibration modes can be easily excited for a two-beam spiral spring designs. Thus in this work, the structure of seismic mass is suspended using a set of three-beam spiral springs is selected for the current energy harvester application.

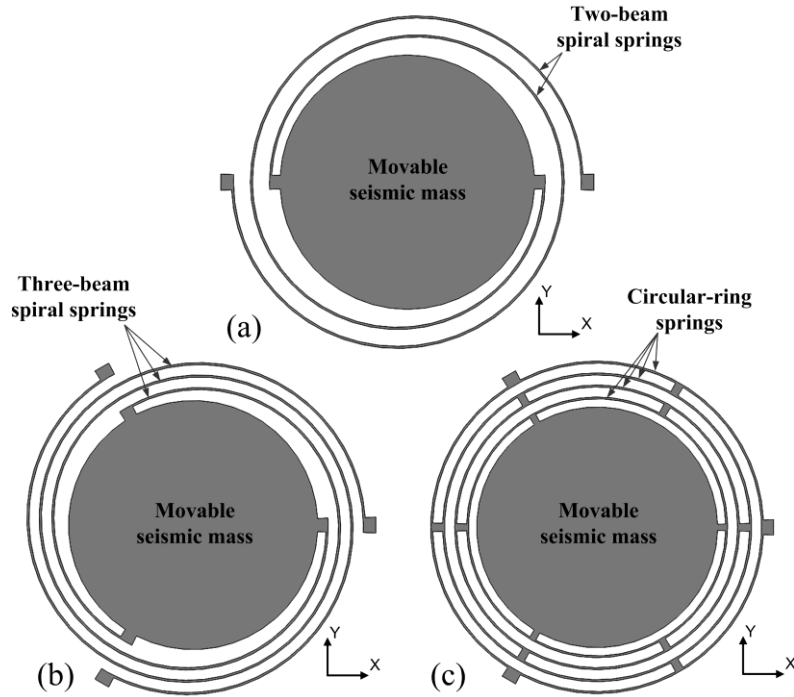


Figure 4.3 Three types of spring configurations in xy plane: (a) two-beam spiral springs; (b) three-beam spiral springs; (c) circular-ring springs

Table 4.1 Comparisons of stiffness for different types of springs

Spring type	$k_x(\text{N/m})$	$k_y(\text{N/m})$	$k_z(\text{N/m})$	k_y/k_x	k_z/k_x
two-beam spiral springs	2.32	2.61	2.04	1.13	0.88
three-beam spiral springs	4.49	4.65	3.62	1.04	0.81
circular-ring springs	2188	2212	2724	1.01	1.24

The analysis of curved beams is quite complex due to the combined effect of shear deformation, bending and torsion as well as coupling of bending and stretching. It is difficult to obtain a mathematical model for the overall multiple-spiral-beam configuration. The theoretical model of single spiral spring composing of two semicircular spring beams with R_1 and R_2 can be derived. The two semicircular springs are tangent to each other at the junction points. Since the radius R is larger than the diagonal measure of the beam cross section, i.e. $R \gg I^{1/4}$, where I is the second moment of the beam cross-sectional area, the strain energy is mainly due to the bending moment. Based on Castigliano's second theorem, $\delta_i = \partial U / \partial F_i$ and disregarding shear and axial stress, it can be expressed as

$$U = \int_0^{2\pi} \frac{[F_x R \sin \alpha + F_y R (1 - \cos \alpha) + M]^2 R d\alpha}{2EI} \quad (4.4)$$

By applying the static force from various directions, a new model of the stiffness of single spiral beam in the x, y, z directions can be derived

$$k_x = \frac{2EI}{\pi(R_1^3 + R_2^3)} \quad (4.5)$$

$$k_y = \frac{2EI}{3\pi(R_1^3 + R_2^3) + 8\pi R_1^2 R_2 - 8\pi R_1 R_2^2} \quad (4.6)$$

$$k_z = \frac{2EI}{\pi(2R_1^3 + R_2^3 + 4R_1^2R_2)} \quad (4.7)$$

According to Euler-Bernoulli theory, adjustments can be done to tune the overall stiffness by changing the spiral beam width, length and height.

The mechanical properties and design specifications of the three-beam spiral springs are further investigated. Figure 4.4 depicts the schematic of proposed resonant architectures with its associated parameters. The three-dimensional overview and top views of the proposed spring-mass resonant architectures are shown in Figure 4.4 (a) and (b), respectively. It can be seen that each single spiral beam is composed of three sections of 120° circular arcs having different radii. The designed specifications and parameters of the 2D e-VEH device are detailed in Table 4.2. These three 120° circular arcs with different radii are designed to be in tangent with each other at the junction points. The ends of the arcs are anchored to the fixed top plate. Finite element method based on ANSYS is used to construct the model to analyze the mechanical properties of the proposed spiral-mass system under various loading conditions. More than 45000 elements are used to mesh the mechanical modal. Each component makes use of an eight-node brick element. Figure 4.4 (c) demonstrates the calculated spring stiffness distributions of the resonator within a 2D plane. It can be found that very uniform stiffness distributions can be achieved in various directions within the 2D plane. The average stiffness of the spiral spring is about 4.4 N/m. Such uniform stiffness distributions in 2D plane with an average low stiffness are beneficial to achieve low-resonant-frequency structures within a small confined space. The multi-directional energy harvesting capabilities would be further investigated and illustrated in the following sections by modal analyses.

Table 4.2 Designed specifications and parameters of the 2D e-VEH device

Components	Physical parameters	Values
Seismic mass	Weight m	19.8 mg
	Radius r	3 mm
	Height h	300 μm
Spiral springs	First section radius r_1	3.4 mm
	Middle section radius r_2	3.7 mm
	Third section radius r_3	4.0 mm
	Width w	40 μm
	Height h	300 μm
	Spacing l_s	260 μm
Conjunctions	length l_c	360 μm
	Width w_c	300 μm
Electrodes	Ti/Au thickness h_e	50/300nm
	Gap between electrodes	350 μm
	Load capacitance	3.36 pF
Electret thin film	Surface potential V_s	-560 V
	Thickness d	50 μm
Device size	Volume V	10×12×1 mm ³

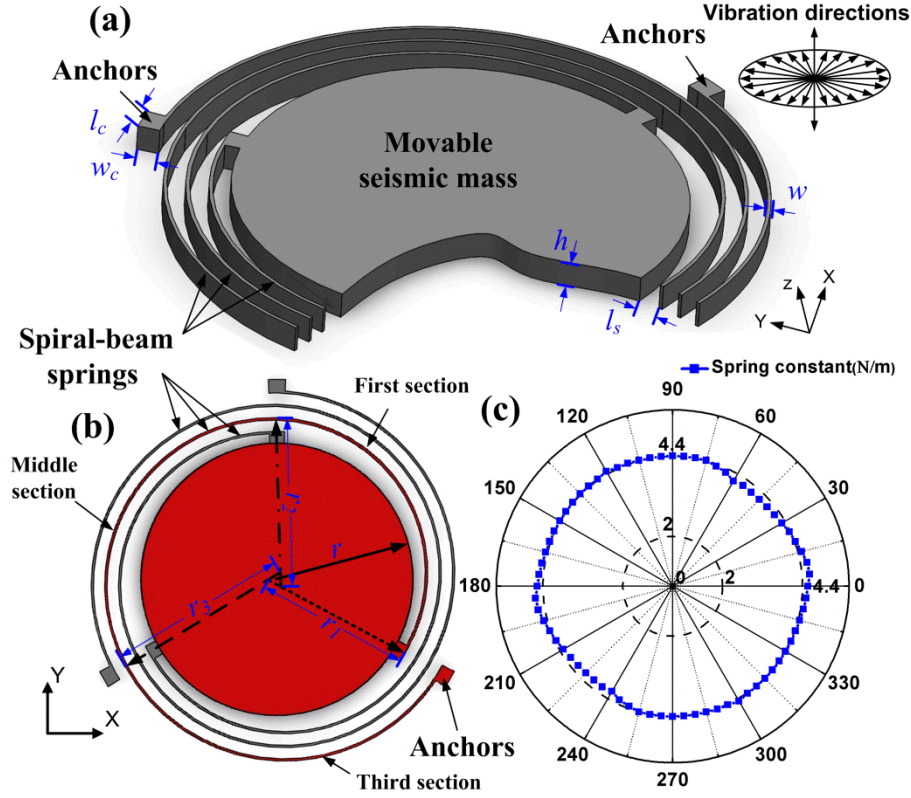


Figure 4.4 Schematic of the proposed resonant architectures with associated parameters: (a) overview of the spring-mass resonant structures; (b) Top view of the configuration; (c) calculated spring stiffness in horizontal 360° plane

4.2.4 Dynamic modal analysis

Modal analysis performed by ANSYS simulation is used to study the dynamic response of the spring-mass resonant system. Figure 4.5(a), 4.5(b) and 4.5(c) demonstrate the resonant frequencies and mode shapes of the resonant system that seeks to harvest energy from 2D plane. The resonant frequencies of the first three primary modes are 66.9, 75.8 and 77.9 Hz, respectively. It can be observed that the circular seismic-mass vibrates in an out-of-plane direction at mode I, while oscillates in the in-plane directions at modes II and III. In specific, the seismic mass oscillates in the excitation direction of 60° (240°) at mode II, while it is 150° (330°) at mode III. It is also noted that the seismic mass oscillates in the two orthogonal directions that is 90° difference with each other. The harvester is thereby able to scavenge kinetic energy from arbitrary directions in the 2D plane by combining these two oscillation

modes, which would be further illustrated in the following sections in this chapter. The out-of-plane energy harvesting capabilities together with broadband characteristics would be discussed in Chapter 5.

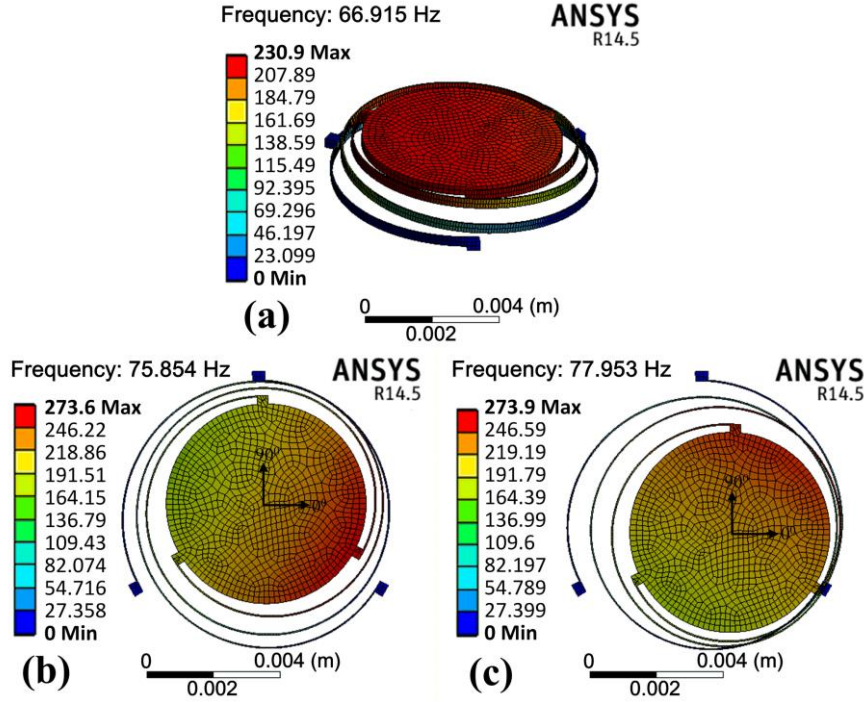


Figure 4.5 First three vibration modes of the spring-mass resonant system

4.3 Comparative study of the effectiveness for 1D and 2D systems

According to the previous modal analysis, it can be implied that the in-plane dynamic behavior of the vibration model is dominated by two horizontal orthogonal oscillation modes (Mode I and II). In order to facilitate the analysis, these two orthogonal directions are set as X and Y coordinates, respectively. By integrating parasitic and electrical damping into an overall viscous damping (defines as b) and applying Newton's second law, the differential equation of mechanical motion of spring-mass system can be described as in the matrix form that follows:

$$m \frac{d}{dt^2} \begin{pmatrix} Z_t \cos(\varphi) \\ Z_t \sin(\varphi) \end{pmatrix} = - \begin{pmatrix} k_x & 0 \\ 0 & k_y \end{pmatrix} \begin{pmatrix} Z_t \cos(\varphi) \\ Z_t \sin(\varphi) \end{pmatrix} - b \frac{d}{dt} \begin{pmatrix} Z_t \cos(\varphi) \\ Z_t \sin(\varphi) \end{pmatrix} \quad (4.8)$$

where Z_t is the relative displacement of mass to the base, φ is the diagonal orientation angle between the harvester and the source, k_x and k_y are the spring stiffness in X and Y directions, respectively. The overall effectiveness depends on the superposition of the oscillation in the two orthogonal directions related to their own resonant frequencies $f_i = (k_i/m)^{1/2}/2\pi$ ($i = x, y$). From the equation, it can be seen that when the external excitation aligned with X- or Y-axis ($\varphi = 0^\circ$ or 90°), only single mode (mode I or II) along X- or Y-axis can be excited. The governing differential equation can be confined to two independent sub equations

$$\begin{cases} m \frac{d^2}{dt^2} Z_t = -k_x Z_t - b \frac{d}{dt} Z_t & \varphi = 0^\circ (\text{X direction}) \\ m \frac{d^2}{dt^2} Z_t = -k_y Z_t - b \frac{d}{dt} Z_t & \varphi = 90^\circ (\text{Y direction}) \end{cases} \quad (4.9)$$

Considering the resonator with a quality factor of Q and excited with excitation amplitude of A_e , the oscillation amplitude of the resonator can be calculated as $A_r = A_e Q$ and the amount energy stored in the overall resonating system per cycle could be expressed as $U_r = \pi k A_e^2 Q$ [128]. If the external excitation direction is at a diagonal with an intercept angle φ to the X- or Y-axis, only the projection of the excitation amplitude onto the resonant oscillation axis of the harvester would contribute to the energy harvesting. The overall performance is the superimposition of projections on two orthogonal directions at their respective frequencies. At such cases, the oscillation amplitude of the resonator in X and Y directions can be calculated as $A_{rx} = A_e Q \times \cos(\varphi)$ and $A_{ry} = A_e Q \times \sin(\varphi)$, respectively. The amount of energy stored in the resonating system per cycle in X and Y directions can be expressed as $U_{rx} = \pi k A_e^2 Q \cos^2(\varphi)$ and $U_{ry} = \pi k A_e^2 Q \sin^2(\varphi)$, respectively. In cases where the external excitations are randomly distributed in different excitations, the overall energy stored can be calculated as

$$U_r = U_{rx} + U_{ry} = \pi k A_e^2 Q \quad (4.10)$$

The energy harvesting effectiveness can be graphically demonstrated in Figure 4.6, where normalized energy harvesting effectiveness is expressed as a function of excitation angle under viscous damped conditions. The 2D energy harvesting effectiveness is compared with two separate 1D orthogonal harvesters. It can be seen that overall effectiveness of the 2D resonator are increased by 100% over the individual 1D resonator when the external excitations are evenly distribute across 360° in horizontal directions. Although the resonant frequencies in the two orthogonal directions could be different due to the anisotropic imperfections of the 2D resonator, the overall effectiveness still is the sum of the two individual directions, which are also superior to the two individual 1D resonators.

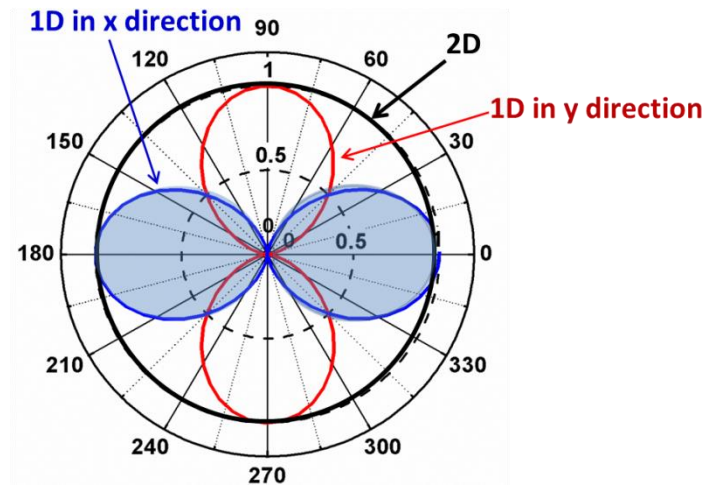


Figure 4.6 Comparison of normalized energy harvesting effectiveness for 1D and 2D resonators as a function of excitation angle under viscous damped conditions

It seems that the device can be regarded as two 1D generators in two orthogonal directions respectively. As the single mass for this proposed device acts at both oscillation modes rather than having two separate masses, the device would therefore expect to yield a higher power density noting that the seismic mass usually constitutes a very large overall volume or weight of the whole device.

4.4 Fabrication

4.4.1 Micro-patterning of electret thin films

As discussed in section 4.1, for in-plane overlapping e-VEH devices, micro-patterning of electret thin films are commonly utilized in order to amplify the capacitance change and enhance the output performance. For polymer-based electret such as CYTOP or inorganic SiO₂-based SiO₂/Si₃N₄, one of the most common micro-patterning processes includes patterning of electret thin film, chemical etching and then corona charging. These processes have low charge efficiency and experience rapid charge decay due to the chemical process of electret thin film and small dimensions of the patterns.

In this study, a localized corona charging method for patterning charge distribution in electret thin films was applied, where any micro-patterning and chemical etching process could be avoided. Figure 4.7 depicted the process flow of localized corona charging of electret thin films. It involved the preparation of the bottom plate with patterned electrodes, formation of the shadow mask and then the localized corona charging process. As previous discussed in section 2.1.3, low-density polyethylene (LDPE) was used in this project as it had a good dielectric strength and was also cost effective and environmentally friendly. Although LDPE is used here, it was envisaged that some other electret materials can also be charged by this localized corona charging method even though specific charging conditions might be applied.

The fabrication began with a 300 μm thick (100) Si wafer with a 1 μm oxide layer which was deposited by plasma-enhanced chemical vapor deposition serving also as an insulation layer (Figure 4.7 (a)). Gold electrodes were patterned on oxide insulation layer by sputtering Ti (50 nm)/Au (300 nm) and followed by a lift-off process (Figure 4.7 (b)). The electret thin film was then mounted on the surface of the

substrate using Su-8 or epoxy as a bonding layer (Figure 4.7 (c)).

Wafer-through DRIE process was used to get an array of micro-scale openings onto a 150 μm thickness silicon wafer which would serve as a shadow mask (Figure 4.7 (A-B)). The shadow mask was then deposited with 300 nm gold as conductive grid on the top and 500 nm silicon oxide as insulation layer on the bottom (Figure 4.7 (C)). Finally, the electret thin film was selectively charged by being placed between the shadow mask on the top and the silicon substrate with gold electrode on the bottom during charging process, as depicted in step (Figure 4.7 (d)), which showed the corona localized charging system configuration.

An array of needles was utilized to deposit uniform charges into the electret thin films. This was as shown in Figure 4.7(d), functioning both as metallic grid and discharge needles in conventional three-electrode charging system. The distances between the shadow mask and the needle tips were about 5~10 mm. During the charging process, the Si shadow mask was negatively biased with hundreds of volts whereas the electrodes beneath the electret were connected to the ground. The discharge voltage was kept around -4 kV. Negative ions generated at the needle tips would therefore be attracted to the lower potential electrode and then be implanted into the electret through the holes.

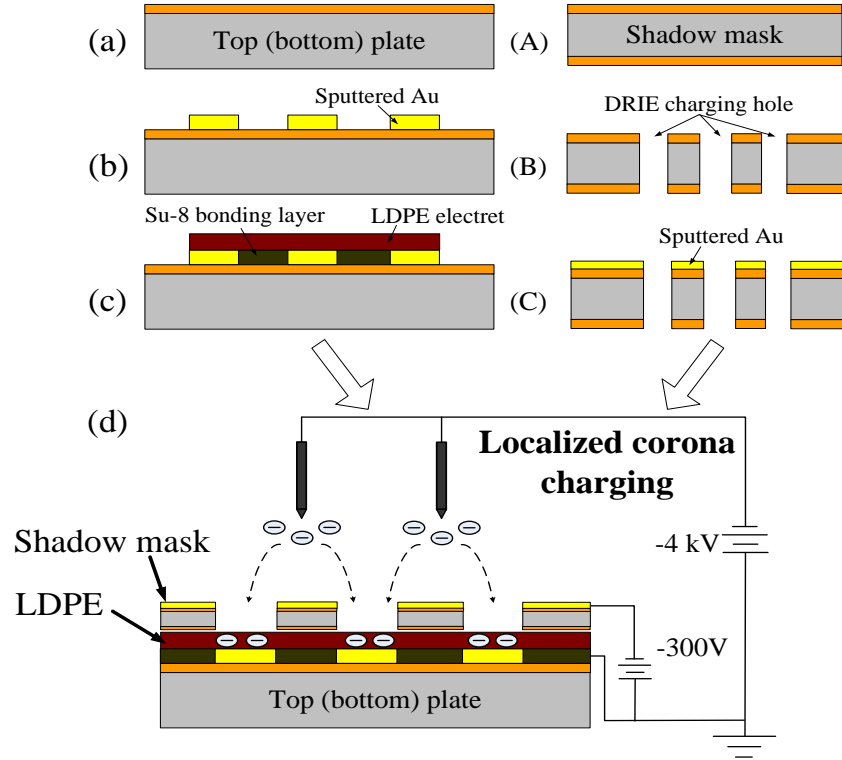


Figure 4.7 Process flow of the localized corona charging of LDPE electret thin films

In order to characterize the charge distribution and surface voltage of the charged LDPE electrets, both the SEM and non-contact potential meter were utilized. Figure 4.8 (a) depicted SEM image of the charge patterns on the electret thin films. The dark and bright regions corresponded to the uncharged charged and negatively areas, respectively. It could be seen that the charges are distributed in a very high resolution as well as in good uniformity. According to the SEM images, no lateral movement of charge [158] was observed within the electret thin film. Similar phenomenon was also observed in our previous study [154]. According to [158], diffusion phenomenon due to the tangential electric field effect usually caused surface conduction and gives rise to the potential decay. This indicated the diffusion phenomenon may not take place in the current experiment. This could be owing to the electric field built between the neighboring charged regions prohibiting the charge migration to the edge with leakage experienced at the surface. Thus, charge density in the center of the micro sized electret was observed to be better maintained than those at the edge. In addition,

non-contact electrostatic voltmeter (Model 542, Trek) was used to record the surface potential development of the charged electret. A short-term charge decay of electrets as a function of time was depicted in Figure 4.8(b) at room temperature conditions. It could be seen that the surface potential suffers a sharp decay at the first 5 hours at the field-dependent stage, then its rate of decay slowed down at a time-dependent stage after several hours. The surface potential was able to maintain at -520 V after three days. However, it was observed that the shape of the charge patterns could remain almost unchanged after 20 days storage even though the surface potential dropped.

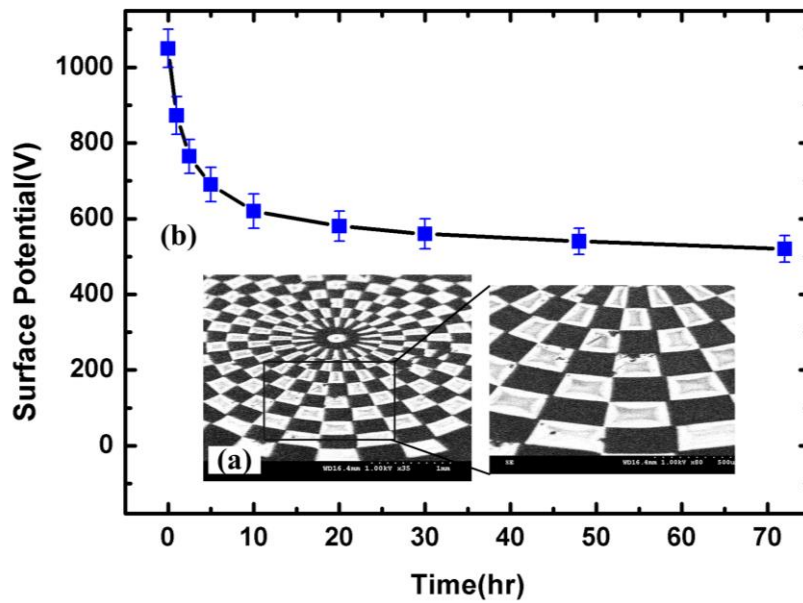


Figure 4.8 SEM images of the charged LDPE electret thin films and associated with the surface potential decay result within three days.

4.4.2 Fabrication of spring-mass architecture and structure assembly

Similar to the bottom electrode fabrication process, Ti (50 nm)/Au (300 nm) electrodes were deposited on the surface of top plate and then patterned through a lift-off process. The substrate was a 300 μm thick Si wafer with a 1 μm oxide layer that functions as an insulation layer. The spring-mass pattern was then fabricated by photoresist through lithography process. The 1 μm oxide layer was then etched by Reactive-ion etching (RIE). This was further followed by deep reactive-ion etching

(DRIE) process to etch through the whole 300 μm thick Si wafer to define the overall shape of the spring-mass structure. Figure 3.9 demonstrated the SEM images of the spiral beam from trimetric view (a), topside view (b) and bottom side view (c). Tapered angle is widely existed in the DRIE process to achieve high aspect ratio (HAR) beams due to the etching and passivation (Bosch process). It was observed that the beam width decreases from about 45 μm at the top to about 31 μm at the bottom, which meant the cross-section of the beam had a 1.3° tapered angle and the HAR was about 8 for this particular device. In order to achieve a small tapered angle of only 1.3° for current device, lots of effort has been made including sputtering thick Al layer at the backside as heat sink, employing heat conductive paste, carefully adjusting the etching and passivation time, etc.

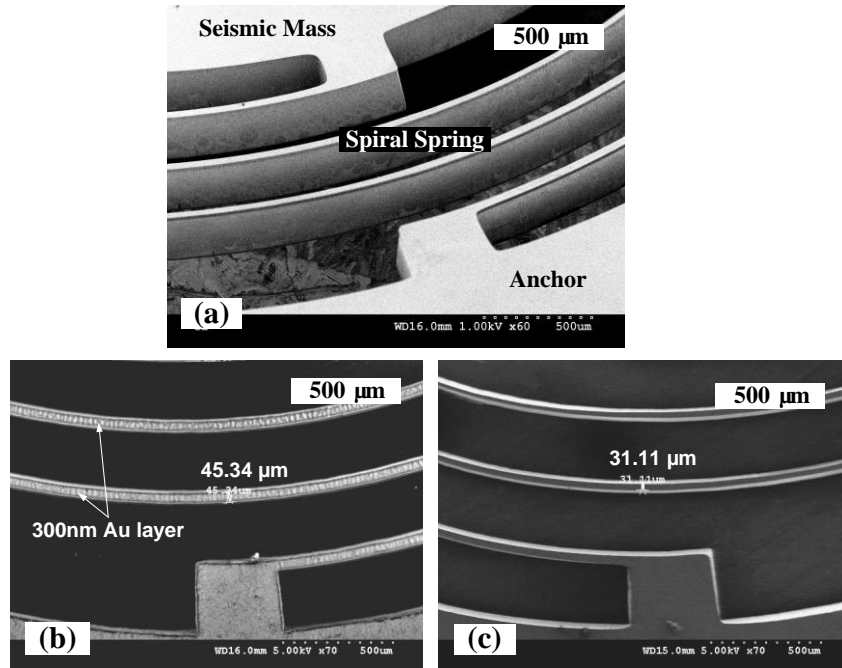


Figure 4.9 SEM images of the fabricated parallel-spiral-spring architectures with associated measurements

After both the bottom plate with charged electret and the top plate with well-defined spring-mass system were prepared, these two plates are assembled to form a two-parallel structure, as shown in Figure 4.10, consisting of the fabricated e-VEH device and the top plate with the spiral spring-mass architecture. In order to make sure

the electrodes on the two plates were precisely aligned with each other; four alignment holes on both plates with a diameter of 300 μm were fabricated simultaneously for the fabricated spring-mass system.

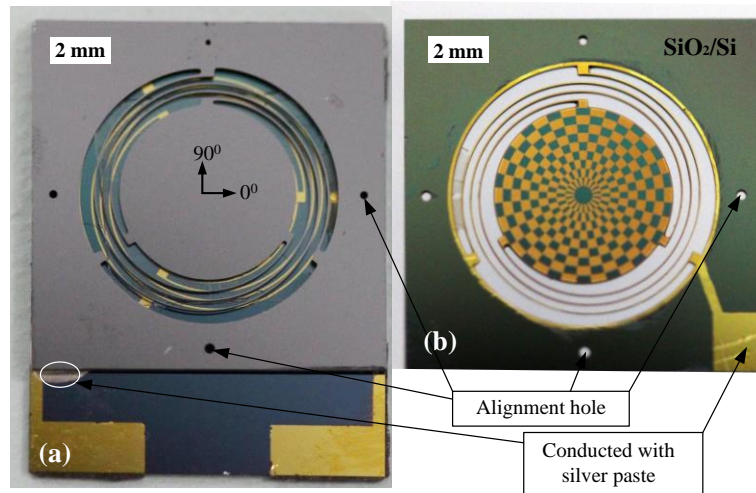


Figure 4.10 Photograph of the fabricated e-VEH device and the top plate with the spiral spring-mass architecture

4.5 Power generation experiment

The schematic of the experimental setup was demonstrated in Figure 4.10. The fabricated e-VEH prototype was bonded to a linear piezoelectric vibrator for characterizations. The whole setup consisted mainly of an accelerometer, a function generator, a voltage amplifier, a data acquisition system, a shaker and high speed camera system. The high speed camera system (PHOTRON FASTCAM-1024 PCI) was used to capture and record the motion of the seismic mass in the horizontal directions at one thousand frames per second (1000 fps). An L-shaped holder along with a rotational stage which was fixed to the vibrator can be used to simulate the ambient excitations from a 360° degree in the in-plane directions. The excitation accelerations were monitored by an acceleration sensor which is to be fixed onto the base of the L-shaped holder. A data acquisition system DAQ (NI USB-6289 M series) is used to record the electrical output. Both high speed camera system and DAQ system were connected a laptop controlling system, as shown in Figure 4.11.

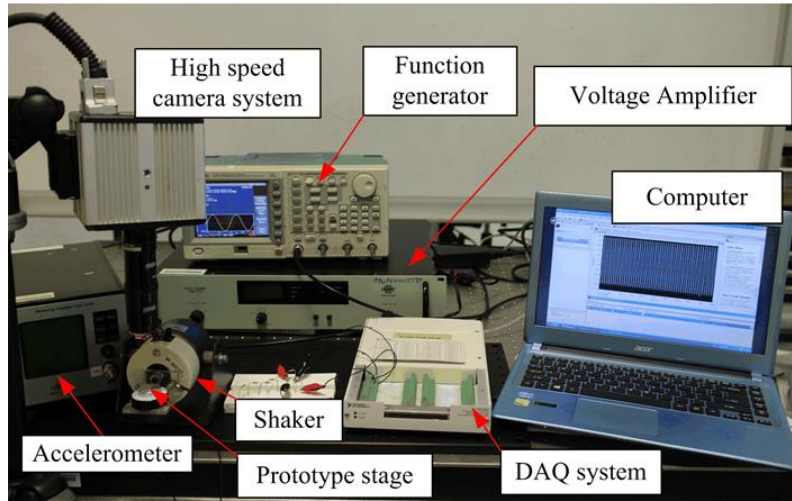


Figure 4.11 Experimental setup

To characterize the performance of the fabricated device from a 360° degree in the in-plane directions, a swept frequency from 60 to 90 Hz was applied to the vibration system at excitation acceleration of 0.05 g and at various excitation directions of 30° interval. Since the whole resonator was rotational symmetrical, only one quarter ($15^\circ \sim 105^\circ$) of the whole 2D plane was investigated in the experiment. The load resistance was fixed at 10 M Ω . The dynamic electrical responses of the fabricated prototype versus various excitation frequencies were demonstrated in Figure 4.12. The prototype composed of five sub figures that depicted different excitation directions. It could be seen that mode II and mode III take place at the frequencies of 75 and 78.5 Hz, respectively. The maximum output voltage of the mode II takes place at the excitation angle of 105° , while the maximum output of mode III occurs at the excitation angle of 15° . According to the previous simulation, modes II and III were expected to take place at 75.8 Hz of angle 60° and at 77.9 Hz of angle 150° , respectively. The excitation angles based on experimental results had an angular shift of about 45° from the simulated ones for both modes II and III. The direction of oscillation modes is dominated by the geometric configurations as well as the anisotropic properties of single crystal silicon. The small drift of resonant direction may be due to the geometric imperfections, such as DRIE, lithography,

micro-patterning, and silicon crystal direction control during fabrications. Both sets of the experimental and simulation results registered a 90° difference between the two in-plane vibration modes, which were in good agreement with each other. Furthermore, it was quite interesting to find that when the excitation directions varied from 15° to 105° , the resonant frequency shifted from mode III of 78.5 Hz to mode II of 75 Hz. The voltage magnitude for mode III decreased gradually, while the peak for mode II increased accordingly. When the excitation directions were between 15° and 105° , two peaks were observed. Take the excitation angle of around 60° as an example; two comparable peak magnitudes having a frequency difference of only 3.5 Hz were obtained. It indicated at such excitation direction, the e-VEH device operated in mode II when the excitation frequency was at 75 Hz, while it worked in the mode III when the excitation frequency was at 78.5 Hz.

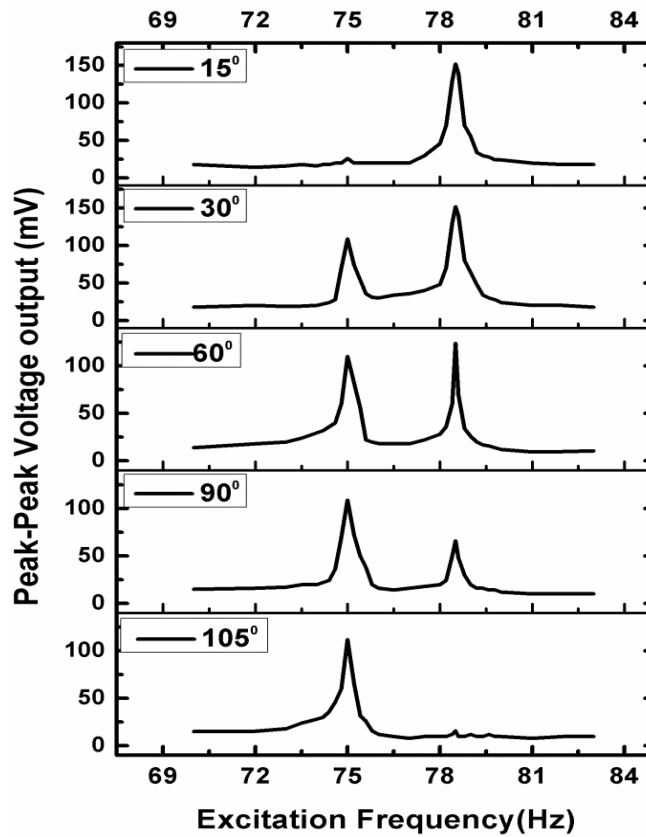


Figure 4.12 Frequency responses of the proposed device when the excitation directions vary from 15° to 105°

To further characterize the output performance at the resonances of modes II and III in different excitation in-plane directions, both the mechanical and electrical responses were recorded with the help of a high speed camera system and DAQ system, respectively. The excitation conditions remained unchanged at an excitation acceleration of 0.05 g with a load resistance of 10 MΩ. The excitation angles ranged from 0° to 180° at 15° increment each time. This could be further expanded to a 360° degree in the 2D plane due to the geometric symmetrical properties of the 2D resonator. Figure 4.13 depicted the peak-to-peak voltages at different excitation angles for modes II and III. The optimum peak-peak voltages of 116 mV and 153 mV could be achieved at the vibration mode II and mode III, respectively. This corresponded to an overall output power of 0.67 and 1.2 nW, respectively. The normalized power densities (NPD) of the proposed e-VEH, defined as power/volume/acceleration² proposed by Beeby *et al.* [39], were up to 2.2 μW•cm⁻³•g⁻² and 4 μW•cm⁻³•g⁻² for this device, respectively.

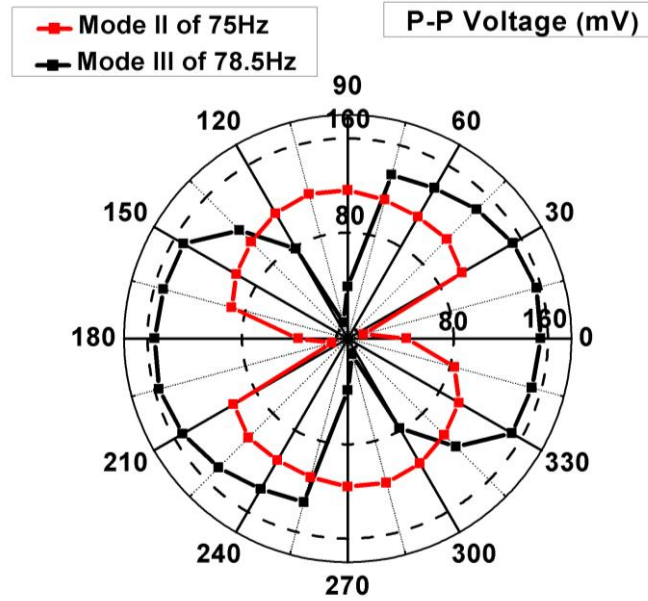


Figure 4.13 Measured output voltages of the proposed device at modes II and III at various excitation directions

Mechanical responses of seismic mass in the in-plane directions at modes II and III at an acceleration of 0.05g were demonstrated in Figure 4.14, which were recorded by

the high speed camera system. The maximum amplitudes as large as $450 \mu\text{m}$ at mode II and $560 \mu\text{m}$ at mode III are obtained, respectively. Since the output power was proportional to the relative displacement of the two electrodes, such large vibration amplitudes of the seismic mass was preferred as this would translate to a larger output power of the e-VEH device. This was also superior to that reported in most electrostatic energy harvesters listed in [79] by Suzuki, where the oscillation amplitudes were usually tens of micros. It was also noted that the minimum oscillation took place at excitation angles of 15° for mode II and 105° for mode III, which was also 90° difference between the two resonant vibration modes. Moreover, the dynamic responses of the two orthogonal vibration modes shown in Figure 4.14 demonstrated a good qualitative match with the calculated energy harvesting effectiveness depicted in Figure 4.3.

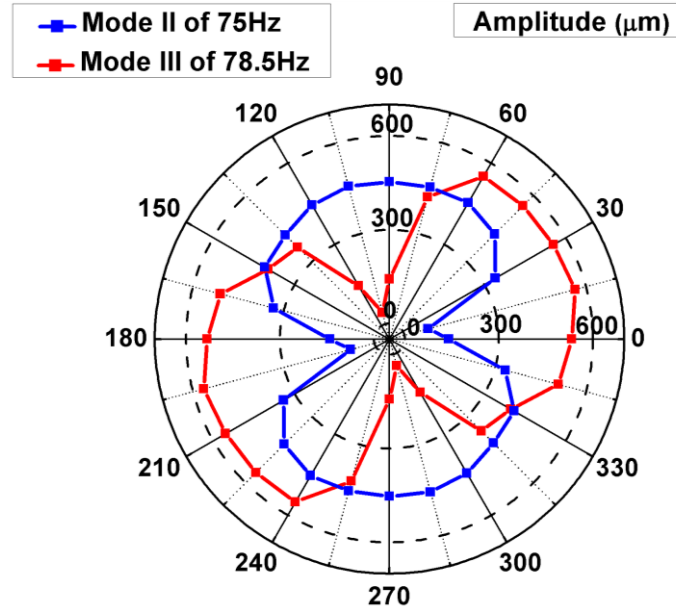


Figure 4.14 Seismic mass oscillation amplitudes for modes II and III at various excitation directions at the acceleration of $0.05g$

Figure 4.15 graphically highlighted the normalized power density (NPD) and output power of the proposed 2D e-VEH device with the state-of-the-art electrostatic energy harvesters. It could be seen that the proposed e-VEH device performs quite favourably with the state of the art while maintaining a comparatively low resonant

frequency of less than 100 Hz. It must also be highlighted that the proposed device can scavenge vibration energy from two-dimensional excitation scenarios, which was a distinct unique feature.

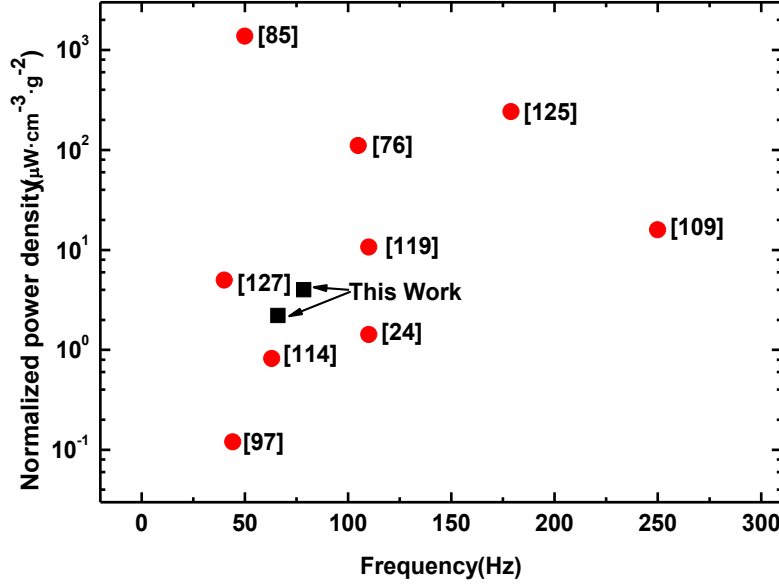


Figure 4.15 Performance comparison of the proposed device with the state-of-the-art electrostatic harvesters

4.6 Summery of findings

In this chapter, a 2D e-VEH device is designed, fabricated and characterized for low-level ambient vibrational energy harvesting. The 2D e-VEH device is designed with a novel rotational symmetrical resonator that consists of a circular seismic mass suspended by three sets of parallel-spiral springs. Finite element analytical models of the low-resonant spiral springs associated with their mechanical and dynamic properties are created and examined. It is found that the three-beam spiral spring configuration used in the proposed device could achieve relatively low spring stiffness ($k_x = 4.49$, $k_y = 4.65$) while maintaining good stability in in-plane directions. Hence, it can be suited for use in low-frequency 2D energy harvesting.

A general numerical model of the 2D resonator is summarized in the matrix form to

describe the dynamic motion of the seismic mass, where mechanical motions in two orthogonal oscillation directions are incorporated. The energy harvesting effectiveness of the proposed 2D resonator is theoretically compared with two separate 1D orthogonal harvesters under viscous damping conditions. Under the condition that the external excitations are evenly distribute in 360 °horizontal directions, it is found that the overall effectiveness of the 2D resonator increases by 100% to that of a single individual 1D resonator.

Low-resonant spring-mass architecture is successfully fabricated via one mask DRIE step without incorporating complicated SOI wafer processes. High aspect-ratio spiral springs are obtained via wafer-through DRIE process. Localized corona charging method is utilized to create micro-sized charge distribution on the LDPE thin film for the prototype fabrication. Uniform charge distribution with high pattern resolution is achieved. For a comparative low acceleration of 0.05 g, power outputs of 0.67 nW and 1.2 nW are achieved at two in-plane vibration modes, respectively. These correspond to normalized power densities (NPD) of $2.2 \mu\text{W}\cdot\text{cm}^{-3}\cdot\text{g}^{-2}$ and $4 \mu\text{W}\cdot\text{cm}^{-3}\cdot\text{g}^{-2}$ for this particular device. The proposed 2D e-VEH device compared favorably with the state of the art electrostatic harvesters and yet is able to perform at low-frequency applications for energy harvesting.

Chapter 5 Out-of-plane nonlinear MEMS electret power generator

This chapter presents an out-of-plane electret-based vibrational energy harvester (e-VEH) that has both positive and negative charged electret plates integrated into a single seismic mass system. Strong electrostatic spring-softening effect was induced due to the electric field provided by the double-charged electret plates. An elastic stopper was incorporated for reliability concern by limiting the motion of seismic mass as well as serving as a functional element to realize spring-hardening effect. Both the spring softening and hardening effect nonlinearities in the proposed e-VEH device were discussed in this chapter.

5.1 Introduction

As discussed in 2.1.3, the e-VEH mainly operates in two schemes: in-plane overlapping scheme and out-of-plane gap-closing scheme. In the previous Chapters 3 and 4, the e-VEHs with in-plane vibration modes are discussed, where the electrical current is generated when the overlapping area is made to vary in response to an external horizontal vibration source. Nevertheless, any slight misalignment or rotation of the seismic mass may severely affect or lower its performance [155]. An alternative approach is to adopt an out-of-plane gap-closing scheme which is more advantageous where a simple and cost-effective fabrication process is employed that neither requires precise alignment nor micro-patterning of the electret thin film. Thereby, out-of-plane e-VEHs employing gap-closing variable capacitors are investigated in the Chapters 5 and 6 for broadband electret-based energy harvesting from ambient environmental vibrations.

In this chapter, an out-of-plane broadband MEMS e-VEH is presented with combined nonlinear effect from electrostatic force and a mechanical elastic stopper. Both

positive and negative charged electret plates are integrated into a single resonant system to induce strong electrostatic nonlinearity. Electrostatic nonlinearity introduced by electret surface potential, as an inherent feature of e-EVHs, is practically more advantageous and readily compatible with MEMS energy harvesting devices.

Figure 5.1 shows the schematic of the conventional single-charged out-of-plane e-VEH and the proposed harvester with double-charged plates and a mechanical elastic stopper. A mechanical elastic stopper as shown in Figure 5.1 (b) is employed not only to avoid stiction problems when large vibrations are excited but also could serve as a spring-hardening component. Due to the combination of nonlinearities induced by the mechanical stopper and the electrostatic force with increased electric field, enhanced output powers as well as broader operational bandwidths are achieved. This aspect will be deliberated in the ensuing sections. In addition, a folded-spiral-spring design that can operate at low frequency of less than 100 Hz can be fabricated using one mask DRIE step without the complicated process with SOI wafers.

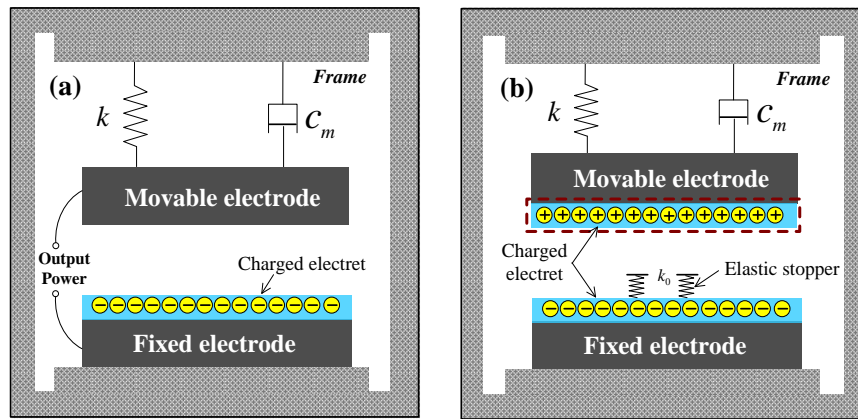


Figure 5.1 Schematic of the conventional out-of-plane e-VEH and the proposed e-VEH with double-charged electrets and a mechanical elastic stopper

5.2 Device design and fabrication

5.2.1 Device configuration

Figure 5.2 depicts a schematic drawing of the proposed e-VEH device. It consists mainly of two parallel plate configurations. The top plate consists of a rotational symmetrical resonant system that has a disk-shaped circular mass suspended by sets of parallel-spiral springs around it. The spring-mass resonant system is similar to the work presented in [123], where a good potential has been demonstrated in the development of a three-dimensional e-VEH device. It is designed with double-charged electret plates in the current work for scavenging vibrational energy through an out-of-plane gap-closing scheme. The dimension of the seismic mass is 6 mm in diameter and 300 μm in height. The spiral beam is 300 μm in height, 60 μm in width with a gap spacing of 240 μm . Electret thin films are mounted on both bottom and top plates which are oppositely charged. This enables the film to provide a constant voltage bias. Polydimethylsiloxane (PDMS) is an elastic, cost-effective and easily-processible insulator with high dielectric strength and low Young's modulus. Micro-sized PDMS with a thickness of about 70 μm serving as a stopper is mounted on the surface of the electrets to minimize 'pull-in' and acts as a spring hardening element. When the structure is excited by an out-of-plane vibration, the relative movement between the mass and electrets would induce an alternating charge flowing through the external load due to the varying capacitance.

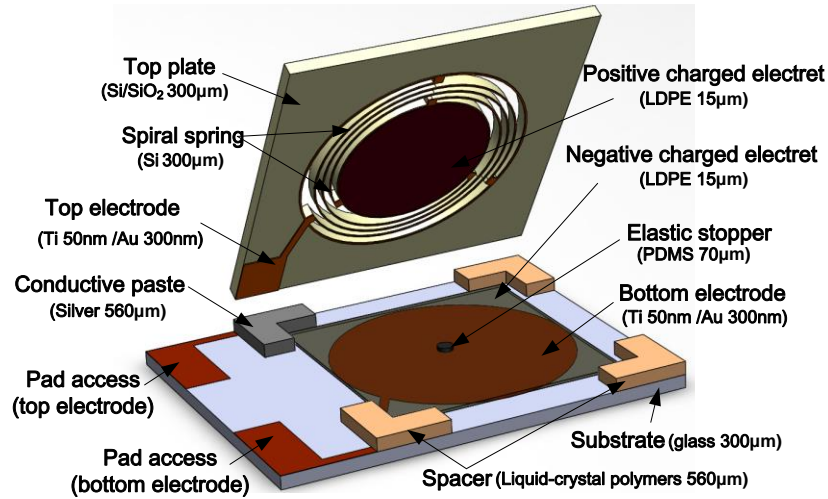


Figure 5.2 Schematic drawing of the proposed e-VEH device

5.2.2 Microfabrication

The proposed micro e-VEH device was fabricated utilizing MEMS compatible micromachining process with Si wafers. It began with deposition of 1 μm SiO_2 layer on the surface of the Si wafer by plasma-enhanced chemical vapour deposition (PECVD) that served as an insulation layer. The top electrode was then patterned on the surface of an oxide insulation layer by sputtering Ti (50nm)/Au (300nm) and then released by the lift-off process. Another sputtering process was made to produce a 600 nm Al thin layer on the backside of the wafer to facilitate heat dissipation in the subsequent etching process. After electrode layer and heat conduction layer were patterned on both sides, the wafer was bonded onto a carrier plate using thermal conductive paste. The overall pattern of spring-mass structure was then defined by reactive-ion etching (RIE) followed by deep reactive-ion etching (DRIE) processes. Subsequently, the whole spring-mass structure was released by removing Al layer along with the remaining photoresist. The bottom plate was prepared with the similar fabrication processes as well. A commercial-grade 15 μm thick thin film, low-density polyethylene (LDPE, GOODFELLOW, USA), was utilized as an electret layer in the micro-fabrication processes. The films were mounted on both bottom and top plates and then corona charged with opposite surface potentials of -800 V and 800V,

respectively. Consequently, the e-VEH prototype was assembled through a flip-chip package with two charged plates. Figure 5.3 exhibited optical images of the assembled MEMS e-VEH device and released spring-mass resonant structure. The e-VEH prototype was wire-bonded onto a printed circuit board. The overall size dimensions of the device were approximate $10 \times 12 \times 1.2 \text{ mm}^3$. Details of other parameters of the MEMS e-VEH device were listed in Table 5.1. The seismic mass weight is calculated by the disk geometry parameter and silicon density. Spring stiffness is derived by $k = (2\pi f)^2 m$, where m is the seismic mass and f is the resonant frequency collected from the experiment. Damping ratio is an estimated value which would be used in the simulation calculation.

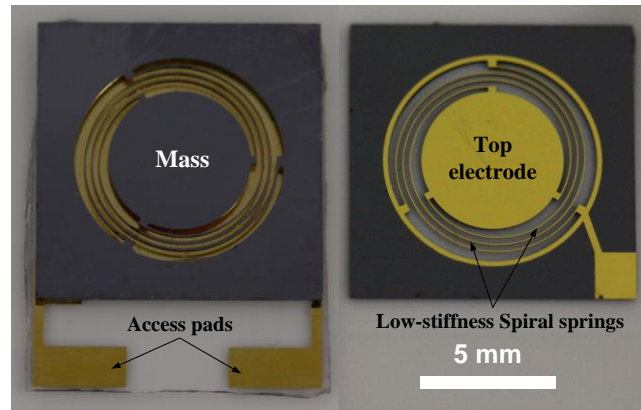


Figure 5.3 Optical images of the assembled MEMS e-VEH device and released spring-mass resonant structure

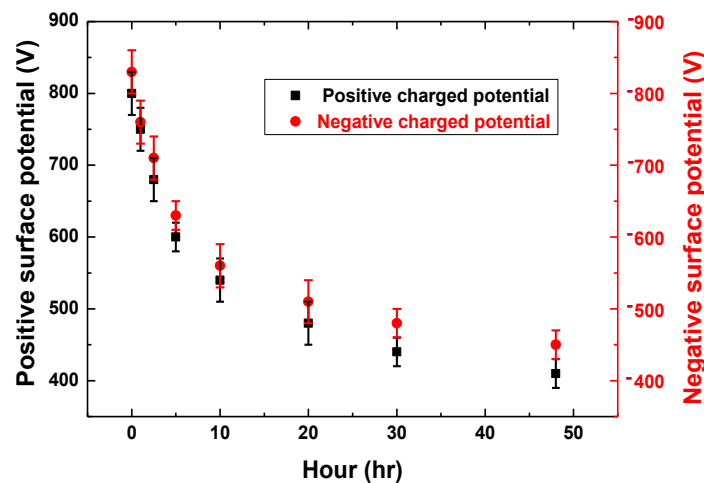


Figure 5.4 Surface potential decay of corona charged LDPE thin film with a thickness of $15 \mu\text{m}$

The surface potential of the charged 15 μm -thick LDPE film was recorded using a non-contact electrostatic voltmeter (Model 542, Trek). Two batches of samples with a dimension of $1\text{cm}\times 1\text{cm}\times 15\mu\text{m}$ were positively and negatively charged for 5 minutes respectively and then observed for surface potential decay for two days. The samples were stored in a climatic chamber with a constant temperature of $25^{\circ}\text{C}\pm 2^{\circ}\text{C}$ and a humidity of 48%-51%. The short-term charge stability of both the positive and negative electrets was depicted in Figure 5.4. It can be seen that both electrets show a decaying trend in the surface charge potential and it decreases slowly to about 400~500V after two days of storage. Thus, the surface potential of the LDPE thin film electret may suffer a decay of about 0~100V in the experiment process at the first several hours.

Table 5.1 Parameters of the proposed e-VEH device

Parameters	Value
Seismic mass weight	19.8 mg
Seismic mass radius	3 mm
Spiral spring width	60 μm
Spiral spring height	300 μm
Spiral spring stiffness	10.9 N/m
Damping ratio	0.003
Stopper stiffness	545 N/m
Impact damping ratio	0.015
Initial capacitance	2.94 pF
Electret thickness	15 μm
Top electret surface voltage	700~800 V
Bottom electret surface voltage	-700~-800 V
Gap between two electrodes	560 μm
Device volume	$10\times 12\times 1.2\text{ mm}^3$

5.3 Modeling

5.3.1 Mechanical modeling

Finite element method software ANSYS is employed to evaluate the stress distribution within the parallel-spiral springs when the seismic mass is displaced at amplitude of $500 \mu\text{m}$. According to the stress contours as shown in Figure 5.5 (a), it can be seen that the stress is almost evenly distributed along the whole length of each spiral spring. The maximum stress is found to be around the beam anchors with magnitude of only 34.2 MPa, which is substantially less than the fracture limit of single-crystal Si, reported up to 6~7 GPa [159, 160]. Even if the fracture strength could be affected by its intrinsic imperfections such as surface defect and stress intensity [161], there is still adequate margin to ensure that the e-VEH device will work in a safe mode without the risk of fracture. The vibrational mode shape and resonant frequency are studied by modal analyses. It is found that the spring-mass system could vibrate in an out-of-plane direction with a low frequency of 118.5 Hz at its fundamental mode as shown in Figure 5.5 (b). Since the natural frequency of resonator is dependent on the beam geometry and proof mass, it can be adjusted by the width and thickness of spiral springs and also affected by imperfections in the fabrication process.

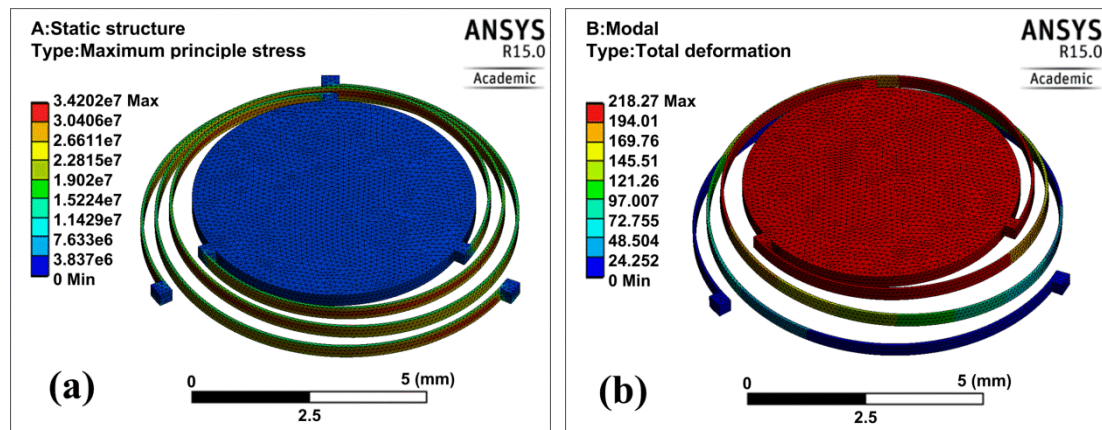


Figure 5.5 (a) Simulated stress distribution of the e-VEH resonant system when displacement of the seismic mass is fixed at $500 \mu\text{m}$; (b) resonant frequency and mode shape of the modal analysis

The influence of widths of the spiral springs on the stress and resonant frequencies of the spring-mass system are further investigated as shown in Figure 5.6. It can be seen that the resonant frequencies of the spring-mass system increases almost linearly with the beam width increment. With the increase of beam width, the stress in the beam also increased but it exhibits a nonlinear relationship. Overall, it can be seen that the stress and resonant frequencies of spring-mass system can be largely reduced by decreasing the beam width. Therefore, it is an effective method to tune the stress level and resonant frequency of the spring-mass resonant system by adjusting the beam width.

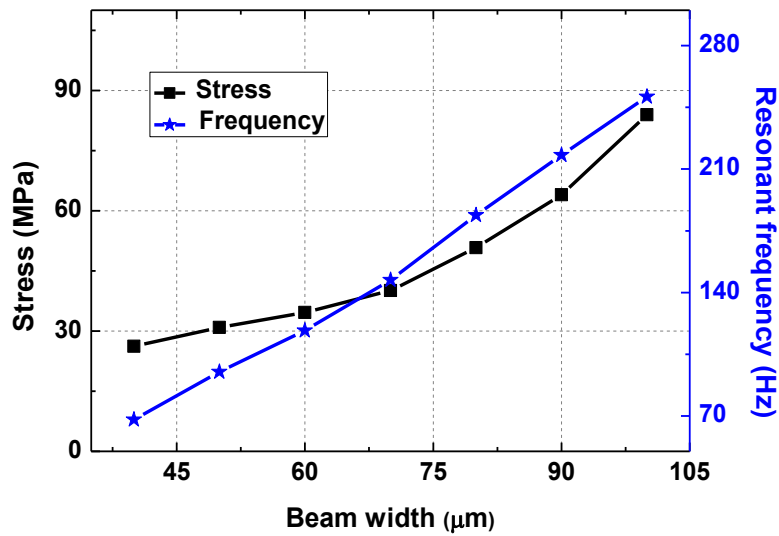


Figure 5.6 Calculated principal stress and resonant frequencies versus different spiral beam widths

Figure 5.7 depicts the calculated principal stress and resonant frequencies versus different wafer thicknesses. It can be seen that by increasing the wafer thickness from 100 μm to 600 μm , the stress level and resonant frequencies change from 32.3 to 37.8 Mpa and from 105 to 123 Hz, respectively. Therefore, it is not an effective method to tune the stress level and resonant frequency of the spring-mass resonant system by adjusting the beam thickness.

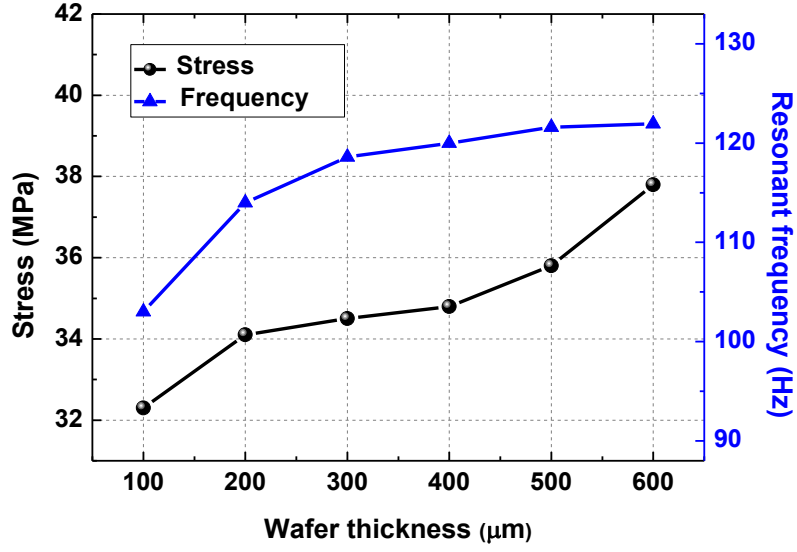


Figure 5.7 Calculated principle stress and resonant frequencies versus different wafer thicknesses

5.3.2 Electro-mechanical dynamic modeling

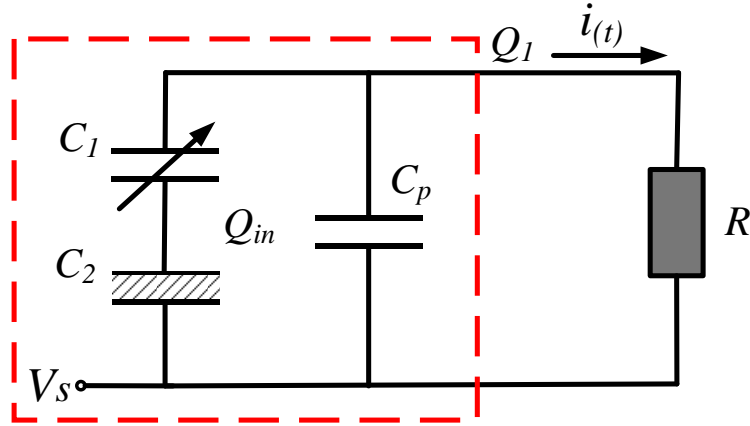


Figure 5.8 Lumped equivalent circuit model of the e-VEH device

To analyze the dynamic behavior, a lumped equivalent circuit model of the e-VEH device is presented in Figure 5.8, where V_s is the surface voltage of the electret, $C(t)$ is the total capacitance between two electrodes and Q_{in} is the charge implanted into the electret. The dynamic behavior of the e-VEH device can be evaluated by two nonlinear ordinary differential equations [85, 119] in (5.1)

$$\begin{cases} m\ddot{x} + c\dot{x} + kx + F_t = -m\ddot{y} + F_e \\ \frac{dQ_1}{dt} = \frac{V_s}{R} - \frac{Q_1}{RC(t)} \end{cases} \quad (5.1)$$

where the first equation is the mechanical motion of the spring-mass system and the second is the circuit equation of the schematic model according to Kirchhoff's current law. For the mechanical part, k is the spring stiffness, c is the mechanical damping, m is the seismic mass, F_e is the electrostatic force and y is the external vibration excitations ($y = Y\sin(\omega t)$), respectively. F_t denotes the restitution force generated by impact which is dependent on the displacement of seismic mass. For the electrical part as depicted in Figure 7, the total capacitance $C(t)$ mainly consists of a variable capacitance $C_1(t)$ and the electret capacitance C_2 , which includes two fixed electret capacitance connected in series for the current energy harvester. The parasitic capacitance normally accounts for a large portion of the total capacitance, which mainly arises from the MEMS structure interconnection and the external signal cables. This is denoted by C_p , to account for the parallel parasitic capacitance. A represents the overlapping area between two electrodes. d and g denote the thickness of the electret thin film and the air gap, respectively. Thus, the total capacitance $C(t)$ of the harvester can be calculated as

$$C(t) = \frac{\varepsilon_0 A}{2d/\varepsilon_1 + g - x(t)} + C_p \quad (5.2)$$

where $\varepsilon_0, \varepsilon_1$ are the vacuum permittivity and the dielectric constant of the electret, respectively. The energy conversion between the charge circulation and mechanical motion is coupled with the electrostatic force F_e , which can be calculated by differentiating the total potential energy of the capacitive system with respect to the position of the movable seismic mass as

$$F_e = -\frac{d}{dx} \left(\frac{Q_1^2}{2C(t)} \right) = \frac{Q_1^2 \varepsilon_0 A}{2[C_p(2d/\varepsilon_1 + g - x) + \varepsilon_0 A]^2} \quad (5.3)$$

It is difficult to obtain the analytical expressions of x and Q_1 due to the nonlinear nature of the governing equations. Therefore, numerical simulation by ordinary differential equation (ODE) solver in Matlab is used to model these relation analyses. The equation of motion (EOM) is written in the state space form and solved numerically by ODE45 solver in Matlab. The state variables can be defined as

$$\begin{cases} q_1(t) = x(t) \\ q_2(t) = \dot{x}(t) \\ q_3(t) = Q_1(t) \end{cases} \quad (5.4)$$

Then the EOM can be described in a three-dimensional state space form as

$$\begin{cases} \dot{q}_1(t) = q_2(t) \\ \dot{q}_2(t) = -\frac{1}{m}[cq_2(t) + kq_1(t) + F_t - F_e] + Y\omega^2 \sin(\omega t) \\ \dot{q}_3(t) = \frac{V_s}{R} - \frac{q_3(t)}{RC(t)} \end{cases} \quad (5.5)$$

To investigate the nonlinear effect of electrostatic softening spring, excitations at different acceleration levels are applied in both frequency-up and -down sweeps. Figure 5.9 presents the simulated results of the seismic mass against frequency-up and -down sweeps at various excitation levels with a damping ratio of 0.003 and load resistance of $1\text{G}\Omega$. It can be seen that the motion of seismic mass follows a quasi-linear response at low excitation levels of 0.6 and 1.2 m/s^2 with little difference between up and down sweep responses. As the excitation acceleration rises up to 2.4 m/s^2 , a notable drift toward a lower frequency appears in the spectrum associated with “jump” phenomenon and thus a hysteresis are observed between the up and down sweeps, as depicted in Figure 5.9, indicating the electrostatic spring softening effect under high excitations. The dynamic response of seismic mass at various load resistances is further calculated at an excitation acceleration of $0.3g$, as shown in Figure 5.10. It can be seen that the nonlinear effect becomes more prominent when the load resistance decreases. There may exist a discrepancy with the measurement, since this harvester has a resonating structure with deviations of dimensions and

material properties. The existence of parasitic capacitance effect would also lower the overall operating load resistance [85, 119]. However, this model can still be used to provide an intuitive insight into the device physics of the spring softening nonlinearity induced by electret.

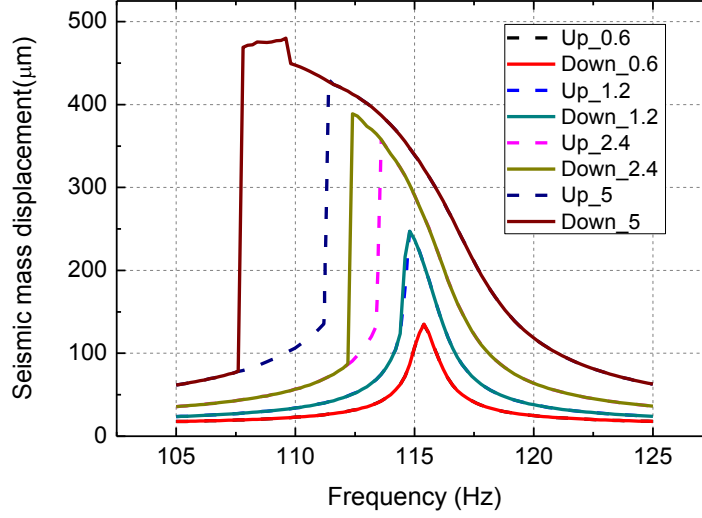


Figure 5.9 Simulated results of seismic mass displacement against frequency-up and -down sweeps at accelerations of 0.6, 1.2, 2.4 and 5 m/s^2 with a load resistance of $1\text{G}\Omega$

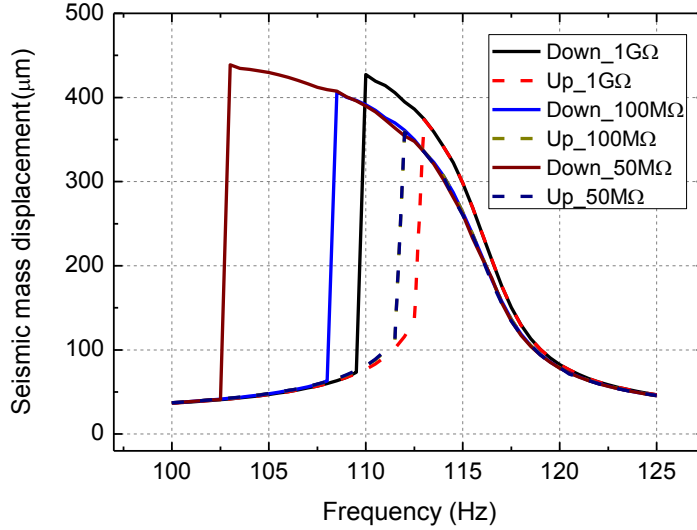


Figure 5.10 Dynamic response of seismic mass at various load resistance from 50 $\text{M}\Omega$ to 1 $\text{G}\Omega$ at an excitation acceleration of 0.3 g

To avoid the electrostatic instability owing to ‘pull-in’ phenomenon caused by further increased excitations, the stopper is added to the model to limit the displacement of seismic mass. The maximum allowable displacement of seismic mass is limited to $g_0 = 460 \text{ } \mu\text{m}$, after which the mass impacts the stopper and an opposite contact force is generated. In the simulation, the magnitude of the restitution force given in (5.6) is dependent on the displacement of seismic mass and its derivative

$$F_t = \begin{cases} k_0(x - g_0)\text{sign}(x) + c_0\dot{x}, & |x| \geq g_0 \\ 0 & |x| < g_0 \end{cases} \quad (5.6)$$

where k_0 and c_0 are the increased effective stiffness and damping coefficient by the elastic stopper. The influence of end-stop impact behavior is affected by various factors including restitution coefficient, squeeze film damping and contact time which are dependent on the two materials involved in the collision as well as the combined mass of the collision system. One of the mainstream methods seems to integrate the experiment results with the simulations and the fitting of approximated analytical models to predict the collision conditions [139, 140]. In the simulation, the stiffness k_0 and damping coefficient c_0 are considered to be increased by 50 times from the spring-mass resonant system to get an intuitive understanding of the spring hardening effect. As depicted in Figure 5.9, it can be seen that at an acceleration excitation of 5 m/s^2 , the electrostatic spring softening effect can be further enhanced by an increased excitation, whereas the displacement of the seismic mass is restricted by the stopper. This effect will be further investigated experimentally in the following section.

5.4 Results and discussion

The dynamic behaviour of the fabricated e-VEH prototype was characterized by using vibrational testing system as depicted in Figure 5.11. The dynamic excitation signal was generated through a function generator, then modified by a power amplifier and

afterwards fed to a linear piezoelectric vibrator. The assembled device was attached to the vibrator that mimics the environmental excitations, which could be monitored by an accelerometer. The electrical output performance was recorded by a data acquisition system (DAQ NI USB-6289 M series) which was connected to a laptop. In the experiment, the excitation frequency was swept up and down in the range of 80~110 Hz at different excitation levels. The frequency response was characterized in three excitation modes: weak excitation mode where the response was quasi-linear, moderate excitation mode where spring softening and hysteresis response occurred and strong excitation mode where the proof mass impacted with the stopper.

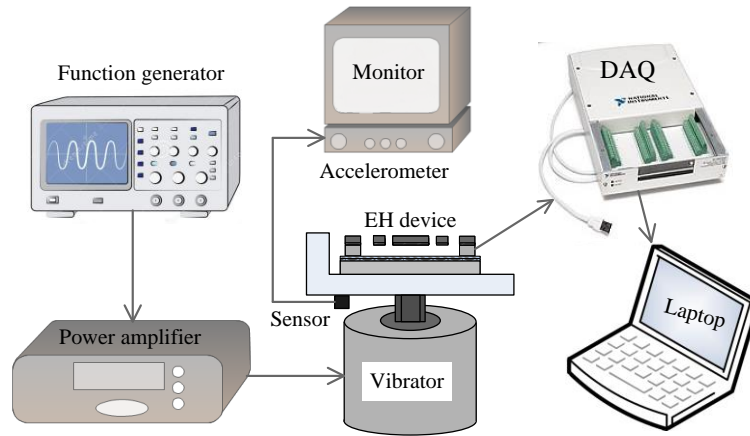


Figure 5.11 Diagram of experiment setup

5.4.1 Weak excitation mode

Figure 5.12 showed the measured output voltage of e-VEH device across a load resistance of 4MΩ at low excitation levels of 0.12 g and 0.18 g with frequency-up and -down sweeps. It could be seen that the frequency response curves are almost identical for both frequency-up and -down sweeps at such low-level excitations. The quality factor of the resonant system was 68.6 for 0.12 g and 72.7 for 0.18 g, respectively, which was calculated by $Q = f_r / \Delta f$, where f_r is the resonant frequency and Δf was the half power bandwidth. The resonant frequency was found to be around 96 Hz, which was a bit smaller than that in the simulations. This discrepancy may be due to the geometrical imperfections during the fabrication

process, such as over-etching in DRIE process. It was also observed that there was a minor resonance down drift from 96.6 Hz to 96 Hz when the acceleration increased from 0.12 g to 0.18 g. This was due to the superimposition effect of the spring restoring and electrostatic forces. For small displacement, both forces were almost constant while the electrostatic force acting as negative stiffness was added to the mechanical stiffness, resulting in an approximate linear response and minor resonance shift. This was similar to the spring softening phenomenon reported in electrostatic MEMS sensors and actuators [162], where a stiffness reduction always existed in the presence of the electric field surrounding the MEMS structure.

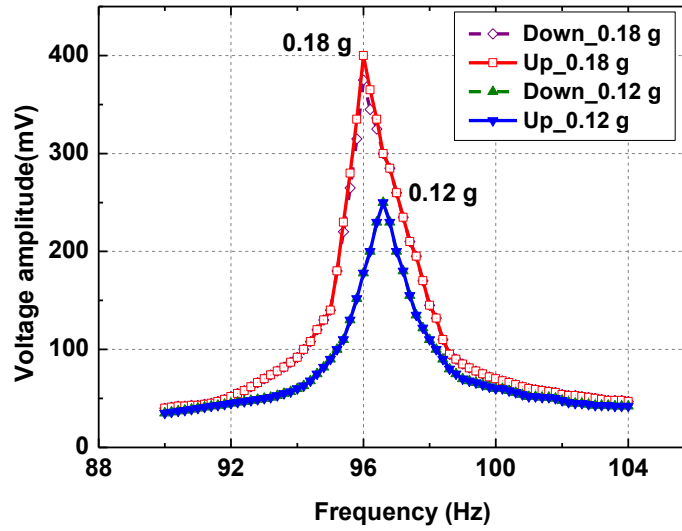


Figure 5.12 Measured peak voltage of frequency-up and -down sweeps at the excitations of 0.12 g and 0.18 g with a load resistance of $4M\Omega$

5.4.2 Moderate excitation mode

With the same load conditions, the frequency-up and -down sweeps were carried out with increased excitations in the range of 0.24~0.36 g. It was noted in Figure 5.13 that a notable drift appeared. This phenomenon further developed to a hysteresis between the up and down sweeps at specific excitation acceleration and jump phenomenon was observed, indicating the strong spring softening effect. The jump-down and jump-up points were sensitive to excitation acceleration levels. For the down sweeps, the

jump-down frequency drifted from 94.8 Hz at 0.24 g to a lower value of 93 Hz at 0.36 g. For the up sweeps, the frequency responses were similar to the trace of that in frequency-down sweeps but with relatively higher resonant frequencies of 95.6 Hz at 0.24 g and 95.2 Hz at 0.36 g. These observations of the nonlinear response were similar to those from the numerical simulation as depicted in Figure 5.9. At the excitation acceleration of 0.36 g, the output voltage and 3-dB bandwidth of down-sweep response were increased by 83.3% from 0.69 V to 1.0 V and by 69.2% from 1.3 Hz to 2.2 Hz compared with that of up-sweep response. At these acceleration levels, the electrostatic force between the movable seismic mass and base electrode became progressively nonlinear. The spring stiffening effect could be induced by large displacement in Duffing resonators, as reported in the literature [163]. In the experiments performed, it was observed that there was no obvious phenomenon of resonance right-drift in up-sweep responses. It could therefore be inferred that the electrostatic spring softening nonlinearity dominates. At such circumstances, the whole resonant system exhibited a spring softening response. Figure 5.14 depicted the output power and voltage against various load resistances at resonance of 93 Hz when the prototype was excited at an acceleration of 0.36 g. It could be seen that maximum output power of $0.56 \mu\text{W}$ was obtained at an optimum resistance of about $50 \text{ M}\Omega$.

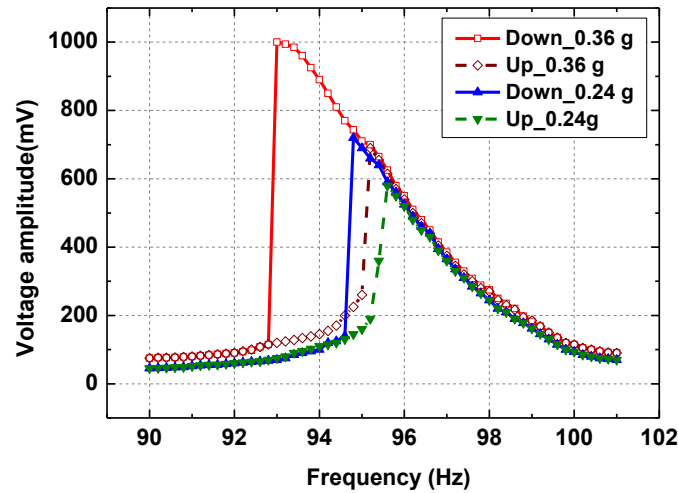


Figure 5.13 Measured peak voltage of frequency-up and -down sweeps at the excitations of 0.24 g and 0.36 g with a load resistance of $4 \text{ M}\Omega$

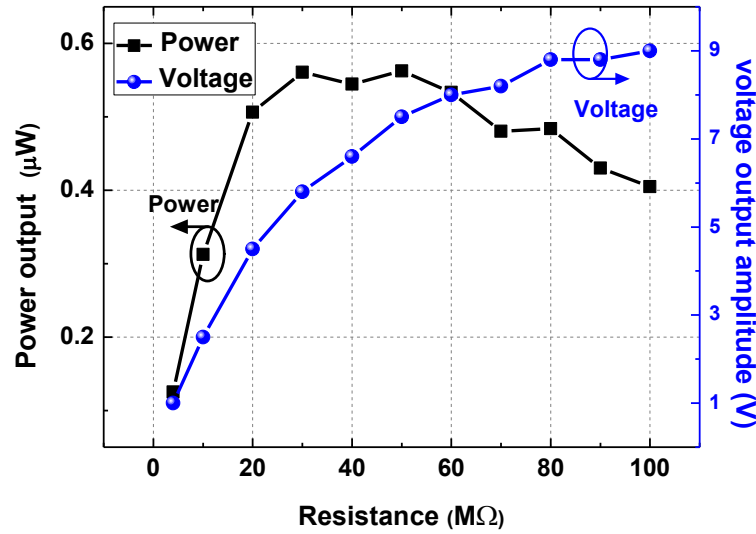


Figure 5.14 Output power and voltage against various resistances at resonance with an excitation acceleration of 0.36 g

5.4.3 Strong excitation mode

In the same manner, frequency sweeps had been applied with further ascended excitations in the range of 0.42~0.48 g. In these conditions, the movable seismic mass began to collide with the stopper, which had been observed through a high speed camera system and further confirmed by the electrical measurements. The impact effect of the elastic stopper was superimposed with the strong nonlinear electrostatic force and the mechanical spring restoring force. The output voltage frequency responses for up- and down-sweeps were depicted in Figure 5.15. Typical properties of both spring-softening and hardening responses were observed. During the down sweeps of 0.48 g, the output voltage first displayed a similar spring softening phenomenon and then arrived at its maximum of 1.1V at the frequency of 93 Hz. It was able to maintain almost the same level of output voltage for a while until it reached at a jump-down frequency of 91.4 Hz, among which the seismic mass continuously collided with elastic stoppers. During the up sweep, the voltage response rose up sharply to 1.15V at the frequency of 94 Hz. Afterwards, it kept the upward

tendency as further increase of excitation frequency reaching its maximum of 1.45 V at resonance of 95.6 Hz and then fell down abruptly to a low level. The 3-dB bandwidth was about 3.7 Hz, which was enlarged by 2.85 times compared to the linear-response bandwidth at the acceleration of 0.12 g. The frequency-up sweep responses were quite different from those under moderate excitation mode (Figure 5.13) due to coupled effect of the strong electrostatic force and stopper impacts. In this strong excitation mode, it was noted that the voltage at jump-up point (indicated by point A) in the up-sweeps could even surpass the voltage at the intersect point with the down-sweep (indicated by point B). This was probably due to the collective contributions of high electromechanical coupling effect, strong electrostatic instabilities as well as the presence of increased squeeze film damping under large excitations.

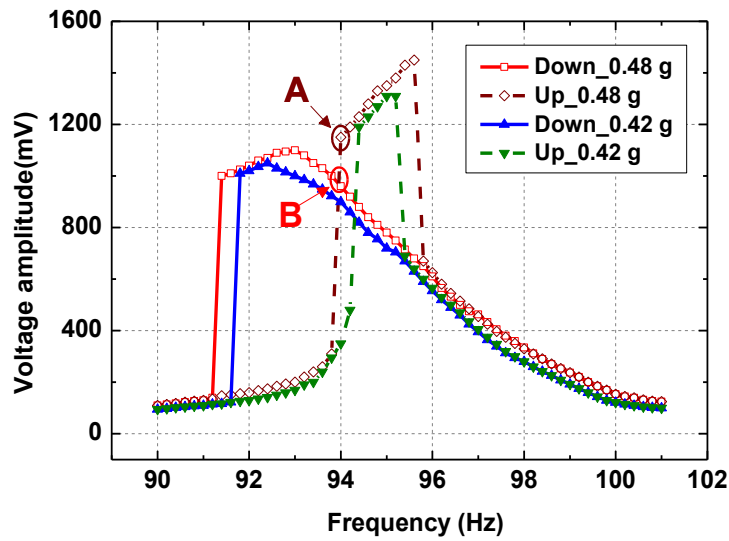


Figure 5.15 Measured peak voltage of frequency-up and -down sweeps at the excitations of 0.42 g and 0.48 g with a load resistance of 4MΩ

5.4.4 Output power evaluation

Figure 5.16 summarized the output voltages and resonant frequencies as a function of various excitation accelerations in the range of 0.12~0.6 g for both up and down

frequency sweeps. As shown in the figure, output voltages for both up and down sweeps increased almost linearly as the external excitations vary in the range of 0.12~0.36 g. During this period, the growth rate of down sweep was faster than that of the up sweep and with a larger frequency-down drift. This was mainly attributed to stronger spring softening nonlinearity in the down sweeps. When the excitation acceleration was above 0.42 g, the elastic stopper began to take effect and the dynamic response started to display spring hardening phenomenon. Meanwhile, the output voltages experienced a gradual increase in up sweeps, while it almost stayed unchanged in down sweeps. It was also noteworthy that there existed a spring softening and hardening transition period between 0.36 g and 0.42 g, below which the performance in frequency-down sweeps was superior to that in the up sweep; otherwise the latter would have registered a better performance.

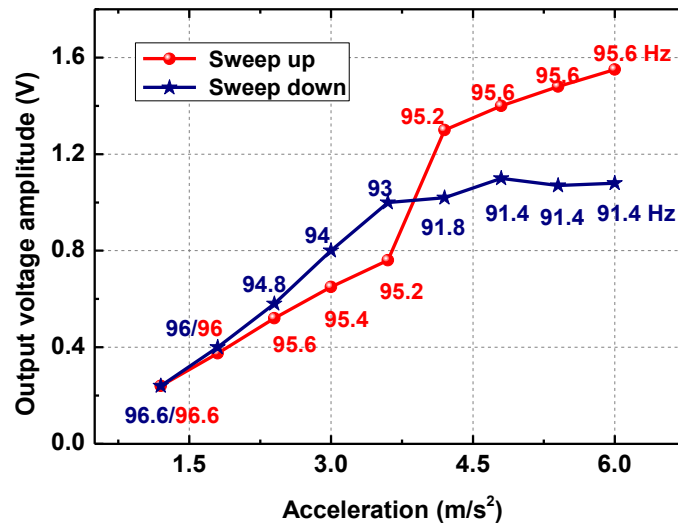


Figure 5.16 Output voltages and resonant frequencies as a function of various excitation accelerations in the range of 0.12~0.6 g for frequency-up and -down sweeps

Figure 5.17 depicted the optimal output power and normalized power density of the e-VEH prototype as a function of various excitation accelerations in the range of 0.12~0.6 g. It was seen that the power output reveals a general trend of steady rise

with the increase of the acceleration and reaches its maximum of 1.3 μW at the acceleration of 0.6 g. Nevertheless, it was not the case for normalized power density (NPD), which is defined as power/volume/acceleration² in [39]. It reached its maximum of up to 37.4 $\mu\text{W}\cdot\text{cm}^{-3}\cdot\text{g}^{-2}$ at the acceleration of 0.42 g for the current device, where the output power was 0.95 μW . The NPD cannot increase any more with further increased acceleration, even though an upward tendency in the output power continues. This was mainly due to the increase of energy loss when the seismic mass collided with the elastic stopper with further increased excitations. Energy harvesting effectiveness of a power generator with spring-mass resonant system could be defined as [4]:

$$E_H = \frac{P_{out}}{P_{VDRG}} = \frac{P_{out}}{\frac{1}{2}m\omega_n^3 y_0 x_m} \quad (5.7)$$

where P_{out} is the power output generated, P_{VDRG} is the maximum output power of a velocity-damped resonant generator, m is the seismic mass, y_0 is the base excitation amplitude, x_m is the maximum displacement of the moving mass, and ω_n the resonant operating frequency. According to this formula, the current fabricated device at the frequency of 95.2 Hz had an effectiveness of 8.3% at an acceleration of 0.42 g. The output power and normalized power density (NPD) for the proposed e-VEH device were compared with the state of the art. This was further graphically highlighted in Figure 5.18 for NPD where at low frequency less than 100 Hz, the proposed device compared quite favorably with most MEMS e-VEH devices. It was also noteworthy that the proposed device demonstrated nonlinear spectrum broadening effect in both frequency sweep-up and sweep-down process, which was a distinct unique feature.

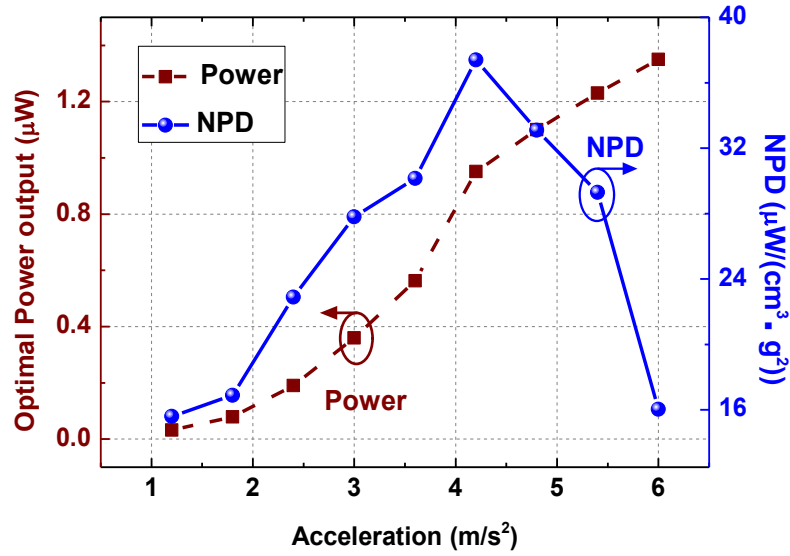


Figure 5.17 Optimal output power and normalized power density as a function of various excitation accelerations in the range of 0.12~0.6 g

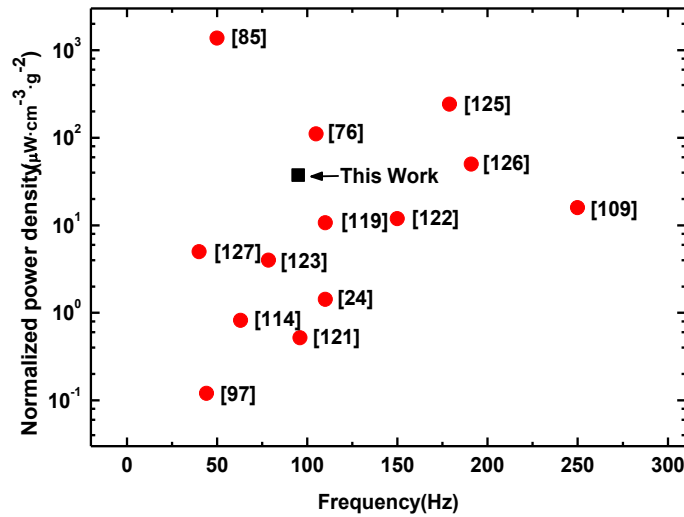


Figure 5.18 Normalized power density comparisons with the state-of-the-art electrostatic vibration energy harvesters

5.5 Summery of findings

A low-frequency broadband e-VEH device employing double-charged electret plates has been designed, fabricated and characterized. The harvester exhibits an approximately linear response at weak excitations below 0.18 g. As the excitation

accelerations increased to 0.24~0.36 g, a strong spring softening nonlinearity takes place, which mainly attributes to the electrostatic force provided by the double charge electret plates. This electrostatic spring softening nonlinear behavior has also been investigated in the electro-mechanical dynamic model, which shows a qualitative match with the experimental results. When the acceleration reaches 0.42 g and afterwards, the elastic mechanical stopper begins to take effect. Both spring-softening and hardening nonlinearity are observed due to the combined effect of the electret-induced electrostatic force and elastic stopper.

For a relative low resonance of 95 Hz at low-level excitations of 0.42 g, a power output of 0.95 μW has been achieved, which corresponds to a normalized power density of 37.4 $\mu\text{W}\cdot\text{cm}^{-3}\cdot\text{g}^{-2}$. The energy conversion effectiveness of the current device is up to 8.3%. Owing to the combined advantages of hardening and softening nonlinearities, the 3-dB bandwidths of 3.7 Hz for frequency-up sweep and 2.8 Hz for frequency-down sweep are obtained, respectively. The results may offer new insights of designing MEMS broadband e-VEH device by using electret induced spring softening nonlinearity and elastic stoppers.

Chapter 6 A nonlinear 2DOF MEMS electret vibrational energy harvester

This chapter examines the out-of-plane MEMS e-VEH device and further expands it into a two-degree-of-freedom (2DOF) system to achieve broadband energy harvesting. The 2DOF resonant system that comprises of a primary mass and an accessory mass was structured on a silicon wafer by double-side deep reactive-ion etching (DRIE). By precisely tuning the accessory mass, the first two resonances of primary mass could be tuned close to each other while maintain comparable magnitudes. Spring hardening effect was also observed during the experimental studies. The 2DOF energy harvesting effectiveness as well as MEMS device design, analysis, fabrication and characterization would be discussed in this chapter.

6.1 Introduction

In Chapter 5, it was reported that frequency spectrum bandwidth increases due to the combined effect of the electret-induced electrostatic force and elastic stopper. Both spring-softening and hardening nonlinearities occurred around the sole resonance are utilized to broaden the bandwidth of the proposed e-VEH device. Consequent interest has arisen in the design of an energy harvesting devices which could further operate at multiple resonant frequencies simultaneously with a wider frequency band. Thereby, another alternative is presented in this chapter that seeks to create a comparable peak adjacent to the primary one by exploiting multiple vibration modes of a 2DOF system to enhance the overall performance. To the best of the author's knowledge, MEMS devices of such multiple degree-of-freedom system have not been reported up to date.

Tuned mass dampers (TMD) or dynamic vibration absorber (DVA) with 2DOF system are widely used to suppress the vibration for human comfort, such as in tall buildings, long bridges and slender towers. The 2DOF system is exploited and

examined here in the current work with respect to energy harvesting capabilities. Figure 6.1 depicts a lumped parameter model of the proposed 2DOF vibrational energy harvester compared with conventional single-degree-of-freedom (1DOF) system. In conventional 1DOF system, only single spring-mass system is utilized for energy harvesting purpose, as shown in Figure 6.1(b). The energy conversion between the mechanical motion and electric power is implemented by the coupling coefficient damping (η_E), which is settled between the movable mass and the fixed frame. Only one resonance can be utilized for energy harvesting capability due to the inherent nature of 1DOF spring-mass system.

Different from the conventional 1DOF system, the proposed 2DOF system comprises two subsystems: the primary subsystem and the accessory subsystem, as shown in Figure 6.1(a). The energy harvesting component is integrated within the primary subsystem for energy transformation. The accessory subsystem mainly serves as a frequency tuning component to adjust the overall performance of the whole 2DOF system. By precisely tuning the accessory mass, the first two resonances of primary mass can be tuned close to each other while maintaining comparable magnitudes. These aspects will be further deliberated in the ensuing sections.

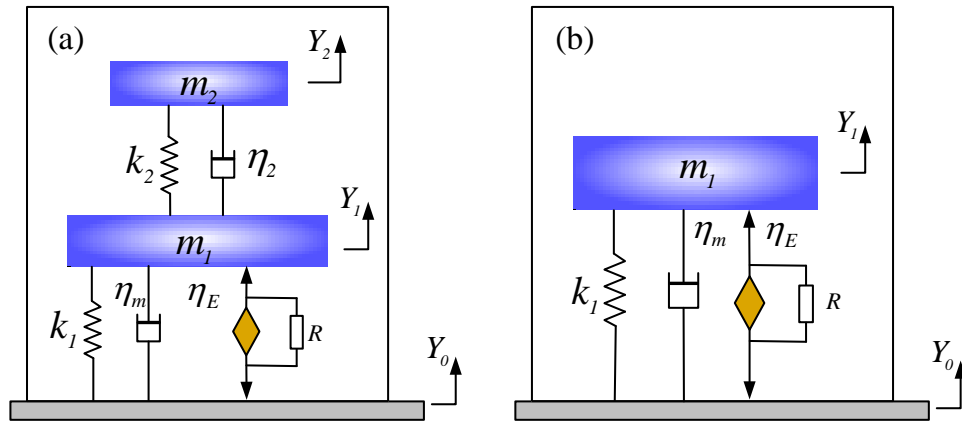


Figure 6.1 Two configurations of harvesters: (a) proposed 2DOF vibrational energy harvesting model; (b) conventional 1DOF vibrational energy harvesting model

6.2 Numerical modeling of 2DOF system

The 1DOF mechanical-to-electrical energy conversion model was first proposed by Williams and Yates [50] and further studied by Stephen *et al.* [164]. It consists of a moving mass (m) suspended by a spring (k) and damped by an energy transducer (η_e) and parasitic damping element (η_m). For a sinusoidal excitation vibration ($y = Y\sin(\omega t)$), Williams and Yates have proved the output power can be derived in equation (6.1) [50] as

$$P_{W\&Y} = \frac{m_1 \zeta_e A^2 \omega^3 \left(\frac{\omega}{\omega_n}\right)^3}{\left(1 - \left(\frac{\omega}{\omega_n}\right)^2\right)^2 + \left[2\zeta_t \left(\frac{\omega}{\omega_n}\right)\right]^2} \quad (6.1)$$

where ζ_e and ζ_t are the electrical and total damping ratios, ω_n is the resonant frequency, A and ω are the amplitude and frequency of the excitation, respectively. Although they mainly focus on the electromagnetic vibrational energy harvesters, this model is applicable to most of 1DOF vibrational resonant system, where both the electrical damping and parasitic damping are modeled as viscous damping. For electret-based vibrational energy harvester, the electrostatic damping force is a function of the differentiation of the total potential energy of the capacitive system with respect to the position of the movable seismic mass.

It is hard to obtain the analytical expressions due to the nonlinear nature of the governing equations. To facilitate the analysis of vibration characteristics of 2DOF system, both mechanical damping and electrical damping are considered as viscous damping to derive an intuitive insight into the energy conversion performance for the proposed 2DOF system. The overall damping of the primary subsystem is denoted as η_1 , which is composed of mechanical damping (η_m) and electrical damping (η_e). The accessory subsystem comprises an accessory mass (m_2), a spring (k_2) and damper (η_2) also depicted in Figure 1(b). Therefore, the governing equation of the

motion of the 2DOF vibrational system can be represented in equation (6.2) as

$$\begin{cases} m_2 \ddot{y} + \eta_2 \dot{y} + k_2 y = -m_2 \ddot{x} - m_2 \ddot{Y}_0 \\ (m_1 + m_2) \ddot{x} + \eta_1 \dot{x} + k_1 x + m_2 \ddot{y} + (m_1 + m_2) \ddot{Y}_0 = 0 \end{cases} \quad (6.2)$$

where x and y are the relative movement defined as $x = Y_1 - Y_0$ and $y = Y_2 - Y_1$, respectively. The instantaneous power transfer in the primary subsystem can be obtained by the product of the electrical damping force f_e and its velocity v expressed in equation (3) as

$$p(t) = f_e v = \eta_e (\dot{x})^2 \quad (6.3)$$

By applying the Laplace transform for the above equations (6.2) and (6.3), it can be derived shown in equation (6.4) as

$$\begin{cases} s^2 \hat{Y} + 2\zeta_2 \omega_2 s \hat{Y} + \omega_2^2 \hat{Y} = -s^2 \hat{X} - s^2 U_0 \\ (1 + \mu) s^2 \hat{X} + 2\zeta_1 \omega_1 s \hat{X} + \omega_1^2 \hat{X} + \mu s^2 \hat{Y} + (1 + \mu) s^2 U_0 = 0 \\ \hat{P} = 2m_1 \zeta_e \omega_1 \hat{X}^2 s^2 \end{cases} \quad (6.4)$$

where $\omega_i = \sqrt{k_i/m_i}$ and $\zeta_i = \eta_i/2m_i\omega_i$ ($i = 1,2$) are the resonant frequencies and damping ratios, respectively. $\mu = m_1/m_2$ is the mass ratio, $\alpha = \omega_2/\omega_1$ is the frequency tuning ratio and $\Omega = \omega/\omega_1$ is the normalized excitation frequency. By setting $s = j\omega$ and neglecting the accessory damping ($\zeta_2 = 0$), the power extracted from the 2DOF system can be obtained in equation (6.5) as

$$|\hat{P}| = \frac{m_1 \zeta_e \omega_1 \omega^2 U_0^2 \Omega^4 (\Omega^2 - (1 + \mu)\alpha^2)^2}{(\Omega^4 - (1 + \mu)\alpha^2 \Omega^2 - \Omega^2 + \alpha^2)^2 + [2\zeta_1 \Omega (\Omega^2 - \alpha^2)]^2} \quad (6.5)$$

When the mass ratio (μ) and frequency tuning ratio (Ω) are to become zero, the dual-mass system degrades to the conventional 1DOF system, and the output power be simplified in equation (6.6) as

$$|\hat{P}| = \frac{m_1 \zeta_e U_0^2 \omega^3 \Omega^3}{(\Omega^2 - 1)^2 + [2\zeta_1 \Omega]^2} \quad (6.6)$$

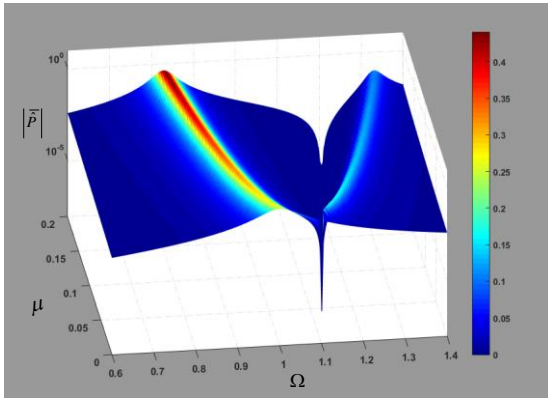
which is consistent with the equation derived by Williams and Yates reported in [50], the current model is more comprehensive that expands to a 2DOF system. The output power can be further normalized to form a dimensionless expression to facilitate the overall performance. The normalized dimensionless power of 2DOF vibrational system can be further written in equation (6.7) as

$$|\tilde{P}| = \left| \frac{\hat{P}}{\frac{m_1(\omega^2 U_0)^2}{\omega_1}} \right| = \frac{\zeta_e \Omega^2 (\Omega^2 - (1 + \mu)\alpha^2)^2}{(\Omega^4 - (1 + \mu)\alpha^2 \Omega^2 - \Omega^2 + \alpha^2)^2 + [2\zeta_1 \Omega (\Omega^2 - \alpha^2)]^2} \quad (6.7)$$

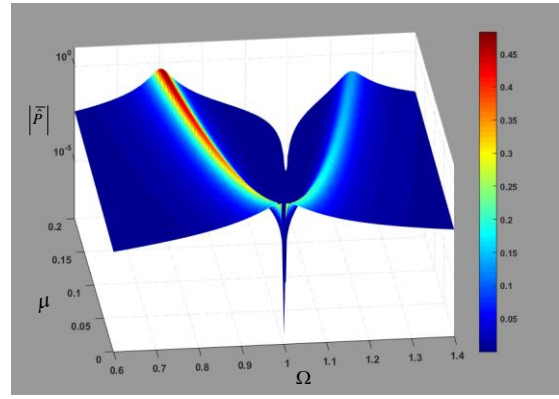
To achieve the optimal configuration for two close resonant peaks with comparable output powers, the influence of the mass ratio μ and frequency ratio α needs to be investigated. In this study, the electrical coupling damping has the same mechanical parasitic damping $\zeta_1 = \zeta_e = 0.004$. Figure 6.2 shows 3D contours of dimensionless power versus various mass ratios (μ) and excitation frequency levels (Ω) for different frequency ratios: (a) $\alpha = 1.1$; (b) $\alpha = 1$; (c) $\alpha = 0.9$; (d) $\alpha = 0.8$. It can be seen that two peaks can be generated by the proposed 2DOF energy harvesting system. Except for the extremely small μ near $\mu = 0$, the magnitude of the first peak generally increases while the second peak decreases with the enhancement of mass ratio (μ), regardless of frequency tuning ratios (α). Furthermore, it is noted that there is always an energy valley implanted between the two peaks, which is corresponding to the anti-resonance of the 2DOF system.

As depicted in these figures with different frequency tuning ratios (α), the frequency gap between the two peaks increases with an increase of the mass ratios (μ). For a relatively small mass ratio close to zero, it seems that the two peaks reach the closest position at $\alpha = 1$ (Figure 6.2 (b)), while the gap becomes comparatively quite large

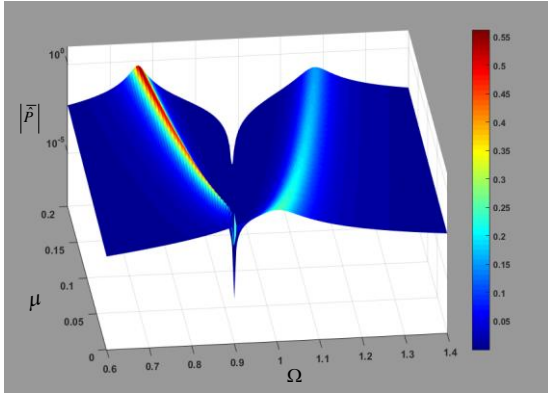
at $\alpha = 0.8$ (Figure 6.2 (d)). For $\alpha = 1$ as shown in Figure 6.2 (b), it can be seen that with the increase of mass ratio (μ), the two peaks move apart from each other and the magnitude of the first peak steadily increases while the second peak monotonically decreases. As the mass ratio (μ) decreases to zero, the two peaks for 2DOF system gradually converge together and merge into one peak eventually, indicating that the 2DOF system degrades to 1DOF system. These observations suggest that by setting a small mass ratio (μ) around zero and frequency ratio around 1, two close peaks with comparable magnitudes is achievable.



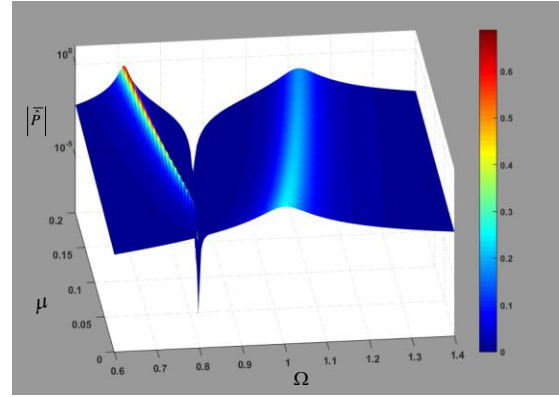
(a) $\alpha = 1.1$



(b) $\alpha = 1$



(c) $\alpha = 0.9$



(d) $\alpha = 0.8$

Figure 6.2 Dimensionless output power at various mass ratios (μ) and frequency tuning ratios (Ω) for different normalized excitation frequencies: (a) $\alpha=1.1$; (b) $\alpha=1$; (c) $\alpha=0.9$; (d) $\alpha=0.8$

Dimensionless power of proposed 2DOF system compared with conventional 1DOF configuration is further studied at various frequency tuning ratios (α) and excitation frequencies (Ω) for specific mass ratios $\mu = 0.04$ and $\mu = 0.16$ as shown in Figure 6.3 (a) and (b), respectively. It can be clearly seen that the two peaks of proposed 2DOF system are located on each side of the conventional 1DOF system. There always existed one peak that has a larger magnitude than that of 1DOF configuration, indicating an enhanced performance can be obtained. Moreover, two resonant peaks enable the proposed 2DOF harvester to be more adaptive to the practical vibration scenarios than the 1DOF configuration.

It is also noted that the magnitudes and resonant frequencies of both peaks are quite sensitive to mass ratios (μ). For a specific frequency tuning ratio $\alpha = 1$, the magnitude and resonant frequency ratios of the first peak to the second one are found to be 3.24 and 1.83 for $\mu = 0.16$, respectively, as shown in Figure 6.3 (b). By decreasing the mass ratio (μ) from 0.16 to 0.04, the magnitude ratio and resonant frequency ratio decrease to 1.49 and 1.21, respectively, as shown in Figure 6.3 (a). It indicates that by carefully tuning the frequency ratio α and designing a comparatively low mass ratio, two close and comparable peaks can be achieved. These numerical modeling results form the basis for the design and fabrication of the 2DOF electret-based energy harvesting device.

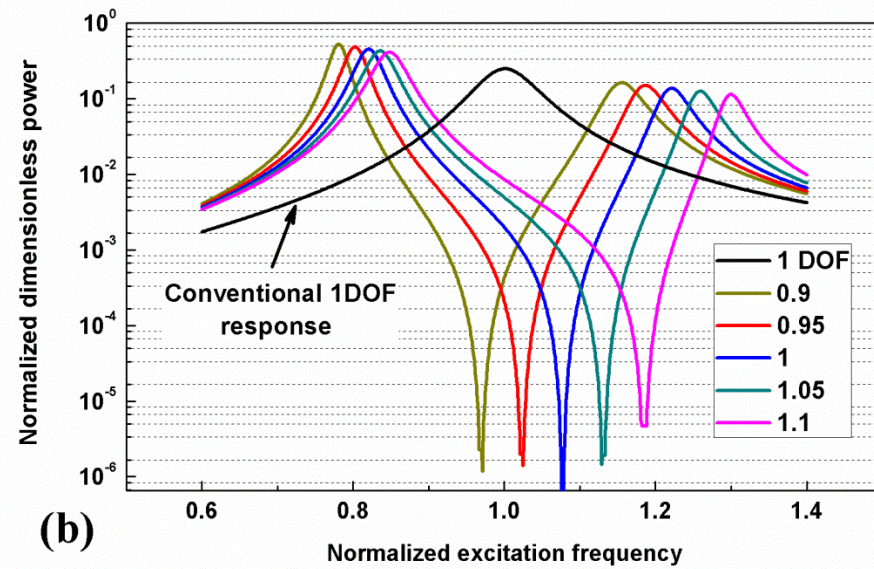
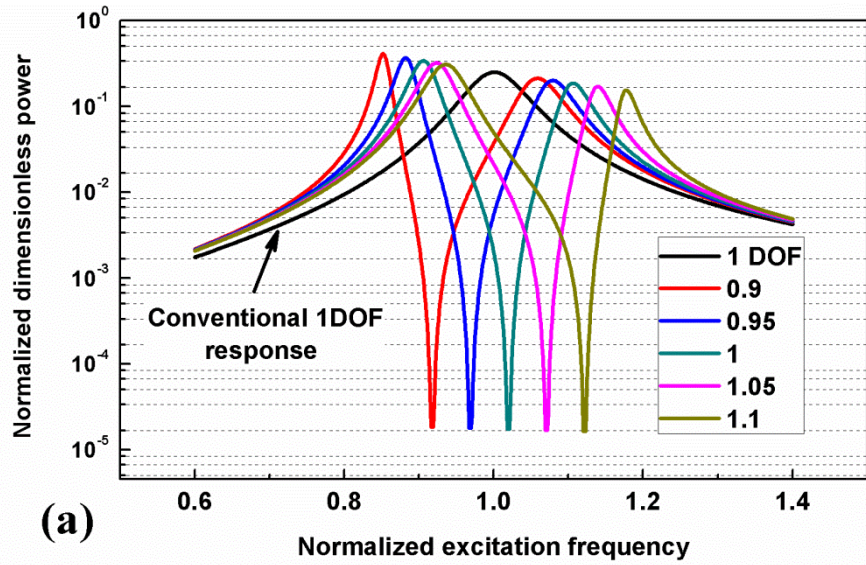


Figure 6.3 Dimensionless power output of proposed 2DOF system compared with conventional 1DOF system at various frequency tuning ratios (α) and excitation frequencies (Ω) for different mass ratios: (a) $\mu=0.04$; (b) $\mu=0.16$

6.3 Device design and fabrication

6.3.1 Device configuration

A schematic drawing of the proposed 2DOF e-VEH device was depicted in Figure 6.4 that sought to achieve multiple frequency vibration energy harvesting with its 2DOF resonant structure. It consisted mainly of two parallel plates. The top plate constructed

with 2DOF spring-mass resonant system was based on Si substrate with SiO₂ on its surface. It could be seen that the 2DOF system mainly comprised a primary mass and an accessory mass suspended by circular and spiral springs, respectively. The center circular accessory mass with a diameter of 3.4 mm and a thickness of 500 μm was suspended by a series of spiral springs around. The spiral springs consisted of three independent curved beams with a width of 200 μm and a height of 50 μm at a spacing of 50 μm . Each single spiral beam was composed of three sections of 120° circular arcs with different radii. These three 120° circular arcs with different radii were designed to be in tangent with each other at the junction points. These spiral spring beams were similar to the spring structures utilized in Chapter 3, where high-aspect-ratio (HAR) spiral structures were employed to achieve low-resonance in-plane energy harvesters. However, the springs in the current chapter formed by double-sided DRIE process were with extremely low aspect ratio and used for out-of-plane energy harvesting applications. The primary mass with a ring shape had an outer radius of 5.4 mm and inner radius of 2.05 mm suspended by three identical 6.3° circular arc beams. Each circular arc beam with an outer radius of 5.75 mm and inner radius of 5.5 mm was arranged in rotational symmetry with respect to an angle of 120°.

The metal electrodes were patterned on the primary mass for energy conversion as shown in Figure 6.4. LDPE thin film was used as electrets that were firstly bonded on the bottom plates to serve as charge pump. When the suspended primary ring mass with electrode was excited by an external oscillation, electrical power was generated via the variation of capacitance change between the two plates.

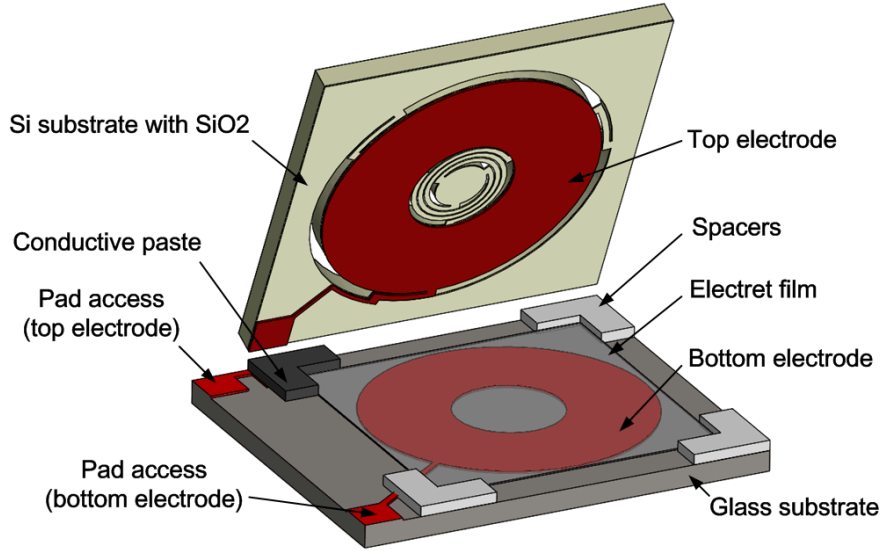


Figure 6.4 3D schematic of 2DOF e-VEH device

6.3.2 Microfabrication

Figure 6.5 depicted fabrication process of the proposed 2DOF spring-mass resonant system by double-side DRIE process. It began with a 1 μm thick SiO_2 insulation layer deposited by plasma-enhanced chemical vapor deposition (PECVD) on the front side of the Si wafer (Figure 6.5(a)). Cr (50 nm)/Au (300 nm) electrode layer were then patterned on the top of oxide layer through a lift-off process (Figure 6.5(b)). The step was followed by another lithography process to pattern the spring-mass system on the top side of wafer (Figure 6.5(c)). The suspension springs were then patterned on the Si device layer with a depth of 50 μm by frontside RIE process to remove the SiO_2 and DRIE process to etch the Si layer (Figure 6.5(d)). After that, the Si wafer was released in acetone and backside patterned by photoresist through a backside lithography process. Subsequently, the Si wafer was bonded to another holding wafer for another DRIE process to define the two seismic mass (Figure 6.5(e)). Finally, the whole spring-mass resonant structure was removed from the holding wafer and released. The bottom plate was prepared with the similar fabrication processes on glass substrates as in Section 5.3.2.

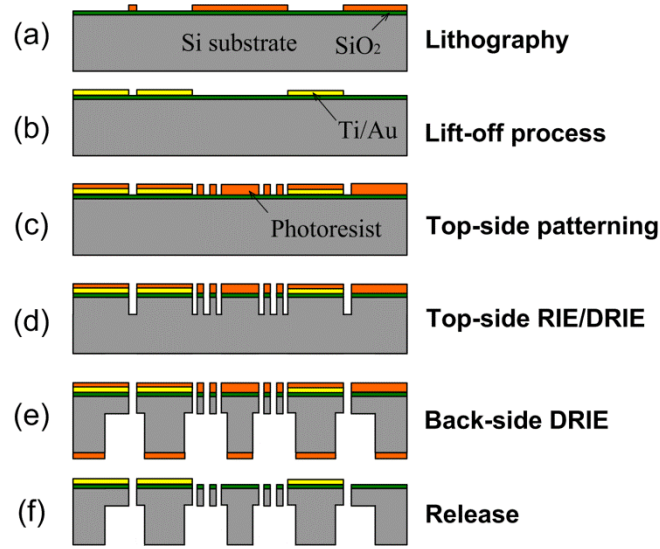


Figure 6.5 Fabrication process of the proposed 2DOF spring-mass system by double-side DRIE process

The optical image of the fabricated energy harvester chip with resonant structures and electrode patterns were shown in Figure 6.6 (a). The overall size of the energy harvester chip was $14.5 \text{ mm} \times 14.5 \text{ mm} \times 500 \text{ }\mu\text{m}$. Figure 6.6 (b) depicted the accessory subsystem that comprised a small center circular mass suspended by three separate sets of spiral beams around. Enlarged SEM image of the top electrode and outer spring beams was depicted in Figure 6.6 (c). It could be seen the primary mass is suspended by the thin circular beams. The detailed SEM of the seismic mass associated with spring layer was further depicted in Figure 6.6 (d).

Consequently, the e-VEH prototype was assembled through a flip-chip package with two parallel plates. Figure 6.7 exhibited optical images of the assembled MEMS e-VEH device compared with a ten cent coin. The e-VEH prototype was wire-bonded onto a printed circuit board for testing. The overall dimension of the device was approximate $14.5 \times 17 \times 1.2 \text{ mm}^3$. Detailed parameters of the MEMS e-VEH device were listed in Table 6.1.

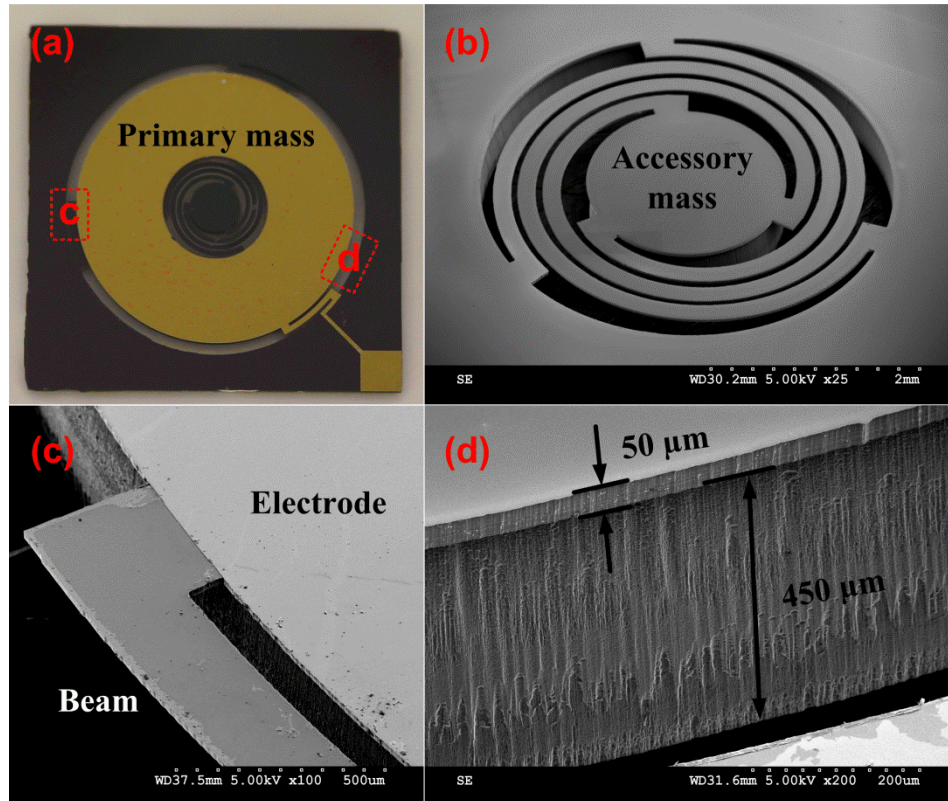


Figure 6.6 (a) Optical image of the fabricated spring-mass structure; (b) SEM images of the secondary mass with inner spiral springs; (c) (d) trimetric views of the primary mass and beam structures

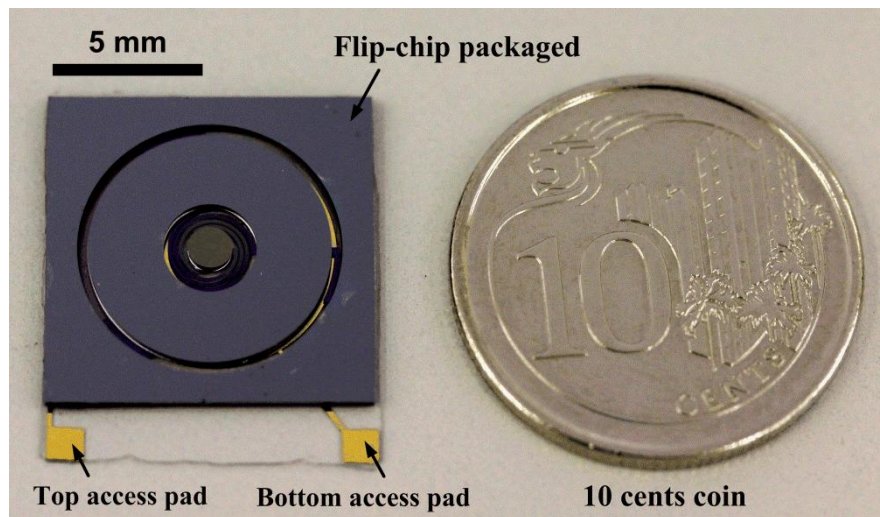


Figure 6.7 Optical images of the assembled MEMS e-VEH device compared with a ten cents coin

Table 6.1 Designed parameters and specifications of the electromagnetic energy harvesting chip

Component	Designed parameter	Values
Accessory mass	Radius R_1	1 mm
	Height h_1	500 μm
	Weight m_1	3.66 mg
Primary mass	Inner radius R_2	2.05 mm
	Outer radius R_3	5.4 mm
	Height h_1	500 μm
	Weight m_2	91.3 mg
Inner spring beam	Width w_c	200 μm
	Height h_2	50 μm
	gap w_g	50 μm
Outer spring beam	Circular arc angle θ	6.3 °
	Inner radius R_4	5.5 mm
	Outer radius R_5	5.75 mm
Capacitance	Load capacitance C	15.2 pF
Electret	Thickness d	50 μm
	Surface potential l_s	300 V
	Resistance r	4 M Ω
Volume	Device volume V_m	14.5 \times 17 \times 1.2 m ³

6.4 Mechanical dynamic analysis

6.4.1 Modal analysis

The dynamic behavior of the 2DOF e-VEH is further studied by a finite element analysis based on ANSYS. Figure 6.8 depicts top view of the 2DOF spring-mass

resonant system. According to the numerical calculation as depicted in Section 6.2, the mass ratio (μ) of accessory mass and primary mass is settled as 0.04 in order to achieve two comparable peaks. Since the thickness of both masses is predefined by the wafer thickness, the mass ratio (μ) can be precisely controlled by the defining the three radii (R_1 , R_2 , R_3) of the center circular mass and outer ring mass, as shown in Figure 6.9. The frequency tuning ratio (α) is controlled by adjusting the tuning angle (θ), which is settled around 6.3° to ensure the frequency tuning ratio to be around 1. Details of the other designed parameters and specifications of the proposed device are found in Table 6.1.

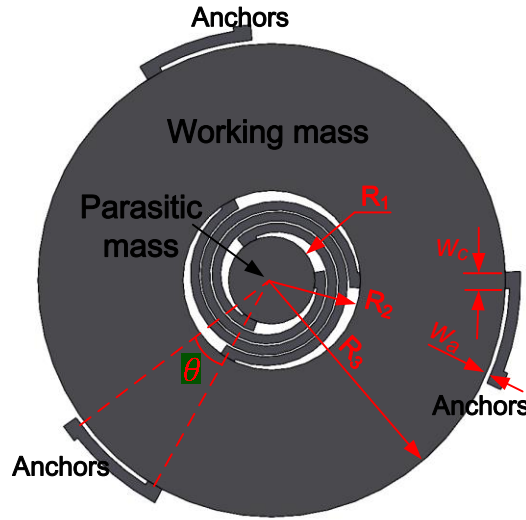


Figure 6.8 Top view of the proposed 2DOF spring-mass resonant system

A conventional SOLID 186 element is used to mesh and model both the spring beam and center masses. Overall more than 11645 elements are used. Zero boundary condition is the only load in the model analysis. The end of the circular beams around primary ring mass is fixed. The mode shapes and the resonant frequencies of the primary two vibration modes are shown in Figures 6.9 (a) and 6.9 (b), respectively. It is found that the resonant frequencies of the primary two vibration modes are 584 and 758 Hz, respectively. The resonant frequency ratio of the second peak to the first one is only 1.30, which is significantly smaller than most of the reported 2DOF resonators.

It is also interesting to observe that the primary mass and the accessory mass vibrate in the same phase at mode I, while it changes to 180° out-of-phase at mode II. Both of these two modes can be employed for vibrational energy harvesting.

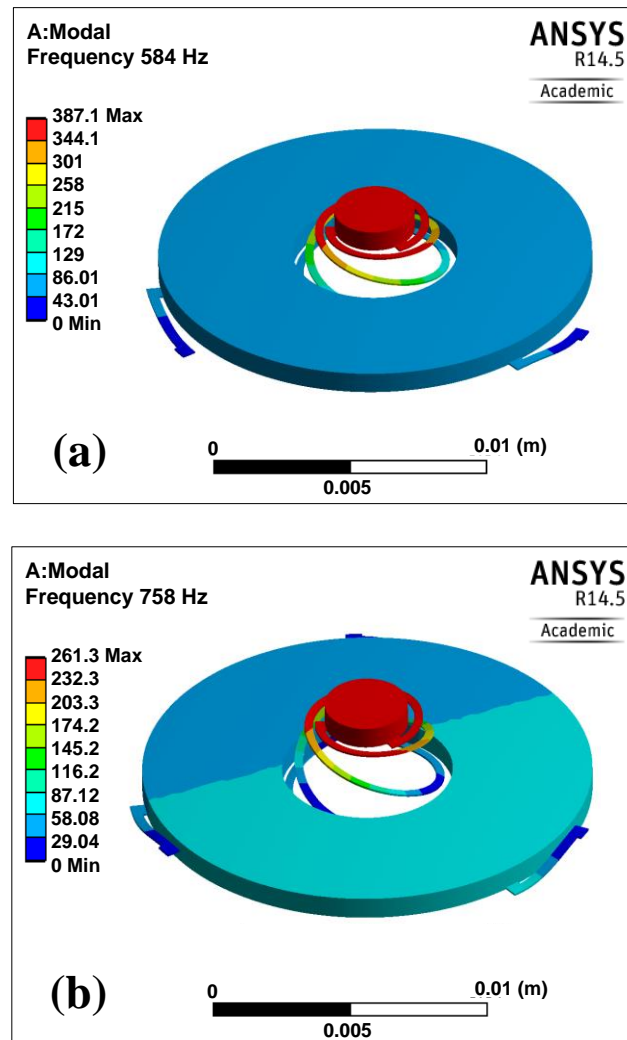


Figure 6.9 Modal simulation of Spring-mass structure: (a) mode I; (b) mode II.

6.4.2 Harmonic analysis

Previous modal analysis in section 6.4.1 has shown the dual mass system could operate in in-phase and out-of-phase vibration modes with a low frequency ratio of 1.30. The comparative magnitude responses will be further studied in this section by harmonic analysis in ANSYS. Harmonic analysis is utilized to analyze the

steady-state response of the linear structure when subjected to the continuous periodic load following the regularity of sinusoidal function. Thus an input excitation with sinusoidal function is applied to the 2DOF resonant system as

$$Z(t) = Z_0 \sin(\omega t + \varphi) \quad (6.8)$$

where Z_0 is the excitation amplitude, ω is the applied vibration frequency, φ is the applied phase angle. The swept excitation frequency spectrum is from 400 to 900 Hz with a step size of 0.5 Hz. The displacement of the primary mass is monitored in the study when a swept frequency is applied to the 2DOF resonant system. Figure 6.10 depicts the dynamic response of the monitored primary mass which is characterized as a displacement-frequency curve associating with the phase angle variation. It can be seen that two resonances take place in the dual-mass system with maximum amplitude of 4.94 μm at 584 Hz and 2.79 μm at 720.5 Hz, respectively.

The resonance found in the harmonic analysis is consistent with the modal analysis. Two effective peaks with comparable magnitudes are also observed by the dual-mass configuration, although the absolute values of the peak magnitudes may vary due to the change in the damping conditions. It can also be found that the phase angle has been changed three times between 180° and 0° according to the harmonic simulation. Each time a resonance takes place, the phase of the two vibration modes has been changed 180° simultaneously.

As shown in Figure 6.10, the magnitude of the first peak is comparatively larger than that of the second peak. This condition can be easily reversed by increasing the stiffness of the outer circular beam. Figure 6.11 shows harmonic response of the primary mass of the 2DOF system with enhanced stiffness of the outer circular. By simply decreasing the circular arc angle θ , the second peak can be tuned larger than the first one. The resonant frequencies also increased a bit to 611 Hz for the first peak and 763 Hz for the second peak. This indicates that the comparative magnitudes of the

two peaks can be easily controlled by adjusting the parameters of beam stiffness.

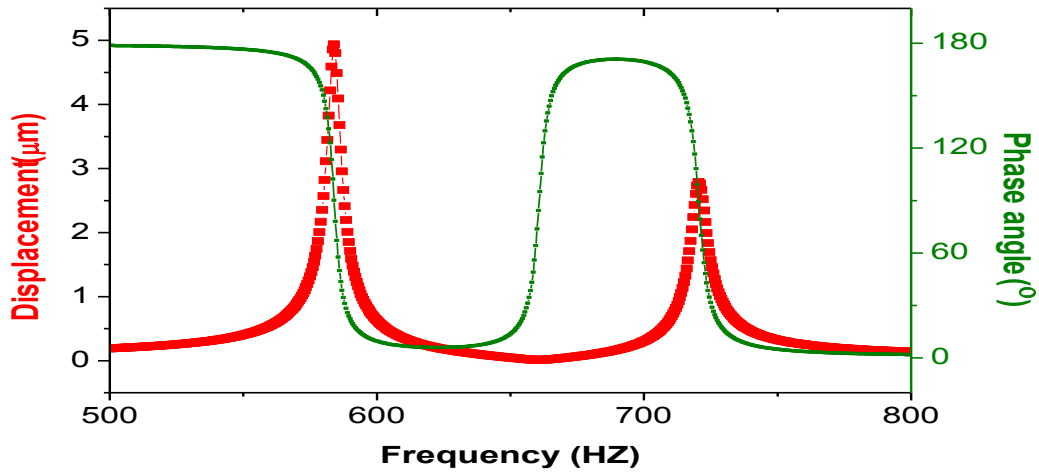


Figure 6.10 Harmonic response of the primary mass for the proposed 2DOF e-VEH device within a frequency spectrum of 500 to 800 Hz

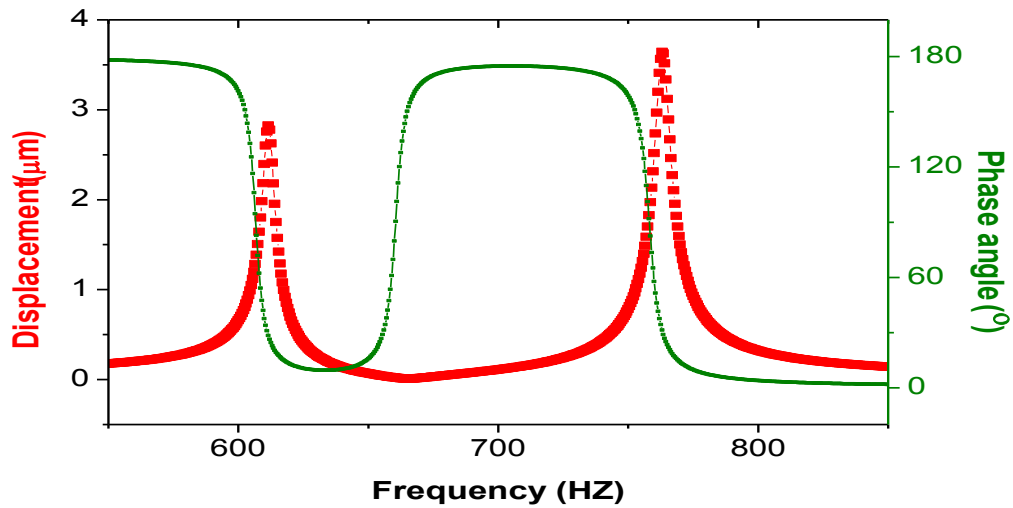


Figure 6.11 Harmonic response of the primary mass with an enhanced stiffness of the outer circular beam within a frequency spectrum of 550 to 850 Hz

6.5 Device characterization

The performance of the proposed 2DOF e-VEH energy harvesting device was characterized by attaching to a vibration testing system similar to the experimental setup presented in Figure 5.11. It mainly contained a shaker, a function generator, a voltage amplifier, an accelerometer, a dynamic signal analyzer and its controlling

system. The two terminal electrodes were connected to an external resistor and monitored by a data acquisition system (DAQ NI USB-6289 M series) to record the electrical output. In the experiment, a swept frequency from 400 to 900 Hz was applied at various excitation levels. Both time-domain and frequency-domain data were collected for characterizing dynamic behavior of the proposed device.

6.5.1 Linear 2DOF frequency responses

In the experiment, excitation frequencies from 400 to 900 Hz with a sweeping time of 6 second were applied to the 2DOF e-VEH device with a load resistance of 4 M Ω . The excitation acceleration was fixed around 1.9 m/s². The design parameters for the prototypes were shown in Table 6.1 similar to the ones used in the previous simulation as shown in section 6.4. The time-domain output voltages directly obtained from two access pads of the energy harvesting device in a swept frequency process were depicted in Figure 6.12 (a). It could be seen that two peaks were clearly detected. The time-domain signal was transferred to a frequency-domain signal by using fast Fourier transform (FFT) as shown in Figure 6.12 (b). The two peaks were found to be 590.5 and 731.2 Hz from the FFT results, which were expected to be about 584 and 720.5 Hz according to the previous simulation. These discrepancies may be due to the actual size variations in the beam width and seismic mass during the long-term DRIE process, such as the real beam width and seismic mass, which are not free of errors [165]. Moreover, double-side DRIE etching was employed in the current device fabrication process. Although the thickness of seismic mass could be precisely controlled by the wafer thickness, the beam thickness was largely influenced by the etching time. Small variations of the beam thickness may also affect the resonant frequencies of the proposed device.

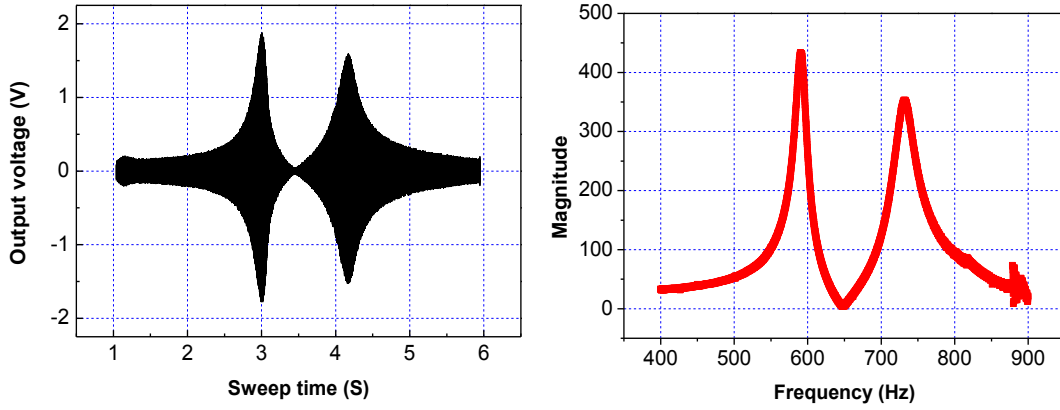


Figure 6.12 Vibration response of the 2DOF energy harvester prototype with a frequency sweeping from 400 to 900Hz: (a) Raw time-domain data records by DAQ system; (b) frequency domain signal by fast Fourier transform

The point-by-point discrete output voltage amplitudes were further recorded in the range of 400~900 Hz at a step size of 5 Hz and with a load resistance of 4 M Ω , as depicted in Figure 6.13. The excitation accelerations were set at 1.9, 3.2 and 4.4 m/s², respectively. Two close and comparable peaks were obtained at different excitation levels as well as both of the peaks are enhanced with increase of the excitation levels from 1.9 to 4.4 m/s². Take the curve of 4.4 m/s² as an example, it could be clearly seen that two close resonances of 590 Hz and 730 Hz with the comparable peaks of 3.7 V and 3.9 V were obtained, respectively. The resonant frequencies were in good consistency with the previous FFT results obtained from sweeping frequency. The frequency ratio of the second peak to the first peak is only 1.24, which showed a qualitative match to the previous numerical lumped models and Finite Element Analysis (FEA) results. The obtained frequency ratio was also much smaller than the previous reported in the literature [148-150] and simultaneously two comparable peaks were achieved as well. The quality factors of the resonant energy harvesting system were 22.4 at 590 Hz and 20.3 at 730 Hz, respectively, which were calculated by $Q = f_r / \Delta f$, where f_r was the resonant frequency and Δf was the half power bandwidth. The quality factor did not exhibit obvious variations when the primary mass and the accessory mass oscillated either in the same phase at mode I or in 180°

out-of-phase at mode II. It indicated the device operates in the same damping conditions. This may be due to the similar damping condition existed when the air gap between the primary mass and the substrate are almost the same.

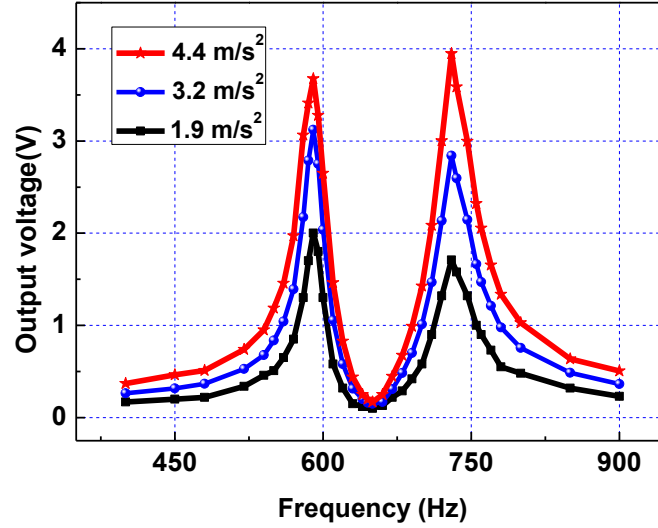


Figure 6.13 Measured output voltage in frequency sweeps at the excitations of 1.9, 3.2, 4.4 m/s^2 with a resistance of 4 $\text{M}\Omega$

6.5.2 Resonant frequency and amplitude responses

The resonant frequency and amplitude responses of the two peaks were further investigated with the increased excitations. Figure 6.14(a) depicted the measured voltage amplitude derivation trend at the various excitation levels from 0.64 to 12.8 m/s^2 . Enlarged portion of the excitations from 0.64 to 5.6 m/s^2 and from 5.6 to 12.8 m/s^2 were demonstrated in Figure 6.14(a) and (b), respectively. For the second peak, it could be seen the output voltage amplitudes were strictly in linear relationship with the excitation accelerations at the first stage from 0.64 to 5.6 m/s^2 , while it was in quasi-linear relationship at the second stage from 5.6 to 12.8 m/s^2 with a comparatively low slope. This may be due to the increased damping between the two plates with the air gap became smaller as the excitation increased. However, the first peak exhibited a totally different phenomenon, where the slope of the amplitude

decreased substantially with increased accelerations beyond 5.6 m/s^2 .

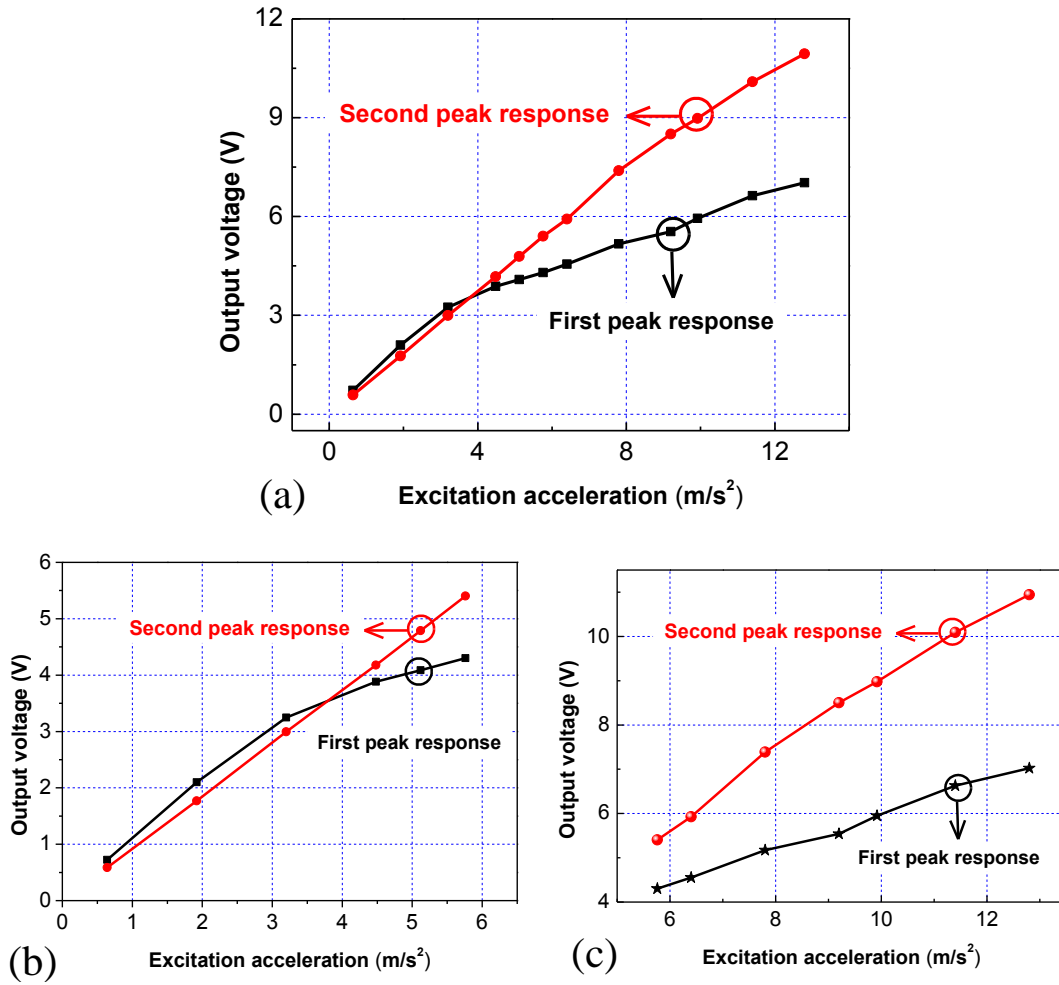


Figure 6.14 Measured voltage amplitude derivation trend at the various excitation levels: (a) Overall range from 0.64 to 12.8 m/s^2 ; (b) enlarged first portion from 0.64 to 5.6 m/s^2 ; (c) enlarge second portion from 5.6 to 12.8 m/s^2

This phenomenon could also be found in the frequency derivation trend as shown in Figure 6.15, where two resonant frequencies at various excitation levels in the range of 0.64 to 15.4 m/s^2 were recorded. At the first stage from 0.64 to 6.4 m/s^2 as shown in Figure 6.15(a), the resonant frequencies of both peaks were almost kept the same with a frequency ratio of 1.24 as previous observed. Nevertheless, the first peak migrated towards to the second peak with increased excitations at the second stage from 6.4 to 13.8 m/s^2 as shown in Figure 6.15(b), while the second peak stayed almost unchanged. This lead to the frequency ratio drifts from 1.24 at 0.64 m/s^2 to 1.13 at

15.4 m/s². This was due to the spring hardening effect occurred at the first peak, which bends the resonant peak to a higher frequency. Figure 6.16 presented the output voltage and power of the proposed 2DOF e-VEH device against different resistances at the resonance of 730 Hz with an excitation acceleration of 2.8 m/s². It could be seen that maximum output power of 1.15 μ W was obtained with an optimum load resistance of 5 M Ω .

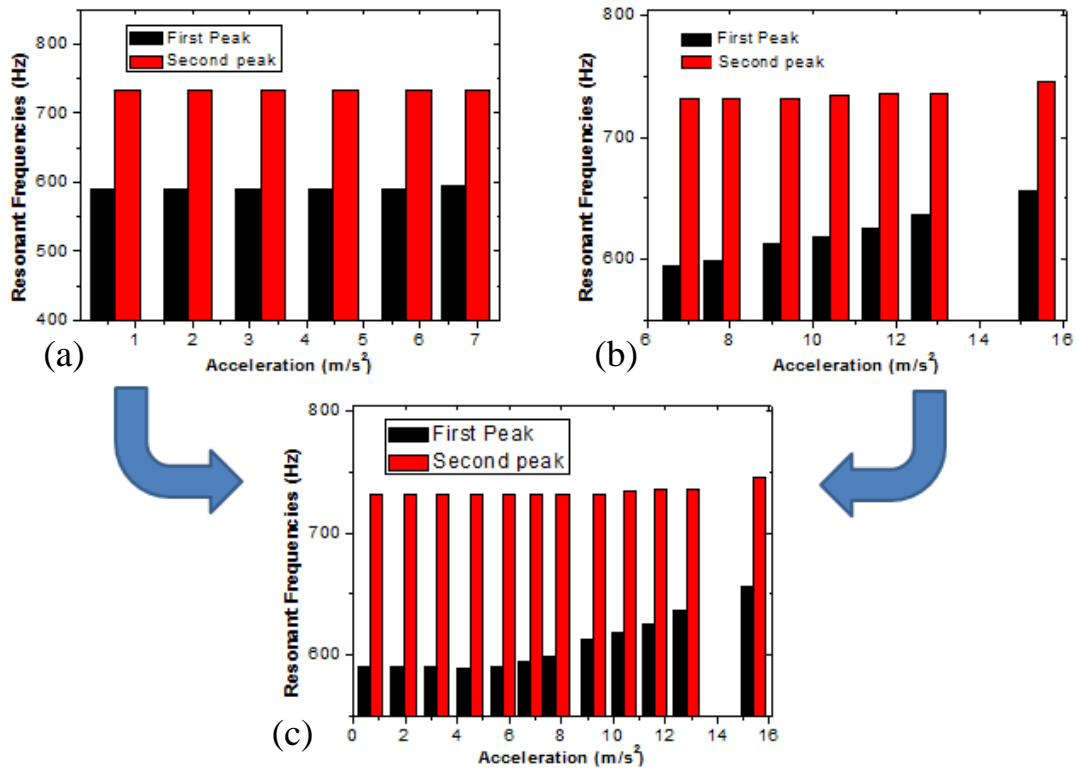


Figure 6.15 Measured two resonant frequencies at various excitation levels in the range of: (a) 0.64 to 6.4 m/s²; (b) 6.4 to 13.8 m/s²; (c) 0.64 to 13.8 m/s²

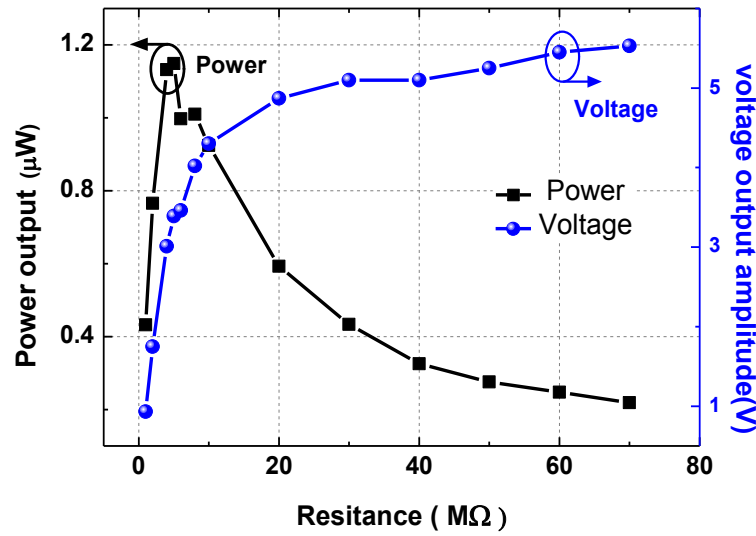


Figure 6.16 Output voltage and power against different resistances at the resonance with an acceleration excitation of 2.8 m/s^2

6.5.3 Nonlinear 2DOF responses with increased excitations

Previous experiments had demonstrated that two close and comparable peaks could be detected that matched well with the lumped parametric simulations. It was also found that there existed of an anti-resonance point that separated the two resonant peaks and forms a deep energy valley in the response curve. This phenomenon could also be found both in Figure 6.2 from numerical model and Figure 6.13 from the experimental results. The presence of the energy valley may deteriorate the broadband performance of the 2DOF system. On the other hand, it had been demonstrated in Chapter 5 that nonlinear effect could effectively broaden the bandwidth of energy harvesting device. Especially at strong excitation acceleration levels, the spring-hardening effect took place and could bend the resonant peak to a higher frequency. Thereby, the proposed 2DOF e-VEH device was characterized under elevated excitation acceleration levels.

Measured voltage time-domain responses by DAQ system at the excitation acceleration levels of 6.4 , 10 and 12.8 m/s^2 were depicted in Figure 6.17, Figure 6.18

and Figure 6.19, respectively. The swept frequency ranged from 400 to 900 Hz at a sweeping time of 5s and with a load resistance of 1 M Ω . It could be seen that the first peak exhibited an obvious spring hardening phenomenon and drifted to the second peak which almost stood still, although the peak magnitude increased with enhanced accelerations.

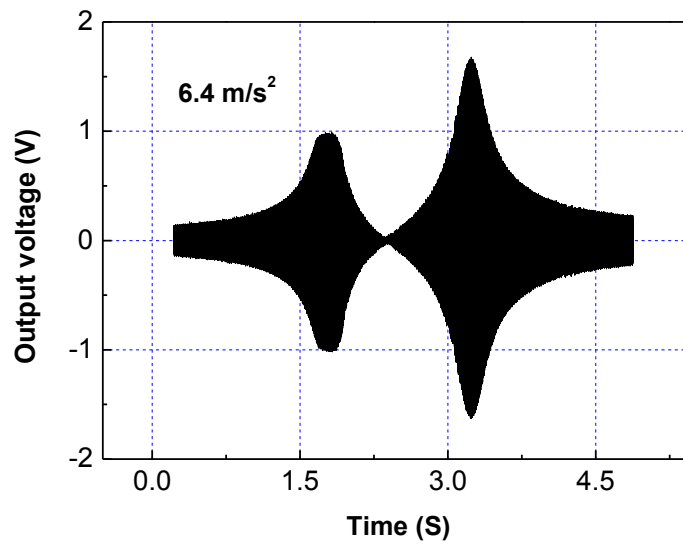


Figure 6.17 Measured raw voltage time-domain response by DAQ system at the excitation acceleration of 6.4 m/s^2

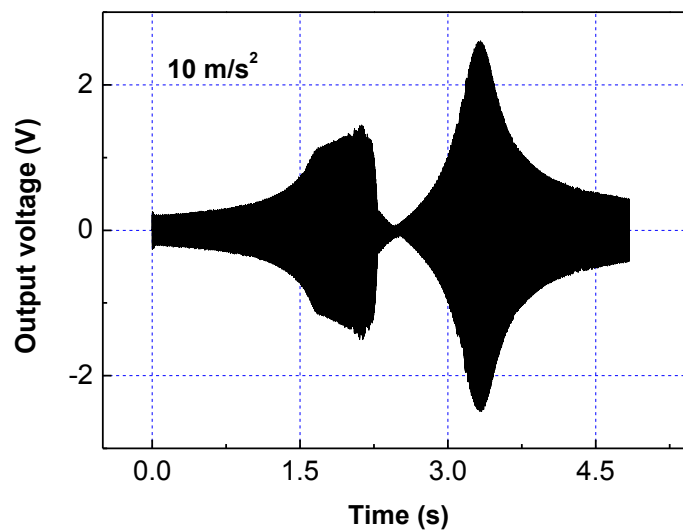


Figure 6.18 Measured raw voltage time-domain response by DAQ system at the excitation acceleration of 10 m/s^2

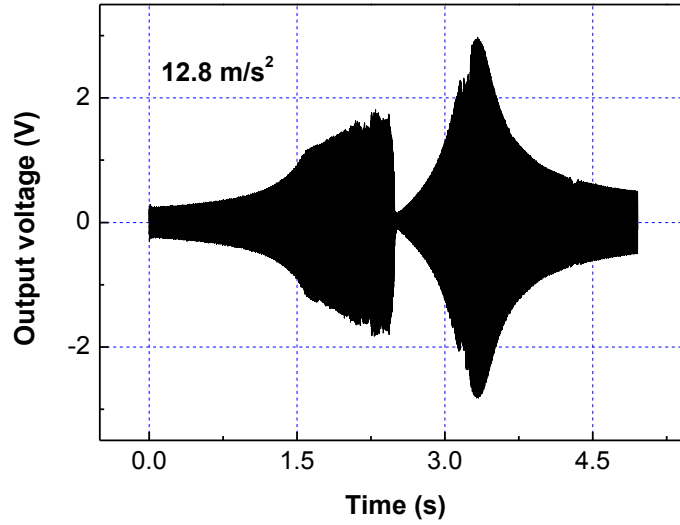


Figure 6.19 Measured raw voltage time-domain response by DAQ system at the excitation acceleration of 12.8 m/s^2

The output voltage responses versus frequencies at different excitation acceleration levels ranging from 6.4 to 12.8 m/s^2 were depicted in Figure 6.20 at a load resistance of $1 \text{ M}\Omega$. It could be seen that at an excitation of 2.8 m/s^2 , both of the two peaks exhibited a linear responses. With further increasing the accelerations above 6.4 m/s^2 , parts of the 2DOF system collided with the bottom plate, and thus a shift of resonant peak was observed. The resonant frequencies of the first peak drifted from 590 Hz at 2.8 m/s^2 to 636 Hz at 12.8 m/s^2 , while the frequencies of the second peak stayed almost unchanged from 731 Hz to 736 Hz . It indicated that the same-phase vibration mode of the 2DOF system was strongly influenced by the spring hardening effect, while its anti-phase mode was hardly affected. This spring hardening phenomenon could be further demonstrated with a frequency-up and -down sweeps.

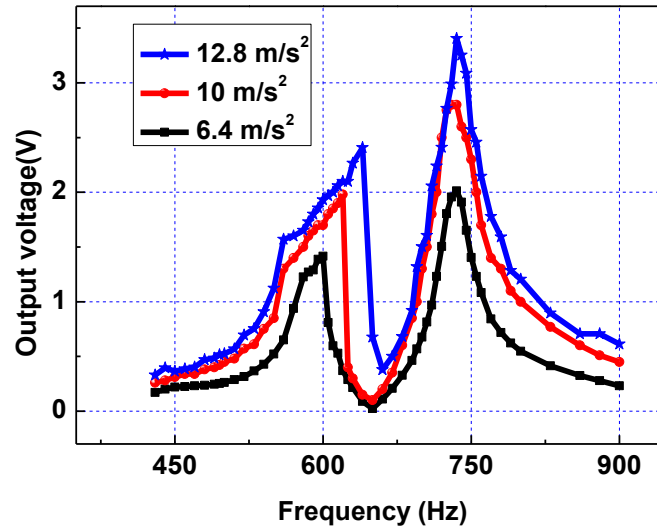


Figure 6.20 Measured output voltage in frequency sweeps at the excitations of 2.8, 6.4, 10 and 12.8 m/s^2

Figure 6.21 (a) depicted the measured voltage time-domain responses were further recorded by DAQ system against frequency-up and -down sweeps at the excitation acceleration of 12.8 m/s^2 with a load resistance of 1 $\text{M}\Omega$. The corresponding frequency-domain response was depicted in Figure 6.21 (b). It could be clearly observed that a notable drift toward a higher frequency appeared in the spectrum associated with obvious jump phenomenon and thus a hysteresis were observed between the up and down sweeps, as depicted in Figure 6.21 (b), indicating the spring hardening effect under such excitation levels. With the assistance of the spring hardening effect existed in the proposed 2DOF e-VEH device, the first peak were driven towards the second peak which made the frequency ratio of the second peak to the first one reduced by 9%. This could provide a new insight of implementing MEMS broadband energy harvesting devices by hybridizing multimodal energy harvesting and nonlinear techniques.

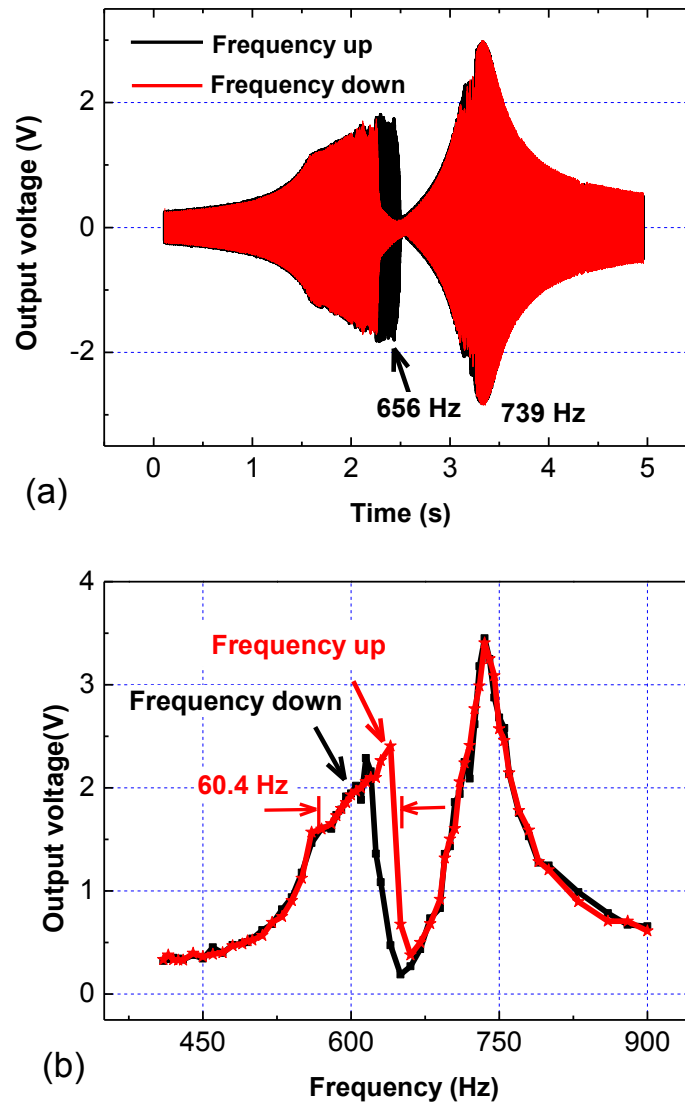


Figure 6.21 Measured voltage time-domain and frequency-domain responses by DAQ system against frequency-up and -down sweeps at the excitation acceleration of 12.8 m/s^2 with a load resistance of $1 \text{ M}\Omega$

6.5.4 Frequency responses at high excitation levels

In the same manner, frequency sweeps had been applied at further increased excitation of up to 19.2 m/s^2 with a load resistance of $1 \text{ M}\Omega$. Figure 6.22 depicted measured frequency responses by DAQ system, suggesting an irregular behaviour of the mobile mass. In this condition, the movable seismic mass began to collide with the

stopper fiercely. Two peaks could be clearly observed with comparable magnitudes. The quality factors of the first and second peak were decreased to 8.4 and 17.3, respectively. These were probably due to the presence of a strong damping component introduced by the squeeze film damping and strong instabilities of collision conditions. It was also noted that an obvious enhancement of magnitude at the anti-frequency point is found. This could bridge the energy valley of the two resonant peaks, which was quite beneficial to the overall broadband energy harvesting capabilities. At such condition, an output power of $9.68 \mu\text{W}$ was obtained at the two resonant peaks.

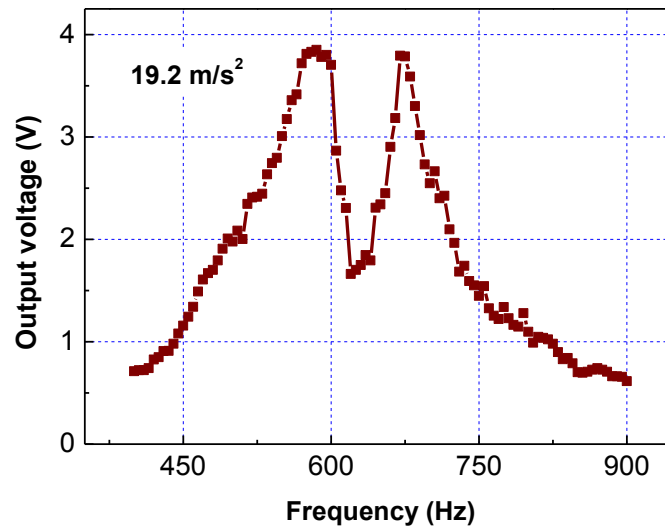


Figure 6.22 Measured frequency-domain responses by DAQ system at the excitation acceleration of 19.2 m/s^2 with a load resistance of $1 \text{ M}\Omega$

6.6 Summery of findings

This chapter studies the out-of-plane MEMS e-VEH device and further expands it into a two-degree-of-freedom (2DOF) system to achieve broadband energy harvesting. A lumped parametric model of 2DOF model is built and examined in respect of energy harvesting capabilities. Through parametric analysis, it is found that the 2DOF structure could have more energy than the conventional 1DOF counterparts and two close and effective peaks can be achieved. By precisely tuning the mass ratio to 0.04 and with a frequency ratio of around 1, the first two resonances of primary mass can

be tuned close to each other while maintain comparable magnitudes.

A novel 2DOF MEMS e-VEH device is then designed, fabricated and simulated. The 2DOF resonant system that comprises a primary mass and an accessory mass is constructed on a silicon wafer by double-side DRIE. The dynamic mechanical response of the proposed 2DOF resonator is investigated through modal and harmonic analysis through ANSYS. It is found the primary mass and the accessory mass vibrate in the same phase at mode I of 584 Hz, while it changes to 180° out-of-phase at mode II of 758 Hz and comparative peaks can be achieved by tuning the stiffness of the outer circular beam of the primary mass.

With the current prototype under an excitation acceleration of 4.4 m/s^2 , the experimental result demonstrates that two close resonances with frequency ratio of only 1.24 (590.5 and 731.2 Hz) and comparable peaks (3.7 V and 3.9 V) are achieved, providing good validation for the previous numerical and finite element modeling results. With further increasing the acceleration to 6.4g, the resonant frequencies of the first peak is driven from 590 Hz at 4.4 m/s^2 to 636 Hz at 12.8 m/s^2 , which leads to the frequency ratio drifts from 1.24 at 4.4 m/s^2 to 1.16 at 12.8 m/s^2 . An obvious spring hardening hysteresis for the first peak is also observed between the up and down sweeps. This may offer new insights of realizing a nonlinear multimodal energy harvesting technique.

Chapter 7 Conclusions and Future work

7.1 Conclusions on current work

The main aim of this research work is to investigate effective methods of e-VEHs to be more adaptive to ambient vibrations that usually have frequency-variant or direction-random characteristics. Two primary challenges faced by conventional vibration-based energy harvesters need to be addressed, namely ‘restricted single-direction issue’ and ‘narrow bandwidth issue’. To achieve this goal, this thesis presents the research work on adaptive methods of e-VEHs to extend frequency spectrum bandwidth and multi-directional response of the harvester from both sophisticated electromechanical coupling of electrostatic energy harvesting systems and advanced mechanical configuration perspectives. The main contributions of the research work carried out can be summarized as follows:

A sandwich-structured MEMS e-VEH device has been successfully developed for enhancement of output performance as well as reduction of unwanted vertical pull-in and horizontal damping electrostatic forces. The electrostatic force has been investigated with the combination of finite element analysis and numerical calculations. With two separate 180 °out-of-phase capacitive circuits integrated into single spring-mass system, it is found that vertical pull-in and horizontal damping electrostatic forces can be reduced by approximately 72.8% and 46.2%, respectively. The multi-directional energy harvesting capabilities have been examined according to frequency-response characterization results. With an acceleration of 0.2 g and resonance of 125 Hz, an overall output power of 0.12 μW and corresponding NPD of 5.56 $\mu\text{W}\cdot\text{cm}^{-3}\cdot\text{g}^{-2}$ have been achieved for the fabricated prototype.

A 2D e-VEH device based on a novel rotational symmetrical resonator has been successfully designed, fabricated and characterized for low-frequency and

low-acceleration ambient vibrational energy harvesting. The design aspects of the low-resonant spiral springs associated with their mechanical and dynamic properties have been examined with finite element analysis. It is found that uniform stiffness distributions in 2D plane with low magnitudes ($k_x = 4.49$, $k_y = 4.65$) can be achieved within a small confined space. It is also able to obtain low-frequency 2D resonators. A general numerical model of the 2D resonator has been summarized in the matrix form to describe the dynamic motion of the seismic mass. The 2D energy harvesting capabilities of the proposed device have been experimentally evaluated at different excitation in-plane directions with a swept frequency from 60 to 90 Hz. For a comparative low acceleration of 0.05g, power outputs of 0.67 nW and 1.2 nW have been obtained at two in-plane vibration modes of 75 and 78.5 Hz, respectively.

A broadband e-VEH device has been designed and implemented that has both positive and negative charged electret plates integrated into a single seismic mass system. Broadband energy harvesting has been successfully demonstrated by combined effect of the electret-induced electrostatic force and elastic stopper for the first time. The nonlinear effect of electrostatic spring softening has been modeled and analyzed through ODE solver in Matlab, where the electromechanical coupling effect arising from mechanical and electrical domains is incorporated. The frequency response of proposed e-VEH device has been evaluated at different excitation levels. Power output of 0.95 μW has been obtained at 0.42g, corresponding to a normalized power density of $37.4 \mu\text{W}\cdot\text{cm}^{-3}\cdot\text{g}^{-2}$. Owing to combined advantages of both spring softening and hardening effect, the device has achieved 3-dB bandwidths of 3.7 Hz for frequency-up sweep and 2.8 Hz for frequency-down sweep, respectively, which demonstrate a large enhancement compared to the linear response (1.3 Hz).

A nonlinear 2DOF e-VEH device has been implemented and investigated for broadband energy harvesting. The proposed system comprises a primary subsystem for power generation, and an accessory subsystem for frequency tuning. Two effective

and close peaks with frequency ratio of only 1.15 have been achieved for the first time for a 2DOF MEMS device. A lumped parametric model of 2DOF model has been built and examined in respect of energy harvesting capabilities, which have demonstrated its superiority to conventional 1DOF counterpart. The frequency tuning process of the proposed 2DOF system has further been studied through modal and harmonic analysis through ANSYS. Two resonances of primary mass have been tuned close to each other with effective magnitudes by adjusting the mass ratio and frequency ratio. With the current prototype under an excitation acceleration of 4.4 m/s^2 , the experimental result have demonstrated that two close resonances with frequency ratio of only 1.24 (590 and 730 Hz) with comparable peaks (3.7 V and 3.9 V) can be achieved. This is consistent with the numerical and finite element modeling results. Upon the increase of acceleration, hardening nonlinearity induced by end-stop effect is involved in the multi-frequency behavior, resulting in resonant frequency drift upwards and further bandwidth convergence.

7.2 Original contributions

This thesis presents the development of adaptive e-VEHs towards broadband and multi-directional ambient vibrations. The original contributions of the research work carried out are described as follows:

- ❖ Derived a general numerical model in matrix form to describe the 2D dynamic motion of the seismic mass, which could form a basis of developing real 2D vibrational energy harvesters.
- ❖ Designed and implemented a novel a rotational symmetrical circular resonator based on parallel spiral springs, by which two in-plane low-resonant frequencies within a confined space could be achieved via one mask DRIE step without incorporating complicated SOI wafer processes.

- ❖ Developed 2D e-VEH device with a compact sandwiched configuration that is capable of enhancing the output power and minimizing the unwanted vertical pull-in and horizontal damping electrostatic forces.
- ❖ Derived an in-plane electrostatic force calculation model with the combination of finite element analyses and numerical calculations, where fringe effect as well as capacitance extreme value variations have been considered.
- ❖ Exploited spring softening nonlinearity induced by strong electromechanical coupling arising from high surface potential provided by charged electret for the first time. An analytical model is derived for the electret-based vibration energy harvesting system, where the electromechanical coupling effect arising from mechanical and electrical domains has been incorporated.
- ❖ Derived a lumped parametric model of 2DOF resonant system that comprises of a primary subsystem and accessory subsystem and its energy harvesting capability has been examined. By carefully tuning process, two close resonances have been obtained.
- ❖ Designed and implemented a novel nonlinear 2DOF MEMS e-VEH device for the first time, where two close resonances (only 1.15) with comparable magnitudes have been achieved.

7.3 Recommendations for future work

While the work presented in this thesis has contributed significantly to the state-of-the-art broadband and multi-direction vibrational harvesters to be more adaptive to various vibration scenarios, a number of challenges and issues have yet to be addressed. These include

(a) Exploit omnidirectional energy harvesters with multi-layer e-VEHs. Current reported multi-directional energy harvesters mostly focus on investigating different vibration modes of a single resonant structure. It encounters challenges in distributing uniform power density in various excitation directions as well as providing sufficient output. To achieve real omnidirectional e-VEHs, one promising method is to extend the proposed sandwich-structured configuration to multi-layer structures, where several resonators with different operating directions could be structured into a compact device. The associated power management circuit should be further improved. This could not only benefit from the enhanced performance but also be more adaptive to arbitrary external excitations.

(b) Enhance the performance of nonlinear harvesters with hybrid mechanisms. In Chapters 5 and 6, spring-hardening nonlinearity introduced by end-stop effect has been presented to extend the bandwidth of e-VEHs device. This would however result in energy loss when the seismic mass collides with stoppers. Recently, triboelectric nanogenerators have been reported to scavenge energy from interfacial electrification. Traditional MEMS energy harvesters based on electrostatic, electromagnetic and piezoelectric mechanisms are confined by the conversion mechanisms themselves. A new concept may replace the mechanical stoppers with PDMS pyramid nano-structures. Thus, the e-VEH device could achieve both wideband behaviors and enhanced electrification performance due to the combined advantages from both energy harvesting mechanisms.

(c) Explore multi-DOF e-VEHs for broadband energy harvesting. To create multi-peak resonances in a certain range is expected to be beneficial to enhance the energy effectiveness. In Chapter 6, a 2DOF e-VEH device has been presented to achieve two close and effective peaks. This could further extended to multi-peak harvesters by integrating an array of small tuning dampers. By adjusting the frequency and mass ratio of several accessory subsystems to the primary subsystem,

close multiple resonances with effective amplitude could be achieved.

(d) Further investigate the nonlinear effect within the 2DOF system. From the numerical modelling of 2DOF system shown in Chapter 6, it is noted that there is always an energy valley implanted between the two peaks, which is corresponding to the anti-resonance of the 2DOF system. Spring hardening effect is found to be able to bend the first peak upward and fill the valley between the peaks. This phenomenon could be further investigated and developed.

(e) Study the power management circuit with external electronics. To maximize the power transfer efficiency from the e-VEH device to the external circuit, it is necessary to investigate the real-time internal impedance variation within the e-VEH according to various excitation conditions. The power management control circuit not only could adjust the maximum voltage across the energy harvester, but also is capable of changing dynamic properties of e-VEH device through electrostatic force variation, making it more adaptive to external excitations.

References

- [1] I. F. Akyildiz, W. Su, Y. Sankarasubramaniam, and E. Cayirci, "A survey on sensor networks," *Communications magazine, IEEE*, vol. 40, pp. 102-114, 2002.
- [2] M. Hautefeuille, C. O'Mahony, B. O'Flynn, K. Khalfi, and F. Peters, "A MEMS-based wireless multisensor module for environmental monitoring," *Microelectronics Reliability*, vol. 48, pp. 906-910, 2008.
- [3] P. D. Mitcheson, E. M. Yeatman, G. K. Rao, A. S. Holmes, and T. C. Green, "Energy Harvesting From Human and Machine Motion for Wireless Electronic Devices," *Proceedings of the IEEE*, vol. 96, pp. 1457-1486, 2008.
- [4] C. Knight, J. Davidson, and S. Behrens, "Energy Options for Wireless Sensor Nodes," *Sensors*, vol. 8, pp. 8037-8066, 2008.
- [5] J. A. Paradiso and T. Starner, "Energy Scavenging for Mobile and Wireless Electronics," *IEEE Pervasive Computing*, vol. 4, pp. 18-27, 2005.
- [6] J. Xie, L. Chengkuo, and F. Hanhua, "Design, Fabrication, and Characterization of CMOS MEMS-Based Thermoelectric Power Generators," *Journal of Microelectromechanical Systems*, vol. 19, pp. 317-324, 2010.
- [7] S. Roundy, P. K. Wright, and J. Rabaey, "A study of low level vibrations as a power source for wireless sensor nodes," *Computer Communications*, vol. 26, pp. 1131-1144, 2003.
- [8] N. S. Hudak and G. G. Amatucci, "Small-scale energy harvesting through thermoelectric, vibration, and radiofrequency power conversion," *Journal of Applied Physics*, Vol.103, pp. 101301, 2008.
- [9] S. Roundy, "On the effectiveness of vibration-based energy harvesting," *Journal of Intelligent Material Systems and Structures*, vol. 16, pp. 809-823, 2005.
- [10] D. Zhu, "Vibration energy harvesting: machinery vibration, human movement and flow induced vibration," *InTech*. pp. 25-54, 2011.
- [11] S. R. Anton and H. A. Sodano, "A review of power harvesting using piezoelectric materials (2003-2006)," *Smart Materials & Structures*, vol. 16, pp. 1-21, 2007.
- [12] E. R. Westby and E. Halvorsen, "Design and Modeling of a Patterned-Electret-Based Energy Harvester for Tire Pressure Monitoring Systems," *IEEE/ASME Transactions on Mechatronics*, vol. 17, pp. 1-11, 2011.

-
- [13] I. Neri, F. Travasso, R. Mincigrucci, H. Vocca, F. Orfei, and L. Gammaitoni, "A real vibration database for kinetic energy harvesting application," *Journal of Intelligent Material Systems and Structures*, Vol. 23, pp.2095-2101, 2012.
- [14] L. M. E. Reilly, R. Fain and P. K. Wright "A study of ambient vibrations for piezoelectric energy conversion," *Proc. PowerMEMS 2009*, pp.312-315, 2009.
- [15] M. Wischke, G. Biancuzzi, G. Fehrenbach, Y. Abbas, and P. Woias, "Vibration harvesting in railway tunnels," *Proc. Power MEMS2010*, pp. 123-126, 2010.
- [16] M. Wischke, M. Masur, M. Kröner, and P. Woias, "Vibration harvesting in traffic tunnels to power wireless sensor nodes," *Smart Materials and Structures*, vol. 20, pp. 085014, 2011.
- [17] L. M. Miller, E. Halvorsen, T. Dong, and P. K. Wright, "Modeling and experimental verification of low-frequency MEMS energy harvesting from ambient vibrations," *Journal of Micromechanics and Microengineering*, vol. 21, pp. 045029, 2011.
- [18] S. D. Nguyen, "wideband MEMS energy harvesters utilizing nonlinear springs," *Dissertation in University of Oslo*, 2012.
- [19] C. P. Le, E. Halvorsen, O. Søråsen, and E. M. Yeatman, "Wideband excitation of an electrostatic vibration energy harvester with power-extracting end-stops," *Smart Materials and Structures*, vol. 22, pp. 075020, 2013.
- [20] E. Halvorsen, "Fundamental issues in nonlinear wideband-vibration energy harvesting," *Physical Review E*, vol. 87, pp. 042129, 2013.
- [21] L. Tang, Y. Yang, and C. K. Soh, "Toward broadband vibration-based energy harvesting," *Journal of Intelligent Material Systems and Structures*, vol. 21, pp. 1867-1897, 2010.
- [22] A. Erturk, J. M. Renno, and D. J. Inman, "Modeling of piezoelectric energy harvesting from an L-shaped beam-mass structure with an application to UAVs," *Journal of intelligent material systems and structures*, vol. 20, pp. 544-579, 2009.
- [23] U. Bartsch, J. Gaspar, and O. Paul, "A 2D Electret-Based Resonant Micro Energy Harvester," *IEEE 22nd International Conference on Micro Electro Mechanical Systems (MEMS 2009)*, pp. 1043-1046, 2009.
- [24] B. Yang, C. Lee, R. K. Kotlanka, J. Xie, and S. P. Lim, "A MEMS rotary comb mechanism for harvesting the kinetic energy of planar vibrations," *Journal of Micromechanics and Microengineering*, vol. 20, pp.065017, 2010.
- [25] Z. Yong, S. O. R. Moheimani, and M. R. Yuce, "A 2-DOF MEMS Ultrasonic Energy Harvester," *IEEE Sensors Journal*, vol. 11, pp. 155-161, 2011.
- [26] H. C. Liu, B. W. Soon, N. Wang, C. J. Tay, C. G. Quan, and C. Lee,

- "Feasibility study of a 3D vibration-driven electromagnetic MEMS energy harvester with multiple vibration modes," *Journal of Micromechanics and Microengineering*, vol. 22, pp.125020, 2012.
- [27] H. Wu, L. Tang, Y. Yang, and C. K. Soh, "Feasibility study of multi-directional vibration energy harvesting with a frame harvester," *In SPIE Smart Structures and Materials+Nondestructive Evaluation and Health Monitoring*, pp. 905703-905703, 2014.
- [28] P. D. Mitcheson, T. C. Green, E. M. Yeatman, and A. S. Holmes, "Architectures for vibration-driven micropower generators," *Journal of Microelectromechanical Systems*, vol. 13, pp. 429-440, 2004.
- [29] W. P. Mason, "Piezoelectricity, its history and applications," *The Journal of the Acoustical Society of America*, vol. 70, pp. 1561-1566, 1981.
- [30] C. Bowen, H. Kim, P. Weaver, and S. Dunn, "Piezoelectric and ferroelectric materials and structures for energy harvesting applications," *Energy & Environmental Science*, vol. 7, pp. 25-44, 2014.
- [31] W. B. Hobbs and D. L. Hu, "Tree-inspired piezoelectric energy harvesting," *Journal of Fluids and Structures*, vol. 28, pp. 103-114, 2012.
- [32] B. Lee, S. Lin, W. Wu, X. Wang, P. Chang, and C. Lee, "Piezoelectric MEMS generators fabricated with an aerosol deposition PZT thin film," *Journal of Micromechanics and Microengineering*, vol. 19, pp. 065014, 2009.
- [33] S. W. Ibrahim and W. G. Ali, "A review on frequency tuning methods for piezoelectric energy harvesting systems," *Journal of Renewable and Sustainable Energy*, vol. 4, pp. 062703, 2012.
- [34] H. S. Kim, J. H. Kim, and J. Kim, "A Review of Piezoelectric Energy Harvesting Based on Vibration," *International Journal of Precision Engineering and Manufacturing*, vol. 12, pp. 1129-1141, 2011.
- [35] S. R. Anton and H. A. Sodano, "A review of power harvesting using piezoelectric materials (2003–2006)," *Smart Materials and Structures*, vol. 16, pp. 1, 2007.
- [36] S. Saadon and O. Sidek, "A review of vibration-based MEMS piezoelectric energy harvesters," *Energy Conversion and Management*, vol. 52, pp. 500-504, 2011.
- [37] J. Kyminsis, C. Kendall, J. Paradiso, N. Gershenfeld, "Parasitic power harvesting in shoes.", *IEEE Second International Symposium on Wearable Computers*, pp. 132-139, 1998.
- [38] R. Elfrink, T. M. Kamel, M. Goedbloed, S. Matova, D. Hohlfeld, Y. V. Andel, *et al.*, "Vibration energy harvesting with aluminum nitride-based piezoelectric devices," *Journal of Micromechanics and Microengineering*, vol. 19, pp.

- 094005, 2009.
- [39] S. P. Beeby, R. N. Torah, M. J. Tudor, P. Glynne-Jones, T. O. Donnell, C. R. Saha, *et al.*, "A micro electromagnetic generator for vibration energy harvesting," *Journal of Micromechanics and Microengineering*, vol. 17, pp. 1257, 2007.
 - [40] R. Mehdi, G. Mohamed El, S. Dan, R. Don, and M. Walied, "Wide-bandwidth piezoelectric energy harvester with polymeric structure," *Journal of Micromechanics and Microengineering*, vol. 25, pp. 015018, 2015.
 - [41] S. Zhiyuan, L. Shuwei, M. Jianmin, W. Lye Sun, and W. Zhihong, "Spiral electrode d33 mode piezoelectric diaphragm combined with proof mass as energy harvester," *Journal of Micromechanics and Microengineering*, vol. 25, pp. 035004, 2015.
 - [42] G. Tang, B. Yang, J.-q. Liu, B. Xu, H.-y. Zhu, and C.-s. Yang, "Development of high performance piezoelectric d33 mode MEMS vibration energy harvester based on PMN-PT single crystal thick film," *Sensors and Actuators A: Physical*, vol. 205, pp. 150-155, 2014.
 - [43] T. Gang, L. Jing-quan, Y. Bin, L. Jiang-bo, L. He-sheng, L. Yi-gui, *et al.*, "Fabrication and analysis of high-performance piezoelectric MEMS generators," *Journal of Micromechanics and Microengineering*, vol. 22, pp. 065017, 2012.
 - [44] H. Liu, C. Lee, T. Kobayashi, C. Tay, and C. Quan, "A new S-shaped MEMS PZT cantilever for energy harvesting from low frequency vibrations below 30 Hz," *Microsystem Technologies*, vol. 18, pp. 497-506, 2012.
 - [45] R. Xu, A. Lei, C. Dahl-Petersen, K. Hansen, M. Guizzetti, K. Birkelund, *et al.*, "Screen printed PZT/PZT thick film bimorph MEMS cantilever device for vibration energy harvesting," *Sensors and Actuators A: Physical*, vol. 188, pp. 383-388, 2012.
 - [46] H. Liu, C. Lee, T. Kobayashi, C. J. Tay, and C. Quan, "Piezoelectric MEMS-based wideband energy harvesting systems using a frequency-up-conversion cantilever stopper," *Sensors and Actuators A: Physical*, vol. 186, pp. 242-248, 2012.
 - [47] Y. Ting-Ta, H. Taku, K. W. Paul, P. P. Albert, and L. Liwei, "Corrugated aluminum nitride energy harvesters for high energy conversion effectiveness," *Journal of Micromechanics and Microengineering*, vol. 21, pp. 085037, 2011.
 - [48] P. Jong Cheol, P. Jae Yeong, and L. Yoon-Pyo, "Modeling and Characterization of Piezoelectric Mode MEMS Energy Harvester," *Journal of Microelectromechanical Systems*, vol. 19, pp. 1215-1222, 2010.
 - [49] D. Shen, J.-H. Park, J. H. Noh, S.-Y. Choe, S.-H. Kim, H. C. Wickle, *et al.*,

- "Micromachined PZT cantilever based on SOI structure for low frequency vibration energy harvesting," *Sensors and actuators A: physical*, vol. 154, pp. 103-108, 2009.
- [50] C. B. Williams and R. B. Yates, "Analysis of a micro-electric generator for microsystems," *Sensors and Actuators a-Physical*, vol. 52, pp. 8-11, 1996.
- [51] C. Shearwood and R. B. Yates, "Development of an electromagnetic micro-generator," *Electronics Letters*, vol. 33, pp. 1883-1884, 1997.
- [52] S. C. L. Yuen, J. M. H. Lee, W. J. Li, and P. H. W. Leong, "An AA-sized vibration-based microgenerator for wireless sensors," *IEEE Pervasive Computing*, vol. 6, pp. 64-72, 2007.
- [53] S. P. Beeby, M. J. Tudor, R. N. Torah, S. Roberts, T. O'Donnell, and S. Roy, "Experimental comparison of macro and micro scale electromagnetic vibration powered generators," *Microsystem Technologies*, vol. 13, pp. 1647-1653, 2007.
- [54] S. D. Moss, O. R. Payne, G. A. Hart, and C. Ung, "Scaling and power density metrics of electromagnetic vibration energy harvesting devices," *Smart Materials and Structures*, vol. 24, pp. 023001, 2015.
- [55] Y. Lei, Z. Wen, and L. Chen, "Simulation and testing of a micro electromagnetic energy harvester for self-powered system," *AIP Advances*, vol. 4, pp. 031303, 2014.
- [56] S. D. Moss, G. A. Hart, S. K. Burke, and G. P. Carman, "Hybrid rotary-translational vibration energy harvester using cycloidal motion as a mechanical amplifier," *Applied Physics Letters*, vol. 104, pp. 033506, 2014.
- [57] H. Liu, Y. Qian, N. Wang, and C. Lee, "An In-Plane Approximated Nonlinear MEMS Electromagnetic Energy Harvester," *Journal of Microelectromechanical Systems*, vol. 23, pp. 740-749, 2013.
- [58] H. Liu, Y. Qian, and C. Lee, "A multi-frequency vibration-based MEMS electromagnetic energy harvesting device," *Sensors and Actuators A: Physical*, vol. 204, pp. 37-43, 2013.
- [59] W. Peihong, D. Xuhan, Y. Zhuoqing, W. Zhongzhu, and Z. Xiaolin, "Development of microelectromechanical systems electromagnetic vibration energy scavengers with a nonlinear electroplated nickel spring," *Micro & Nano Letters*, vol. 7, pp. 1173-1175, 2012.
- [60] X. Dai, X. Miao, L. Sui, H. Zhou, X. Zhao, and G. Ding, "Tuning of nonlinear vibration via topology variation and its application in energy harvesting," *Applied Physics Letters*, vol. 100, pp. 031902-4, 2012.
- [61] K. Tao, G. Ding, P. Wang, Z. Yang, and Y. Wang, "Fully integrated micro electromagnetic vibration energy harvesters with micro-patterning of bonded

- magnets," *IEEE 25th International Conference on Micro Electro Mechanical Systems (MEMS 2012)*, pp. 1237-1240, 2012.
- [62] C. Cepnik and U. Wallrabe, "A flat high performance micro energy harvester based on a serpentine coil with a single winding," *16th International on Solid-State Sensors, Actuators and Microsystems Conference (TRANSDUCERS 2011)*, pp. 661-664, 2011.
- [63] Q. Zhang, S. J. Chen, L. Baumgartel, A. Lin, and E. S. Kim, "Microelectromagnetic energy harvester with integrated magnets," *16th International on Solid-State Sensors, Actuators and Microsystems Conference (TRANSDUCERS 2011)*, pp. 1657-1660, 2011.
- [64] Y. Jiang, S. Masaoka, T. Fujita, M. Uehara, T. Toyonaga, K. Fujii, *et al.*, "Fabrication of a vibration-driven electromagnetic energy harvester with integrated NdFeB/Ta multilayered micro-magnets," *Journal of Micromechanics and Microengineering*, vol. 21, pp. 095014, 2011.
- [65] I. Sari, T. Balkan, and H. Kulah, "An electromagnetic micro power generator for low-frequency environmental vibrations based on the frequency upconversion technique," *Journal of Microelectromechanical Systems*, , vol. 19, pp. 14-27, 2010.
- [66] N. Wang and D. P. Arnold, "Fully batch-fabricated MEMS magnetic vibrational energy harvesters," *Proc. Power-MEMS*, pp. 348-351, 2009.
- [67] S. Meninger, J. O. Mur-Miranda, R. Amirtharajah, A. P. Chandrakasan, and J. H. Lang, "Vibration-to-electric energy conversion," *IEEE Transactions on Very Large Scale Integration (VLSI) Systems*, vol. 9, pp. 64-76, 2001.
- [68] S. Meninger, "A low power controller for a mems based energy convertor" Ph.D dissertation Department of electrical engineerig and computer science, MIT, 1999.
- [69] S. Roundy, P. K. Wright, & K. S. Pister, "Micro-electrostatic vibration-to-electricity converters," *ASME 2002 International Mechanical Engineering Congress and Exposition*, pp. 487-496, 2002.
- [70] P. Miao, P. D. Mitcheson, A. S. Holmes, E. M. Yeatman, T. C. Green, and B. H. Stark, "Mems inertial power generators for biomedical applications," *Microsystem Technologies-Micro-and Nanosystems-Information Storage and Processing Systems*, vol. 12, pp. 1079-1083, 2006.
- [71] P. D. Mitcheson, "Analysis and optimization of energy harvesting micro-generator systems," Ph.D, Department of Electrical and Electronic Engineering, Imperial College London, London, 2005.
- [72] P. D. Mitcheson, P. Miao, B. H. Stark, E. M. Yeatman, A. S. Holmes, and T. C. Green, "MEMS electrostatic micropower generator for low frequency

- p operation,"
- Sensors and Actuators A: Physical*
- , vol. 115, pp. 523-529, 2004.
- [73] D. Hoffmann, B. Folkmer, and Y. Manoli, "Fabrication, characterization and modelling of electrostatic micro-generators," *Journal of Micromechanics and Microengineering*, vol. 19, pp.094001 2009.
 - [74] G.-J. Sheu, S.-M. Yang, and T. Lee, "Development of a low frequency electrostatic comb-drive energy harvester compatible to SoC design by CMOS process," *Sensors and Actuators A: Physical*, vol. 167, pp. 70-76, 2011.
 - [75] J. A. Yeh, C. N. Chen, and Y. S. Liu, "Large rotation actuated by in-plane rotary comb-drives with serpentine spring suspension," *Journal of Micromechanics and Microengineering*, vol. 15, pp. 201-206, 2005.
 - [76] G. M. Sessler, *Electrets*: Laplacian Press, 1998.
 - [77] P. R. Scheeper, A. G. H. Vanderdonk, W. Olthuis, and P. Bergveld, "A review of silicon microphones," *Sensors and Actuators a-Physical*, vol. 44, pp. 1-11, 1994.
 - [78] K. Li and Y. M. Jo, "Dust Collection by a Fiber Bundle Electret Filter in an MVAC System," *Aerosol Science and Technology*, vol. 44, pp. 578-587, 2010.
 - [79] Y. Suzuki, "Recent Progress in MEMS Electret Generator for Energy Harvesting," *Ieej Transactions on Electrical and Electronic Engineering*, vol. 6, pp. 101-111, 2011.
 - [80] J. Boland, C. Yuan-Heng, Y. Suzuki, and Y. C. Tai, "Micro electret power generator," *IEEE 16th Annual International Conference on Micro Electro Mechanical Systems(MEMS 2003)*, pp. 538-541, 2003.
 - [81] V. Leonov, P. Fiorini, and C. Van Hoof, "Stabilization of positive charge in SiO₂/Si₃N₄ electrets," *IEEE Transactions on Dielectrics and Electrical Insulation*, vol. 13, pp. 1049-1056, 2006.
 - [82] V. Leonov and R. V. Schaijk, "Patterning of inorganic electrets," *IEEE Transactions on Dielectrics and Electrical Insulation*, vol. 17, pp. 994-1000, 2010.
 - [83] E. Halvorsen, E. R. Westby, S. Husa, A. Vogl, N. P. Ostbo, V. Leonov, *et al.*, "An electrostatic energy harvester with electret bias," in *International conference on Solid-State Sensors, Actuators and Microsystems (TRANSDUCERS 2009)*, pp. 1381-1384, 2009.
 - [84] S. Boisseau, A.-B. Duret, J.-J. Chaillout, and G. Despesse, "New DRIE-Patterned Electrets for Vibration Energy Harvesting," *EPJ Web of Conferences*, vol. 33, pp. 02010, 2012.
 - [85] S. Boisseau, G. Despesse, T. Ricart, E. Defay, and A. Sylvestre, "Cantilever-based electret energy harvesters," *Smart Materials & Structures*,

- vol. 20, pp. 105013, 2011.
- [86] Y. Naruse, N. Matsubara, K. Mabuchi, M. Izumi, and S. Suzuki, "Electrostatic micro power generation from low-frequency vibration such as human motion," *Journal of Micromechanics and Microengineering*, vol. 19, pp. 094002, 2009.
 - [87] H. W. Lo and Y. C. Tai, "Parylene-based electret power generators," *Journal of Micromechanics and Microengineering*, vol. 18, pp. 104006, Oct 2008.
 - [88] J. Boland, "Micro electret power generators," Ph.D, Thesis, California institute of technology, California, 2005.
 - [89] L. Hsi-wen and T. Yu-Chong, "Parylene-HT-based electret rotor generator," *IEEE 21st International Conference on Micro Electro Mechanical Systems (MEMS 2008)*, pp. 984-987, 2008.
 - [90] T. Tsutsumino, Y. Suzuki, N. Kasagi, and Y. Sakane, "Seismic Power Generator Using High-Performance Polymer Electret," *19th IEEE International Conference on Micro Electro Mechanical Systems (MEMS 2006)*, pp. 98-101, 2006.
 - [91] T. Tsutsumino and Y. Suzuki, "High-Performance Polymer Electret for Micro seismic Generators," *18th IEEE International Conference on Micro Electro Mechanical Systems (MEMS 2005)*, pp. 98-101, 2005.
 - [92] Y. Sakane, Y. Suzuki, and N. Kasagi, "The development of a high-performance perfluorinated polymer electret and its application to micro power generation," *Journal of Micromechanics and Microengineering*, vol. 18, pp. 104011, 2008.
 - [93] S. Boisseau, "Electrostatic conversion for vibration energy harvesting," *arXiv preprint arXiv:1210.5191*, 2012.
 - [94] M. S. Khalil, "The role of BaTiO₃ in modifying the dc breakdown strength of LDPE," *IEEE Transactions on Dielectrics and Electrical Insulation*, vol. 7, pp. 261-268, 2000.
 - [95] Z. Dang, L. Fan, S. Zhao, and C. Nan, "Dielectric properties and morphologies of composites filled with whisker and nanosized zinc oxide," *Materials research bulletin*, vol. 38, pp. 499-507, 2003.
 - [96] S. Liu, Z. Yang, Y. Zhang, F. Xue, S. Pan, J. Miao, *et al.*, "Micro triple-hot-wire anemometer on small sized glass tube fabricated in 5DOF UV lithography system," *28th IEEE International Conference on Micro Electro Mechanical Systems (MEMS 2015)*, pp. 714-717, 2015.
 - [97] S. W. Liu, S. W. Lye, and J. M. Miao, "Sandwich structured electrostatic/electrets parallel-plate power generator for low acceleration and low frequency vibration energy harvesting," *25th IEEE International Conference on Micro Electro Mechanical Systems (MEMS 2012)*, pp. 1277-1280, 2012.

- [98] S. W. Liu, J. M. Miao, and S. W. Lye, "High Q and low resonant frequency micro electret energy harvester for harvesting low amplitude harmonic of vibration," *26th IEEE International Conference on Micro Electro Mechanical Systems (MEMS 2013)*, pp. 837-840, 2013.
- [99] L. Bu, X. Wu, X. Wang, and L. Liu, "Silicon based polytetrafluoroethylene electrets: Preparation and corona charging characteristics," *Journal of Electrostatics*, vol. 71, pp. 666-672, 2013.
- [100] L. Bu, X. M. Wu, X. H. Wang, and L. T. Liu, "A packaged electrostatic energy harvester with micro-molded bulk electrets," *26th IEEE International Conference on Micro Electro Mechanical Systems (MEMS 2013)*, pp. 853-856, 2013.
- [101] J. W. Zhang, L. Lebrun, B. Guiffard, P. J. Cottinet, R. Belouadah, D. Guyomar, *et al.*, "Influence of corona poling on the electrostrictive behavior of cellular polypropylene films," *Sensors and Actuators: A-Physical*, vol. 175, pp. 87-93, 2012.
- [102] H. Amjadi and C. Thielemann, "Silicon-based inorganic electrets for application in micromachined devices," *IEEE Transactions on Dielectrics and Electrical Insulation*, vol. 3, pp. 494-498, 1996.
- [103] T. Genda, S. Tanaka, and M. Esashi, "Charging method of micropatterned electrets by contact electrification using mercury," *Japanese Journal of Applied Physics Part 1-Regular Papers Brief Communications & Review Papers*, vol. 44, pp. 5062-5067, 2005.
- [104] T. Genda, S. Tanaka, and M. Esashi, "Micro-patterned electret for high power electrostatic motor," *17th IEEE International Conference on Micro Electro Mechanical Systems (MEMS 2004)*, pp. 470-473, 2004.
- [105] M. Kranz, M. G. Allen, and T. Hudson, "In situ wafer-level polarization of electret films in MEMS acoustic sensor arrays," *16th International Solid-State Sensors, Actuators and Microsystems Conference (TRANSDUCERS 2011)*, pp. 914-917, 2011.
- [106] T. Fujita, T. Toyonaga, K. Nakade, K. Kanda, K. Higuchi, and K. Maenaka, "Selective electret charging method for energy harvesters using biased electrode," *Procedia Engineering*, vol. 5, pp. 774-777, 2010.
- [107] M. Honzumi, A. Ueno, K. Hagiwara, Y. Suzuki, T. Tajima, and N. Kasagi, "Soft-X-ray-charged vertical electrets and its application to electrostatic transducers," *IEEE 23rd International Conference on Micro Electro Mechanical Systems (MEMS 2010)*, pp. 635-638, 2010.
- [108] Y. Feng, K. Hagiwara, Y. Iguchi, and Y. Suzuki, "Trench-filled cellular parylene electret for piezoelectric transducer," *Applied Physics Letters*, vol.

- 100, p. 262901, 2012.
- [109] P. Basset, D. Galayko, A. M. Paracha, F. Marty, A. Dudka, and T. Bourouina, "A batch-fabricated and electret-free silicon electrostatic vibration energy harvester," *Journal of Micromechanics and Microengineering*, pp.115025, vol. 19, 2009.
 - [110] Y. Suzuki, "Energy Harvesting from Vibration Using Polymer Electret," *International Symposium on Micro-NanoMechatronics and Human Science*, , pp. 180-183, 2008.
 - [111] C. Kamezawa, Y. Suzuki, and N. Kasagi, "Mechanical Response Evaluation of High-Thermally-Stable-Grade Parylene Spring," *22nd IEEE International Conference on Micro Electro Mechanical Systems(MEMS 2009)*, pp. 615-618, 2009.
 - [112] D. Miki, Y. Suzuki, and N. Kasagi, "Effect of nonlinear external circuit on electrostatic damping force of micro electret generator," *International Solid-State Sensors, Actuators and Microsystems Conference (TRANSDUCERS 2009)*, pp. 636-639, 2009.
 - [113] M. Edamoto, Y. Suzuki, N. Kasagi, K. Kashiwagi, Y. Morizawa, T. Yokoyama, *et al.*, "Low-Resonant-Frequency Micro Electret Generator for Energy Harvesting Application," *22nd IEEE International Conference on Micro Electro Mechanical Systems(MEMS 2009)*, pp. 1059-1062, 2009.
 - [114] D. Miki, M. Honzumi, Y. Suzuki, and N. Kasagi, "Large-amplitude MEMS electret generator with nonlinear spring," *23rd IEEE International Conference on Micro Electro Mechanical Systems(MEMS 2010)*, pp. 176-179, 2010.
 - [115] Y. Suzuki, D. Miki, M. Edamoto, and M. Honzumi, "A MEMS electret generator with electrostatic levitation for vibration-driven energy-harvesting applications," *Journal of Micromechanics and Microengineering*, vol. 20, pp.104002, 2010.
 - [116] Y. Suzuki and S. Kawasaki, "An autonomous wireless sensor powered by vibration-driven energy harvesting in a microwave wireless power transmission system," *Proceedings of the 5th European Conference on Antennas and Propagation (EUCAP)*, pp. 3897-3900, 2011.
 - [117] T. Takahashi, M. Suzuki, T. Hirata, N. Matsushita, R. Yoneya, J. Onishi, *et al.*, "Electret energy harvesting based on fringe electrical field change inside trenched ferroelectric," *24th IEEE International Conference on Micro Electro Mechanical Systems(MEMS 2011)*, pp. 1305-1308, 2011.
 - [118] F. Wang, C. Bertelsen, G. Skands, T. Pedersen, and O. Hansen, "Reactive ion etching of polymer materials for an energy harvesting device," *Microelectronic Engineering*, vol. 97, pp. 227-230, 2012.

-
- [119] Y. Chiu and Y.-C. Lee, "Flat and robust out-of-plane vibrational electret energy harvester," *Journal of Micromechanics and Microengineering*, vol. 23, pp. 015012, 2013.
- [120] L. Yi, e.-B. Zeynep, and P. B. Donald, "A hybrid electrostatic micro-harvester incorporating in-plane overlap and gap closing mechanisms," *Journal of Micromechanics and Microengineering*, vol. 25, pp. 035027, 2015.
- [121] F. Wang and O. Hansen, "Electrostatic energy harvesting device with out-of-the-plane gap closing scheme," *Sensors and Actuators A: Physical*, vol. 211, pp. 131-137, 2014.
- [122] P. Basset, D. Galayko, F. Cottone, R. Guillemet, E. Blokhina, F. Marty, *et al.*, "Electrostatic vibration energy harvester with combined effect of electrical nonlinearities and mechanical impact," *Journal of Micromechanics and Microengineering*, vol. 24, pp. 035001, 2014.
- [123] K. Tao, S. Liu, S. W. Lye, J. Miao, and X. Hu, "A three-dimensional electret-based micro power generator for low-level ambient vibrational energy harvesting," *Journal of Micromechanics and Microengineering*, vol. 24, pp. 065022, 2014.
- [124] S. D. Nguyen, E. Halvorsen, and I. Paprotny, "Bistable springs for wideband microelectromechanical energy harvesters," *Applied Physics Letters*, vol. 102, pp. 023904-4, 2013.
- [125] C. Andrea, W. Fei, and H. Ole, "An electret-based energy harvesting device with a wafer-level fabrication process," *Journal of Micromechanics and Microengineering*, vol. 23, pp. 114010, 2013.
- [126] K. C. S. Kim, "2D vibration based MEMS energy harvester," *International Conference on Renewable Energies and Power Quality*, pp.1-4, 2012.
- [127] K. Matsumoto, K. Saruwatari, and Suzuki, Y. Vibration-powered battery-less sensor node using MEMS electret generator. *Proc. Power MEMS2013*, pp. 134-137, 2013.
- [128] U. Bartsch, J. Gaspar, and O. Paul, "Low-frequency two-dimensional resonators for vibrational micro energy harvesting," *Journal of Micromechanics and Microengineering*, vol. 20, pp. 035016, 2010.
- [129] J. Yang, X. Yue, Y. Wen, P. Li, Q. Yu, and X. Bai, "Design and analysis of a 2D broadband vibration energy harvester for wireless sensors," *Sensors and Actuators A: Physical*, vol. 205, pp. 47-52, 2014.
- [130] M. I. Younis, *MEMS Linear and Nonlinear Statics and Dynamics*, Springer Science Business Media, 2011.
- [131] L. Tang, Y. Yang, and C. Soh, "Broadband Vibration Energy Harvesting Techniques," in *Advances in Energy Harvesting Methods*, Springer New York,

- pp. 17-61, 2013.
- [132] S. C. Stanton, C. C. McGehee, and B. P. Mann, "Reversible hysteresis for broadband magnetopiezoelectric energy harvesting," *Applied Physics Letters*, vol. 95, pp. 174103, 2009.
 - [133] A. Hajati and S.-G. Kim, "Ultra-wide bandwidth piezoelectric energy harvesting," *Applied Physics Letters*, vol. 99, pp. 083105, 2011.
 - [134] P.-C. Huang, T.-H. Tsai, and Y.-J. Yang, "Wide-bandwidth piezoelectric energy harvester integrated with parylene-C beam structures," *Microelectronic Engineering*, vol. 111, pp. 214-219, 2013.
 - [135] M. S. M. Soliman, E. M. Abdel-Rahman, E. F. El-Saadany, and R. R. Mansour, "A wideband vibration-based energy harvester," *Journal of Micromechanics and Microengineering*, vol. 18, pp. 115021, 2008.
 - [136] L. Huicong, L. Chengkuo, K. Takeshi, T. Cho Jui, and Q. Chenggen, "Investigation of a MEMS piezoelectric energy harvester system with a frequency-widened-bandwidth mechanism introduced by mechanical stoppers," *Smart Materials and Structures*, vol. 21, pp. 035005, 2012.
 - [137] B. Andà, S. Baglio, C. Trigona, N. Dumas, L. Latorre, and P. Nouet, "Nonlinear mechanism in MEMS devices for energy harvesting applications," *Journal of Micromechanics and Microengineering*, vol. 20, pp. 125020, 2010.
 - [138] S. L. Eli and K. W. Paul, "Resonance tuning of piezoelectric vibration energy scavenging generators using compressive axial preload," *Smart Materials and Structures*, vol. 15, pp. 1413, 2006.
 - [139] C. P. Le and E. Halvorsen, "MEMS electrostatic energy harvesters with end-stop effects," *Journal of Micromechanics and Microengineering*, vol. 22, pp. 074013, 2012.
 - [140] M. Soliman, E. M. Abdel-Rahman, E. F. El-Saadany, and R. R. Mansour, "A Design Procedure for Wideband Micropower Generators," *Journal of Microelectromechanical Systems*, vol. 18, pp. 1288-1299, 2009.
 - [141] D. S. Nguyen, E. Halvorsen, G. U. Jensen, and A. Vogl, "Fabrication and characterization of a wideband MEMS energy harvester utilizing nonlinear springs," *Journal of Micromechanics and Microengineering*, vol. 20, pp. 125009, 2010.
 - [142] L. G. W. Tvedt, D. S. Nguyen, and E. Halvorsen, "Nonlinear Behavior of an Electrostatic Energy Harvester Under Wide- and Narrowband Excitation," *Journal of Microelectromechanical Systems*, vol. 19, pp. 305-316, 2010.
 - [143] X. Huan, H. Yuntai, and W. Qing-Ming, "Broadband piezoelectric energy harvesting devices using multiple bimorphs with different operating frequencies," *IEEE Transactions on Ultrasonics, Ferroelectrics, and*

- Frequency Control*, vol. 55, pp. 2104-2108, 2008.
- [144] M. Ferrari, V. Ferrari, M. Guizzetti, D. Marioli, and A. Taroni, "Piezoelectric multifrequency energy converter for power harvesting in autonomous microsystems," *Sensors and Actuators A: Physical*, vol. 142, pp. 329-335, 2008.
 - [145] J.-Q. Liu, H.-B. Fang, Z.-Y. Xu, X.-H. Mao, X.-C. Shen, D. Chen, *et al.*, "A MEMS-based piezoelectric power generator array for vibration energy harvesting," *Microelectronics Journal*, vol. 39, pp. 802-806, 2008.
 - [146] I. Sari, T. Balkan, and H. Kulah, "An electromagnetic micro power generator for wideband environmental vibrations," *Sensors and Actuators A: Physical*, vol. 145-146, pp. 405-413, 2008.
 - [147] S. Roundy, E. S. Leland, J. Baker, E. Carleton, E. Reilly, E. Lai, *et al.*, "Improving power output for vibration-based energy scavengers," *Pervasive Computing, IEEE*, vol. 4, pp. 28-36, 2005.
 - [148] B. Yang, C. Lee, W. F. Xiang, J. Xie, J. H. He, R. K. Kotlanka, *et al.*, "Electromagnetic energy harvesting from vibrations of multiple frequencies," *Journal of Micromechanics and Microengineering*, vol. 19, pp. 035001, 2009.
 - [149] Y. Tadesse, Shujun Zhang, and S. Priya, "Multimodal Energy Harvesting System: Piezoelectric and Electromagnetic," *Journal of Intelligent Material Systems and Structures*, vol. 20, pp. 625-632, 2009.
 - [150] Q. Ou, X. Chen, S. Gutschmidt, A. Wood, N. Leigh, and A. F. Arrieta, "An experimentally validated double-mass piezoelectric cantilever model for broadband vibration-based energy harvesting," *Journal of Intelligent Material Systems and Structures*, vol. 23, pp. 117-126, 2012.
 - [151] L. Hsi-wen, W. Rus, and T. Yu-Chong, "A simple micro electret power generator," *20th IEEE International Conference on Micro Electro Mechanical Systems (MEMS 2007)*, pp. 859-862, 2007.
 - [152] A. Modafe, N. Ghalichechian, A. Frey, J. H. Lang, and R. Ghodssi, "Microball-bearing-supported electrostatic micromachines with polymer dielectric films for electromechanical power conversion," *Journal of Micromechanics and Microengineering*, vol. 16, pp. 182, 2006.
 - [153] S. Boisseau, G. Despesse, and A. Sylvestre, "Optimization of an electret-based energy harvester," *Smart Materials & Structures*, vol. 19, pp. 075015, 2010.
 - [154] S. W. Liu, Z. Y. Shen, S. W. Lye, and J. M. Miao, "Stable micro sized electret array produced by localised charging using a silicon shadow mask," *Micro & Nano Letters*, vol. 7, pp. 1094-1096, 2012.
 - [155] Y. Minakawa, R. Chen, and Y. Suzuki, "X-shaped-spring enhanced MEMS electret generator for energy harvesting," *17th International Conference on*

-
- Solid-State Sensors, Actuators and Microsystems (TRANSDUCERS 2013 & EUROSENSORS XXVII)*, pp. 2241-2244, 2013.
- [156] A. Krishnan and Y. J. Suresh, "A simple cubic linear element for static and free vibration analyses of curved beams," *Computers & Structures*, vol. 68, pp. 473-489, 1998.
 - [157] S. Srpčič and M. Saje, "Large deformations of thin curved plane beam of constant initial curvature," *International Journal of Mechanical Sciences*, vol. 28, pp. 275-287, 1986.
 - [158] E. A. Baum, T. J. Lewis, and R. Toomer, "The lateral motion of charge on thin films of polyethylene terephthalate," *Journal of Physics D: Applied Physics*, vol. 11, pp. 963, 1978.
 - [159] K. E. Petersen, "Silicon as a mechanical material," *Proceedings of the IEEE*, vol. 70, pp. 420-457, 1982.
 - [160] F. Ericson and J. Å. Schweitz, "Micromechanical fracture strength of silicon," *Journal of Applied Physics*, vol. 68, pp. 5840-5844, 1990.
 - [161] A. McCarty and I. Chasiotis, "Quantitative Failure Analysis for MEMS Materials with Multiple Active Flaw Populations," *Proc. Soc. Exper. Mech*, pp. 1103, 2005.
 - [162] M. A. Fadi, I. Y. Mohammad, and M. O. Hassen, "On the nonlinear resonances and dynamic pull-in of electrostatically actuated resonators," *Journal of Micromechanics and Microengineering*, vol. 19, p. 045013, 2009.
 - [163] M. Dhiman, A. Andreas, and R. Saibal, "A nonlinear stretching based electromagnetic energy harvester on FR4 for wideband operation," *Smart Materials and Structures*, vol. 24, pp. 015013, 2015.
 - [164] N. G. Stephen, "On energy harvesting from ambient vibration," *Journal of Sound and Vibration*, vol. 293, pp. 409-425, 2006.
 - [165] C. Bangtao and M. Jianmin, "Influence of deep RIE tolerances on comb-drive actuator performance," *Journal of Physics D: Applied Physics*, vol. 40, pp. 970-976, 2007.

Author's publications

Invited Book Chapter

[1] **K. Tao**, S.W. Lye, J.M. Miao and X. Hu, "Micro electret-based power generator for ambient vibrational energy harvesting" in *Energy Harvesting: Technology, Methods and Applications* (New York: Nova Science Publishers Inc.), pp. 19-54, 2016.

Journal Publications

[1] **K. Tao**, S.W. Lye, J.M. Miao, L.H. Tang and X. Hu, "A novel two-degree-of-freedom MEMS electromagnetic vibration energy harvester", *Journal of Micromechanics and Microengineering* vol. 26, pp. 035020, 2016.

[2] **K. Tao**, S.W. Lye, L.H. Tang, X. Xia, J.M. Miao, and X. Hu, "Out-of-plane electret-based MEMS energy harvester with the combined nonlinear effect from electrostatic force and a mechanical elastic stopper", *Journal of Micromechanics and Microengineering*, vol. 10, pp. 104014, 2015.

[3] **K. Tao**, J.M. Miao, S.W. Lye and X. Hu, "Sandwich-structured two-dimensional MEMS electret power generator for low-level ambient vibrational energy harvesting", *Sensors and actuators A: Physics* vol. 228, pp. 95-103, 2015.

[4] **K. Tao**, S.W. Lye, J.M. Miao and X. Hu, "Design and implementation of an out-of-plane MEMS electret power generator for low-level ambient vibrational energy harvesting", *Microelectronics Engineering* vol. 135, pp. 32-37, 2015.

[5] **K. Tao**, S.W. Lye, J.M. Miao, and X. Hu, "Performance enhancement of an out-of-plane electret-based vibrational energy harvester with dual charged plates", *Journal of Physics: Conference Series* vol. 557, pp. 012064, 2014.

[6] **K. Tao**, S.W. Liu, S.W. Lye, J.M. Miao and X. Hu, "A three-dimensional electret-based micro power generator for low-level ambient vibrational energy harvesting", *Journal of Micromechanics and Microengineering* vol. 24, pp. 065022, 2014.

Conference proceedings

[1] **K. Tao**, J. Wu, N. Wang, S.W. Lye and J.M. Miao, "Broadband energy harvesting using a nonlinear 2DOF MEMS electret-based micro power generator", *29th IEEE International Conference on Micro Electro Mechanical Systems (IEEE MEMS 2016)* Shanghai, 24-28 January (**Acceptance rate 39%**)

[2] **K. Tao**, S.W. Lye, J.M. Miao and X. Hu "A sandwich-structured MEMS electret power generator for multi-directional vibration energy harvesting", *18th International Conf. on Solid-State Sensors, Actuators and Microsystems (TRANSDUCERS 2015)*, Alaska, 22-26 June (**Oral presentation, oral acceptance rate 20.7%**)

[3] **K. Tao**, S.W. Lye, J.M. Miao and X. Hu "Experimental Study of a Micro-patterned PDMS/PTFE Composite Electret for MEMS Energy Harvesting Devices", *8th International Conference on Materials for Advanced Technologies of the Materials Research Society of Singapore (ICMAT 2015)*, Singapore, 28 June to 03 July

[4] **K. Tao**, S.W. Lye and J.M. Miao "A three-dimensional electrostatic/electret micro power generator for low acceleration and low frequency vibrational energy harvesting", *27th IEEE International Conference on Micro Electro Mechanical Systems (IEEE MEMS 2014)* San Francisco, 26-30 January (**Acceptance rate 36%**)